Observations of Active Galactic Nuclei from Radio to Gamma-rays

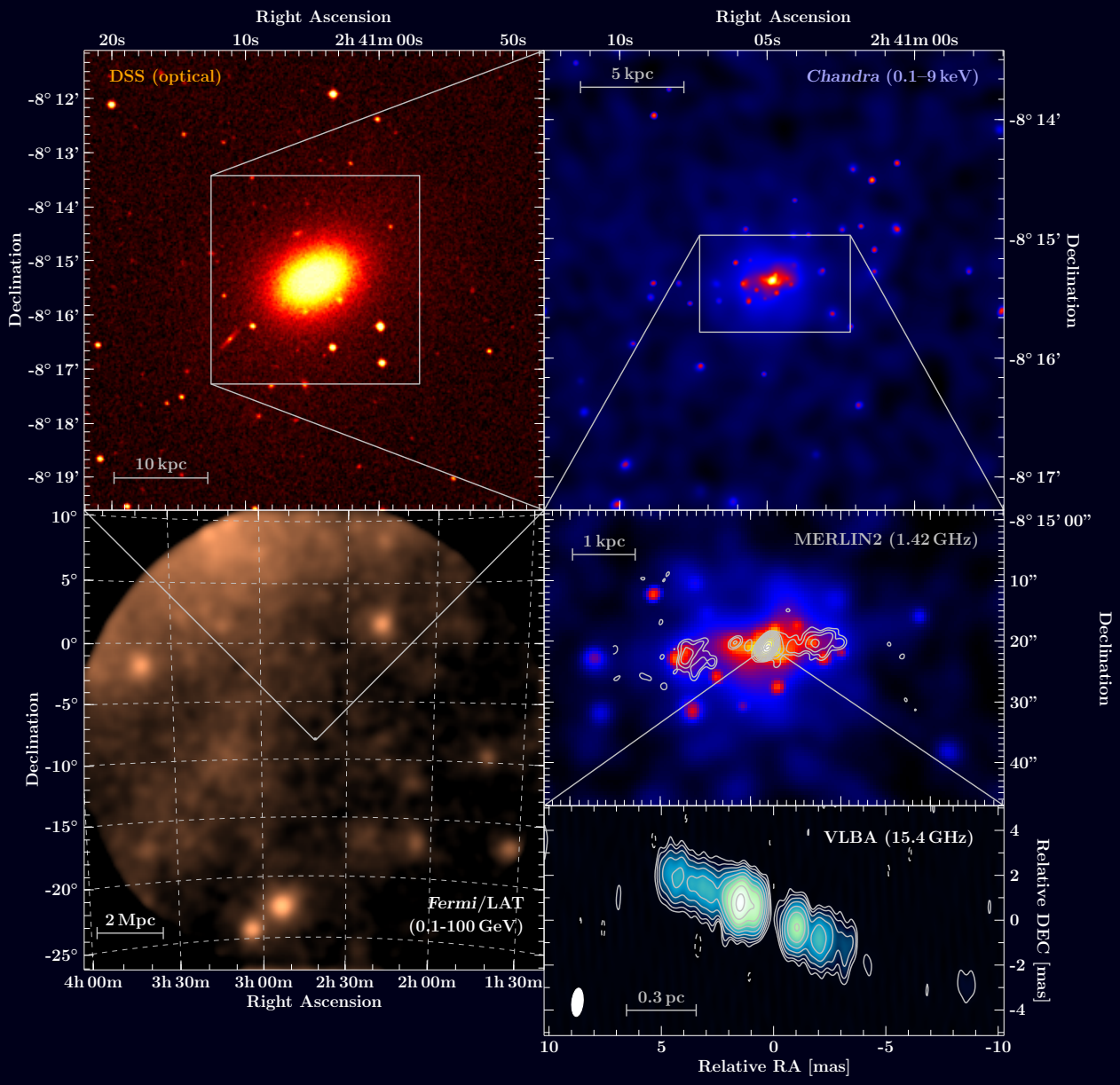

Moritz Böck

Supervisors:
Prof. Dr. Jörn Wilms and Prof. Dr. Matthias Kadler

performed at:
Dr. Karl Remeis-Sternwarte Bamberg
Erlangen Centre for Astroparticle Physics

The cover picture shows images of the Active Galactic Nucleus NGC 1052 in different energy ranges and with different angular resolution. The scale bar indicates the projected length in the distance of the source. A high-energy (0.1–100 GeV) image in the bottom left has been obtained with *Fermi*/LAT (integrated exposure of years). An optical image is shown in the top left and a soft X-ray image obtained with *Chandra* in the top right. An overlay of this image with radio emission (contour lines) seen with MERLIN has been created (middle right). In the bottom right a VLBA radio image with high angular resolution is shown. More information on this source and the used observation techniques are provided within this thesis.

Observations of Active Galactic Nuclei from Radio to Gamma-rays

Beobachtungen aktiver galaktischer Kerne von Radiowellen bis zu Gammastrahlen

Der Naturwissenschaftlichen Fakultät der
Friedrich-Alexander-Universität Erlangen-Nürnberg

zur

Erlangung des Doktorgrades Dr. rer. nat.

vorgelegt von

Moritz Böck

aus Regensburg

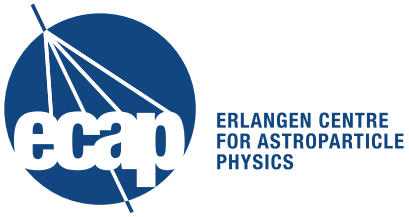

Als Dissertation genehmigt
von der Naturwissenschaftlichen Fakultät
der Friedrich-Alexander-Universität Erlangen-Nürnberg

Tag der mündlichen Prüfung:	September 2012
Vorsitzender der Promotionskommission:	
Erstberichterstatter:	Prof. Dr. Jörn Wilms
Zweitberichterstatter:	Prof. Dr. Matthias Kadler

Erweiterte deutsche Zusammenfassung

In dieser Arbeit werden aktive galaktische Kerne – die hellsten Objekte mit dauerhafter Emission im Universum – behandelt. Nach aktuellem Wissensstand bestehen sie aus mehreren Komponenten. Das zentrale Objekt solcher Systeme ist ein supermassives schwarzes Loch, das sich im Zentrum einer Galaxie befindet. Abschätzungen der Masse von schwarzen Löchern dieser Art liegen im Bereich von Millionen bis zu mehreren Milliarden von Sonnenmassen. Es wird heute vermutet, dass jede größere Galaxie ein zentrales schwarzes Loch beherbergt. Per Definition ist es selbst nicht direkt sichtbar, kann aber aufgrund des Einflusses auf seine Umgebung nachgewiesen werden. Der Unterschied zwischen einem supermassiven schwarzen Loch als nahezu unsichtbares oder als eines der hellsten Objekte im Universum beruht somit auf dessen Umgebung. Das enorme Gravitationsfeld eines schwarzen Lochs wirkt auf Material in seiner Nähe. Derartiges Material, beispielsweise Gaswolken, Staubpartikel und Sternwinde, stellt gewissermaßen den Treibstoff des aktiven galaktischen Kerns dar. Aufgrund der Drehimpulserhaltung wird das Material auf Umlaufbahnen um das schwarze Loch gezwungen und eine Akkretionsscheibe kann sich bilden. Reibung und Turbulenzen führen zu einer Drehimpulsübertragung und damit dazu, dass sich das Material dem schwarzen Loch nähert und Energie abstrahlt. Der Akkretionsprozess ist äußerst effizient und erklärt teilweise die extremen Leuchtkräfte aktiver galaktischer Kerne. Die erwartete thermische Emission einer Akkretionsscheibe reicht jedoch nicht aus, um die komplette Strahlung aktiver galaktischer Kerne zu erklären. Beobachtungen zeigen, dass manche dieser Objekte im kompletten elektromagnetischen Spektrum sichtbar sind. Der Ursprung der Emission im Radio- sowie vermutlich auch im Hochenergiebereich scheinen Jets zu sein. Im Gegensatz zu Material, das vom schwarzen Loch eingesaugt wird, handelt es sich dabei um gebündelte Teilchenstrahlen, die sich von diesem mit nahezu Lichtgeschwindigkeit entfernen. Aktive galaktische Kerne sind noch nicht komplett verstanden. Es gibt noch zahlreiche offene Fragen, wie zum Beispiel die exakte Akkretionsgeometrie, die Entstehung und Zusammensetzung der relativistischen Jets, die Wechselwirkungen zwischen den Bestandteilen dieser Systeme, sowie die genauen Ursprungsorte und die zugrundeliegenden physikalischen Prozesse der Emission in verschiedenen Energiebereichen. Um diese Fragen zu adressieren wird in dieser Arbeit eine Multiwellenlängenanalyse aktiver galaktischer Kerne durchgeführt. Die unterschiedlichen Energiebereiche und Beobachtungesmethoden erlauben Einblicke in verschiedene Prozesse und Eigenschaften dieser Objekte.

Eine Studie des Zusammenhangs zwischen Akkretion und Eigenschaften des Jets erfolgt anhand des Objekts NGC 1052 unter Verwendung von Radio- und Röntgenbeobachtungen. Es handelt sich dabei um eine Galaxie mit einem aktiven Kern. Im Radiobreich zeigt sich ein doppelseitiger Jet mit einer projizierten Länge von mehreren kpc. Zusätzlich befindet sich im Zentrum von NGC 1052 eine deutliche Röntgenquelle. Der umfangreiche Datensatz besteht aus zahlreichen Beobachtungen mit verschiedenen Instrumenten und erlaubt detaillierte Analysen. Im Röntgenbereich sind dabei lange Beobachtungen mit empfindlichen Teleskopen verfügbar, mit welchen einerseits die Verteilung der Röntgenstrahlung innerhalb der Galaxie mit hoher Winkelauflösung und andererseits spektrale Details untersucht werden können. Es zeigt sich, dass es ausgedehnte Röntgenemission gibt, deren Verteilung vereinbar mit der Position des im Radiobereich sichtbaren Jets ist. Das Spektrum dieser Komponente kann mit Bremsstrahlung und der Emission eines thermischen Plasmas modelliert werden. Ihr Ursprung ist vermutlich die Wechselwirkung des Jets mit interstellarer Materie innerhalb der Galaxie. Die Röntgenstrahlung bei höheren Energien stammt größtenteils aus dem Kern der Galaxie und erlaubt Rückschlüsse auf die Umgebung des supermassiven schwarzen Lochs. Die beobachtete starke Absorption gewährt Einblicke in die Eigenschaften des Materials in dieser Region.

Interferometrische Radiobeobachtungen mit großen Entfernungen zwischen Teleskopen ermöglichen Winkelauflösungen, die feiner als Millibogensekunden sind. Damit ist es möglich, Strukturen im Jet auf Größenordnungen eines Zehntel Parsecs zu untersuchen. Im Rahmen dieser Arbeit

wurden die verfügbaren Radiobeobachtungen dieser Art untersucht, die im Zeitraum von 1995 bis 2012 durchgeführt wurden. Es lässt sich damit die zeitliche Entwicklung der Strukturen im Jet verfolgen und deren Bewegungsgeschwindigkeit bestimmen. Zusätzlich konnte die typische Intensitätsentwicklung dieser Jetkomponenten auf ihrer Bewegung entlang der Jetachse bestimmt werden. Eine Extrapolation der Trajektorien zeigt, dass es bis zu einem Jahr dauert, bis eine Komponente vom schwarzen Loch die Region erreicht, ab welcher sie bei 15 GHz sichtbar wird. Wenn neue Komponenten den (im Radiobereich nicht sichtbaren) Kern verlassen, zeigt sich Variabilität im Röntgenbereich. Es werden Intensitätseinbrüche sowie Erhöhungen beobachtet. Ein starkes Ausstoßereignis im Jet ereignete sich bei niedriger Röntgenintensität. Diese erhöhte sich in den beiden folgenden Jahren, bis weitere Jetkomponenten ausgestoßen wurden.

Für ein besseres Verständnis aktiver galaktischer Kerne ergänzen Studien größerer Samples die Analysen individueller Quellen. In dieser Arbeit werden das TANAMI und das MOJAVE Programm erläutert, sowie die dadurch ermöglichten Studien. In beiden Programmen werden Auswahlen aktiver galaktischer Kerne mit Jets mit einer radiointerferometrischen Beobachtungskampagne untersucht. Mit diesen Langzeitstudien ist es möglich, Eigenschaften, wie etwa die Jetgeschwindigkeit, zu bestimmen und mit Beobachtungen in anderen Energiebereichen zu vergleichen. Diese Arbeit stellt einen wichtigen Beitrag zum TANAMI-Programm dar. Es wurden beispielsweise Visualisierungsmethoden für Radiobilder entwickelt.

Im letzten Abschnitt der Arbeit werden die γ-Strahlungseigenschaften der aktiven galaktischen Kerne der TANAMI- und MOJAVE-Samples behandelt. Hierfür wird zunächst ein Überblick über die γ-Strahlenastronomie und die *Fermi*-Mission, die seit 2008 in Betrieb ist, gegeben. Basierend auf Daten, die mit *Fermi*/LAT gemessen wurden, werden die Eigenschaften der Objekte in den Samples im Energiebereich von 100 MeV bis 100 GeV analysiert. Dazu wurde nach γ-Strahlungsquellen gesucht, die signifikant mit *Fermi*/LAT detektiert wurden. Es zeigte sich, dass fast alle BL Lac-Objekte detektiert sind, sowie die Mehrheit der Quasare. Im Gegensatz dazu sind nur wenige Radiogalaxien in diesem Energiebereich sichtbar. Für aktive galaktische Kerne, die nicht mit *Fermi*/LAT detektierbar sind, wurden obere Grenzen für deren γ-Strahlungsfluss bestimmt. Unter Verwendung der Entfernung der Quellen wurden die Leuchtkräfte bestimmt. Diese sind am geringsten für Radiogalaxien und größer für BL Lacs. Die höchsten Leuchtkräfte sind die der Quasare. Ein Vergleich der vom MOJAVE-Team bestimmten Jetgeschwindigkeiten mit Eigenschaften der Quellen im Hochenergiebereich unterstützt die Vermutung, dass die γ-Strahlung ihren Ursprung im Doppler-Boosting in relativisitischen Jets hat, die unter einem kleinen Winkel zur Sichtlinie ausgerichtet sind. Die Jetgeschwindigkeiten zeigen, dass Lorentzfaktoren von mindestens $\gamma = 45$ im MOJAVE-Sample existieren. Aufgrund der hohen Geschwindigkeiten wird die Strahlungsintensität in Bewegungsrichtung um ein Vielfaches erhöht.

Extended Abstract

In this work, Active Galactic Nuclei (AGN) – the brightest persistent objects in the universe – are discussed. According to current knowledge they consist out of several components. The central object of such systems is a supermassive black hole located in the center of a galaxy. Estimated masses of such black holes range from millions to billions of solar masses. It is assumed that every larger galaxy hosts a central black hole. By definition, the black hole itself is not visible directly, but information on it can be obtained based on the influence on its environment. Wether a supermassive black hole is almost invisible or is one of the brightest objects in the universe depends on its environment. The enormous gravitational field of the black hole affects material in its surrounding. Matter, such as gas, dust particles or stellar wind virtually provides the fuel for the AGN. Due to conservation of angular momentum, material can orbit the black hole and an accretion disk can form. Friction and turbulences lead to a transfer of angular momentum and thus cause the material to approach the black hole and to radiate energy. The accretion process is highly efficient and partly explains the extreme luminosities of Active Galactic Nuclei. The thermal emission of the accretion disk is, however, insufficient for explaining the total emission of AGN. Observations show that some of these objects are visible throughout the complete electromagnetic spectrum. The emission in the radio regime as well as, most likely, high-energy emission seem to originate from jets. Unlike material accreted by the black hole, jets are collimated outflows with velocities near the speed of light. AGN are not completely understood. There are numerous open questions remaining, such as the exact accretion geometry, the formation and composition of the relativistic jets, the interaction between different components of these systems, as well as the place of origin and the underlying physical processes of the emission in different energy ranges. In order to address these questions a multiwavelength analysis of AGN has been performed in this work. The different energy regimes and observational techniques allow for insights into different processes and properties of such objects.

A study of the connection between the accretion disk and properties of the jet has been done based on the object NGC 1052 using radio and X-ray observations. This object is a galaxy with an active nucleus. In the radio regime a double-sided jet with a projected length of several kpc is visible. In addition, the center of NGC 1052 hosts a clear X-ray source. The massive data set consists of numerous observations with different instruments allowing for detailed analyses. In the X-ray regime deep observations with sensitive telescopes are available, with which the distribution of X-ray emission within the host galaxy can be studied with high angular resolution. Furthermore the spectral properties can be analyzed in detail. It turned out that there is extended X-ray emission, whose distribution is consistent with the position of the jet visible in the radio regime. The spectrum of this X-ray component can be modeled with bremsstrahlung and the emission of a thermal plasma. The origin of this emission is most likely the interaction of the jet with interstellar material within the host galaxy. X-ray emission at higher energies originates from the nucleus of the galaxy and allows one to draw conclusions on the environment of the supermassive black hole. The observed strong absorption provides insights into properties of material in this region.

Interferometric radio observations with long baselines yield angular resolutions higher than milliarcseconds. In this way it is possible to resolve structures in jets on scales of a tenth of a parsec. Within the scope of this work the available radio observations with this technique, which were performed between 1995 and 2012, were analyzed. With it, the temporal evolution of structures in the jet can be tracked and velocities can be determined. In addition, the typical intensity evolution of features in the jet could be determined. An extrapolation of the trajectories reveals that it takes up to a year for a component to move from the black hole to the region where it becomes visible at 15 GHz. At times when new components are ejected from the region close to the black hole, variability in the X-ray regime is visible. Dips and flares are observed. A strong ejection event occurred at low X-ray intensity, which increased during the two subsequent years

until new components were ejected.

For a better understanding of AGN, studies of AGN samples complement analyses of individual sources. In this work the TANAMI and MOJAVE programs are described, as well as the thereby enabled studies. In both programs AGN samples are monitored with very-long-baseline-interferometry (VLBI). In these long-term studies it is possible to determine jet properties, such as the jet speed, and to compare them with observations in other energy regimes. Contributions to the TANAMI program have been done within the scope of this work, e.g., visualization methods for radio images have been developed.

In the last section of this work, the γ-ray properties of the AGN in the TANAMI and MOJAVE samples are discussed. Initially an overview on γ-ray astronomy and the *Fermi* mission, which has been in operation since 2008, is given. Based on data obtained with *Fermi*/LAT, the properties of the objects in the sample in the energy range of 100 MeV to 100 GeV are analyzed. For this purpose γ-ray sources were searched that are detected with *Fermi*/LAT. It turned out that almost all BL Lac objects are detected, as well as the majority of the quasars in the samples. In contrast, only a few of the radio galaxies are visible in this energy range. For AGN in the sample that are not detected with *Fermi*/LAT, upper limits on the γ-ray flux have been calculated. Given the distances of the sources, the luminosities were determined. These are smallest for radio galaxies and larger for BL Lacs. The highest luminosities are those of the quasars. A comparison of the jet speeds, which are provided by the MOJAVE team, with properties of the sources in the high-energy regime confirms the assumption that γ-rays in AGN originate from Doppler boosting in relativistic jets oriented close to the line of sight. The jet speeds show that there are Lorentz factors of at least $\gamma = 45$ included in sources of the MOJAVE sample. Based on the high velocities the intensity is increased by multiples.

Contents

Chapter 1

Introduction

AGN – this compact expression is the central object of this thesis. AGN is the abbreviation of Active Galactic Nuclei. As the name says these objects are located in the center of galaxies and are "active". Their activity makes them the most luminous persistent objects in the universe. Huge amounts of material are being devoured by supermassive black holes, gas is ionized turbulent electromagnetic fields of gigantic size are formed, and particles are accelerated to relativistic velocities. The emission covers all wavelengths. In this work, multiwavelength observations of AGN are presented.

The structure of this work is the following: In an extended introduction (Sect. 1) an overview on Active Galactic Nuclei and their relativistic outflows is given. The subsequent chapters deal with the analysis of radio and X-ray data (Sect. 2) and a study of the individual source NGC 1052 (Sect. 3) in these energy regimes. The aim of this study is to obtain insights into the connection between the radio jet on subparsec scales, which are seen with radio interferometry, and the inner accretion flow, which is probed with X-ray observations. After the analysis of an individual source, the complementary capabilities of research based on monitoring AGN samples are discussed (Sect. 4). Having discussed analyses from the radio regime up to X-rays, high-energy astronomy is adressed in the last chapter (Sect. 5), in which the γ-ray properties of AGN are discussed and compared with results obtained at other wavelengths. The thesis concludes with a summary and an outlook (Sect. 6).

1.1 Active Galactic Nuclei

1.1.1 Observational history

Discovery of galaxies Previous to the detection of AGN there was obviously the discovery of galaxies, which started with the understanding of the Milky Way, the galaxy in which our solar system is located. The Milky Way is a clear bright band of the night sky, which is visible with the naked eye. It had been known by early civilizations, but the understanding of its true nature took place just in the modern era. In the following the history of understanding galaxies and AGN is briefly outlined (more information is given, e.g., by Carroll & Ostlie, 2006). Galileo Galilei (1564–1642) found that the Milky Way is characterized by a large amount of individual stars.[1] Based on the distribution of stars on the sky, Immanuel Kant and Thomas Wright proposed in the 18th century that the solar system is located within a disk-like distribution of stars. Thomas Wright already had the idea that the Galaxy is a rotating collection of stars, which are bound by gravity. First attempts to determine the size and structure of this system of stars have been performed by William Herschel in the end of the 18th century. The used method was to count stars

[1] It had been already suggested about four centuries before Christ by the Greek philosopher Democritus that the band of the Milky Way could consist of numerous distant stars (Plutarch, 2006).

in selected regions of the sky. Later, more detailed models of the Milky Way were developed by Jacobus Kapteyn (1851–1922) and Harlow Shapley (1885–1972) (see, e.g., Carroll & Ostlie, 2006, for a detailed discussion of these models).

The idea that some of the observed nebulae could be galaxies, such as the Milky Way, which consist of stars themselves, was first brought up by Thomas Wright in the middle of the 18th century. Good candidates for other galaxies beyond the Milky Way were spiral nebulae, which have been observed in the end of the 19th century. That they were not located in the Galactic plane was supported by their distribution on the sky: spiral nebulae were not concentrated within the band of the Milky Way, but were mainly found at higher Galactic latitudes. The discussion about the origin of spiral nebulae between Harlow Shapley and Heber Curtis in 1920 became famous as the "Great Debate" (Curtis, 1921; Shapley, 1921). The existence of extragalactic nebulae was finally established by measuring the distance to the Andromeda nebula (Öpik, 1922). In the following time galaxies were studied in detail (see, e.g., Hubble, 1938). Today the number of galaxies in the observable universe is estimated to be above 100 billions. A review on galaxies is given, e.g., by Sparke & Gallagher (2007).

Discovery of AGN A first detection of AGN activity took place in 1908 in a study of the optical spectra of spiral nebulae (Fath, 1909), when bright emission lines in NGC 1068 had been observed. At that time it was, however, not established that these objects were extragalactic, and similar emission line spectra had already been observed in planetary nebulae. In 1918 the first image of an AGN was observed in M87 by Curtis (1918).[2] His description of the optical jet is well-known today: The image of M87 showed a "curious straight ray [...] apparently connected with the nucleus by a thin line of matter." Seyfert (1943) studied the spectra of spiral nebulae in detail and found that a fraction of them have bright nuclei and emission lines. Based on the observed properties, Seyfert 1 and Seyfert 2 galaxies are today used as an AGN classification due to optical spectra.

Numerous new insights in AGN were obtained, when it became possible to observe the sky at wavelengths different from the optical regime. A new epoch of AGN studies started with the detection of radio galaxies and quasars in the middle of the 20th century. Baade & Minkowski (1954) identified the bright radio source Cygnus A with an extragalactic object. It was the first detected radio galaxy. The name quasar refers to "quasi-stellar radio source" and goes back to the way in which these objects were detected. When optical counterparts for some radio sources were searched, no extended structures, such as radio galaxies, were found. Instead, only for a few objects optical counterpart candidates were found, which were unresolved point sources similar to stars. However, the optical spectra of these associations were not completely consistent with stellar spectra and in many cases unknown emission lines have been found. A solution was found in 1962 by Maarten Schmidt. Based on a firm association of the radio source 3C 273, the strange emission lines in the optical spectrum of the counterpart could be explained as known emission lines with a significant redshift of $z = \Delta\lambda/\lambda = 0.16$ (Schmidt, 1963). A redshift of $z = 0.37$ of 3C 48 was determined immediately after that. An average quasar spectrum in the source frame is shown in Fig. 1.1. Using the Doppler effect, such high redshift values correspond to very large velocities. Given the "relation between distance and radial velocity among extra-Galactic nebulae" found by Hubble (1927), these quasars could be very distant. A large distance, however, implies an extreme intrinsic luminosity given the measured brightness of these objects. These high luminosities were a problem as no known energy conversion mechanisms, such as nuclear fusion, could explain them. A possible underlying mechanism was finally found to be accretion onto massive objects (see, e.g., Salpeter, 1964). In the case of quasars this indicated that supermassive black holes, with masses in the range of 10^6–10^{10} of solar masses, were located in the center of AGN.

Extreme emission mechanisms beyond nuclear fusion were required since the detection of lumi-

[2] M87 is the 87th object in the "Catalog of Nebulae and Star Clusters" of Messier (1781)

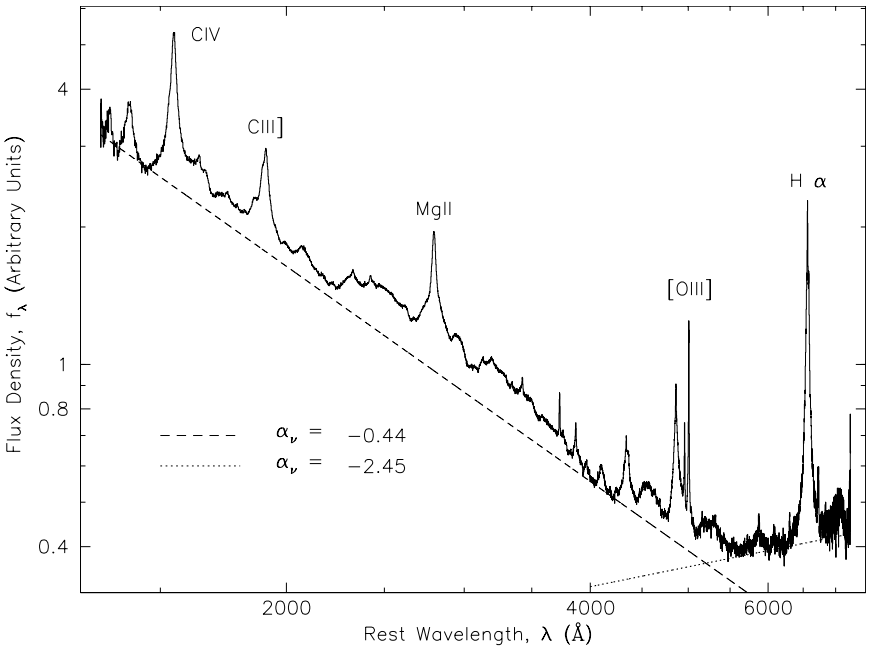

Figure 1.1: Average of about 2200 spectra of optically selected quasars in the source frame by Vanden Berk et al. (2001).

nous celestial X-ray sources in 1962 by Giacconi et al..[3] It was the beginning of X-ray astronomy. After balloon and rocket experiments the first X-ray satellites had been launched from 1970 on (see, e.g., Giacconi et al., 1971, for an overview on the *Uhuru* mission). X-ray emission of AGN was detected in the following.

The development of satellite-borne γ-ray detectors revealed that a subset of AGN are even sources of γ-rays (Swanenburg et al., 1978; Hartman et al., 1992). A detailed discussion of γ-ray astronomy is given in Sect. 5.

An overview on different AGN types is presented in the following Sect. 1.1.2. The current understanding of AGN and the unification of the different classes are outlined in Sect. 1.1.3. The different components of AGN and their physical emission processes are described in the Sects. 1.2, 1.3, and 1.4.

Estimates on AGN populations are given, e.g., by Peterson (1997) and Marzke et al. (1994). Table 1.1 shows the estimated averaged number of sources per volume. In total about 10% of all galaxies host AGN and only about 2% of the AGN are radio loud. The classes used in Table 1.1 are briefly introduced in Sect. 1.1.2.

1.1.2 AGN Phenomenology

AGN show a variety of properties. In the following a brief summary on AGN classes is given. A complete review on AGN including the AGN nomenclature is, e.g., given by Krolik (1999). An overview on AGN classes can be found as well in Ch. 28 of Carroll & Ostlie (2006). The classification of AGN in the defined classes is, however, difficult. On the one hand there are no distinct boundaries between some of the classes, and many properties of AGN distributed relatively continuously. On the other hand AGN can be variable and may even evolve from one class to another in certain time scales.

Seyfert galaxies As mentioned in Sect. 1.1.1 one of the first classification schemes of AGN relies on their optical spectra. In Seyfert 1 galaxies broad emission lines are observed. The line broadening can be mapped to a velocity distribution of the emitting material. The velocities v can

[3]The first detected celestial X-ray source was the Sun. Golian et al. (1946) detected it with a detector onboard a V-2 rocket.

Table 1.1: Space density of different galaxy and AGN types (Marzke et al., 1994; Peterson, 1997). The dimensionless parameter h given from the value of the Hubble constant $H_0 = 100\ h\ \mathrm{km\,s^{-1}\,Mpc^{-1}}$ (an overview on cosmological effects is given in Sect. 1.6). Recent measurements show that $h = 0.705 \pm 0.013$ (Komatsu et al., 2009).

	Type	Density ($\mathrm{Gpc^{-3}}$)
Galaxies	Spiral Galaxies	$1.5 \times 10^7 h^3$
	Elliptical Galaxies	$1.0 \times 10^7 h^3$
Radio Quiet AGN	Seyfert 2	$8 \times 10^5 h^3$
	Seyfert 1	$3 \times 10^5 h^3$
	QSO	$8 \times 10^2 h^3$
Radio Loud AGN	FR 1	$2 \times 10^4 h^3$
	BL Lac	$8 \times 10^2 h^3$
	FR 2	$8 \times 10^1 h^3$
	radio load QSO	$2 \times 10^1 h^3$

be obtained from the Doppler effect $\Delta\lambda/\lambda = v/c$, where λ is the rest wavelength of the line and c the speed of light (the expression is only valid for $v \ll c$). From the line profiles, velocity distributions with a full width at half maximum (FWHM) of up to $10^4\,\mathrm{km\,s^{-1}}$ can be observed. The velocities responsible for the broad lines are typically on the order of a few thousand $\mathrm{km\,s^{-1}}$. Additionally forbidden emission lines, which are narrower (velocities of several hundred $\mathrm{km\,s^{-1}}$) can be observed as well in the spectra of Seyfert 1 galaxies. In the case of Seyfert 2 galaxies only narrow emission lines are found in the optical spectra. There are, however, galaxies with properties inbetween of both classes. Depending on ratios of line widths intermediate classes of Seyfert galaxies have been introduced. Even evolutions between these classes have been observed. The majority of Seyferts that can be optically resolved are spiral galaxies.

LINERs The class of Low-Ionization Nuclear Emission Line Region galaxies (LINERs) is very similar to Seyfert 2 galaxies. The difference in the optical spectra is that the continuum emission of LINER nuclei is weaker, whereas the low-ionization emission lines are stronger. Most spiral galaxies which can be observed with sufficient sensitivity show a weak LINER activity. It is, however, not clear in all cases if the observed emission originates from the nucleus of the galaxy or if it can be associated with other emission regions, such as starburst emission.

Radio Galaxies Radio galaxies can be considered as a radio-loud analogy of Seyfert galaxies. The main similarity are the optical spectra, based on which radio galaxies can as well be separated into Narrow Line Radio Galaxies (NLRGs) and Broad Line Radio Galaxies (BLRGs). Contrary to Seyferts, radio galaxies are typically found in (giant) elliptical galaxies. The main difference is the radio luminosity. Seyferts are radio-quiet, although weak radio emission can be detected (with sufficient sensitivity) from the nuclei of Seyferts. The radio luminosity of radio galaxies is significantly larger than that of Seyferts. In most of the radio loud galaxies, jets are seen.

Fanaroff-Riley 1 and 2 Based on the morphology of the jets, Fanaroff & Riley (1974) introduced a further classification scheme for resolved radio loud objects. For the classification they used the ratio between the distance of the positions of the brightest radio emission on each side of the central source (which is excluded) to the total size of the radio structure. Objects in which this ratio is below 0.5, and the radio emission is brightest in the inner jet regions, belong to class I. Class II is defined by a ratio above 0.5. The classes are now known as Fanaroff-Riley 1 (FR 1) and Fanaroff-Riley 2 (FR 2). Fanaroff & Riley (1974) found that the radio luminosity of FR 1 objects

tended to be smaller than that of FR 2 objects, with a separating luminosity at 178 MHz of about $2 \times 10^{25}\,\mathrm{W\,Hz^{-1}\,sr^{-1}}$.

The radio morphology of members of the FR 1 class typically shows a double-sided jet structure. The intensity is highest at the center, often with a dominating nucleus. The brightness decreases with increasing distance from the center. The jets can be asymmetric and curved, have large opening angles, and often end in plumes. The jets of the more luminous FR 2 objects are usually straight with less pronounced emission along the jet and often the counterjet remains undetected. The jets end in powerful radio lobes which often show hotspots. The emission of the two lobes is often dominating.

Quasars are the most luminous AGN, which are typically very distant. As noted in Sect. 1.1.1 'quasi-stellar radio sources" were found based on the search of optical counterparts for unidentified radio sources. Using optically selected samples, however, showed that many quasars are radio-quiet. These objects have been called only "Quasi-Stellar Objects" (QSOs). There are about 10 times more radio-quiet than radio-loud objects. A definition of radio-loud and radio-quiet is, e.g., given by Kellermann et al. (1989, see also the references therein for more information on the ratio between the number of radio-loud and radio-quiet objects): Using the radio luminosities at 5 GHz and the optical luminosity at 4400 Å, a ratio between radio and optical brightness is given. This ratio is in the range of 10–1000 for radio-loud objects and about 0.1–1 for radio-quiet objects.

Blazars are characterized by rapid variability and a high degree of linear polarization at visible wavelengths. The class of BL Lac objects is named after the well-known representative of this class: BL Lacerta, which was originally classified as a variable star. The optical spectra of BL Lac objects are typically dominated by continuum emission and do not include prominent emission lines, or source intrinsic absorption lines. Even significant variability during one day as well as luminosity changes by orders of magnitude could be observed. The majority of host galaxies of these objects are elliptical galaxies. In phases of lower luminosity, broad emission lines, as well as further properties of different AGN classifications could be detected in the optical spectra of some BL Lacs. Vermeulen et al. (1995) thus discuss the question: "When is a BL Lac not a BL Lac?". The flat-spectrum radio quasars (FSRQs) are similar to BL Lacs but have higher luminosities.

1.1.3 Understanding and Unification of AGN

As noted previously, the extreme luminosities of AGN and the bright X-ray sources can be explained by accretion of matter by supermassive black holes. A simple outline of the components which are assumed to be underlying AGN is given in the following.

Given the mass and density in the central region and the energy output, there is no known state of matter known except a black hole. The engine powering an AGN is a central supermassive black hole (see, e.g., Shapiro, S. L. and Teukolsky, S. A., 1983, and the references therein for a description of astronomical compact objects). Black holes are summarized in Sect. 1.2.

The accreted material, i.e. the "fuel" of the system, is provided from the surrounding of the supermassive black hole. Material, such as interstellar gas and dust, orbits the black hole. It can lose angular momentum, approach the black hole, and heat up. In this way an accretion disk can form (see Sect. 1.3). Colder material can form large structures farther away from the black hole.

Contrary to the accreted material, which is approaching the black hole, collimated jets of charged particles, which are ejected with relativistic speeds, are observed in a fraction of AGN. Jets are launched along the rotation axis of the inner accretion disk and the black hole. For symmetry reasons it is assumed that jets have counter-jets. An overview on jets is given in Sect. 1.4.

A well-known AGN unification scheme of AGN has been discussed by Urry & Padovani (1995). A large fraction of the different AGN classes (Sect. 1.1.2) can be explained by considering the

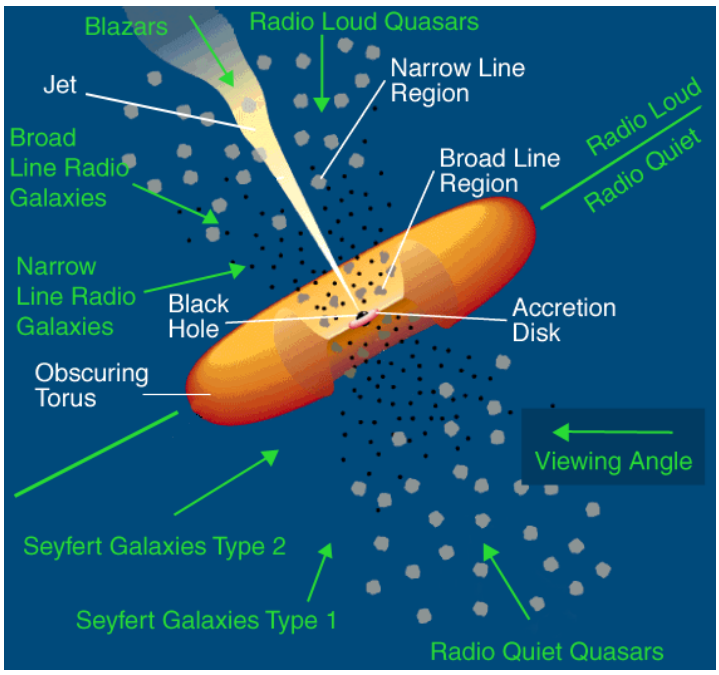

Figure 1.2: Illustration of AGN and unification. In the unification model the different AGN classes are explained by different viewing angles of the same AGN model. The white labels indicate the components of AGN. Viewing angles are indicated with green arrows and labeled with the AGN type, an observer sees from the corresponding direction. The separation in radio-loud and radio-quiet along the orbital plane is only used for explanation. It is assumed that AGN are relatively symmetric, i.e., if there is a jet there is also a counter-jet. In the illustration the size scales increase (about logarithmically) with increasing distance from the black hole. (Illustration after Urry & Padovani, 1995)

viewing angle of the AGN with respect to the observer. Figure 1.2 illustrates the components of AGN and which AGN type an observer would see under which viewing angle of the system. The only intrinsic property, which is responsible for the separation in radio-loud and radio-quiet AGN, are jets. The other AGN classes are explained by the viewing angle in this simple unification scheme.

The unification model is based on the geometry of the AGN components. The highest velocities of material orbiting the black holes occur where the material is close to the black hole. The Broad Line Region (BLR) is thus located in the inner region of AGN. It is likely to include fast moving gas structures and winds from the accretion disk. Due to a large velocity dispersion, the spectra of emission lines from material in the BLR are broad. Line profiles originating from the Narrow Line Region (NLR), which is located farther away from the central region, are narrower due to the smaller velocity dispersion. A reason why broad lines are observed only in a fraction of AGN is given by the inclination of these systems. Here, the inclination is measured with respect to the normal of the orbital plane. An inclination of 0° thus means that the system, such as the accretion disk, is seen from the top. Analogously the system is seen form the side in the case of 90° inclination. In the unified model absorbing material with a torus-geometry is located in the orbital plane. If the system is observed from the side, this structure obscures the inner region of the AGN. For that reason the accretion disk and the BLR cannot be observed directly from such viewing angles. As the inclination decreases, more of the inner region becomes visible and broad lines can be seen. The picture of the obscuring torus as a "donut" is, however, a strong simplification or even misleading (see, e.g., Elitzur & Shlosman, 2006). The true distribution of material is much more complicated, e.g., observations indicate distributions of clumpy structure. A more advanced model of the ionization structure and the absorbing features is for example presented by Elvis (2000). Regardless of the exact structure and ionization distribution of the absorbing material, it is still commonly accepted that the inner region of an AGN is typically obscured when the system is seen from the side. In this case the AGN is seen as a Seyfert 2 galaxy, or as a Narrow Line Radio Galaxy if it is a radio-loud AGN with jet. Seen at lower inclinations with visible broad lines, the AGN appear as Seyfert 1 galaxies, or as Broad Line Radio Galaxies in the radio-loud case.

Radio-loud AGN include quasars, for which the inclination is assumed to be even lower. As the jets are relativistic flows, their emission is boosted in the movement direction. An observer

with a viewing angle close to the jet axis thus sees increased intensity and decreased variability time scales of the emission. The most extreme case are the blazars, where the jets are pointing directly at the observer. The relativistically boosted emission from the jet outshines the emission of other components, such as line emission, and explains the feature-less spectra, as well as the short variability time scales. Whereas jets are boosted toward the observer in this case, the counter-jets are moving away from the observer and their intensity is decreased. Often the counter-jets are undetectable and only "single-sided" jets are visible.

Different viewing angles explain the diversity of AGN classes quite well, but there are other obvious parameters which influence the properties of AGN. Two main characteristics are the mass of the central black hole and the accretion rate. The close environment of the black hole and the way how material is provided for it, can strongly influence the accretion process and geometry, as it is known, e.g., from galactic X-ray binaries (Sect. 1.7). Additionally the environment on larger scales can influence properties of AGN. For example in the separation of FR 1 and FR 2, interactions between the jets and the interstellar medium might play an important role, e.g., how fast the jets can propagate through the medium.

A description of the components in AGN is given in the following sections.

1.2 Black Holes

1.2.1 Theory of Black Holes

Objects of such high masses that not even light could escape due to their gravity, which were thus considered as "dark" or "black", have been proposed in the end of the 18th century (see, e.g., Israel, 1987, and the references therein). Such objects became interesting when they appeared in the theory of General Relativity by Einstein (1916), according to which space time is curved by mass. A metric describing the spacetime (with the space in polar coordinates r, θ, ϕ) around a point mass M has been found by Schwarzschild (1916)

$$\mathrm{d}s^2 = c^2\mathrm{d}t^2\left(1-\frac{2R_g}{r}\right) - \frac{\mathrm{d}r^2}{1-2R_g/r} - r^2\mathrm{d}\theta^2 - r^2\sin^2\theta\mathrm{d}\phi^2 \tag{1.1}$$

where the gravitational radius R_g of the mass m is given by:

$$R_g(m) = \frac{G\,m}{c^2} \tag{1.2}$$

where $G = 6.673\times10^{-11}\,\mathrm{m^3\,kg^{-1}\,m^{-2}}$ is the gravitational constant and $c = 299\,792\,458\,\mathrm{m\,s^{-1}}$ the vacuum speed of light. This metric yields a critical distance, below which even light (which fulfills $\mathrm{d}s^2 = 0$) can only approach the center ($\mathrm{d}r/\mathrm{d}t < 0$). The surface from which light cannot escape is called event horizon. For a "black hole" of mass m it is a sphere with the Schwarzschild radius:

$$R_\mathrm{S}(m) = 2R_g \approx 3\,\mathrm{km}\frac{m}{M_\odot} \qquad \text{or more suitable for AGN}: \quad R_\mathrm{S}(m) \approx 0.020\,\mathrm{AU}\frac{m}{10^6\,M_\odot}, \tag{1.3}$$

where $M_\odot = 1.9891\times10^{30}\,\mathrm{kg}$ is the solar mass and AU the astronomical unit – the distance between the Sun and the Earth, which is about $1.5\times10^{11}\,\mathrm{m}$.

Moreover, angular momentum of matter affects spacetime. The close environment of rotating black holes is thus different to that of an above mentioned non-rotating Schwarzschild black hole. A metric around a rotating mass has been found by Kerr (1963). Given the mass m and the angular momentum J, the Kerr parameter is defined

$$a = \frac{cJ}{GM^2}. \tag{1.4}$$

The parameter a describes the "spin" of a black hole. It is 0 in the case of a non-rotating black hole and 1 in the case of a maximally rotating black hole. Larger values would yield naked singularities (which are not allowed according to the hypothesis of cosmic censorship, see Penrose & Floyd, 1969). Thorne (1974) showed that due to interaction with the radiation field surrounding the black hole the maximum spin is 0.998 instead of the unperturbed theoretical limit of 1. The outer event horizon of a rotating black hole decreases with increasing a and approaches R_g in the case of a maximally rotating black hole. Besides the characterizing parameters mass and angular momentum, a black hole can have a charge (the metric of a rotating charged mass is discussed by Newman et al., 1965). However, the charge is usually neglected for astrophysical black holes, because on these scales the universe is typically neutral and significantly charged black holes would neutralize quickly.

As black holes cannot be seen directly, but only detected indirectly based on the interaction with their surrounding, it is important to know the closest orbits around black holes. Bardeen et al. (1972) discuss circular orbits around rotating black holes. The radius of the "innermost stable circular orbit" (ISCO) around a non-rotating black hole is $6\,R_g$. For a maximally rotating black hole the ISCO of a particle co-rotating with the black hole (i.e., the angular momentum of the particle is aligned with that of the black hole) approaches $1\,R_g$. In the case of a maximally counter-rotating black hole, the ISCO increases to $9\,R_g$. In order to characterize the rotation of the black hole with respect to orbiting material (in particular the accretion disk, see Sect. 1.3), the spin parameter is equipped with a sign in the following, where $a > 0$ indicates co-rotation and $a < 0$ counter-rotation. Based on the different ISCO values, black hole spin can in principle be estimated observationally, using timing signatures or emission lines from accretion disks (Sect. 1.3.2), once the black hole mass is determined. A method to determine the black hole spin independently of the mass is described in Sect. 1.3.2.

1.2.2 Black Holes in the Universe

First clear observational indications of the existence of astronomical black holes have been found with the detection of X-ray Binaries. In some of these systems, which consist of a compact object accreting material of a companion star, orbital periods could be derived from the X-ray emission as well as the optical emission of the corresponding companion stars. Here, the mass of the compact objects could be estimated.

For a given mass there are limits on the density up to which the gravitational force of the material can be counterbalanced by pressure within the material.[4] Above a limiting mass located within a given volume there is no known pressure, that is able to counterbalance gravity, and thus the assumption is that the subsequent gravitational collapse leads to a black hole.

The first promising black hole candidate was Cygnus X-1 (for a summary see, e.g., Böck, M., 2008, Ch. 2.5 and references therein). The mass of the compact object was determined to be about 10 times the solar mass (Gies & Bolton, 1986).[5]

As mentioned previously, the observed energy density in AGN is indicating the existence of supermassive black holes. Constraints on the size of the central region can, e.g., be obtained from variability studies and reverberation mapping (see, e.g., Blandford & McKee, 1982; Kaspi et al., 2000). A detailed mass estimate is possible for a supermassive black hole within the Milky Way. The supermassive black hole Sagittarius A* in the Galactic center, can be studied based on stars orbiting it (see, e.g., Ghez et al., 2000; Eckart et al., 2002; Schödel et al., 2002). The determined mass is about 4 million solar masses. Based on the analysis of the star S0-2, Ghez et al. (2008)

[4] There is the Chandrasekhar limit, which gives the maximal mass of white dwarfs based on the electron degeneracy pressure (Chandrasekhar, 1931). The maximal mass of a neutron star is the Tolman-Oppenheimer-Volkoff limit, which is based on the neutron degeneracy pressure (Tolman, 1939; Oppenheimer & Volkoff, 1939).

[5] Different mass estimates are in the range of 8–45 solar masses (see, e.g., Ziółkowski, 2005; Shaposhnikov & Titarchuk, 2007).

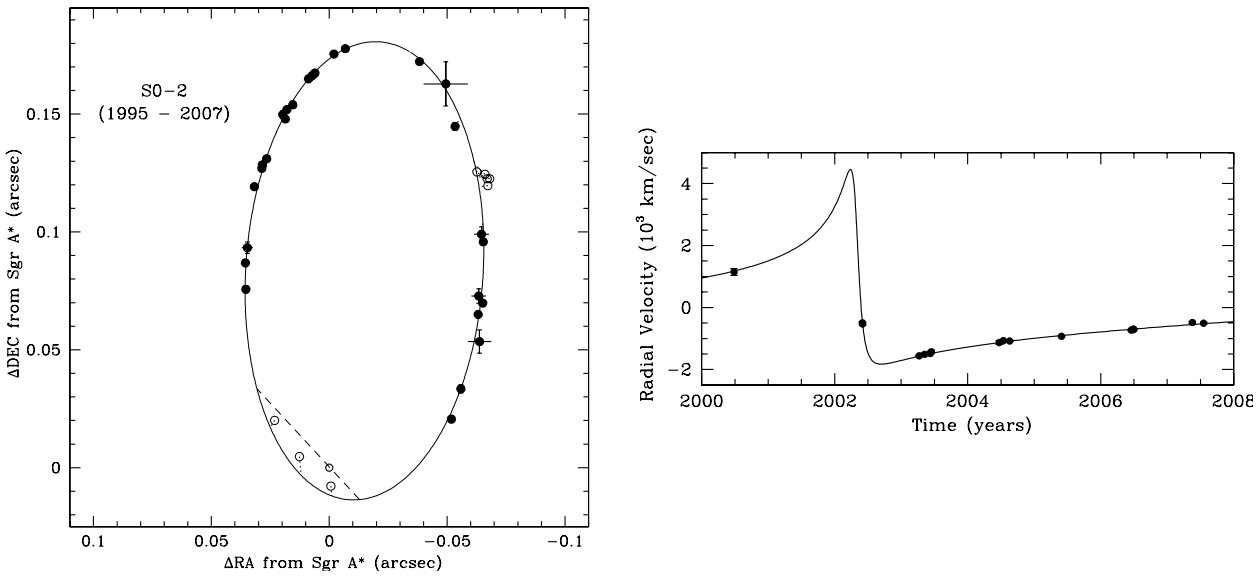

Figure 1.3: Indication of a supermassive black hole in the center of our Galaxy. *Left:* Measurements of the position of the star S0-2 from 1995 until 2007 and a fit of a Keplerian orbit around the Galactic Center Sgr A* published by Ghez et al. (2008). *Right:* Radial velocity of the star. (Figure from Ghez et al., 2008, Fig. 1)

obtain a mass of $(4.8 \pm 0.3) \times 10^6\, M_\odot$ and a distance of 8.3 ± 0.3 kpc of Sgr A*. The orbit and the radial velocity of the star is shown in Fig. 1.3.

With increasing angular resolution it could be possible to image the black hole in the center of our Galaxy directly within the next decade. The Event Horizon Telescope (EHT; an overview is given by Doeleman, 2010) consists of a telescope array, which applies interference techniques at (sub)millimeter wavelengths in order to achieve extreme resolutions (see Fish et al., 2011, for a discussion of a recent observation of Sgr A*).

There are indications that the majority of galaxies host a central supermassive black hole. The correlations between black hole mass and bulge luminosity, as well as the velocity dispersion in the bulge (see, e.g., Kormendy & Richstone, 1995; Ferrarese & Merritt, 2000, and the references therein), are indications for a connection between the formation and evolution of supermassive black holes and that of the their host galaxies.

1.3 Accretion Disks

Accretion onto the black hole is the fuel for the energy output. Material in the environment of the black hole is affected by gravity. The conservation of angular momentum foreces the material to build an accretion disk.

1.3.1 Spectrum of an accretion disk

The standard model of an accretion disk is an geometrically thin and optically thick disk described by Pringle & Rees (1972) and Shakura & Syunyaev (1973), where a parameter describing the disk's viscosity is introduced. Here, geometrically thin means that the vertical thickness of the disk at each radius is significantly smaller than the radius. As it can be easily seen, e.g., by considering a particle on a Keplerian orbit, the total energy decreases with the radius of circular orbits. For that reason a steady accretion disk, with a given accretion rate $\dot{m}$, has to dissipate energy at each radius as material moves inward. In the optically thick case a local thermal equilibrium can be assumed,

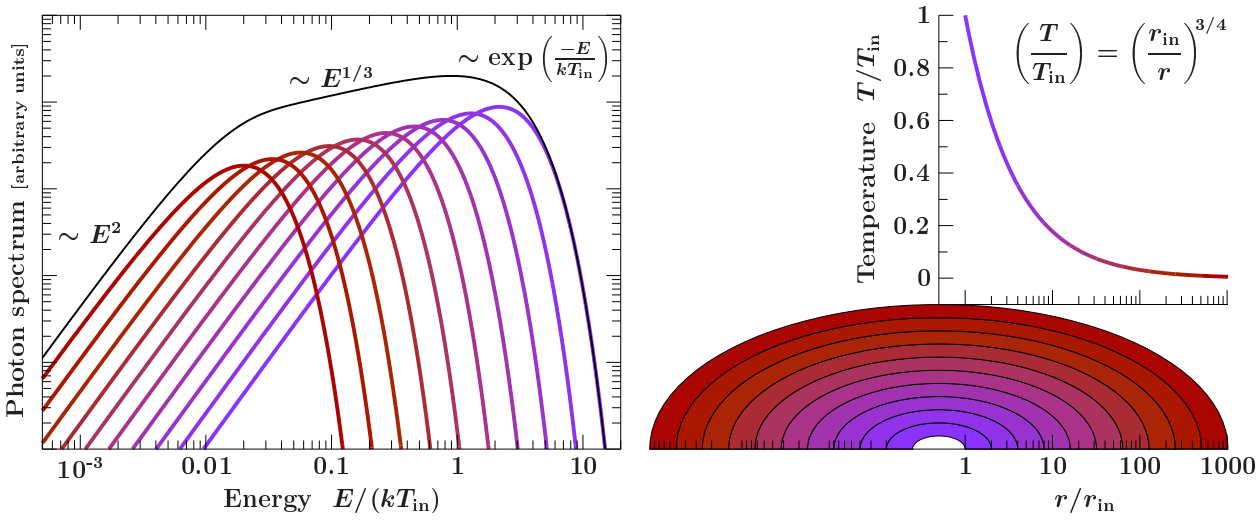

Figure 1.4: Spectrum of an accretion disk. The right figure visualizes the temperature profile of an accretion disk. The left image shows the composite spectrum as a sum of the contributions from all radii. (Credit: Hanke, 2011, Fig. 1.6)

which yields the following radial temperature profile (see, e.g., Pringle, 1981, for a review):

$$T(r) \propto r^{-\frac{3}{4}} \tag{1.5}$$

The spectrum of the thermal emission at each radius (with constant temperature $T(r)$) can be described with Plank's law:

$$B(\nu, T) = \frac{2}{c^2} \frac{h\nu^3}{e^{h\nu/(k_{\rm B}T)} - 1}. \tag{1.6}$$

The total spectrum of an accretion disk is given by adding the thermal emissions of each radius, as it is shown in Fig. 1.4. The result appears like a stretched black body spectrum. It approaches the Rayleigh-Jeans law at low frequencies and the Wien law at high frequencies, in between the spectrum is proportional to $\nu^{1/3}$. This dependence can be derived from the temperature profile of the disk $T(r)$ (Eq. 1.5) and a $2\pi r$ weight which is required for adding the emission contributions of all radii.

Using the complete solution of $T(r)$ and considering the fact that the ISCO is directly proportional to the mass m of the black hole (for a given spin), the temperature of the inner radius of the accretion disk $T_{\rm in}$ depends on the accretion rate $\dot{m}$ and the mass:

$$T_{\rm in} \propto \left(\frac{\dot{m}}{m^2}\right)^{1/4} \tag{1.7}$$

Based on the different mass scales of supermassive black holes (10^5–$10^{10}\,M_\odot$) and that of compact objects in X-ray binaries (on the order of a few solar masses), the inner disk temperatures are significantly lower in AGN compared to X-ray binaries. While accretion disks of X-ray binaries are visible in soft X-rays (typical values of $k_{\rm B}T_{\rm in}$, e.g., in the case of Cyg X-1, are in the range from 0.1 to 1 keV Böck et al., 2011), AGN accretion disks are typically visible in the ultraviolet (UV) regime. Many AGN show even infrared (IR) emission from dust disks or more complicated structures, which are located significantly farther away from the central black hole and thus colder (see, e.g., Phinney, 1989)

The above mentioned model of thin accretion disks describes many observed properties well. It is, however, obvious that the model is an approximation and that real accretion disks can be by far more complicated. For example the consideration of magnetohydrodynamic (MHD) effects, i.e.,

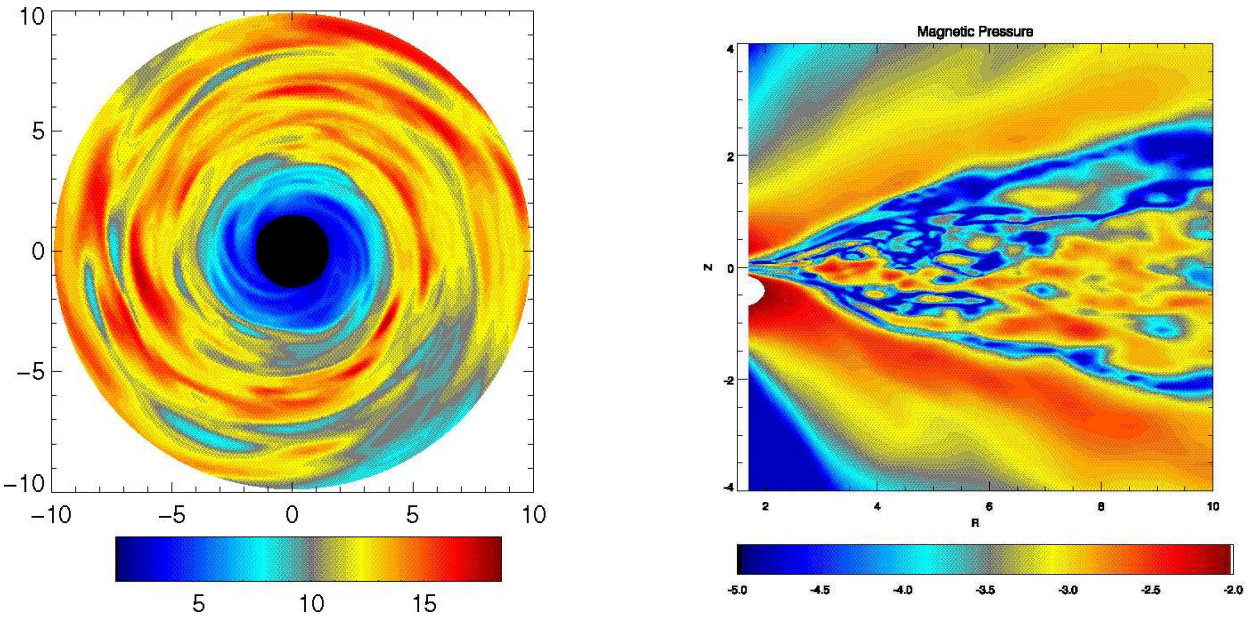

Figure 1.5: 3D MHD Simulation of an accretion disk by Hawley & Krolik (2001). *Left:* The image shows the density of the disk in the equatorial plane. *Right:* Azimuthally averaged magnetic pressure in the disk (seen from the side, the color scale is logarithmic). (Credit: Hawley & Krolik, 2001, Fig. 2,3)

effects caused by the dynamics of plasma, in order to explain the disk's viscosity makes a description of accretion disks difficult. Magnetohydrodynamic (Alfvén, 1942) simulations of accretion disks typically yield substructures in the disk and include turbulent effects (see, e.g., Hawley & Krolik, 2001). An example of a simulated disk is shown in Fig. 1.5. Accretion disks can also be warped, e.g., when the angular momentum of the accreted material is not aligned with the black hole spin, by external perturbations, or by self-induced warping (Pringle, 1997). A fragmentation of the disk is possible as well. Another indication of substructures in accretion disks is given by disk-induced variability (see, e.g., Uttley et al., 2011; Reynolds & Miller, 2009).

1.3.2 Emission Lines from Accretion Disks

Accretion disks around black holes are located in extreme regions. At the inner radii of the disk material is exposed to strong gravitational fields. Besides the curvature of the space time by the black hole, the spacetime is additionally affected by the black hole's spin which yields frame dragging effects. For that reason the values of the ISCO depend on the spin on the black hole (Sect. 1.2.1), thus the inner edge of the accretion disk depends on the spin.[6]

A photon emitted at a position in the accretion disk with a given energy in the local rest frame of the disk is generally not observed at the same energy by a distant observer. The main influences on the energy shift are the position, where the photons has been emitted, and the disk's orientation with respect to the observer. The closer to the black hole a photon is originating, the stronger is its gravitational redshift. Additionally material in the (inner) accretion disk is moving at relativistic speeds, which affects the emission, too. Due to relativistic boosting, emission from material approaching the observer is strongly blueshifted, whereas that of material moving away is redshifted. As the velocities in the disk increase toward the black hole, this effect is stronger at

[6]Material closer to the black hole than the ISCO will fall into the hole on much shorter time scales than required for the inward propagation in the disk, which depends on the disk's viscosity.

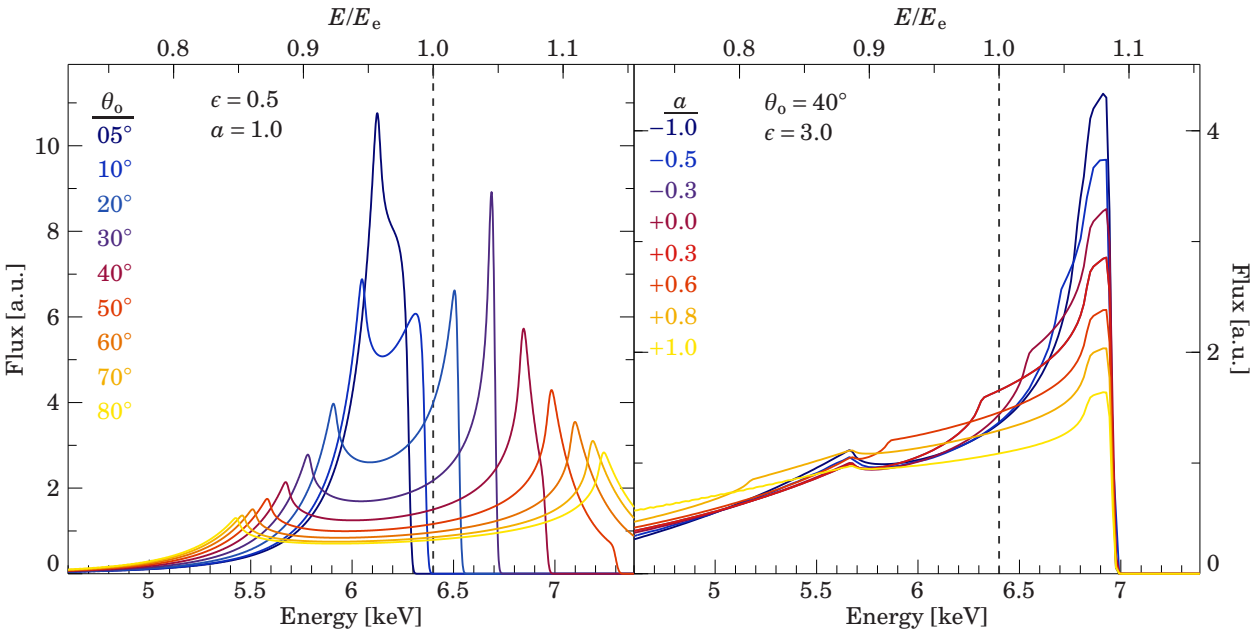

Figure 1.6: Relativistically broadened line profile form an accretion disk. *Left:* Line profiles for different disk inclinations for a maximally rotating black hole. The emissivity index has been set to a low value of $\epsilon = 0.5$ for visualization. *Right:* Dependence of the line profiles on the black hole spin. The inclination has been set to 40° and the emissivity to $\epsilon = 3$. Here, the profiles are not normalized with respect to each other for visualization. (Credit: Th. Dauser, priv. comm.)

smaller radii, as it is the case for the gravitational redshift. Besides further direct effects from the black hole spin, it also influences the inner radius of the accretion disk, which in turn is important for the two effects described above. Not only the energies of emitted photons are changed, but also the intensity of emission is modified due to time dilatation.

Seen from a distant observer the spectrum of an emission line, i.e., monochromatic photons, from the accretion disk, is not a line but a broadened profile. A suitable line is the Fe Kα line at about 6.4 keV in the X-ray band (see, e.g., Fabian et al., 2009, for a recent observation of relativistically broadened iron lines in an AGN). Due to high temperatures and ionization, lines at significantly lower wavelengths are less suitable for probing the close environment of black holes. The fluorescent iron line, which is caused when material is irradiated with X-rays of higher energies, is typically prominent and isolated. The emitted line flux at each position, and thus the total line profile, depends on the irradiation of the disk. Typically a radial dependence of the disk emissivity of the form $\propto r^{-\epsilon}$ is assumed, where ϵ is the emissivity index. Figure 1.6 shows how the line profiles (for a selection of inclination, black hole spin, and emissivity index) change with inclination and spin, respectively. Line profiles including counter-rotating black holes ($a < 0$) are shown by Dauser et al. (2010).

Using the observed line profiles, models can be used to determine the parameters listed above and their uncertainties. Such line diagnostics are a direct method to determine the spin of black holes. The determined spin values, however, have to be regarded with care, as they might be influenced from systematic issues, such as model assumptions. While the transfer functions for photons emitted somewhere in the disk to the observer can be calculated with high accuracy using general relativity, other parts of the model are approximations. In order to model the line profiles, the shape of an accretions disk is usually approximated as a planar two-dimensional ring with an inner and outer limiting radius. A more complicated disk which is, e.g., thick and includes substructures and other features, yields modified profiles. Another important influence on the line profile is the irradiation of the disk. Depending on the origin of the incident emission, i.e., the

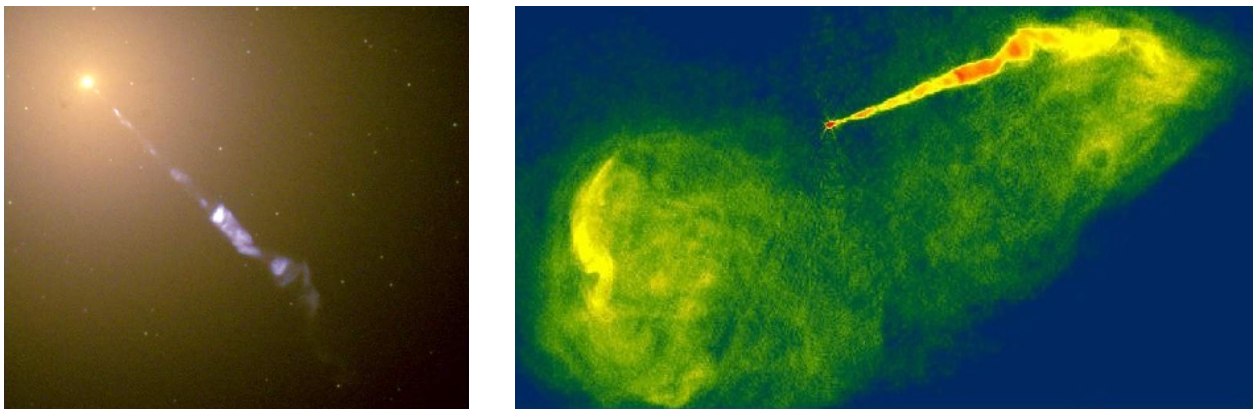

Figure 1.7: Jet of M87. *Left:* The optical jet as seen by the Hubble Space Telescope. *Right:* Radio image of the jet with the Very Large Array (VLA). The collimated jet which can be seen in both images has a length of several kpc. The bright emission structures at both wavelengths agree very well, only the images are rotated with respect to each other. (Credit: NASA/ESA, NRAO)

location and geometry of the emitter, the disk is illuminated in a different way. Typically there is larger emissivity index at small radii, where emission is focused by the black hole. Changes of the irradiation of the disk, based on different parameters in a lamp post model (where the irradiating source is located above the black hole on the rotation axis) are discussed by Dauser et al. (2012). In a detailed modeling of the profiles, the ionization has to be considered as well, as energy of the Fe Kα transition changes with the ionization state. In general the accretion disk has zones of different degrees of ionization (e.g., García & Kallman, 2010; García et al., 2011).

1.4 Relativistic Jets

In several AGN collimated jets can be observed directly. As described in Sect. 1.1.1, the first optical jet was seen in the object M87 (Curtis, 1918). Figure 1.7 shows an image of the jet of M87 with the Hubble Space Telescope at optical wavelengths, and a radio image obtained with the Very Large Array. Using radio interferometry (Sect. 2.1) high angular resolutions are possible, with which numerous jets of radio-loud AGN can be resolved. Frequent observations of individual sources even allow to monitor features in the jets and determine jet kinematics. These observations prove that jets are high-velocity outflows.

1.4.1 Jet Kinematics and Apparent Superluminal Motion

Comparing observations at 2.3 GHz, Gubbay et al. (1969) found that "an apparent expansion velocity greater than that of light seems to be required for the recent outburst in 3C 273". Cohen et al. (1971) confirmed that result and found the same in the case of 3C 279. These were the first findings of "apparent superluminal motion" in AGN jets.

Figure 1.8 shows an example for apparent superluminal motion based on the object 3C 111. With high-resolution imaging observations structures in the jet can be resolved. By conducting several observations the temporal evolution of these structures can be studied. If the distance to the object is known, the transversal velocity, i.e., the velocity component in the plane of the sky, can be calculated. In many cases velocities are determined which seem to exceed the speed of light.

This finding is, however, not a violation of the Theory of Relativity, but it can be easily explained by the finite speed of light. It is nevertheless a proof that there have to be relativistic velocities

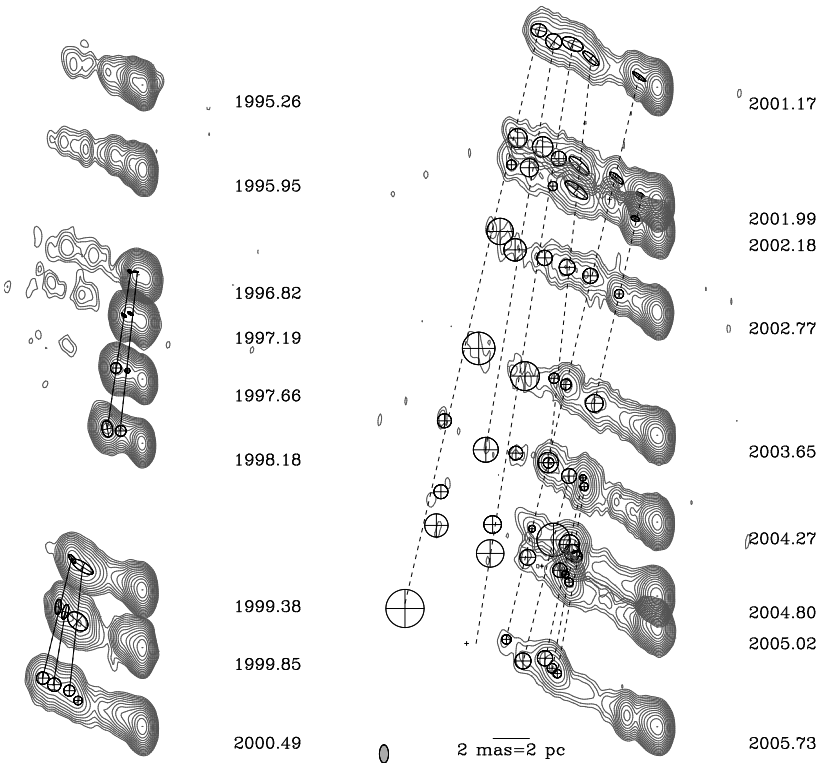

Figure 1.8: Example of apparent superluminal motion: the Jet Kinematic of 3C 111 determined by Kadler et al. (2008). Jet structures seem to travel projected distances of about 5 light years in only one year. (Figure from Kadler et al., 2008, Fig. 3)

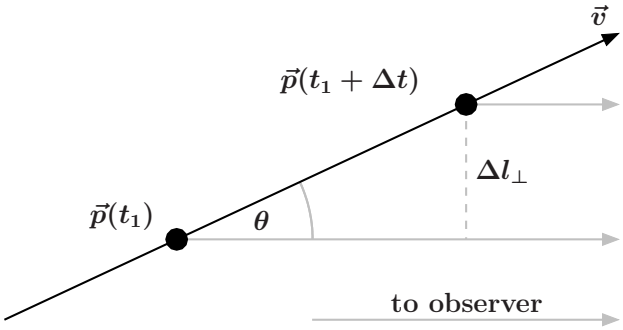

Figure 1.9: Sketch of the geometry which can lead to apparent superluminal motion. A feature is moving with velocity $\vec{v}$ with an angle θ to the line of sight. The projected transversal distance is $\Delta l_\perp$.

in jets. The effect of superluminal motion is explained based on the sketch shown in Fig. 1.9. In this model a feature (e.g., in a jet) propagates with a constant velocity $\vec{v}$. The angle between its trajectory and the line of sight of a distant observer is θ. In a time interval Δt the feature moves from $\vec{p}(t_1)$ to $\vec{p}(t_1 + \Delta t)$. The time interval Δt is the time required for the propagation of the feature. It is not measured in the rest frame of the moving feature, where time dilation effects would occur, but in a rest frame relative to the observer. The observer can see the movement projected on the plane of the sky. The time interval required for the projected change of positions is Δt_{obs}. It is the difference of the arrival times of the signals at the observer. Due to the finite light travel time the observed time interval Δt_{obs} is different from Δt, because the position $\vec{p}(t_2)$ is closer to the observer by $v\Delta t \cos\theta$, thus

$$\Delta t_{\mathrm{obs}} = \Delta t \left(1 - \frac{v \cos\theta}{c}\right) \tag{1.8}$$

The projected distance in the plane of sky is

$$\Delta l_\perp = v \Delta t \sin\theta \tag{1.9}$$

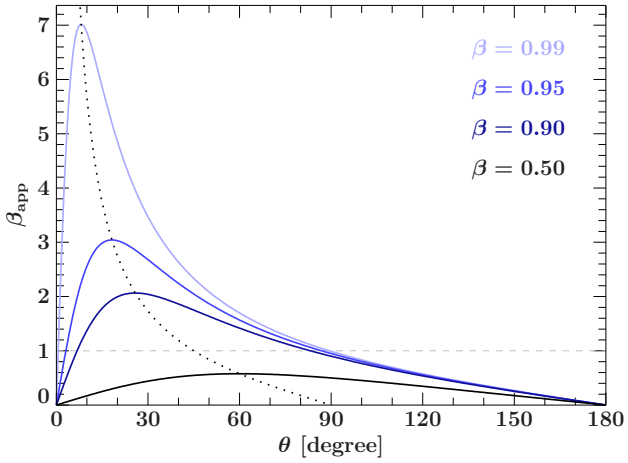

Figure 1.10: Dependence of the apparent projected speed on the viewing angle θ for different velocities of the moving feature. The velocities are given in $\beta = v/c$. The dashed line indicates an apparent velocity equal to the speed of light. The dotted line shows at which viewing angle the maximal apparent speed occurs, which is 90° for $\beta \ll 1$.

and the apparent projected velocity seen by the observer is

$$v_{\mathrm{app}} = \frac{\Delta l_{\perp}}{\Delta t_{\mathrm{obs}}} = \frac{v \sin\theta}{1 - \frac{v}{c}\cos\theta}. \tag{1.10}$$

The apparent speed for different viewing angles θ and different velocities v is shown in Fig. 1.10. The maximal velocity is observed for $\theta_{v_{\mathrm{max}}} = \arccos(\beta)$, where $\beta = v/c$ (and $\beta_{\mathrm{app}} = v_{\mathrm{app}}/c$).

Eq. 1.10 can be solved easily for β

$$\beta = \frac{\beta_{\mathrm{app}}}{\sin\theta + \beta_{\mathrm{app}}\cos\theta}. \tag{1.11}$$

In order to obtain the real speed v, the viewing angle θ has to be known. Even if θ is unknown, a lower limit on v can be obtained based on the value of the observed apparent speed. For a given β_{app} the minimal real speed characterized by β_{min}, which can cause the observed v_{app}, occurs at the angle:

$$\theta_{v_{\mathrm{min}}} = \operatorname{arccot}(\beta_{\mathrm{app}}) \tag{1.12}$$

and is given by:

$$\beta_{\mathrm{min}} = \frac{\beta_{\mathrm{app}}}{\sin\theta_{v_{\mathrm{min}}} + \beta_{\mathrm{app}}\cos\theta_{v_{\mathrm{min}}}} = \frac{\beta_{\mathrm{app}}}{\sin\theta_{v_{\mathrm{min}}}\,(1 + \beta_{\mathrm{app}}\cot\theta_{v_{\mathrm{min}}})} \tag{1.13}$$

$$= \frac{\beta_{\mathrm{app}}\sqrt{1+\cot^2\theta_{v_{\mathrm{min}}}}}{1 + \beta_{\mathrm{app}}\cot\theta_{v_{\mathrm{min}}}} = \frac{\beta_{\mathrm{app}}}{\sqrt{1+\beta_{\mathrm{app}}^2}}. \tag{1.14}$$

For $\beta = v/c$ the Lorentz factor is $\gamma = (1-\beta^2)^{-1/2}$. Using the lower limit on β determined from the apparent projected velocity v_{app}, a lower limit on the Lorentz factor is given by:

$$\gamma_{\mathrm{min}} = \frac{1}{\sqrt{1-\beta_{\mathrm{min}}^2}} = \sqrt{1+\beta_{\mathrm{app}}^2} \tag{1.15}$$

An important quantity in the analysis of relativistic jets is the relativistic Doppler factor D, which is defined as the ratio between the frequencies of the emission in the rest frame of the source and that of the observer:

$$D := \frac{\nu_{\mathrm{obs}}}{\nu_{\mathrm{emit}}} = \frac{1}{\gamma\,(1 - \beta\cos\theta)} \tag{1.16}$$

The Doppler factor as a function of the viewing angle is shown in Fig. 1.11 for different values

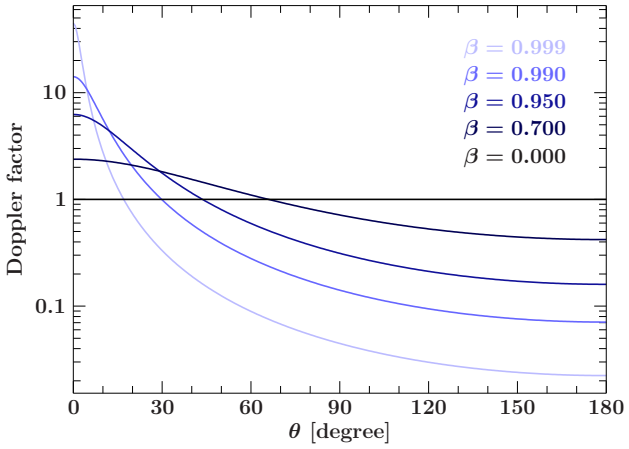

Figure 1.11: Dependence of the Doppler factor on the viewing angle θ for different velocities of the source. The velocities are given in $\beta = v/c$.

of β. Given the apparent projected velocity, lower limits on the Doppler factor can be derived. A determination of Doppler factors for AGN of different classes is, e.g., provided by Hovatta et al. (2009). The Doppler factor can be used directly to obtain the change in intensity due to boosting, the change in the angular distribution of emission with a focus in the direction of $\vec{v}$ (relativistic beaming), and the time dilatation, which affects the variability time scales. Using the flux density $S(\nu)$ and the frequency ν, the Lorentz invariant quantity $S(\nu)/\nu^3$ (see, e.g., Rybicki & Lightman, 1979, Ch. 4.9) yields for the emission of a moving source:

$$\frac{S(\nu_{\mathrm{obs}})}{\nu_{\mathrm{obs}}^3} = \frac{S(\nu_{\mathrm{emit}})}{\nu_{\mathrm{emit}}^3} \tag{1.17}$$

and thus:

$$S(\nu_{\mathrm{obs}}) = D^3 S(\nu_{\mathrm{emit}}). \tag{1.18}$$

As shown in Fig. 1.11 the Doppler factor can obtain very large values for sources approaching the with a small angle to the line of sight, whereas it is small for receding sources. This larger difference is the reason why often only "single-sided" jets are observed. Jets approaching the observer can be several orders of magnitude brighter than the counter-jets, which remain undetected.

1.4.2 Formation and Structure of Jets

Given the observed characteristics that jets are fast, highly collimated, and include a huge amount of energy, the question arises which underlying physical processes cause these properties.

Soon after the description of space time around rotating black holes, it had been discussed that they could be powering jets. Penrose & Floyd (1969) described a processes, in which energy can be extracted from black holes by frame dragging effects. A promising method for launching jets is the Blandford-Znajek mechanism. Blandford & Znajek (1977) showed that a black hole with sufficient angular momentum can accelerate charged particles under the presence of a large enough magnetic field. The acceleration is based on the deformation of the magnetic field lines. The twisting of field lines caused by the rotation of space time causes helical fields in which charged particles can be accelerated along the rotation axis. In this way outflows perpendicular to the accretion disk can be formed: a jet - counter-jet system. Via this mechanism the black hole can lose energy and angular momentum. This scenario works without the presence of external magnetic fields, as magnetic flux can be transported by the accretion disk. Blandford & Payne (1982) discuss "Hydromagnetic flows from accretion discs and the production of radio jets".

It is possible to gain insights in jet formation based on simulations using the Blandford-Znajek mechanism. Figure 1.12 shows results of a three dimensional, time-dependent, general-relativistic magnetohydrodynamic simulation of an accreting black hole by Tchekhovskoy et al. (2011). In

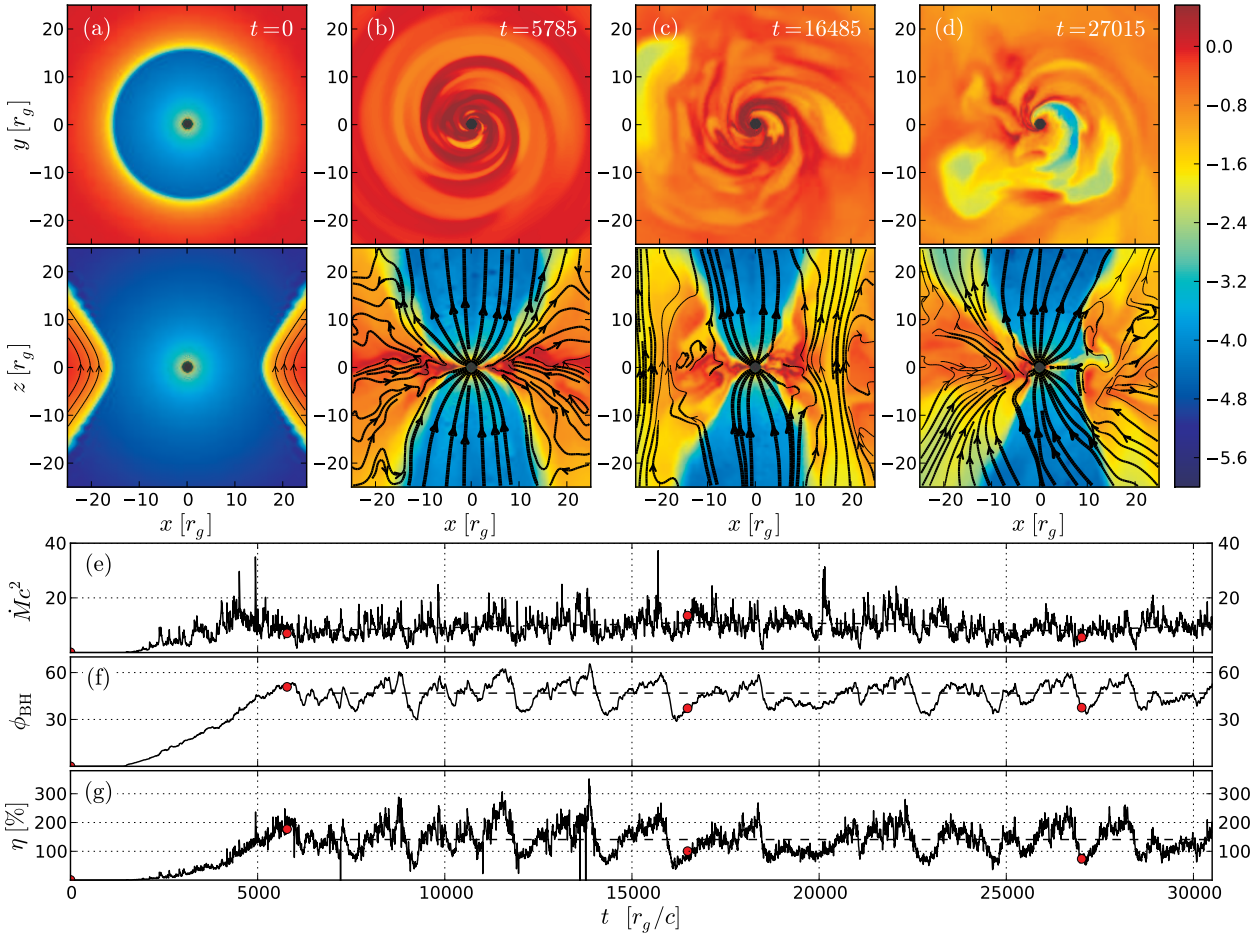

Figure 1.12: Formation of a jet in a general relativistic magnetohydrodynamic simulation by Tchekhovskoy et al. (2011, Fig. 1). The color scale represents the logarithm of the density. The panels *a–d* show slices of the inner region around the black hole at different times of the simulation (*top:* slice through orbital plane seen from the top, *bottom:* system seen from the side). In the simulation the Blandford-Znajek mechanism has been been applied in the case of a maximally rotating black hole and a disk which carries a large amount of magnetic flux. In this case spin energy of the black hole is extracted, the efficiency exceeds 100% on average (panel *g*). Panel *e* shows the (smoothed) temporal evolution of the accretion rate and panel *f* the magnetic flux (see Tchekhovskoy et al., 2011, for detailed information).

their simulation, where a large amount of magnetic flux is transported to the black hole and the Blandford-Znajek mechanism is applied, the authors were able to obtain powerful outflows. For a extremely spinning black hole ($a = 0.99$) the averaged efficiency of the obtained outflow is 140%. With 100% corresponding to the total energy of the accreted material, it is obvious that a significant amount of spin energy is extracted from the black hole in this extreme case. The accretion process in this simulation is turbulent and the efficiency shows a quasi-periodic behavior. For a smaller spin parameter of $a = 0.5$ a lower averaged efficiency of about 30% has been found by the authors. Contrary to some semi-analytical models, which suggested higher efficient jets from retrograde than from prograde black holes, in these simulations about three times higher efficiencies are found for prograde black holes (see Tchekhovskoy & McKinney, 2012, and the references therein).

In contrast to several theoretical predictions and results from simulations, current observations do, however, not show a clear relation between jet power and black hole spin. For example Fender et al. (2010) did not find observational evidence for this relation based on a study of black hole

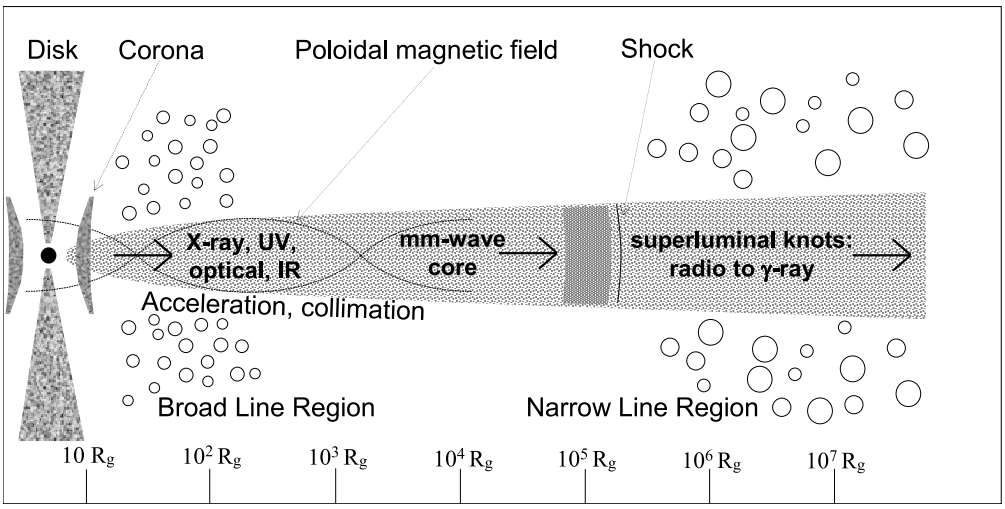

Figure 1.13: Illustration of the structure of a jet. The image has been taken from Lobanov (2007, Fig. 1), and has been adapted from Marscher (2005, Fig. 1).

X-ray binaries in our galaxy. They conclude that "*one or more of the following is correct: (i) the calculated jet power and speed measurements are wrong, (ii) the reported spin measurements are wrong and (iii) there is no strong dependence of the jet properties on the black hole spin*" and discuss other possibilities which can lead to variations of the jet power and the radiative efficiency. As discussed in Sect. 1.7 many X-ray binaries show different accretion states with varying jet power. Transitions between these states can occur on times scales which are much shorter than expected for significant changes of the black hole spin. In the discussion of a relation between spin and jet power, it has to be considered that accreting systems which do not include black holes can launch jets as well. Collimated outflows have been observed in systems in which the accreting objects are, e.g., neutron stars (see, e.g., Migliari & Fender, 2006, for a comparison of jets from neutron stars and black holes), white dwarfs (see, e.g., Galloway & Sokoloski, 2004, and the references therein), and even protostars (see Ferreira et al., 2006, for information on jets from T Tauri stars). Relations between properties of the inflow and outflow (scaled with the system) indicate that the jet power in accreting systems depends on fundamental accretion properties. For black hole systems of all masses, Falcke et al. (2004) discuss radiatively inefficient accretion at low accretion rates, where the spectral energy distribution is dominated by emission from a relativistic jet, whereas it is dominated by emission from the accretion disk in the case of high accretion rates.

A standard structure of an AGN jet is shown in Fig. 1.13. Accelerated and collimated particles propagate in the jet and emit electromagnetic radiation. Blandford & Rees (1978) suggested propagating shocks in the jets, which can explain the relativistically moving features. The emission mechanisms in jets are, e.g., described Blandford & Königl (1979), where emission is proposed to originate from quasi-steady jets and emission induced by propagating shock waves. An important component of jets in radio astronomy is the "core". In radio images the core is typically a bright and usually unresolved feature. The core is located at a certain distance of the black hole, where the jet starts to be optically thin and can be seen in the radio regime. Closer to to the black hole the jet is optically thick and self-absorbed. For a summary on the structure of jets, shocks, and the core see, e.g., Ch. 2 of Schinzel (2011) and the references therein.

1.4.3 Radiation from jets

Jets are typically powerful radio sources, but they can be as well observed in other frequency bands. *"Relativistic jets as compact radio sources"* are described in detail by Blandford & Königl (1979). Given the synchrotron and inverse-Compton mechanisms, which were considered in the

explanation of jet emission, it was expected that AGN jets were sources of high-energy emission as well (see, e.g., Königl, 1981, and references therein for a discussion of jets as X-ray and γ-ray sources). Tananbaum et al. (1979) studied X-ray emission from quasars and Swanenburg et al. (1978) detected γ-rays from 3C 273.

Synchrotron radiation The radiation of accelerated high-energy electrons has been described by Schwinger (1949). Alfvén & Herlofson (1950) suggested that this synchrotron radiation could be the underlying physical process explaining the radio emission in jets. It was a promising explanation, as it was consistent (contrary to thermal processes) with the high degree of polarization of the observed radio emission. A description of synchrotron radiation in the context of astrophysical jets is, e.g., given by Rybicki & Lightman (1979, Ch. 6), Krolik (1999, Ch. 9), and Begelman et al. (1984). In the latter work a comprehensive overview on jets with a focus on the theory of jets as radio sources is provided.

Charged particles moving in magnetic fields are influenced by the Lorentz force, when their velocity has a non-zero component perpendicular to the magnetic field. Accelerated charges emit electromagnetic radiation. In the case of relativistic charged particles the radiation is called synchrotron radiation. The average emitted power, $\langle P_{\mathrm{emit}} \rangle$, of relativistic electrons with an isotropic velocity distribution depends on the strength of the magnetic field, B, and the electron's velocity, β, (see, e.g., Rybicki & Lightman, 1979):

$$\langle P_{\mathrm{emit}} \rangle = \frac{1}{6\pi} \beta^2 \gamma \sigma_{\mathrm{T}} B^2. \tag{1.19}$$

A non-thermal distribution of electrons, which has a power law distribution, yields an integrated spectrum that is a power law, due to superposition.

Compton Scattering Compton scattering describes the process of photons scattering with charged particles, where energy is transferred. This mechanism was first detected by Compton (1923). When the photon energy decreases with the scattering the processes is typically called Compton scattering, whereas the process is considered as "Inverse Compton scattering" when the photon gains energy from the charged particle. The averaged energy change, ΔE_{ph}, of a photon scattering with an electron from a thermal distribution (with temparature T) can be approximated as (see, e.g., Rybicki & Lightman, 1979, Sects. 7.2–7.4):

$$\left\langle \frac{\Delta E_{\mathrm{ph}}}{E_{\mathrm{ph}}} \right\rangle \approx \frac{4 k_{\mathrm{B}} T - E_{\mathrm{ph}}}{m_e c^2}. \tag{1.20}$$

Multiple scattering processes can lead to a power law photon spectrum (see, e.g., Rybicki & Lightman, 1979, Sects. 7.5–7.7). The spectrum obtained from inverse Compton scattering with thermally distributed electrons is expected to have an exponential cutoff at $E \approx k_{\mathrm{B}} T$ (Sunyaev & Titarchuk, 1985). Equation 1.20 is not valid at high photon energies or with relativistic electrons, such that the production of electron positron pairs becomes possible in the scattering.

The existence of relativistic charged particles in jets is indicated from observations (synchrotron emission and jet kinematics), it is thus natural that Compton scattering occurs in jets, as different photon fields can be available. There is the so-called synchrotron self-Compton (SSC) process (see, e.g., Marscher & Gear, 1985). Here, photons which originate from jet's synchrotron radiation scatter with the charged particles in the jet. Additionally there is the external Compton process (EC; see, e.g., Dermer & Schlickeiser, 1993). As indicated by the name, the seed photons originate from external sources, such as the accretion disk, the broad line region, the torus, etc., as well as emission of these sources or the jet, which has been reflected by surrounding material.

Jets as Gamma-ray Sources The observed γ-ray emission of AGN can be explained by different models (a review is, e.g., given by Böttcher, 2007). The most likely origin for this high-energy emission are relativistic jets. Supporting arguments are for example that the large energy output at high energies seems too large to be isotropic, instead this emission is probably beamed. Additionally (as mentioned before) high-energy emission from jets is expected from the physical process explaining their radio properties.

In leptonic models, the high-energy emission is dominated by radiation processes of electrons and/or electron-positron pairs, mainly the previously described SSC and EC mechanism.

In hadronic models the particles in the jet, in particular protons, are accelerated to such high energies that pions can be procured in scattering processes. The scattering of high-energy baryons leads to cascades and thus to further emission processes (see, e.g., Mannheim & Biermann, 1992). γ-rays can be produced directly by the decay of the π^0 meson. Other scattering products, such as charged pions, which decay to muons and further to electrons or positrons, can further interact with other fields and, e.g., emit synchrotron photons.

Jet-internal shocks leading to time lags in the optical, X-ray and γ-ray regime are described by Böttcher & Dermer (2010).

1.5 Multiwavelength Studies of AGN

Although the main components in AGN, which were introduced in the previous sections, have been studied for decades with improving quality of observational data and further developed theoretical models, still numerous questions remain open. Individual components are better understood than the connections between them. Often emission in certain energy regimes can be clearly identified with components, in order to understand the relation between different components multiwavelength observations are thus required. Based on the geometry of AGN, where different components are spatially separated, significant delays in the coupling of emission of different components is expected due to causality. For that reason multiwavelength monitoring campaigns are necessary in order to obtain insights in the complete emission mechanisms of AGN.

In this work, mainly radio, X-ray and γ-ray observations are used. Radio interferometry observations, which provide high resolution images of jets and allow direct measurements of jet parameters, are described in Sect. 2.1. In the X-ray regime it is possible to study the close environment of the accreting objects (see Sect. 2.2), and γ-ray observations provide insights in the most extreme processes occurring in AGN and their jets.

Many AGN emit radiation throughout the electromagnetic spectrum. Figure 1.14 shows the spectral energy distribution (SED) of AGN and the different model components. The radio emission of radio-loud AGN is typically dominated by synchrotron emission form the jet. Contributions from thermal emission from the accretion disk and dust, as well as emission from the host galaxy can be found at higher frequencies, i.e., from the infrared to the ultraviolet regime. As discussed previously, the main mechanism causing high-energy emission is the inverse Compton process. The top left spectrum in Fig. 1.14 shows modeled contributions of different populations of seed photons, i.e., different sources of upscattered photons. In addition to synchrotron-self-Comptonization there is external Comptonization of photons, e.g., from the BLR or the accretion disk. In blazars typically the boosted emission components dominate and the resulting SED shows a structure consisting of two humps as it can be clearly seen in the left spectra shown in Fig. 1.14. The low-energy hump can usually be well-described with synchrotron models and the high-energy hump by mainly Comptonization models. There are currently various models available, which are able to describe the broad band spectra. A goal in the development of models are self-consistent physical models. Modeling each component individually typically implies larger numbers of free parameters. The relation and interaction between different components is crucial for a complete understanding of accreting objects.

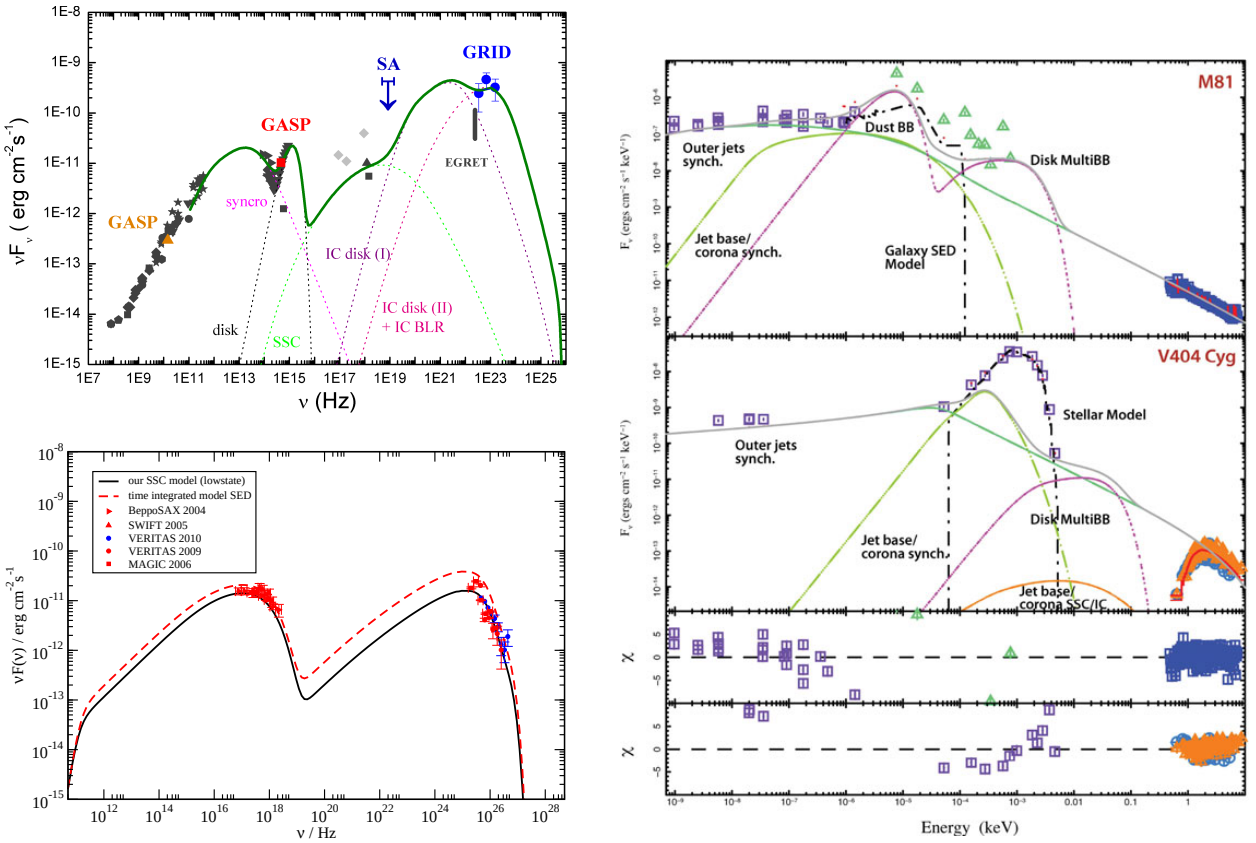

Figure 1.14: Models for broad band spectra of AGN. *Left (top):* Spectral energy distribution of the source PKS 1510−089 (Pucella et al., 2008, Fig. 5). The spectrum includes the synchrotron emission (low-energy hump), thermal emission from the disk, and an inverse Compton component (IC; high-energy hump). *Left (bottom):* Self-consistent synchrotron-self Compton model for FBQS J1221+3010 by Weidinger & Spanier (2010). *Right:* SED models for the low-luminosity AGN M81 and the X-ray binary V404 Cyg using the self-consistent jet model of Markoff et al. (2005) (Markoff et al., 2011, Fig. 1).

The right spectra in Fig. 1.14 show fits to the data of a low-luminosity AGN and a X-ray binary using the same self-consistent model of Markoff et al. (2005), which can be scaled with black hole mass.

The analysis of broad band spectra and high-quality data of improving instruments yields constraints on models and thus contributes to insights in the underlying processes in accreting objects.

Blazar Sequence Studying a sample of blazars, Fossati et al. (1998) found a relation between the bolometric luminosity of blazars and their spectra: The typical double-hump structure in their SEDs is shifted to higher frequencies with decreasing bolometric luminosities. Additionally the ratio between the luminosity of the high-frequency component and that of the low-frequency component decreases with decreasing bolometric luminosity. This relation is shown in Fig. 1.15.

Different underlying mechanisms which can cause the blazar sequence are discussed. For example, Ghisellini & Tavecchio (2008) propose that the mass of the black hole in the AGN and the accretion rate are sufficient to explain the observed relations. Meyer et al. (2011) present indications that the blazar sequence is formed from two populations of objects, which are discussed in the context of FR I and FR II classes. Nieppola et al. (2008) suggest that the blazar sequence is an artifact of Doppler boosting and disappears when Doppler-corrected values are used. Even pure

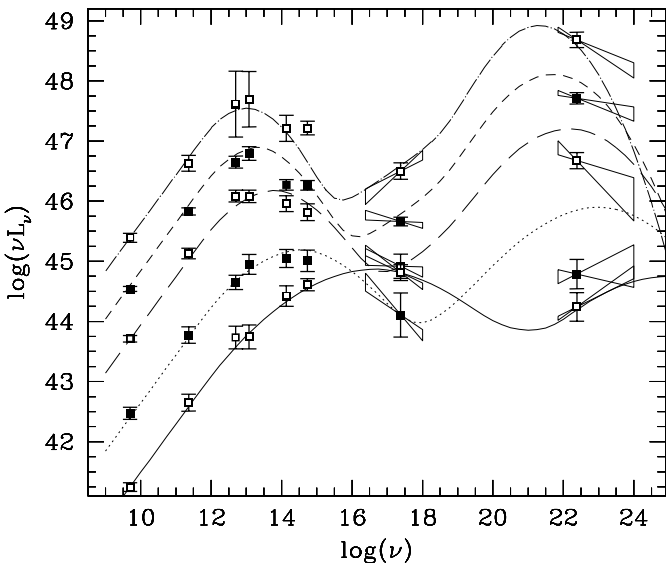

Figure 1.15: Blazar sequence: The two humps in the SED peak at higher frequencies for blazars with lower bolometric luminosities. (Fossati et al., 1998, Fig. 12)

selection effects have been considered to explain the blazar sequence.

1.6 Luminosities and Cosmological effects

Flux density With observations the flux density of sources can be determined. At high energies (X-rays and γ-rays) typically individual events are resolved, i.e., the number of photons per time can be counted. A natural quantity in high-energy astronomy is thus the photon flux density $N_{\rm ph}(E)$, which is typically given in units of photons $\mathrm{cm}^{-2}\,\mathrm{s}^{-1}\,\mathrm{erg}^{-1}$. The energy flux density is then simply given by multiplying each photon with its energy $F(E) = E\,N_{\rm ph}(E)$. The quantity $E\,F(E)$ is equivalent to $\nu\,F(\nu)$, which is often used to show the broad band spectra of AGN and other sources throughout the electromagnetic spectrum.[7]

As real instruments do not provide infinite energy resolution, data obtained from measurements is typically binned in energy, i.e., the flux density is integrated over the limits of the bin. At lower energies, where individual photons are usually not resolved, the fluxes can determined directly, e.g., via gain factors of the instrument.

Luminosity The luminosity characterizes the total radiated energy per time of a source. Given the measured flux of a source, the distance to the source and the angular distribution of its emission are required in order to determine its luminosity. In the standard approximation of isotropic emission (and a size of the source negligible compared to the distance), the luminosity is given by

$$L(E) = 4\,\pi\,d^2\,S(E), \tag{1.21}$$

where d is the distance to the source. The determination of the distance is usually difficult. For large distances the cosmological expansion of space is used to estimate the distance. On the other hand, as described in the following, the expansion of space implies difficulties in the calculation of the luminosity.

Expanding Universe First indications of an expanding universe have been found by Hubble (1927), who discovered a relation between radial velocity and distance (which had been obtained, e.g., by observing Cepheids). The radial velocity had been determined from the redshift, which is defined as $z = \Delta\lambda/\lambda$. The linear relation of the redshift on the distance and the isotropic

[7] The photon energy $E = h\,\nu$ is directly related to its frequency ν via the Plank constant $h = 4.135447 \times 10^{-15}\,\mathrm{eV\,s}$.

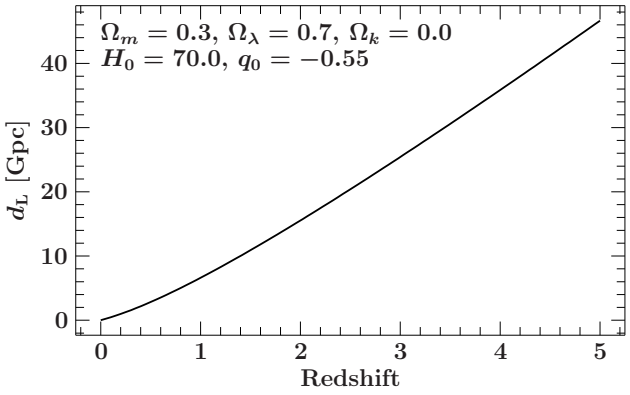

Figure 1.16: Luminosity distance as a function of redshift, where the cosmological parameters are set to the default parameters described in the text.

distribution of objects fulfilling this relation indicated that the redshifts are not based on the individual movement of sources, but that space itself is expanding. The expansion can be written written in the form $v = H_0 d$, where v is the recessional velocity of an object at distance d, and H_0 is the Hubble constant. It is parametrized with the dimensionless h in the following form:

$$H_0 = 100\, h\, \mathrm{km\,s^{-1}\,Mpc^{-1}}. \tag{1.22}$$

The precision of the value of h is still improved. Komatsu et al. (2009) find $h = 0.705 \pm 0.013$.

Luminosity distance Using the above mentioned relation between redshift and distance, the distance of a source can be estimated directly when its redshift is known. The distance could then be used to calculate the source's luminosity from the measured flux density with Eq. 1.21. This is, however, problematic because of the following reasons. For example not only the wavelength of the photons, which travel through expanding space, is increased, but the arrival times between between two photons is increased as well. For that reason the measured flux is decreased. In addition, the expansion rate is not constant over long time scales. A photon traveling large distances is thus exposed to different expansions and the linear relation between redshift and distance is not valid in this case. Because of the temporal evolution of space, a measure of (large) distances in the universe is difficult.

There are different cosmological distances defined. One of them is the luminosity distance d_L, which takes cosmological effects (as those mentioned above) into account such that Eq. 1.21 is fulfilled. The value of $d_\mathrm{L}(z)$ depends on the cosmology model. A comprehensive discussion of cosmological physics is provided by Peacock (1999).

Throughout this work the luminosity distance in the Friedmann-Robertson-Walker model, e.g., described by Carroll et al. (1992), is used:

$$d_\mathrm{L}(z) = \frac{c(1+z)}{H_0\sqrt{\Omega_k}} \sinh\left(\sqrt{\Omega_k}\int_0^z \frac{dz'}{(1+z')^2(1+2z'(q_0+\Omega_\lambda)) - z(2+z')\Omega_\lambda}\right) \tag{1.23}$$

where the following set of cosmological parameters has been used: H_0 is the Hubble parameters in units of $\mathrm{km\,s^{-1}\,Mpc^{-1}}$. The used default value of this parameter is 70. q_0 is the deceleration parameter with a default value of -0.55. The remaining parameters are the curvature constant $\Omega_k = 0$, the matter density Ω_m, and the cosmological constant Ω_λ. They are normalized to the closure density such that $\Omega_k + \Omega_m + \Omega_\lambda = 1$. The default values used here are $\Omega_k = 0$, $\Omega_m = 0.3$, and $\Omega_\lambda = 0.7$ (see, e.g., Carroll et al., 1992; Peacock, 1999, for a detailed discussion of these parameters). The luminosity distance, which has been calculated using this set of default parameters, is shown as a function of redshift in Fig. 1.16.

Within the scope of the current work Eq. 1.23 has been implemented in local software packages (including numerical integration). The luminosity can be calculated as well for modified values of

the parameters. By specifying two of the four parameters (q_0, Ω_k, Ω_m, Ω_λ) the remaining two can be determined. In the case $\Omega_\lambda = 0$ a simplified expression can be used to obtain the luminosity distance:

$$d_{\mathrm{L}}(z) = \frac{c\,z}{H_0} \frac{1 + z\,(1 - q_0)}{\sqrt{1 + 2q_0 z} + 1 + q_0 z} \tag{1.24}$$

K-correction With the measured flux density of a source and the calculated luminosity distance its luminosity can be determined. Due to the redshift of the source it is required to consider energy shifts. The measured energy band differs from emitted energies in the source frame. In order to compare luminosities of different sources, and to obtain the luminosity in certain energy bands in the source frame, this effect has to be accounted for. For this correction, which is known as K-correction, spectral information of the source is required.

In the radio, X-ray, and γ-ray regime it is usually a good approximation to use a power law photon spectrum of the form:

$$\frac{\mathrm{d}N_{\mathrm{ph}}}{\mathrm{d}E} \propto \left(\frac{E}{E_0}\right)^{-\alpha} \tag{1.25}$$

where α is the spectral index. In this case the K-correction can be done as, e.g., in Ghisellini et al. (2009):

$$L = 4\pi d_{\mathrm{L}}^2 \frac{S_E}{(1+z)^{2-\alpha}} \tag{1.26}$$

1.7 Connection to Galactic Sources

For a full understanding of physical processes in accreting black holes it is very helpful to consider X-ray binaries in addition to AGN. A combination of the study of both object classes offers complementing insights. AGN and accreting stellar mass black holes can be understood as scaled versions of each other. There are only a few essential properties characterizing these system. On the one hand the properties of the central compact objects, which are in the case of black holes their mass and spin, and on the other hand the surrounding material, especially the accretion rate. The size of the black hole's event horizon scales linearly with its mass (Eq. 1.3). For that reason the system size scales in the same relation, and thus the characteristic variability time scales as well. The temporal evolution in AGN and X-ray binaries can thus be studied on completely different time scales. Given the mass ratio, time scales in systems including accreting stellar mass black holes are shorter than those in AGN by factors in the range of 10^5–10^9. Due to their similarity to AGN accreting stellar mass black holes (with jets) are often considered as microquasars.

There are X-ray binaries in our Galaxy that are significantly brighter in some energy bands, especially in the X-ray band, than AGN. Observations of these source yield high signal-to-noise data, which are important for certain studies, such as timing analyses with high resolution.

1.7.1 State Transitions

X-ray binaries are typically highly variable sources. In the X-ray regime variability can be studied from time scales less than milliseconds up to years. Especially the long-term evolution in these sources cannot be studied in AGN as due to the above mentioned scaling, the corresponding time scales are beyond those that humans can observe. Figure 1.17 shows a selection of X-ray binaries including stellar mass black hole candidates. The light curves covering several years show a different behavior of variability. It has been found that some objects are persistent sources whereas others are transient. This difference can be explained by different accretion rates. On the one hand there are high-mass X-ray binaries (HMXBs), where the companion star is a massive star. Their strong stellar wind provides material to be accreted and thus continuously fuels the compact object. A

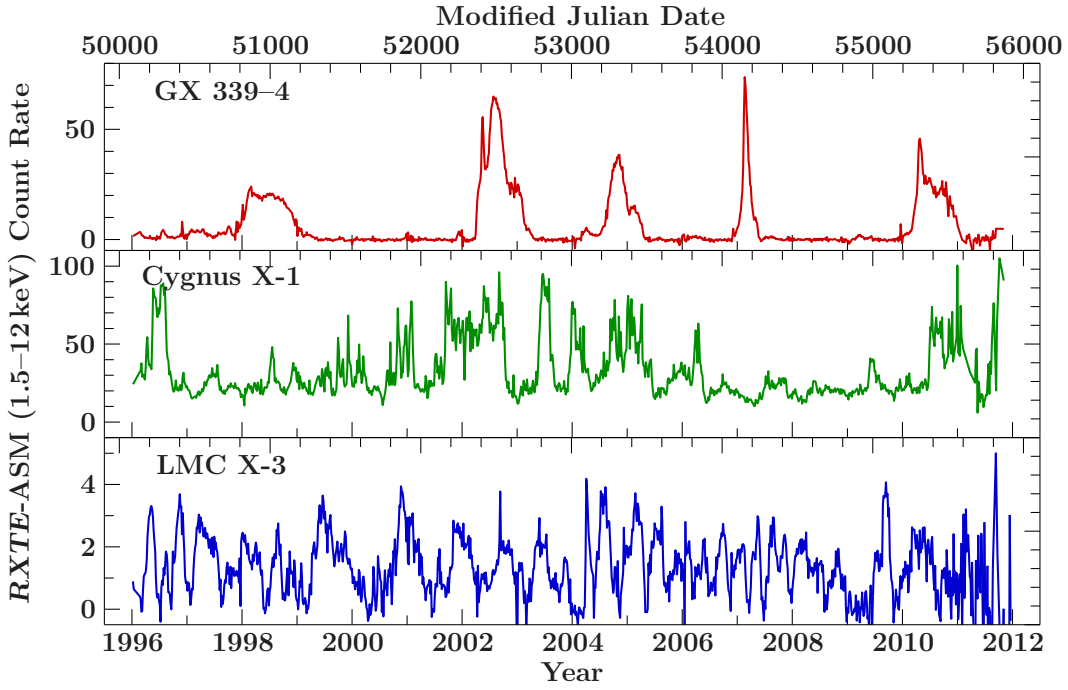

Figure 1.17: Different variability patterns of X-ray binaries as seen by *RXTE*-ASM (1.5–12 keV). In order to show only the long-term variability, the light curves have been binned on (multiples of) the orbital period in each system. (The orbital periods are on the order of days. For these sources see, e.g., Hynes et al., 2003; Gies et al., 2008; Cowley et al., 1983, respectively)

typical example of a HMXB is Cygnus X-1. The transfer of material is different in low-mass X-ray binaries (LMXBs). The stellar winds of low-mass stars are significantly weaker than those of massive stars. In LMXBs material is mainly transferred from the donor star to the compact object vie Roche-Lobe overflow. A summary on Roche-Lobe overflow and wind accretion is, e.g., given in Sect. 1.1.1 and 1.1.2 of Hanke (2011) and the references therein.

Especially interesting for the understanding of the emission processes occuring in accreting systems and the connection between different spectral components is their temporal evolution, because several sources show different emission states and transitions between them. These states can be characterized based on spectral and timing properties, and indicate strong changes in the emission components. The basic classification scheme for X-ray binaries are the so-called hard and soft states, which are mainly based on the spectral shape in the X-ray regime. The dominating continuum components in the spectra are thermal emission from the accretion disk and a power law component, which is explained by inverse Compton scattering in a hot Corona or a jet (base). Compared to the hard state, the contribution of the thermal emission is stronly increased in the soft state and the spectral index of the power law is steeper. The detailed behavior and the absolute values depend on the source. In some sources the soft X-ray spectra are completely dominated by the thermal emission in the soft state. In the hard state many sources show indications of (steady) jets and radio emission can be observed. In the soft state the radio emission is significantly weaker, or even undetectable. It has been discussed that in intermediate states, where the luminosity is large and often flaring occurs, there is the so-called "jet line", which is the separation between states with steady jet and strongly quenched jets. A review on states and transitions is given by Belloni (2010). For transient sources typical temporal evolutions are observed (see Fig. 1.18 and, e.g., Fender et al., 2004, for more information). The different states are not only characterized by spectral properties, but the timing properties depend on the state as well (some sub-classifications are even mainly based on the timing properties). There are correlations between timing and spectral properties,

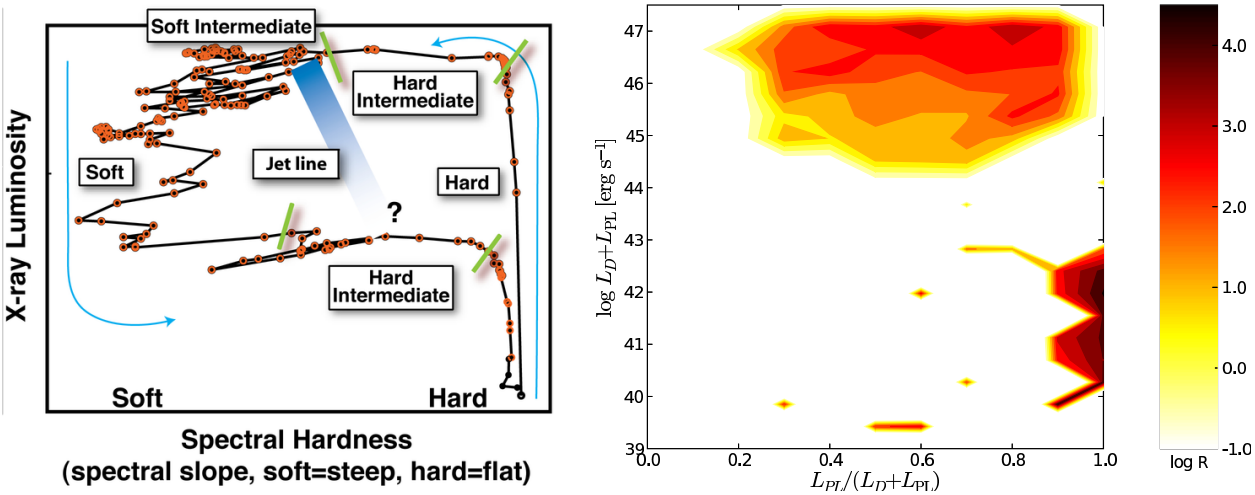

Figure 1.18: *Left:* Hardness-intensity diagram in the X-ray regime showing the typical temporal evolution of an individual transient black hole X-ray binaries. The states are labelled. (Credit: T. Belloni et al., ISSI, see http://www.issibern.ch/teams/proaccretion/) *Right:* Distribution of an AGN sample in a hardness-intensity diagram by Körding et al. (2006, Fig. 7). Hardness and intensity are given from the ratio and the sum of the disk L_D and the power law luminosity L_{PL} in the sources, respectively. The color scale represents the radio loudness of the AGN. The gap between the luminous quasars and the radio-loud low-luminosity AGN is a selection effect.

e.g., Böck et al. (2011) study relations between these properties during a state transition in Cygnus X-1. High-frequency quasi-periodic oscillations and time delays between the variability in different energy bands, allow for insights in the accretion geometry and mechanims. Using the frequencies and delays, it is possible to determine the energy band from which the variability originates and thus the emission component. Additionally the propagation of the variability and the reprocession of emission can be studied. Uttley et al. (2011) find X-ray variability, which is induced in the accretion disk. Such detailed studies are only possible with data with a high signal-to-noise ratio.

Considering the above mentioned scaling, numerous analogies between Galactic black hole binaries and AGN are found. Markowitz & Uttley (2005) found that the low-luminosity AGN show analog variability in the X-ray regime (similar shape of the power spectral density; PSD) than Galactic black holes in the hard state. McHardy et al. (2006) discuss the scaling between AGN and Galactic black holes based on the black hole mass and the accretion rate.

Due to scaling, only variability occuring in short time scales in Galactic objects can be observed in AGN as well. The long-term behavior in Galactic objects, such as transitions between different states cannot be observed in AGN due to the long required time scales. This problem can be solved by considering samples of AGN. Given the analogy between accreting black holes of all masses, large AGN samples would thus include objects in different states. Comparisons, e.g., by Körding et al. (2006), revealed further similarities between these objects. Figure 1.18 (right plot) shows the distribution of AGN samples in a hardness-intensity diagram. The energy bands are scaled in order to cover same emission components (accretion disk and power law) which are typically observed with X-ray observations of Galactic black holes.

Considering that AGN might be in different states is a clear extension to the unified model, in which different source classes are explained mainly by different viewing angles.

1.7.2 Jets as high-energy Sources

Cygnus X-3 Cyg X-3 is a microquasar which is detected in the γ-ray regime. This object is a HMXB. The massive companion star is a Wolf-Rayet star, which provides larger accretion rates onto

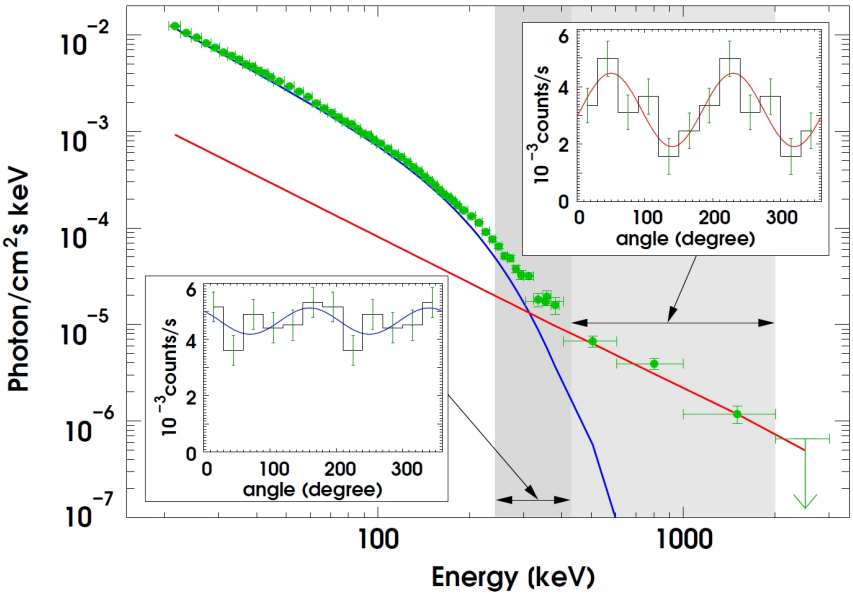

Figure 1.19: *INTEGRAL* observation of Cyg X-1 showing polarized γ-ray emission for the hard tail in the spectrum. (Credit: J. Wilms, priv. comm.; more information is given by Laurent et al., 2011)

the compact object due to its extreme stellar wind. The system is strongly variable throughout the electromagnetic spectrum. Detections of Cyg X-3 in the high-energy regime have been claimed by studies of data from early missions and it is firmly detected with *Fermi*/LAT (a detailed discussion is given by Abdo et al., 2009c, and the references therein). Cyg X-3 shows correlated variability between γ-rays and radio emission, leading to a clear identification of the γ-ray emission with this object. Based on the relation between radio emission from a relativistic jet and the γ-ray emission, Abdo et al. (2009c) suggest that origin of the high-energy emission could be inverse Compton scattering of photons from the companion star with electrons in the jet. In combination with the variabilty, insights on the jet physics and its formation could be gained from monitoring observations, as the source changes between states of strong emission and a quenched jet.

Cygnus X-1 A clear indication of jets as the origin of γ-ray emission has been found in the case of the well-studied Galactic Black Hole Cyg X-1. Laurent et al. (2011) discovered that a hard tail in the spectrum has large polarized fraction. The polarization measurement is based on a large total exposure time (about 5 Ms) on the source with the IBIS telescope (Ubertini et al., 2003) onboard the *INTEGRAL* mission (Winkler et al., 2003). The integrated spectrum, which is shown in Fig. 1.19, reveals two spectral components in the energy band between 20 keV and 2 MeV. The first component dominates the emission up to about 300 keV and is consistent with Compton scattering on electrons with a thermal distribution. In the energy regime of about 250 keV to 400 keV, in which there is still a large contribution of the component at lower energies, only an upper limit on the polarized fraction of $\sim$20% has been obtained. At higher energies in the band 0.4–2 MeV, where the second component dominates the emission, a large polarized fraction of 67 ± 30% has been measured in contrast. Due to the high degree of polarization, the emission of the second component is not consistent with Compton upscattering by thermal electrons, e.g., in a hot corona. A coherent magnetic field is required for the emitting region in order to yield the observed polarization. The underlying emission process of the second component is thus interpreted as synchrotron radiation or inverse Compton scattering in the jet. A more detailed discussion is given by Laurent et al. (2011) and in the references therein.

Chapter 2

Radio and X-ray data

2.1 Radio Astronomy

Radio astronomy started with the discovery of a signal of interstellar origin by Jansky (1933), who measured at a wavelength of about 14.6 m. The determined position of the source (right ascension $\sim 18^{\mathrm{h}}$, declination of about $-20°$) is consistent with that of the Galactic center, although uncertainties of up to $\pm 30°$ were assumed. Since then radio astronomy strongly developed. Today numerous quantities of radio sources are known and wide frequency regimes can be observed with high spectral resolution. A description of radio astronomy and its tools is, e.g., provided by Rohlfs & Wilson (2004).

On of the major breakthroughs of radio astronomy is radio interferometry, which is described in the following section. With this technique extremely high angular resolutions can be obtained, down to fractions of milliarcseconds.[1]

2.1.1 Radio telescopes and interference

The observable wavelength range in the radio regime covers orders of magnitude. The typical range reaches from about 30 meters (corresponding to $\sim$10 MHz) to sub-millimeter wavelengths ($\gtrsim$300 GHz). For different wavelengths different telescope types are suitable. For example dipole antennas are used for long wavelengths, e.g., by LOFAR (see, e.g., Falcke et al., 2007), which operates in the $\sim$30–240 MHz regime. At shorter wavelengths one typically uses radio telescopes that consist of a parabolic reflector dish which focuses the incoming radio waves on a detector converting it to an electronic signal. A detailed description of radio telescopes is, e.g., provided by Rohlfs & Wilson (2004).

Radio observations with single antennas are typically restricted by low angular resolution θ, which is limited according to the Rayleigh criterion:

$$\sin\theta \approx 1.220\frac{\lambda}{D} \tag{2.1}$$

where λ is the observed wavelength and D the diameter of the aperture, which is assumed to be circular. Due to the long wavelengths even radio telescopes with an aperture diameter of $\sim$100 m still cannot reach the angular resolution of the human eye in the visible light. As it is technically difficult to further increase the size of individual radio telescopes (especially if they are movable to change the pointing position), another solution is required to circumvent the diffraction limit on

[1] Besides astronomical studies radio interferometric observations allow for other fruitful applications as well. Given the extreme angular resolution, radio observations of celestial reference sources can be used for geodesy and studies of the Earth itself. For example the rotation of the Earth can be studied in detail. For the high resolution the positions of the telescopes have to be known with centimeter precision, which on the other hand allows to measure relative motions of the telescopes and thus to track the movement of the Earth's tectonic plates.

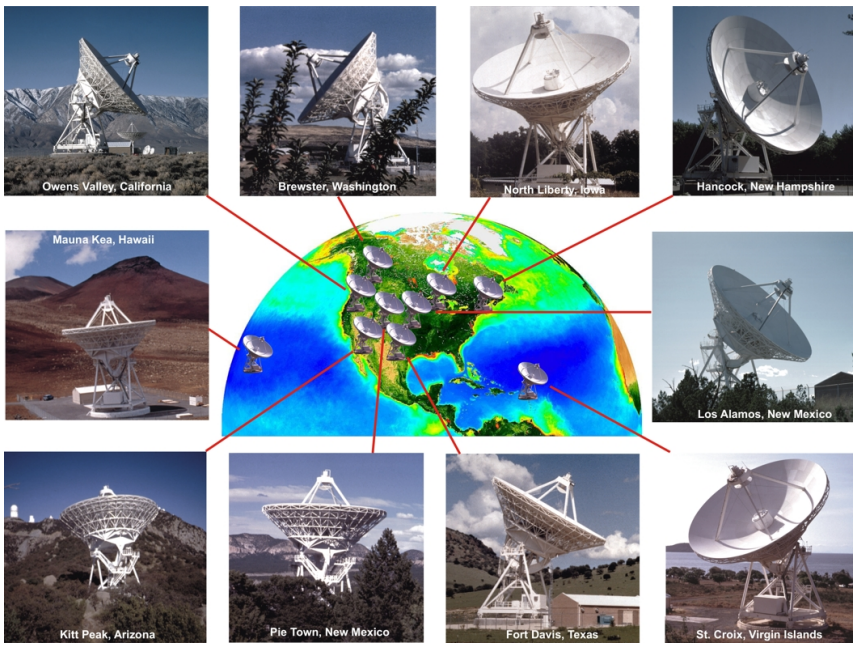

Figure 2.1: Montage of the radio telescopes of the VLBA and their locations in the USA. (Image courtesy of NRAO/AUI and Earth image courtesy of the SeaWiFS Project NASA/GSFC and ORBIMAGE)

the angular resolution of in Eq. 2.1. This can be done by combining several radio telescopes to an interferometric array. With the interferometric signals of more telescopes higher angular resolutions than with the individual telescopes can be obtained, which are almost comparable to the angular resolution of a telescope with the diameter of the maximal distance between the telescopes. A very comprehensive description of "Interferometry and Synthesis in Radio Astronomy" is given by Thompson et al. (2001). Combining radio telescopes spread all over the Earth (and even satellite borne instruments) the radio regime is currently the one in which the highest angular resolutions (significantly below milliarcseconds) are obtained. The technique in which such long distances between the telescopes are used is called Very Long Baseline Interferometry (VLBI).

For the purpose of radio interferometry observations dedicated arrays of telescopes have been constructed. Within the current work data has been analyzed, which has been obtained with the Very Long Baseline Array (VLBA) of the National Radio Astronomy Observatory (NRAO).[2]. The VLBA consists of 10 antennas, which have parabolic dishes with a diameter of 25 m and are located in the USA. The images and positions of the VLBA stations are shown in Fig. 2.1. An advantage of the VLBA is that is constructed for the purpose of interferometry and, e.g., all antennas are identical. In this way the correlation and calibration of the data is easier than with a heterogenous array of radio telescopes. But radio interferometry observations are also possible with the combination of other telescopes. For example the telescope array used for TANAMI observations is described in Sect. 4.1.4.

2.1.2 *uv*-coverage and baseline weighting

The obtained angular resolution and image quality depend on the orientation and length of baselines used in the observation. The baseline is the distance between two telescopes projected on a plane orthogonal to the line of sight to the observed source. Radio interferometric observation are characterized by the coverage of the so-called *uv*-plane. It can be understood as the above mentioned plane, in which all the baselines of the observation are projected. The u coordinate is measured in east-west direction and v in north-south. The used unit for distances in this plane is typically the observation wavelength. The *uv*-coverage describes how well the *uv*-plane is sampled with baselines. The configuration of the baselines depends on the positions of the telescopes

[2] https://science.nrao.edu/

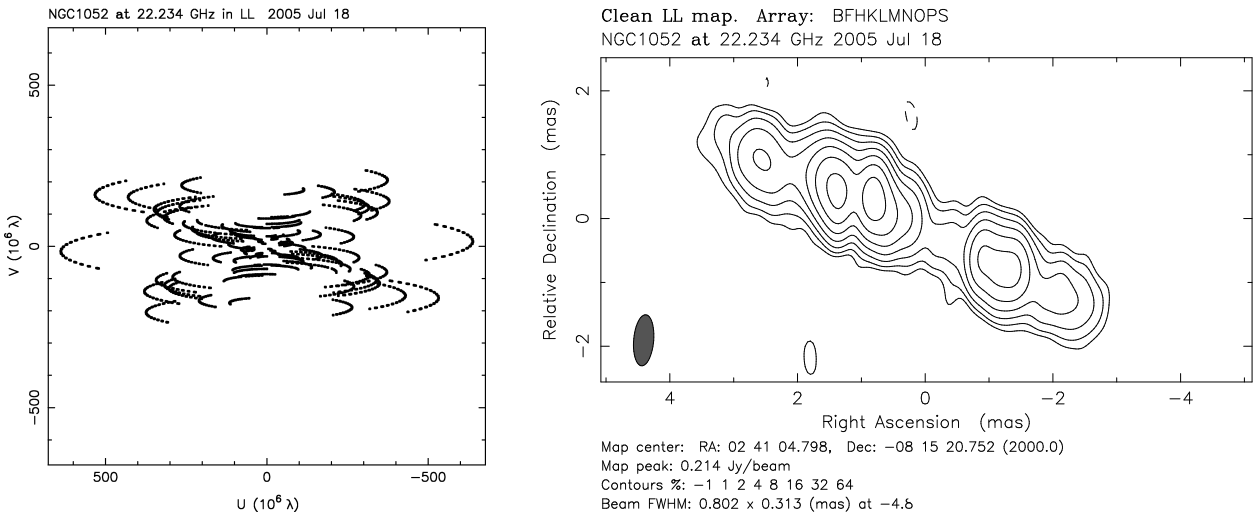

Figure 2.2: VLBI observation of NGC 1052 at 22 GHz. *Left:* *uv*-coverage of the observation. *Right:* Corresponding VLBI image. The filled ellipse in the bottom left corner characterizes the resolution (Gaussian approximation), which is higher in east-west direction, as longer baselines are available in this direction.

(the telescope array) that are used for the observation. Whereas the positions of the telescopes are typically not moving with respect to each other (except, e.g., satellite borne instruments), the projected baselines can change with time due to the rotation of the Earth. For that reason one method to improve the *uv*-coverage is the usage of several snapshot observations of the source with the telescope array during time scales of hours (e.g., a day or the time in which the source is visible). An example of an *uv*-coverage is shown in Fig. 2.2, where NGC 1052 has been observed with the VLBA. The curved structures in the *uv*-plane are due to the Earth's rotation. The reason why a good *uv*-coverage is required in order to obtain good images of the source is the following. Given the connection between an aperture and the diffraction pattern via Fourier transformations, it can be understood that every baseline corresponds to one spatial frequency and therefore to one component of the source's image. In order to obtain a good intensity map of the source with reduced artifacts, a good coverage of the *uv*-plane is required. Long baselines yield high resolutions, whereas shorter baselines are more sensitive to extended structures on larger scales.

Based on one observation it is possible to obtain images with different resolutions by weighting baselines, e.g., by applying tapers in the *uv*-plane. Two commonly used weightings are natural and uniform weighting. In contrast to natural weighting, the contributions of baselines are weighted according to the inverse of the local density of the *uv*-coverage in uniform weighting. With observations of most telescope arrays, more short baselines are typically available, thus the inner region of the *uv*-plane is sampled denser. For that reason long baselines usually contribute more in the case of uniform weighting, whereas larger, extended structures can be seen better with natural weighting.

The resolution of an image is characterized by the so-called synthesized beam. It is the response of the telescope array with the given *uv*-coverage to a point source. The main peak of the beam is typically approximated with a two dimensional Gaussian profile, which is described by the position angle and its semimajor and semiminor axis.

In radio astronomy it is possible to record the signal of the source individually with each telescope and use a computer for a correlation with software afterward. For this purpose it is necessary to record the signals with an exact time information, which requires precise synchronized clocks at each radio telescope. In this way time delays between the recorded signals can be determined with high precision.

2.1.3 Radio Data Analysis

The high-precision observations require a careful calibration and analysis of the data. It is, e.g., necessary to know the positions (phase center) of the telescope with high accuracy and numerous effects have to be considered in the calibration and analysis process in order to obtain radio images of high quality.

Calibration The correlated data are further processed and calibrated. For data used in this work that was done with the Astronomical Image Processing System ($\mathcal{AIPS}$; Fomalont, 1981; Greisen, 1998). With this program calibration and flagging tables for the data can be created, atmospheric effects can be accounted for, and calibrator sources can be considered for the calibration. The so-called *a-priori* calibration contains amplitude and phase calibration, which are described in more detail by Diamond (1995). An overview on VLBI data reduction is provided, e.g., by Schinzel (2011, Sect. 4.3).

Imaging For imaging of the VLBI observations the program DIFMAP (Shepherd, 1997) has been used in this work. This program allows further editing, adaptive (self-)calibration, and the creation of source images using deconvolution. For the latter the so-called clean algorithm is used (Högbom, 1974). A detailed description of the clean algorithm is provided in Sect. 11.2 of Thompson et al. (2001). Here, a model for the flux distribution of the source is created out of point sources and the "clean image" is given by the point-source response with the "clean beam". The clean beam is the main peak of the response ("dirty beam") where the side lobes are ignored.

Model Fitting In order to identify features in the images and, e.g., track them in several observation epochs, it is more suitable to model them with certain profiles instead of a combination of point sources. Typically two dimensional Gaussian profiles are used (suitable for the fast Fourier transforms used in the convolution). These profiles are characterized by their position, the total flux, the semimajor and minor axis, and the position angle. In this work mainly circular components have been used, thus the last two parameters are fixed. The parameters of the model components for the flux distribution of the source can then be obtained from fitting the data. Proper determination of uncertainties is difficult in the analysis of interferometric data. The systematic absolute uncertainty inherent in VLBI observations cannot be precisely determined. Calibration issues, discrete combinations of baselines, and complex transformations underlying interferometry make analytic error propagation difficult. It is however possible to get constraints on the systematic uncertainties in images, e.g., via simulations of observations.

In order to obtain uncertainties on parameters of a model fit to an image, we use the method described by Fomalont (1999). This method is, however, only considering statistical image uncertainties, and has thus to be treated with care. For a model component in one dimension, which has the parameters S_{peak} (peak intensity), p (position), w (width of the component), and S_{int} (integrated intensity), uncertainties can be estimated using the noise in the post-fit image, where the noise is specified in rms. The approximated uncertainties are then (Fomalont, 1999, Eq. 14-5):

$$\Delta S_{\mathrm{peak}} = \mathrm{rms} \tag{2.2}$$

$$\Delta p = \frac{w\,\mathrm{rms}}{2S_{\mathrm{peak}}} \tag{2.3}$$

$$\Delta w = \frac{w\,\mathrm{rms}}{S_{\mathrm{peak}}} \tag{2.4}$$

$$\Delta S_{\mathrm{int}} = \sqrt{\mathrm{rms}^2 + \left(\frac{S_{\mathrm{int}}\Delta w}{w}\right)^2} \tag{2.5}$$

$$\tag{2.6}$$

2.2 X-ray Astronomy

As described in the intruction (Sect. 1), the different components of AGN are visible in different energy regimes. For a complete understanding of these systems it is thus crucial to combine information of different frequency ranges. An excellent complement for the high resolution of the (sub-)parsec structure of jets with the radio VLBI technique is X-ray astronomy. X-ray observations are important for studies of accreting black holes, as they allow to probe the environment of the black hole. As the Earth's atmosphere is opaque for X-rays, ground based observations are impossible. First measurements of celestial X-rays have been performed with detectors in balloon and rocket flights. During the last decades numerous satellite-borne X-ray instruments have been used, which provided important insights in high-energy astrophysics.

In the following section a brief overview on instruments, which are important for studies within the frame of the current work, is given and their main characteristics are summarized.[3] The X-ray data analysis is described in Sect. 2.2.2.

2.2.1 X-ray instruments

ASCA The Advanced Satellite for Cosmology and Astrophysics had a time of operation from 1993 until 2001. Among other things its energy range of 0.4–10 keV allowed studies of broad iron lines in AGN. The *ASCA* mission is described by Tanaka et al. (1994).

BeppoSAX This X-ray mission was in operation from 1996 until 2002. A comprehensive overview on the mission is given by Boella et al. (1997). The instruments on board cover the energy range from about 0.1 keV to ∼300 keV. In this work only data obtained with the Low and Medium Energy Concentrator Spectrometers (LECS, MECS) have been used. Their spectral coverage is 0.1–10 keV and 1.3–10 keV, respectively. Long exposure observations with these narrow field instruments are used in this work to study the soft X-ray emission in AGN.

RXTE The *Rossi X-ray Timing Explorer* had been launched in the end of 1995 and operated until the begin of 2012. An important characteristic of the mission is its capability of high temporal resolution. More important for the current work was the relatively large collecting area (in a field of view of about one degree). With *RXTE* monitoring campaigns were possible. Typical exposure times of a few kiloseconds were sufficient to determine the brightness of an AGN and estimate the spectral shape. The resolution of the instruments on board was only moderate, but the energy range was large. The Proportional Counter Array (PCA; Jahoda et al., 1996) can measure from 2–60 keV and the High Energy X-ray Timing Experiment (HEXTE; Rothschild et al., 1998) from 15–250 keV (due to calibration issues and effective area the usable energy range is typically slightly smaller).

Chandra The *Chandra X-ray Observatory* was launched in 1999. Instruments onboard the spacecraft operate at energies of 0.1–10 keV. *Chandra* is currently considered as NASA's flagship mission for X-ray astronomy. One of its most outstanding features is the capability for high-resolution imaging in the X-ray regime, where X-rays are focused with a Type 1 Wolter (1952) telescope. With *Chandra* a arcsecond angular resolution is obtained (even slight sub-arcsecond resolution can be achieved). Besides the imaging mode with the AXAF Charged Coupled Imaging Spectrometer (ACIS; Garmire et al., 2003), *Chandra* can be used as a high-resolution spectrometer with the Low and High Energy Transmission Gratings (LETG and HETG).

[3] An overview on active and past high-energy missions is provided by NASA's High Energy Astrophysics Science Archive Research Center (HEASARC) at http://heasarc.gsfc.nasa.gov/docs/heasarc/missions/.

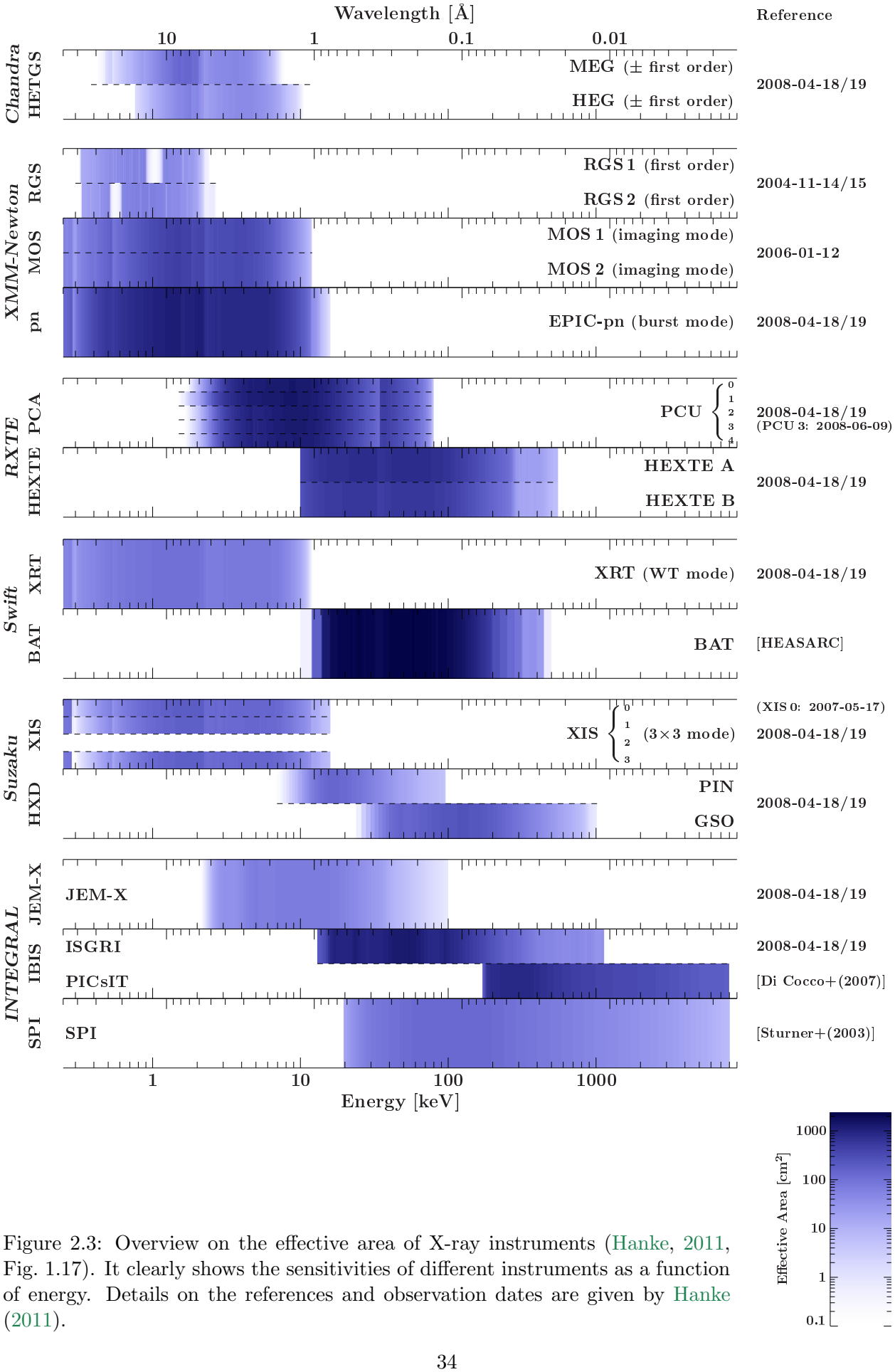

Figure 2.3: Overview on the effective area of X-ray instruments (Hanke, 2011, Fig. 1.17). It clearly shows the sensitivities of different instruments as a function of energy. Details on the references and observation dates are given by Hanke (2011).

XMM-Newton One of the main characteristics of the X-ray Multi-Mirror Mission (*XMM-Newton*), which was launched in the end of 1999, is its very large collecting area. The included instruments measure in the energy range 0.1–15 keV. The mission is described by Jansen et al. (2001). Especially the European Photon Imaging Camera-PN (EPIC-PN) has been used for detailed spectra of AGN obtained in observations with long exposures. Further instruments are the two EPIC-MOS, Reflection Grating Spectrometers (RGS), and the optical monitor (OM).

Swift This mission, which is in operation since 2004, is capable to react quickly to transient events. The detection and localization of γ-ray bursts is a particular goal of the mission. Main instruments of *Swift* are the X-Ray Telescope (XRT; Burrows et al., 2000), which covers the energy range of 0.2–10.0 keV and the Burst Alert Telescope (BAT; Barthelmy et al., 2005). With its large field of view BAT is used for a survey of the hard X-ray sky in the energy range of 15–150 keV. The XRT is a CCD imaging spectrometer. Target of Opportunity (ToO) observations, allow for easy access to data of AGN (typically up to several kiloseconds of exposure are possible).

Suzaku The operation of this mission started in 2005. One of its main features is the coverage of a large energy band with high sensitivity (a description of the mission is given by Mitsuda et al., 2007). Important for the current work were in particular the X-ray Imaging Spectrometer (XIS; Koyama et al., 2007), which consists of four units and covers the 0.2–12 keV energy band. The Hard X-ray Detector (HXD; Takahashi et al., 2007) covers energies in the range 10–600 keV. It consists of the silicon PIN diodes (<60 keV) and the GSO crystal scintillator (>30 keV).

An overview on the sensitivity of a selection of the previously mentioned instruments is shown in Fig. 2.3.

2.2.2 Analysis of X-ray data

In the following a brief overview on the analysis methods of X-ray data in this work is given.

Binned spectra and detector response The aim of every measurement is to determine the properties of the observed quantity with optimal precision. In the case of X-ray observations the goal is to study the spectral properties of the source, its temporal behavior, and the spatial flux distribution of the source. Measurements of the temporal variability in this work are limited by the detectors, as the studied sources are relatively weak (compared to typical Galactic X-ray binaries). and individual X-ray events can be separated and the arrival times measured sufficiently accurate. One advantage of the study of weak sources is, however, that no problems such as pile-up or detector dead-time arise, as individual X-ray events can be separated and the arrival times measured sufficiently accurate. The only analysis of the spatial flux distribution in the current work has been performed with *Chandra* data. Here, an image of the source was directly obtained with the standard data extraction of the events focused on the CCD chip. The study of spectral information based on the X-ray observations is more difficult and is briefly described in the following (for a more detailed discussion see, e.g., Sects. 2.2 and 3.2 of Hanke, 2007).

Due to the functioning of detectors it is not possible to obtain the source flux directly. The following limiting factors have to be considered. Based on the finite (relatively low) energy resolution, the events are typically binned into detector energy channels (which are labeled i from now on). It is obvious that the sensitivity of a detector is energy-dependent. A characteristic quantity is its effective area $A(E)$ (the ancillary response function ARF). Additionally to the uncertainty in the energy determination of incident photons, it can happen that the energy reconstruction of events suffers from further detector effects, such as pile up or escape peaks. The measured energy can thus differ significantly from that of the incident event. The quantity $R(i, E)$ characterizes the probability that a photon of energy E is measured in the detector channel i. The number of

counts C_i in each detector channel from an observation with exposure $t_{\rm exp}$ can thus be written in the following simplified form:

$$C_i = B_i + t_{\rm exp} \int {\rm d}E \, R(i, E) \, A(E) \, F_S(E) \tag{2.7}$$

where B_i is the (scaled) background contribution in the detector channels and $F_S(E)$ is the flux density of the source. $R(i, E)$ is called redistribution matrix function (RMF), because the energy E is typically not considered continuously, but on a relevant (fine) energy grid. With a discretized $R(i, E)$ Eq. 2.7 can be written as a matrix multiplication. From the detector count rates are given by folding the flux density with the instrument response, it is not possible to obtain the source flux density. It is generally not feasible to invert the RMF, as it might even depend on the input flux density. A proper analysis of the properties of the flux density can be done by fitting models and estimating parameters.

Fitting For a model of the flux density of the source $F_M(E; \{p_k\})$, which depends on a set of parameters $\{p_k\}$, the expected number counts $M_i(\{p_k\})$ in the detector bins can be obtained by folding the model with the detector response and adding the background contribution (Eq. 2.7). The goal of the parameter estimation is to find the set $\{p_k\}$ that describes the data best. The agreement between model and data can be quantified with a statistic. Based on the dependence of the statistic on the values of the parameters confidence intervals for the parameters can be determined. One of the most used statistics is the simple χ^2-statistic:

$$\chi^2 = \sum_i \frac{(C_i - M_i)^2}{\sigma_i^2} \tag{2.8}$$

where the σ_i characterize the uncertainty in each bin. In the limit of large C_i the Gaussian approximation for the Poisson uncertainties can be applied and per default the σ_i are set as $\sigma_i^2 = C_i$. Often $\sigma_i^2 = M_i$ is used alternatively. As a guide line this Gaussian approximation in the χ^2 statistic is valid when the number of counts C_i in each bin is larger than 25 (see, e.g., Gehrels, 1986, for a discussion of small number statistics). If the number of counts is too low, neighboring bins can be grouped such that χ^2 statistic is applicable. In this way the number of bins is decreased, but the number of counts per bin increased. Grouping bins corresponds, however, to a loss of information, as for example narrow features cannot be resolved anymore. A better technique is to use more suitable statistics. A statistic which is valid for low numbers of counts is the Cash statistic (which is described in detail by Cash, 1979):

$$S_{\rm cash} = 2 \sum_i (M_i - C_i) + C_i \ln \left(\frac{C_i}{M_i} \right). \tag{2.9}$$

The model counts M_i in each bin depend on the values of the model parameters $\{p_k\}$. The set of parameters which describe the data best are obtained with minimization algorithms. Such fitting algorithms, as well as various models, are implemented in the commonly used analysis software. Common programs used to analyze X-ray data are XSPEC (Arnaud et al., 2007) and ISIS (Houck & Denicola, 2000; Houck, 2002; Noble et al., 2006). Throughout the current work ISIS - the Interactive Spectral Interpretation System - has been used. It is a powerful tool, which is a very flexible and easily configurable software (see, e.g., Noble & Nowak, 2008, for a description).

Flux estimation The above described spectral fitting can be used to obtain the best fit parameters and their confidence intervals. It is, however, not trivial to determine a precise value and proper uncertainties of the source flux in a certain energy band. A simple example is given by a

power law model for a source. Spectral fitting yields best fit values and the corresponding uncertainties for the normalization and the index of the power law. Using the best fit values, the best fit flux in an energy band can be directly obtained by integrating the model over this energy range. In this way the photon flux as well as the energy flux (by integrating the product of the model with energy over the energy band) can be obtained. It is less easy to determine the confidence intervals of the parameters, which requires error propagation and in particular the knowledge of the parameter correlation. It gets more difficult for more complicated models, e.g., with several components with numerous parameters.

Another method is a Monte Carlo approach, where random configurations of the parameters are selected according to their best fit values and uncertainties. For each set of parameters the flux is calculated and the χ^2 of the corresponding fit is considered. The resulting distribution of fluxes directly yields the confidence intervals for the fluxes. This method suffers, however, from severe problems. When random values for a parameter are selected, the distribution from which the values are drawn is important. For example a normal distribution can be used, or a log-normal distribution might describe the "nature" of a parameter better, e.g, in the case of strongly asymmetric uncertainties. The final distribution of the fluxes will be influenced by the sampling of the individual parameters. Even if a perfect sampling could be achieved for each individual parameter, the sampling of the total parameter space is still not representative if some parameters are not independent. For that reason this method is problematic.

A proper technique to determine the best fit flux and its uncertainty has been introduced within the scope of this work. It is based on the inclusion of the flux as a fit parameter. For that purpose a convolution model has been implemented for ISIS. This model can be used to convolve the source model or parts of it. After an energy range is specified, the convolved component is renormalized to the current value of the parameter in each model evaluation, before the model is compared with the data and the fit statistic is calculated. Due to the normalization of the flux, the normalization of the convolved model loses its meaning and can be frozen. For that reason the number of the degrees of freedom remain unchanged. If the convolved model consists of different components, and therefore several normalizations are included, it is sufficient to freeze the value of one normalization (for logical reasons a relevant one) and leave the others variable. Although the absolute meaning of these normalizations is lost, the other convolved model components are scaled with respect to the one with fixed normalization. Spectral fitting directly yields the best fit value for the flux. Given the statistic, its uncertainties can be obtained by searching up to which values the model is still consistent with the data using the intrinsic routines of the spectral analysis software. Two functions have been implemented in the local software packages, one to determine the photon flux (`phflux`) and one for the energy flux (`enflux`). When it was planned to publish the technique for public usage within a research note, it was found that a similar model (`cflux`) to determine the energy flux was already included in the public XSPEC (and thus ISIS) models since 2008. Although this technique is the best one for properly determining the flux and its uncertainties, it is not well-known yet among X-ray astronomers and unfortunately only rarely used.

2.3 Measuring Correlations

For the understanding of physical process it is crucial that theoretical models agree with observed data. Before theories can be confirmed, strengthened, or falsified by observational data or experiments, these theories and models obviously have to be formulated. The necessary underlying ideas are often based on relations of observables. Often, e.g, in astronomy, properties of the studied objects cannot be changed directly in an experimental way, but mainly observational data with spectral and temporal information is collected. It is important to find and quantify dependencies between observables. Then it is necessary to obtain probabilities if a "correlation" is real and not a random event. In addition an estimation of the influence of selection effects is required.

A typical example for such an analysis are parts of this work, in which multiwavelength observations of AGN are studied. As discussed in Sect. 1 their broad band emission contains contributions of different components and different regions. For a complete understanding of the underlying physical mechanisms, the source geometry, and the connection between the emitting components, it is required to figure out relations between emission properties in different energy regimes, which can be identified with certain emission components. A selection of methods to quantify correlations and their advantages and disadvantages is presented in the following.

2.3.1 Kendall tau rank correlation coefficient

While the degree of linear correlations can be quantified easily, it is more difficult for more complicated dependencies. A method of quantifying non-linear correlations are rank correlation coefficients, which can be applied in the case of any strictly monotonic dependencies. Assuming a relation f between two observables X and Y such that $y_i = f(x_i)$, a perfect increasing ranking is given in the case of $f(x_i) < f(x_j)$ for all x_i and x_j with $x_i < x_j$. Analogously, a decreasing ranking is given for $f(x_i) > f(x_j)$. For a data set (X, Y) consisting of n pairs (x_i, y_i) with $i \in [1, 2, 3, \ldots, n]$ a coefficient can be defined measuring the ranking. A simple definition is the difference between the number of pairs (x_i, x_j) with the properties $x_i < x_j$, $y_i < y_j$ and the number of pairs fulfilling the inequations $x_i < x_j$ and $y_i > y_j$. Normalizing this difference by the total number of pairs $x_i < x_j$ yields a result in in the interval $[-1, 1]$, where 1 and -1 are the prefect rankings as described above. A result close to 0 indicates that the observables X and Y are independent. This coefficient can be formulated in the following way (Akritas & Siebert, 1996):

$$\tau_{xy} = \frac{2}{n(n-1)} \sum_{i=2}^{n} \sum_{j=1}^{i-1} \operatorname{sgn}(x_i - x_j) \operatorname{sgn}(y_i - y_j), \tag{2.10}$$

where sgn is the sign function, which is defined as:

$$\operatorname{sgn}(x) = \begin{cases} -1 & \text{for} \quad x < 0, \\ 0 & \text{for} \quad x = 0, \\ 1 & \text{for} \quad x > 0. \end{cases} \tag{2.11}$$

2.3.2 Partial Correlation

The correlation between two sets of observables X and Y can be strongly influenced if the values of both observables are affected by another observable Z. The partial correlation between X and Y given Z, is the correlation between X and Y with "removed" influence of Z. This partial correlation can be defined as (Akritas & Siebert, 1996):

$$\tau_{xy,z} = \frac{\tau_{xy} - \tau_{xz}\tau_{yz}}{\sqrt{\left(1 - \tau_{xz}^2\right)\left(1 - \tau_{yz}^2\right)}}. \tag{2.12}$$

For example a typical scenario of possible partial correlations arises when comparing luminosities of sources, e.g., the radio and γ-ray luminosities of AGN as in Sect. 5. A clear linear correlation can be induced by the distances of the sources. Neglecting spectral corrections, such as required for cosmological effects (see, e.g., Sect. 1.6), luminosities are proportional to the measured flux multiplied with the square of the luminosity distance.

Selection effects can occur in flux limited samples. Distant source are luminous, as for a given redshift the luminosity has to exceed certain value in order to be detectable and to exceed the limiting flux value.

2.3.3 Extension to Censored Data

In observations the measured value can be often censored, due to sensitivity limitations of the instrument. The detection limit provides an upper limit for the observable and can thus be understood as left-censoring of data (analogously right-censored data include lower limits). As described by Akritas & Siebert (1996) an extension of Kendall's τ to censored data was introduced in biostatistics (Brown et al., 1974) and studied in more detail by Oakes (1982). Akritas & Siebert (1996) discuss an extension of to censored data for partial correlations. In their work they use right-censored data, as that had been discussed in the before mentioned biostatistical context.[4] Left- and right-censored data set can easily be exchanged by inverting the complete ranking of the data set, e.g., by multiplication with -1 or by taking the inverse value. In this work mainly upper limits of observations are used, thus the extended Kendall's τ is defined accordingly here. For that purpose its definition by Akritas & Siebert (1996, Sect. 2.2) has been modified as presented in the following. In order to consider limits, the function

$$I(x_i < x_j) = \begin{cases} 1 & \text{if} \quad x_i < x_j \\ 0 & \text{else} \end{cases} \tag{2.13}$$

is used to express the sign function in Eq. 2.10

$$\mathrm{sgn}(x_i - x_j) = I(x_j < x_i) - I(x_i < x_j). \tag{2.14}$$

A function δ is introduced in order to distinguish between measured values and upper limits:

$$\delta(x_i) = \begin{cases} 1 & \text{if } x_i \text{ is a measured value} \\ 0 & \text{if } x_i \text{ is an upper limit} \end{cases} . \tag{2.15}$$

Using the expression

$$J(x_i, x_j) = \delta(x_i) I(x_j < x_i) - \delta(x_j) I(x_i < x_j) \tag{2.16}$$

the extended Kendall's τ correlation coefficient between the observables $X = \{x_1, c_2, \ldots, x_n\}$ and $Y = \{y_1, y_2, \ldots, y_n\}$ (as in Sect. 2.3.1) is given by

$$\hat{\tau}_{\mathrm{xy}} = \frac{2}{n(n-1)} \sum_{i=2}^{n} \sum_{j=1}^{i-1} J\left(x_i, x_j\right) J\left(y_i, y_j\right). \tag{2.17}$$

Considering Eq. 2.16 it is obvious how upper limits can contribute to the correlation coefficient. Assuming that x_i is an upper limit whereas x_j is a measured value, a true statement $x_i < x_j$ contributes while no information can be gained in the case $x_j < x_i$.

Analogously to Eq. 2.12 in Sect. 2.3.2 a partial Kendall's τ correlation coefficient extended to censored data can be defined between data sets X and Y given Z:

$$\hat{\tau}_{xy,z} = \frac{\hat{\tau}_{xy} - \hat{\tau}_{xz}\hat{\tau}_{yz}}{\sqrt{\left(1 - \hat{\tau}_{xz}^2\right)\left(1 - \hat{\tau}_{yz}^2\right)}} \tag{2.18}$$

The probability that the null hypothesis is rejected is discussed by Akritas & Siebert (1996).

[4] Brown et al. (1974) use right-censored data, as in their work "An extension of the definition of Kendall's coefficient of concordance is proposed for testing independence in bivariate censored survival times". The title of their work is "Nonparametric Tests of Independence for Censored Data with Applications to Heart Transplant Studies".

Chapter 3

NGC 1052 – Disk-Jet Interaction?

Powerful relativistic jets are observed in radio-loud AGN. As described in Sect. 1.4.2 the formation of these jets is still not well understood. An important question in AGN research is why there is a population of radio-loud AGN whereas a majority of AGN do not show powerful jets and are radio-quiet. In theoretical models it is typically suggested that the formation of relativistic jets in AGN is triggered in the vicinity of the central supermassive black hole. For a better understanding of the involved processes it is therefore necessary to gain insights into the close environment of the black hole. Two methods are especially suitable for such observations. First, there are radio observations using Very Long Baseline Interferometry (Sect. 2.1.1). With this technique sub-milliarcsecond angular resolutions can be achieved. For nearby AGN, with distances in the Mpc regime, such angular resolutions correspond to spatial resolutions of the source on the order of light-weeks. With this resolution, it is possible to study the small-scale structure and behavior of the relativistic jets. A complementary method to probe the closest environment of the black hole are X-ray observations. With this technique, the angular resolution is by far not high enough to resolve features on scales comparable to the radio VLBI resolution, but emission components can be resolved spectroscopically. Using timing studies and modeling spectral components it is possible to obtain constraints on scales as small as a few Schwarzschild radii of the black hole. X-ray emission in AGN is assumed to originate from regions close to the black hole, such as a hot corona or the base of the jet. As described in Sect. 1.3.2, reflection lines, which originate from the X-ray irradiation of the accretion disk, allow for constraints on the accretion disk and the black hole spin in principle. Based on absorption and reflection signatures it is possible to determine properties of the material close to the black hole. Techniques such as reverberation mapping provide information on the accretion geometry.

Studies of the connection between accretion and outflows are crucial for the understanding of jets and their formation. Combined radio X-ray studies have led to interesting results for AGN as well as for stellar-mass black holes in X-ray binaries. As discussed in Sect. 1.7, both source types allow for studies on different variability scales, which scale with the black hole mass. Besides the state-dependence of jet properties in X-ray binaries (see the description in Sect. 1.7 and references therein), correlated events have been observed. For example Fender et al. (2006) discuss disk-jet coupling in the source Cyg X-1 based on radio properties of the jet and a bright radio flare. They find that *"a steady jet appears to persist initially when the X-ray spectrum starts softening, and that once the spectral softening is complete the core radio emission is suppressed and transient ejecta/shock observed"*. A correlated radio-X-ray flare of this source is described by Wilms et al. (2007), who find a delay of about 7 minutes between the X-ray flare and the subsequent radio flare. Such time lags constrain, e.g., distances between emitting regions and are helpful for modeling the radiation processes of the ejecta. Rodriguez et al. (2008, see the references therein for previous studies) discuss a *"soft X-ray dip and spike cycles, followed by radio flares"* observed in the source GRS 1915+105, which is interpreted as partial ejections of the corona. Since black hole masses in

AGN are by a factor of 10^5–10^{10} higher than in X-ray binaries, the typical variability time scales are increased accordingly. For that reason comparable events can be studied as snapshots or in extreme slow motion in AGN. The disk-jet connection in AGN was, e.g., studied by Marscher et al. (2002), who find indications that *"dips in the X-ray emission are followed by ejections of bright superluminal knots in the radio jet"* of the source 3C 120. Tombesi et al. (2012) find this relation between X-ray dips and jet ejections in the case of 3C 111, too. In addition, they describe a connection between ultra-fast outflows observed in the X-ray regime, which are mildly relativistic, and the ejection of highly relativistic jet components.

In this chapter the connection between X-ray variability and the evolution of the radio jet seen with VLBI observations is discussed on the basis of the source NGC 1052. At first the properties of the target NGC 1052 and its suitability for the aimed studies are outlined (Sect. 3.1). In the following, the monitoring campaign of this source led by M. Kadler and E. Ros is presented (Sect. 3.2). The data analysis and results of the X-ray and radio observations, as well as their combination are discussed in the Sects. 3.3, 3.4, 3.5, respectively. Preliminary results of the analyses discussed in this chapter have been published by Böck et al. (2010a).

3.1 The AGN NGC 1052

NGC 1052 is a giant elliptical galaxy, which has unusually strong emission lines in its optical spectrum and is classified as a LINER (see, e.g., Mayall, 1939; Fosbury et al., 1978; Ho et al., 1997). The optical spectrum of NGC 1052 has been studied in detail (see e.g., by Gabel et al., 2000, and references therein). In J2000 coordinates, the source has a right ascension of $02^{\mathrm{h}}41^{\mathrm{m}}04\overset{\mathrm{s}}{.}7985$ and a declination of $-08°15'20\overset{''}{.}751$ according to the VLBA Calibrator Survey (Beasley et al., 2002). In the current work we use a redshift of the source of $z = 0.005$, which is a commonly used value.[1] The distance to this source has been determined with different redshift-independent methods. The values listed by the NASA/IPAC Extragalactic Database (NED) have a mean value of 19.6 Mpc with a standard deviation of 1.5 Mpc.[2] These values are used in the current work. At this distance, an angular separation of 1 mas corresponds to a projected length of about 9.5×10^{-2} pc. A proper motion of $1\,\mathrm{mas\,yr^{-1}}$ corresponds to an apparent speed of $0.31\,c$.

NGC 1052 has been studied in detail in the radio regime. The following summary of the radio morphology and properties follows that of Vermeulen et al. (2003). A Very Large Array (VLA) image at 1.4 GHz of this source shows a two-sided radio structure on arcsecond scales with a bright central core dominating the emission with about 85 % of the flux (Wrobel, 1984). This morphology contains two radio lobes with indications of hot spots. The structure is oriented in east-west direction and covers about 3 kpc. Kellermann et al. (1998) determine a luminosity of the radio core of $1.3 \times 10^{23}\,\mathrm{W\,Hz^{-1}}$ at 5 GHz. The central radio source has a relatively flat spectrum in the GHz regime with typical flux densities in the range of 1–2 Jy. VLBI images show a milliarcsecond jet and counterjet extending over about 15 mas (e.g., Jones et al., 1984). Additionally to synchrotron self-absorption there are indications of free-free absorption in the central region of NGC 1052, which were interpreted as a torus-like structure (Kellermann et al., 1999; Kameno et al., 2001; Vermeulen et al., 2003; Kadler et al., 2004b). Untypically for elliptical galaxies, NGC 1052 hosts a bright H_2O maser (see, e.g., Braatz et al., 2003, and the references therein). Interestingly the maser emission has been observed from positions aligned with the radio jet (Claussen et al., 1998), whereas in other sources they are usually found perpendicular to the jet (e.g., in NGC 4258; Miyoshi et al., 1995).

The radio morphology of this source is ideal for the comparison of radio properties with X-ray variability. NGC 1052 has a bright and compact radio jet and a counter-jet, thus the ejection times

[1] The redshift of NGC 1052 has been measured by several authors, for example $z = 0.0049$ (Sargent et al., 1977), $z = 0.004953 \pm 0.000040$ (Wegner et al., 2003), and $z = 0.005037 \pm 0.000020$ (Denicoló et al., 2005).

[2] The determined distances are in the range from 17.8 Mpc to about 22 Mpc (e.g., Tully, 1988; Willick et al., 1997; Blakeslee et al., 2001).

of components in the radio jet can be constrained more easily than for the above mentioned AGN, which show single-sided jets. For single-sided jets, the distance between the radio core and the position of the black hole has to be estimated.

In addition to the suitable radio properties, the X-ray emission of the source is bright enough for X-ray monitoring as well as for the detailed analysis of features in the X-ray spectra. Several X-ray observations of NGC 1052 have been analyzed. Kadler et al. (2002, 2004a) find indications of extended X-ray emission in addition to the emission from the nucleus in a *Chandra* image, which agrees with radio emission from the large scale jet seen with MERLIN at 1.4 GHz. These authors furthermore find agreement of these emissions with the optical jet seen in the *Hubble Space Telescope* image published by Pogge et al. (2000). X-ray spectra of NGC 1052 have been studied in detail since *ASCA* and *BeppoSAX* observations (Weaver et al., 1999). A hard and strongly absorbed continuum was found (see, e.g., Guainazzi et al., 2000). Using a 101 ks *Suzaku* observation, Brenneman et al. (2009) study the X-ray spectrum of NGC 1052 in detail. In their analysis a relativistically broadened Fe Kα is considered, which originates within a few gravitational radii from the central object.

The existence of a strong, relativistically broadened iron line would be especially interesting, as prominent lines of this kind are typically not detected a radio-loud objects. It would very important for studies of the connection between the accretion flow, of which the broad iron line is a diagnostic, and the formation of relativistic jets. Modeling this line profile would yield direct information on the accretion disk and thus be highly important for studies of the disk-jet connection. This spectral feature was interesting as well, as such broad iron lines are typically only found in radio-quiet AGN and so far no prominent relativistically broadened lines have been detected in the X-ray spectra of radio-loud AGN (one rare example is 4C 74.26, where Ballantyne & Fabian, 2005, carefully suggest the existence of a relativistically broadened iron line). Several explanations have been suggested for the lack of such line profiles. If broad fluorescence lines, which originate from the accretion disk, exist in radio-loud AGN, there have to be reasons why they are not detected. One possibility is for example that the emission is dominated by boosted emission of the jet, which outshines the line emission. Considering larger angles between the jet and the observer's line of sight, another possibility is the geometry of absorbing material, such that emission from the accretion disk is strongly absorbed and emission from other regions dominates the spectrum. Alternatively it is possible that indeed no pronounced lines of this kind are formed in radio-loud AGN. For this case the explanations are, e.g., that the material in accretion disks of radio-loud AGN is highly ionized, such that not even fluorescent Fe Kα lines are formed. Furthermore, optically thin, radiatively inefficient accretion flows have been discussed. Recently, Dauser et al. (2012) have shown that broad profiles of fluorescence lines from accretion disks can only be formed if the X-ray emission originates from a compact source close to the black (within a few gravitational radii).

However, it will be shown within this work that all available X-ray data of NGC 1052 can be modeled consistently without the necessity of a broad Fe Kα line.

3.2 Monitoring Campaign

Based on the indication of a broad Fe Kα line (originating from an accretion disk) in the radio-loud AGN NGC 1052 and the possible association of a change of the line profile with the ejection of a new jet component, a multiwavelength observation campaign was initiated in 2005. It was led by E. Ros and M. Kadler (see, e.g., Kadler et al., 2005; Ros et al., 2007, for detailed information). The goal of this project was a study of the connection of accretion and outflow. For an optimal analysis of the disk-jet interaction, a large data set has been collected within the scope of this monitoring campaign.

Several radio observations have been included in the campaign in order to determine the jet properties of NGC 1052. Data of single-dish radio observations were planned to be used for a

study of the total temporal variability and the spectral evolution in this energy regime. Especially important for the study of the intrinsic jet properties are VLBI radio observations. In addition to the ongoing VLBA monitoring at 15 GHz, VLBA observations at higher frequencies have been performed in the scope of this campaign. Between 2005 and 2009, 22 epochs of simultaneous observations at 22 GHz and 43 GHz have been done.[3]

In order to probe the close environment of the central black hole in detail and to obtain information on the accretion process, a large set of X-ray observations was planned and included in the multiwavelength observation campaign. Different instruments with different advantages have been used. With the deep observations with *XMM-Newton*, *Suzaku*, and *Chandra* it is possible resolve the X-ray spectra in detail and to obtain a consistent model, which describes the data well and allows to study the spectral components. The long exposures of the observations with these instruments yield a good signal-to-noise ratio and allow for such detailed analysis. In addition, spatially resolved spectroscopy is possible with *Chandra*, which allows to separate the emission of components with a sufficient distance. Using the spectral model obtained from these observations, the monitoring observations with *RXTE* and *Swift* can be analyzed. Data obtained by these instruments with short exposures cannot constrain spectral features in detail due to the low signal-to-noise ratio. In order to determine the overall X-ray activity of NGC 1052 on time scales of weeks to years from these monitoring observations, the spectral models obtained from data of the other instruments can be used. Model parameters that are not expected to vary can be fixed, while only the continuum normalization and the spectral slope are modeled. For this purpose, more than 140 pointed observations with *RXTE*, as well as three deep *XMM-Newton* observations have been scheduled between 2005 and 2010.

Using the large set of X-ray observations, the long-term variability of NGC 1052 and a detailed study of its spectral components is shown in the following.

3.3 X-ray Analysis

Numerous X-ray observations of this source are available including archival data as well as data obtained at the time of this work within the above mentioned dedicated multiwavelength monitoring campaign. The spectral analysis in this work was performed with the Interactive Spectral Interpretation System (ISIS, Version 1.6.2-3; Houck & Denicola, 2000). For the modeling of interstellar X-ray absorption, the `vern` cross sections (Verner et al., 1996) and the `wilm` abundances (Wilms et al., 2000) have been used. The available observations, the analysis, and the obtained results are discussed in the following section.

3.3.1 X-ray Observations

NGC 1052 has been observed with different X-ray instruments, which have different properties and thus offer complementary insights in the source's X-ray emission. The full temporal sampling of X-ray observations of the source is shown in Fig. 3.1. In the following a short overview on the available X-ray observations is given and the aims of the analysis are described. Properties of the corresponding X-ray instruments are discussed in Sect. 2.2.1.

Chandra In this work both available *Chandra* observations of NGC 1052 are analyzed. There is one 2.4 ks observation from 2000, August (ObsID 285, PI Garmire) and a 60 ks observation from 2005, September (ObsID 5910, PI Irwin).[4] The *Chandra* observations are especially important to

[3] The analysis of the radio data is discussed in Sect. 3.4.

[4] In addition, two further observations in 2009 and 2010 of nearby sources are available (ObsIDs 11355 and 12988, exposures ∼6 ks and 30 ks). In both observations NGC 1052 is a few arcminutes away from the pointing position, but unfortunately the emission of NGC 1052 does not fall on one of the CCD chips due to the orientation of the telescope. For that reason these observations cannot be used here.

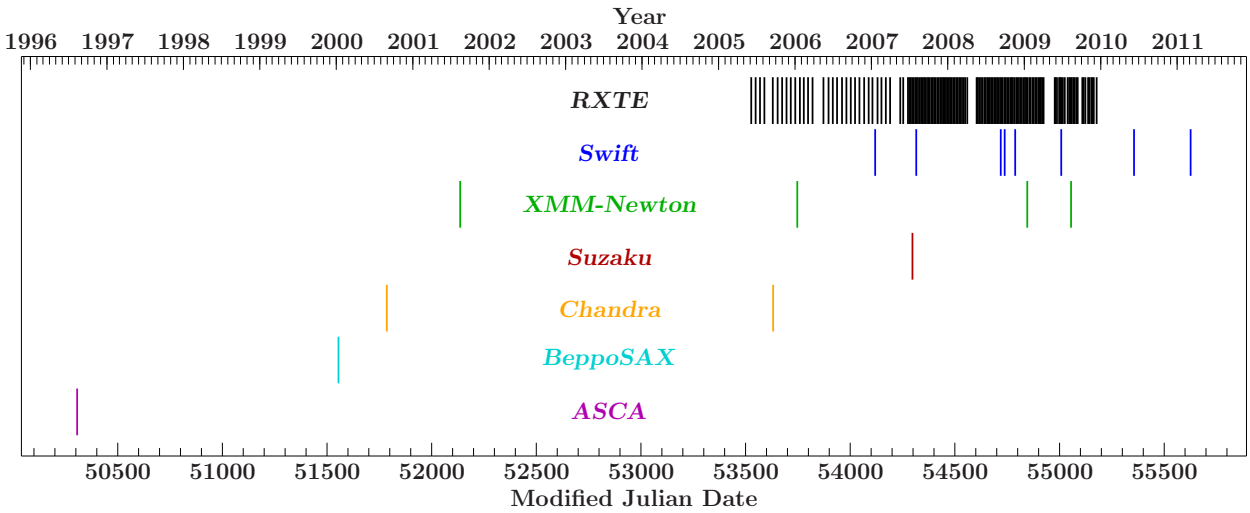

Figure 3.1: Sampling of X-ray observations of NGC 1052. The vertical dashes represent the observation dates. Different instruments are indicated by different colors. The later *Swift* observations are grouped from shorter observations within a few days at that time (see text).

constrain the extended emission in the source. It can be used to spatially separate extended X-ray emission. In this way it can, e.g., be distinguished if the previously observed soft excess originates from partial covering of the nucleus emission or from extended emission from material in the host galaxy or starburst regions. The agreement between X-ray emission regions and extended radio jet emission, which is discussed by Kadler et al. (2004a), is based only on the 2.4 ks and thus on a small number of X-ray photons. With the long exposure observation these features can be studied in significantly more detail. Results of the *Chandra* data analysis are shown in Sect. 3.3.2.

XMM-Newton With the large effective area of *XMM-Newton*, the data obtained with long exposures allow for modeling spectral features in detail. Several observations with *XMM-Newton* are available. A 16 ks observation from 2001, August (ObsID 0093630101, PI Weaver) and three further observations from 2006, December and 2009, January and August with exposures of 55 ks, 52 ks, and 59 ks (ObsIDs 0306230101, 0553300301, 0553300401, PI Kadler).

Suzaku One long *Suzaku* observation of NGC 1052 is available. The 101 ks observation has been performed in 2007, July. Additionally to the data below 10 keV with CCD energy resolution and high signal-to-noise ratio, the other instruments included in the mission have a good spectral coverage at higher energies. With this observation it is thus possible to constrain the spectrum of the continuum emission. The additional information at high energies is important as the presence of strong absorption and additional spectral components in the soft X-ray regime make it difficult to constrain the continuum emission of the nucleus from the low-energy spectrum alone.

***RXTE* Monitoring** A monitoring campaign of the source with *RXTE* started in 2005 (PI Kadler). Since then, there are 145 observations available with an average exposure of 2.7 ks. In total, four and a half years are covered with the monitoring. From 2005, June, until 2007, June, the source has been observed once every 2–3 weeks for about 2 ks. After that, NGC 1052 has been observed almost weekly for 3 ks until the end of 2009. The monitoring observations are crucial to study the temporal variability of NGC 1052. For that purpose, the pointed *RXTE* observations were the ideal method, because the source is to weak to be reasonably studied with available X-ray all-sky monitoring instruments. On the other hand similar monitoring campaigns are not possible for the before mentioned missions due to scheduling and the strongly requested observation time for their

instruments. As mentioned above, the source is not bright enough to constrain different spectral components from the data obtained with *RXTE* observations with such short exposures. For that reason the spectral source model determined from the deep observations with other instruments is used in order to determine the overall variability from the *RXTE* data.

Swift *Swift* observations are used to complete the monitoring with *RXTE*. Within the scope of this work, *Swift* target of opportunity (ToO) observations have been proposed for that purpose. The observations were scheduled such that they can be grouped to blocks of about 10 ks, which yields a large enough signal-to-noise ratio to constrain more parameters than possible with the *RXTE*/PCA data. The *Swift* observations cover time periods between and after deep observations with *XMM-Newton* and *Suzaku*. In addition to the pointed *Swift* ToO observations, public data from *Swift*/BAT is used in this work. With *Swift*/BAT the so far *most sensitive all-sky survey in the hard X-ray band* (14–195 keV) is performed (Tueller et al., 2010). NGC 1052 is associated with the source SWIFT J0241.3−0816 in the 22 Month *Swift*/BAT All-Sky Hard X-ray Survey (Tueller et al., 2010). An average spectrum and a light curve of NGC 1052 are provided in the *Swift*/BAT 58 month catalog.[5]

ASCA* and *BeppoSAX Additionally to the above described data set, further archival X-ray data were included, which allows snapshots of the source's behavior before the start of the monitoring campaign. There is a 110 ks observation with *ASCA* in 1996, August (ObsID 74061000, PI Wilson) and a 75 ks one with *BeppoSAX* in 2000, January (ObsID 50828001). The exposures of these observations are long enough to constrain several model parameters and provide a further check if the developed model is consistent over time scales of years.

3.3.2 Disentangling emission components with *Chandra*

With its angular resolution of less than one arcsecond *Chandra* allows high-quality X-ray imaging in the 0.1–10 keV band. In this way spatial resolved spectroscopy is possible. Such studies are especially interesting in the case of NGC 1052, as the previous studies of its soft 0.5–12 keV X-ray spectra revealed various spectral components in this energy range, of which a few are extended and could be resolved with *Chandra* (see, e.g., Weaver et al., 1999; Brenneman et al., 2009). Extended X-ray emission, which was directly seen in the 2.4 ks *Chandra* imaging observation, was discussed by Kadler et al. (2004a). The 60 ks *Chandra* observation (2008, September 18) allows studies of the extended emission in greater detail.

Possible X-ray binaries in NGC 1052 From the data obtained with the long *Chandra* observation, an X-ray image in the 0.1–9 keV band has been created. Figure 3.2 (right) shows the region of NGC 1052 with field of view of several arcminutes. In addition, an optical image from the Digitized Sky Survey (DSS; see, e.g., Lasker, 1994) of the bright elliptical host galaxy is shown in this figure (left).[6] The X-ray images shows a string central source, which is located in the nucleus of the galaxy. This source is surrounded by structured diffuse X-ray emission. Besides these components, numerous weak point sources are visible in the X-ray image. Since their distribution shows a clear concentration at the location of the host galaxy, the majority of these sources are probably accreting stellar-mass objects within the host galaxy. For a selection of the brightest of these objects individual spectra have been extracted and modeled with a power law (due to the low signal-to-noise ratio pure power laws are sufficient to describe the spectra well). This selection of sources and their X-ray spectra are shown in Fig. 3.3.

[5] Averaged spectra and light curves for sources in the *Swift*/BAT 58 month catalog are provided online at `http://heasarc.nasa.gov/docs/swift/results/bs58mon/`.

[6] A further detailed sky survey in the optical regime, which should not be confused with the DSS, is the Sloan Digital Sky Survey (SDSS; Fukugita et al., 1996; York et al., 2000).

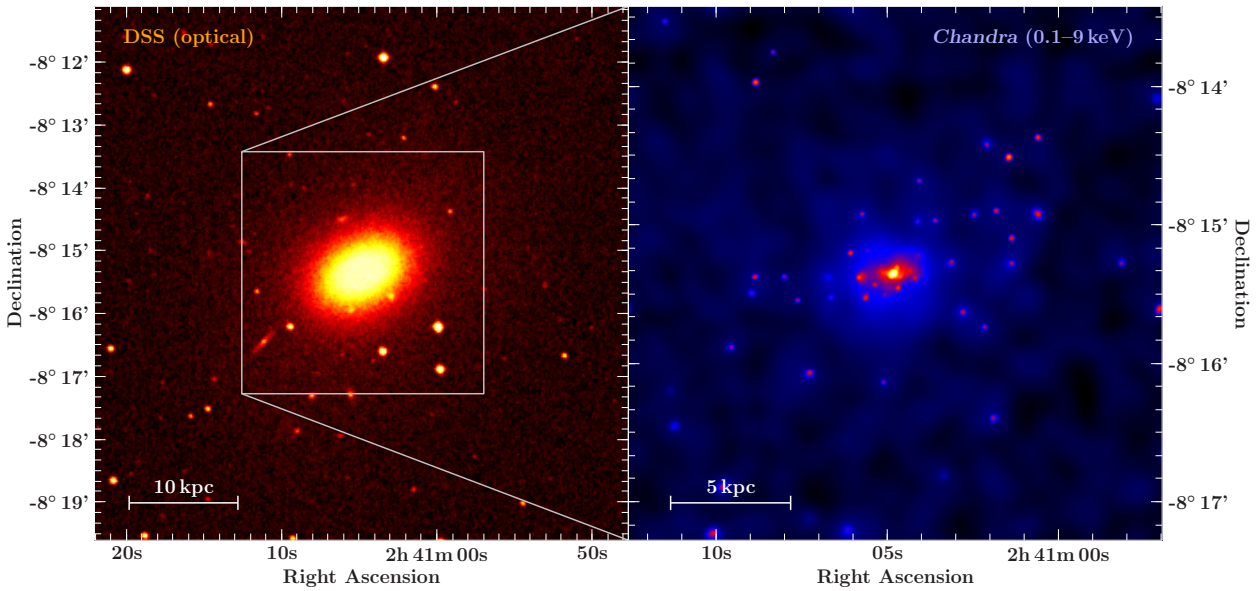

Figure 3.2: Images of NGC 1052. The left DSS image in the optical regime shows the elliptical galaxy NGC 1052. The scale bar characterizes the projected length scales at the distance of the source. In the right a (slightly smoothed) soft X-ray image of the NGC 1052 is shown. The used color code in both images represents the logarithmic total intensity of the used energy regime.

The X-ray luminosities of these sources in the 2–10 keV band have been determined from modeling the spectra. The typical luminosities are $L_{2-10\,\mathrm{keV}} = 1.0^{+0.7}_{-0.6}\,10^5\,L_\odot$, where $L_\odot$ is the total luminosity of the Sun ($L_\odot \approx 3.84 \times 10^{33}\,\mathrm{erg\,s^{-1}}$; see, e.g., Foukal et al., 2006). These values are consistent with that of relatively luminous X-ray binaries. For example, a study of bright point sources with X-ray luminosities above $2.4 \times 10^4\,L_\odot$ in nearby galaxies is discussed by Winter et al. (2006). In a search of point sources in data obtained with *Chandra* observations of nearby galaxies, Liu (2011) associate 86 point sources with the host galaxy NGC 1052 (the used *Chandra* observation is the same as the one used in this work).

Extended emission in NGC 1052 As it can be seen in Fig. 3.2, the X-ray image of NGC 1052 shows bright central nucleus with diffuse extended emission. An enlarged X-ray image of the central region is shown in Fig. 3.4. Images are shown in different X-ray bands. In the softest regime of 0.1–1 keV a central source and a large contribution of extended emission with an elongated structure in east-west orientation is visible. In addition, several point sources are clearly visible. In a medium X-ray band of 1–3 keV the contribution of the diffuse emission is lower and the emission from a few point sources, in particular that of the nucleus, appear more distinct and brighter. Furthermore a point source appears in the south-west. In the energy band of 3–9 keV the emission from the nucleus dominates. There remain only slight indications of a source in the west. The color image created from the three images in different X-ray energy bands indicates the spectral shape at each position in the image. Softest spectra (red) are seen for the elongated extended structures, medium spectra for the point sources, and the hardest spectrum is found for the central X-ray source (blue).

An overlay of the MERLIN radio image published by Kadler et al. (2004a) with the central region of the Chandra image is shown in Fig. 3.5.[7] The diffuse soft X-ray emission is co-aligned with the radio jet. The bright central features agree very well, as well as the larger structures extended in east-west direction. The eastern feature appears like a hot spot.

[7]The Multi-Element Radio Linked Interferometer Network (MERLIN) is operated by the University of Manchester, UK (for more information see, e.g., Thomasson, 1986; Garrington et al., 2004, or http://www.merlin.ac.uk/).

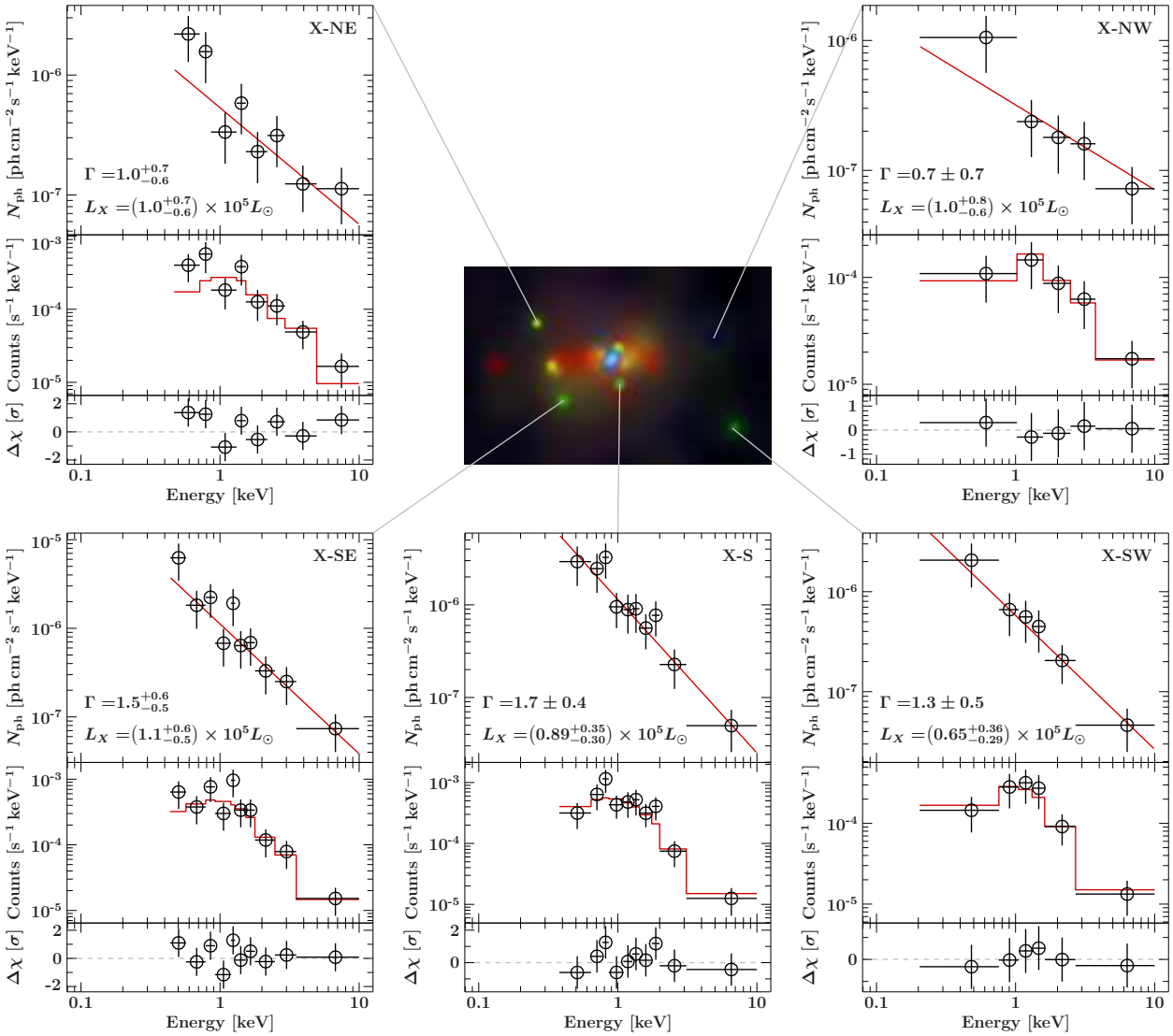

Figure 3.3: Spectra of possible stellar-mass X-ray sources in NGC 1052. The positions of the sources in the X-ray image of NGC 1052 (center) are highlighted and for each of the five shown sources a unfolded spectrum, the counts spectrum and the residuals of the power law fit are shown (from top to bottom). The central color image of NGC 1052 is described in Fig. 3.4.

In order to disentangle the spectral components for the X-ray spectral fitting, spectra for different regions have been extracted. As shown in Fig. 3.6 two regions were studied in detail. On the one hand, a region covering the emission of the nucleus was selected, as its emission properties are of interest for a comparison with the radio jet properties on parsec scales and even below. On the other hand, a larger region that includes the diffuse emission associated with the jet was defined. For the latter region the inner nucleus region has been excluded. Emission from the extended emission spanning a few kpc in the source is not expected to show significant variations on time scales of months or a few years. Separating both contributions is crucial for a development of a proper model of the X-ray spectra of NGC 1052. The separation is especially important for observations with other X-ray instruments, as their lower angular resolution does not allow them to resolve the components spatially in such a good way. For example the typical extraction regions for spectra with *XMM-Newton* and *Suzaku* used in this work were of comparable size as the outer region shown in the *Chandra* image (Fig. 3.6).

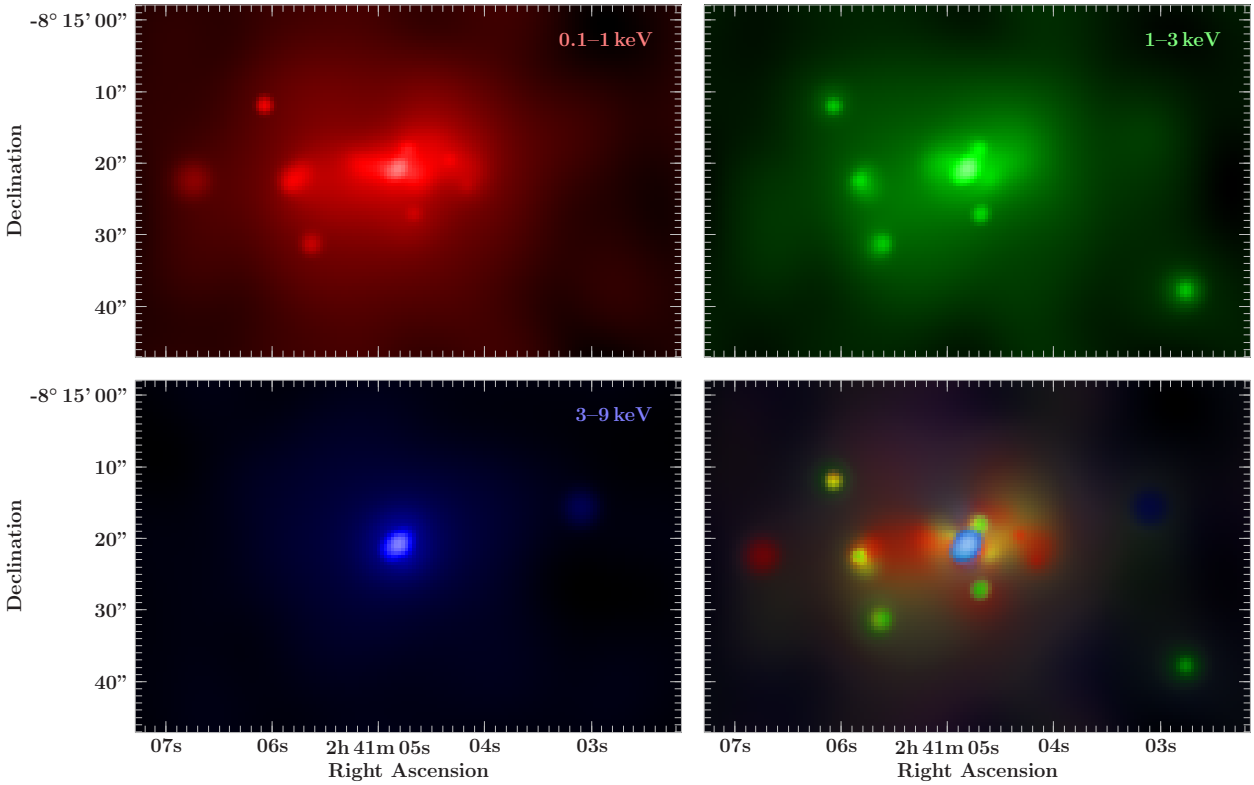

Figure 3.4: *Chandra* images of the inner region of NGC 1052 in different energy bands. The softest observed X-rays (0.1–1 keV) are shown in the top left, the top right image has been created using photons in the 1–3 keV band, and an image in the 3–9 keV regime is shown in the bottom left. In these three images the color-scale indicates the number of counts in the given energy bands. The color image in the bottom right is an overlay of the previous images using the red, green, and blue channels.

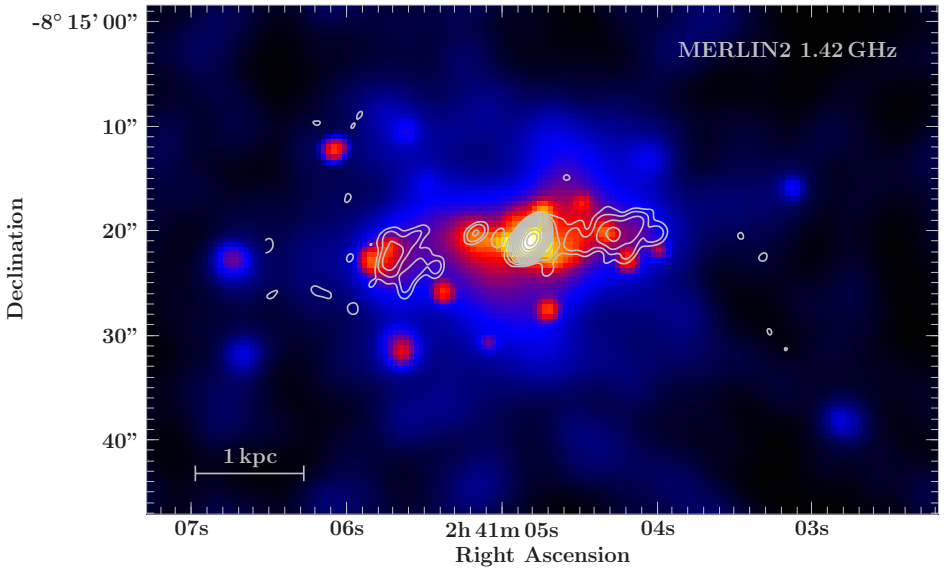

Figure 3.5: *Chandra* image of the central region of NGC 1052. The color scale represents the photon count rates in the 0.1–1 keV energy band, in which the extended emission is strongest. The overlaid contour lines show the 1.4 GHz radio emission observed with MERLIN.

An important step in the spectral X-ray analysis of NGC 1052 was modeling the extended emission properly. For that purpose, the data from the outer region in the *Chandra* image (Fig. 3.6) were studied carefully. For fitting models to these data, they were grouped to a minimal signal-to-noise ratio of 5. In order to account for the previously discussed point sources, which are

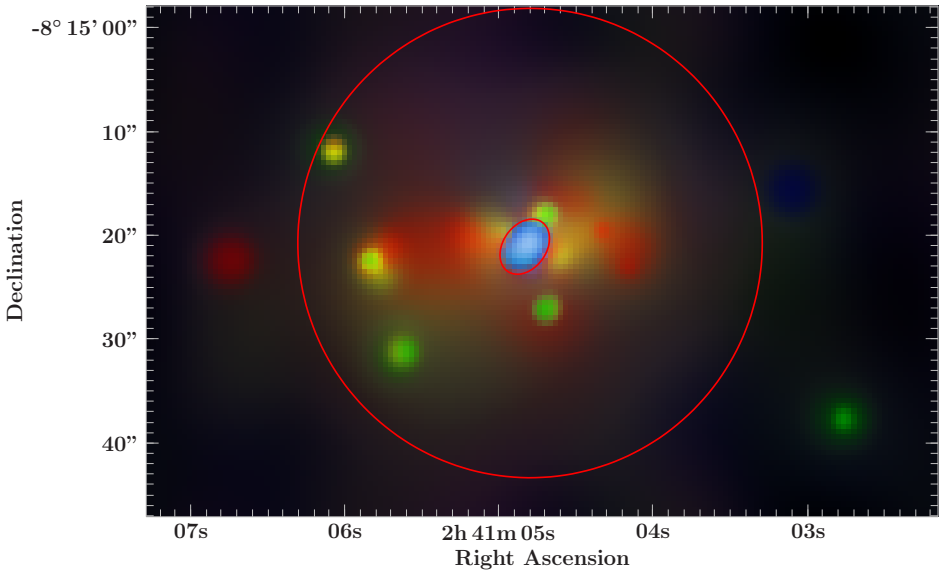

Figure 3.6: Extraction regions for *Chandra* spectra. The X-ray image of the central region of NGC 1052 is that of Fig. 3.4. X-ray spectra have been extracted for the inner core region (red ellipse) and for the region surrounding the core (red circle without red ellipse).

assumed to be stellar mass X-ray sources in the host galaxy, the individually studied spectra of these sources were included in the model. The parameters of the power law models, which have been obtained from a fit to the individual spectra of the three brightest point sources in the region of this kind, were frozen and the models added to the total model of the outer region. As visible in Fig. 3.7, the contribution of these point sources to the total emission in the outer region is small. As a first major component for the analysis of the region, the `apec` model (Astrophysical Plasma Emission Code; Smith et al., 2001; Brickhouse et al., 2005) was used. It describes the emission from collisionally-ionized gas.[8] In earlier X-ray studies of NGC 1052, such a component was used as well in order to account for the soft excess seen in the total X-ray spectrum of the source. From the fit (χ^2/d.o.f. = 636/54 ≈ 11.8) it is clear that one thermal component is not sufficient to describe the data, as strong residuals remain above 1 keV and below 0.6 keV. Adding a thermal bremsstrahlung spectrum (`bremss`; see, e.g., Kellogg et al., 1975) significantly improves the fit (χ^2/d.o.f. = 128/52 ≈ 2.46). Instead of the bremsstrahlung spectrum a simple power law can be used as well, but as the spectral slope (photon index of about 1–1.5) is consistent with that expected for bremsstrahlung, it is a convenient choice to use the physical model. The residuals at low energies in the *Chandra* spectrum can be smoothed by adding a second `apec` model, which can be associated with the emission of a thermal plasma with a lower temperature. These emission components, as well as the fact that the X-ray image shows an alignment of X-ray and radio emission from the jet, indicate that the soft X-ray emission is caused by interaction of the jet with material in NGC 1052. The complete model is multiplied with the `tbnew` model to account for neutral absorption by the interstellar medium (with the abundances and cross sections specified at the beginning of Sect. 3.3). The resulting fit is good (χ^2/d.o.f. = 59.3/47 ≈ 1.2), but the residuals are slightly rising above ∼3 keV. This excess can be interpreted as leaked emission from the nucleus. This assumption is strengthened by the fact that the contribution decreases when the excluded nucleus region is enlarged for the extraction of the outer spectrum. The amount of emission is consistent with the expected contribution from the wings of the *Chandra* point spread function. Adding a contribution of the model for the nucleus emission, which can be modeled with an absorbed power law component as described later in this work, describes the data extremely well (χ^2/d.o.f. = 40.4/47 ≈ 0.86). The resulting parameters of the spectral model are shown in Table 3.1. The obtained column density for the absorption is consistent with the value of 2.8×10^{20} cm^{-2} measured in the Leiden–Argentine–Bonn 21-cm survey (LAB survey; Kalberla et al., 2005). No

[8] The APEC model uses the atomic database (AtomDB) for modeling the X-ray emission of plasma. More information is provided, e.g., by Foster et al. (2012) and online at `http://www.atomdb.org/`.

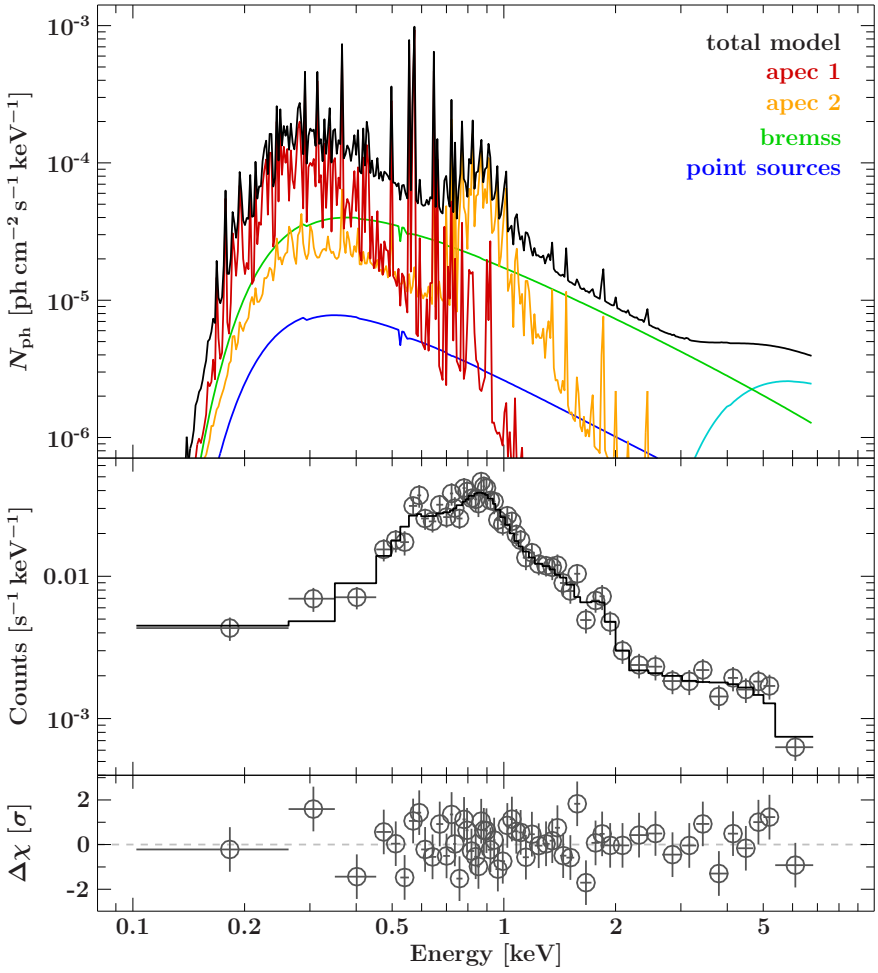

Figure 3.7: Fit to the outer *Chandra* region (shown in Fig. 3.6). The top panel shows the used model and its components. The middle panel shows data and model, and the bottom panel the residuals. The model consists of the emission of thermal plasmas with two temperatures, a thermal bremsstrahlung spectrum, possible stellar mass X-ray sources, and leaked emission from the nucleus. The complete model is modified by absorption in the ISM.

Table 3.1: Results from spectral fitting of the outer *Chandra* region, which is defined in Fig. 3.6.

Parameter	Value	Unit
Obs. Start	2005-09-18, 09:52:13	
ACIS Exp.	59.20	ks
N_H (ISM)	$0.029^{+0.016}_{-0.013}$	$[10^{22}\,\mathrm{cm}^{-2}]$
APEC_1 norm	$0.000039^{+37.252912}_{-0.000012}$	
$T_{\mathrm{APEC},1}$	0.17 ± 0.04	[keV]
APEC_2 norm	$\left(2.3^{+0.5}_{-0.6}\right) \times 10^{-5}$	
$T_{\mathrm{APEC},2}$	$0.78^{+0.10}_{-0.07}$	[keV]
Bremsstrahlung norm	$0.000031^{+37.252907}_{-0.000008}$	
T_{bremss}	$\left(0.25^{+0.76}_{-0.22}\right) \times 10^{2}$	[keV]
χ^2/dof	0.86	

intrinsic absorption in NGC 1052 is required for this emission.

For the later analysis of the total X-ray spectrum obtained with other instruments, where the emission is not spatially resolved, it is helpful to compare the contribution from the nucleus region and the extended emission. The spectra of the different regions obtained with *Chandra* are shown in Fig. 3.8, where the measured counts from the central and the surrounding regions are shown

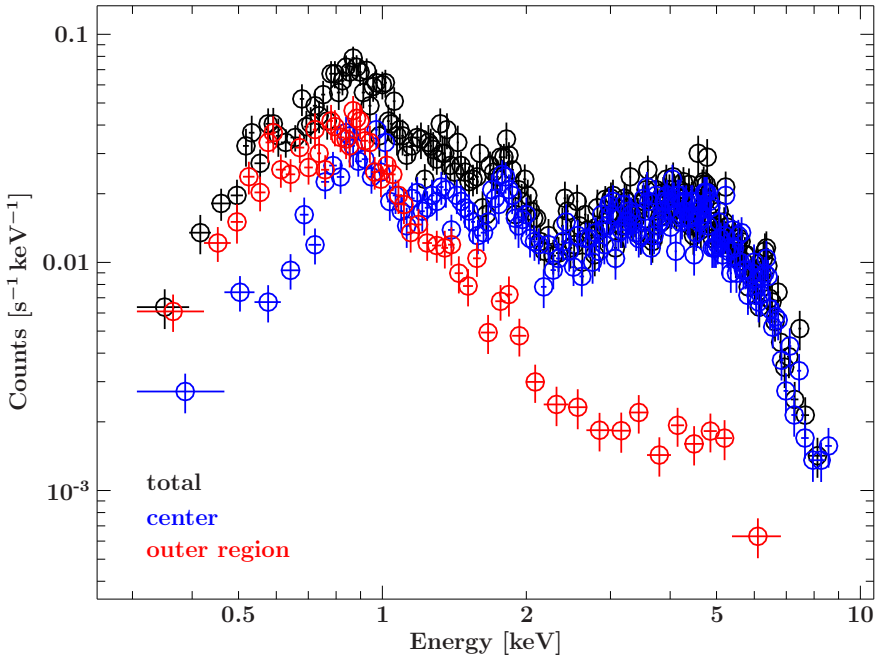

Figure 3.8: *Chandra* spectra of all regions, which are shown in Fig. 3.6: The central region around the nucleus (blue), the outer region (annulus with excluded central region; red), and the total region (sum of both; black). The data are grouped to a signal-to-noise ratio of five.

separately, as well as the sum of both. At very soft X-rays the majority of the counts originate from the outer extraction region. Contrary, the photons with higher energies (> 2 keV) are mainly originating from the central region. At these energies, the emission from NGC 1052 is dominated from emission from the nucleus (see Fig. 3.4). As the X-ray continuum emission in AGN can typically be approximated with power law spectra, the decreased X-ray emission at low energies in NGC 1052 is a clear indication of strong X-ray absorption.

Given the observation of the extended soft X-ray emission and the indication of strongly absorbed emission from the nucleus, the spectrum of the central region has been modeled. The data and the model are shown in Fig. 3.9. As the model for the spectrum of the outer extraction region, the model for the central region contains the emission of a thermal plasma and a thermal bremsstrahlung spectrum. It is a natural step to include these components in the model for the central emission, because the region from which the spectrum has been extracted covers still several hundred parsec in NGC 1052, as can be inferred from Figs. 3.5 and 3.6. If emission from a thermal plasma and bremsstrahlung is observed around the inner region, it is as well expected from the inner region, where the interaction with the jet and the surrounding material might be stronger. Densities are typically higher in the center of galaxies and furthermore the jet is not expected to be weaker in the inner region. Consistent with this assumption the emission from the colder thermal plasma used for the outer region is not necessary for the spectrum of the inner region, but a model with a large contribution of the hot plasma and a strong bremsstrahlung component describe the spectrum of the central region very well. Both components model the soft part of this spectrum sufficiently. For the remaining emission at higher energies the absorbed power law model is used. The strong absorption is source intrinsic, i.e., the nucleus region, from where the X-ray emission originates, has to be embedded in material with a large hydrogen column density.

Contrary to previous studies of this source (e.g., Weaver et al., 1999; Brenneman et al., 2009, and references therein), where no components could be spatially separated, the soft X-ray emission of NGC 1052 has been disentangled from emission from the nucleus, and is modeled only with extended emission. In previous models, a partial covering model was used to explain a large fraction of the soft excess. In a partial covering model, different values of absorption are possible for fractions of the emission. This is possible spatially, i.e., an extended X-ray source is covered with an inhomogeneous absorber. In the most simple case there are two zones with different column density. On the other hand partial covering is possible temporally, i.e., the column density varies

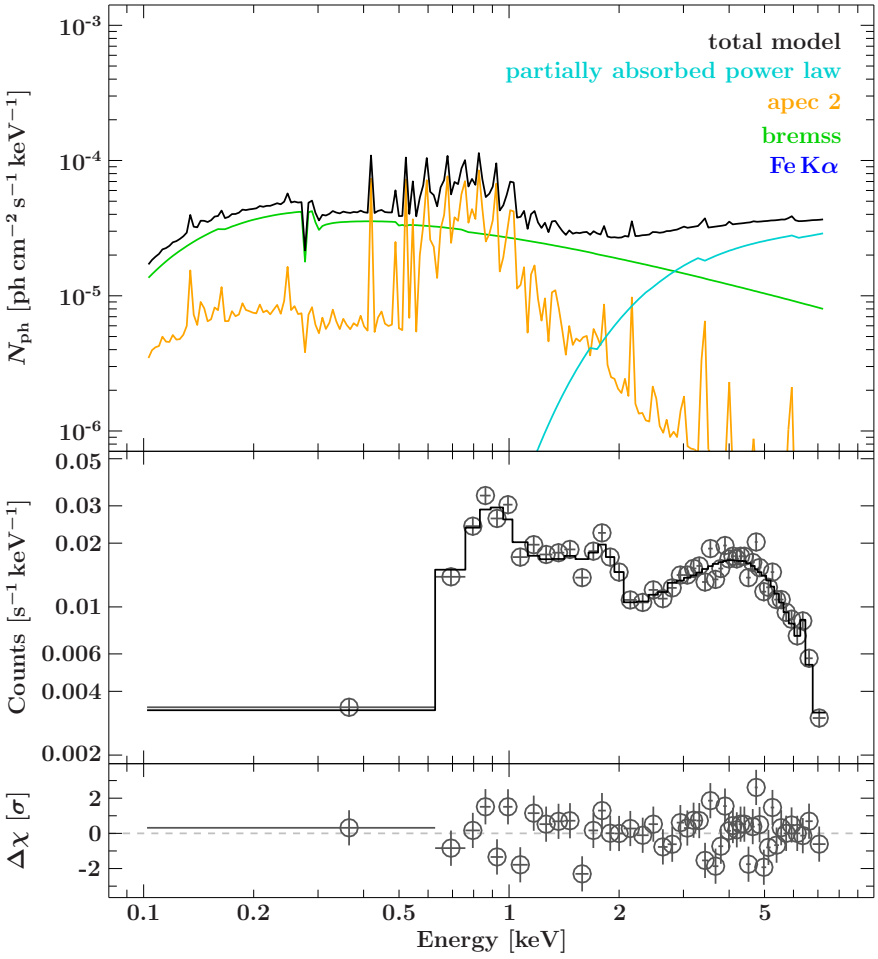

Figure 3.9: Model for the *Chandra* spectrum of the central region around the nucleus of NGC 1052. The model and its components are shown in the top panel. The data and model in the detector space are shown in the middle panel, and the residuals in the bottom panel.

throughout the observation.

3.3.3 Spectral Features

Deep *Suzaku* and *XMM-Newton* observations Given the results from the spatially resolved spectroscopy, the analysis of the observations without comparable angular resolution is significantly easier, because several emission components are identified. For example the power law model for the point sources that are possibly X-ray binaries in the host galaxy, which has been determined from the individually extracted *Chandra* spectra, are frozen in the analysis, i.e., they are not further varied. Their contribution to the total X-ray emission in the observed band is only very small. Another component that is added to the total model using the parameters obtained from the *Chandra* analysis, is the $\texttt{apec}_1$ model that accounts for the plasma emission at lower temperatures. For most of the observations studied in the following (*Suzaku*, *XMM-Newton*, *RXTE*), no data below 0.5 keV were included following the calibration recommendations. For that reason the energy range with strong contribution from this plasma emission is not seen in the following. The contribution of this component to the observed energies is not further varied in the analysis. The remaining components which are required to model the spectral are the bremsstrahlung component, the thermal plasma emission, and the absorbed power law emission associated with nucleus. The complete model can be written in the following way:

$$\texttt{TBnew}_{\text{gal}} \times \{\texttt{XRB} + \texttt{apec}_1 + \texttt{apec}_2 + \texttt{bremss} + \texttt{gauss} + \tag{3.1}$$

$$[\texttt{powerlaw} \times (C \times \texttt{TBnew}_1 + (1 - C) \times \texttt{TBnew}_2)] * \texttt{enflux}\}, \tag{3.2}$$

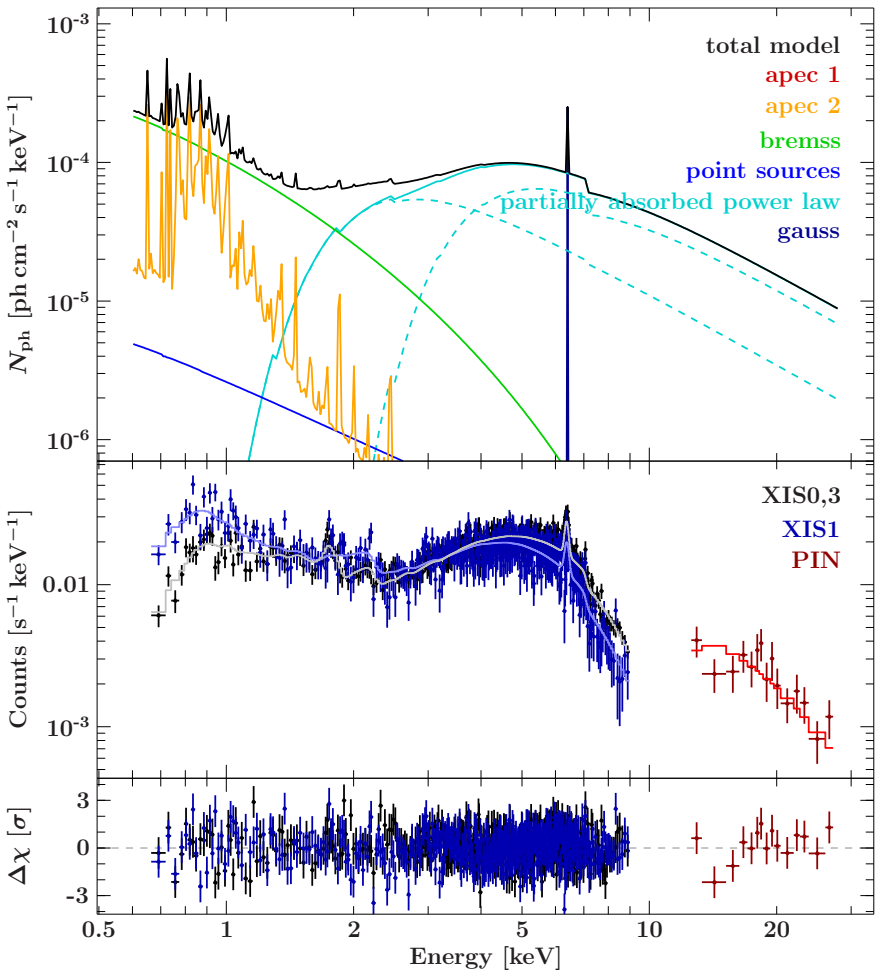

Figure 3.10: Fit to the *Suzaku* observation. The top panel shows the used model and its components. The middle panel shows data of the XIS and PIN detectors and the model. The residuals are shown in the bottom panel.

where `XRB` is the sum of power law models describing the emission of the possible X-ray binaries within in NGC 1052. $\texttt{TBnew}_{\text{gal}}$ describes the Galactic absorption and thus affects the complete model. Contributions from the host galaxy and extended emission are modeled with the `XRB`, $\texttt{apec}_1$, $\texttt{apec}_2$, and `bremss` models. The emission from the nucleus is described with a `powerlaw` continuum with partial covering absorption, where a fraction C of the emission is absorbed with $\texttt{TBnew}_1$ and the remaining fraction $1 - C$ with $\texttt{TBnew}_2$. This contribution from the nucleus is convolved with `enflux` in order to determine the flux in the 2–10 keV energy band. This model is used for the analysis of the X-ray data sets. The number of free parameters has been adapted based on the covered energy range and the signal-to-noise ratio. Parameters that were not expected to vary were the first to be frozen to the expected values, which are values that could be determined better from other observations or completely independently, such as the source's redshift. The results of these fits and the obtained values for the free parameters are discussed in the following.

A fit to the *Suzaku* data with this model is shown in Fig. 3.10, where the spectral shape of the individual components is shown additionally. The model includes a narrow Fe Kα fluorescence line at an energy of about 6.4 keV in the rest frame. This emission line is expected from the interaction of the X-ray emission with surrounding material. The existence of a large amount of such material is proven by the strong X-ray absorption. The best fit to the data was obtained, when not a simple absorbed power law emission was used for the continuum emission of the nucleus, but a more complex absorption structure. A partial covering absorption, with two relatively strong neutral absorbers, was required. A similar model has been used by Weaver et al. (1999). But as mentioned before, the soft X-ray emission does not include a strong contribution from the nucleus, as the column densities of the partial covering absorber are larger. The obtained parameter from the

Table 3.2: Results from spectral fitting of the *Suzaku* region.

Parameter	Value	Unit
Obs. Start	2007-07-16, 10:31:45	
XIS Exp.	100.67	ks
$S_{2-10\,\mathrm{keV}}$	5.17 ± 0.08	$[10^{-12}\,\mathrm{erg\,cm^{-2}\,s^{-1}}]$
APEC$_2$ norm	$3.6^{+0.9}_{-0.8}$	$[10^{-5}]$
$T_{\mathrm{APEC},2}$	0.77 ± 0.07	[keV]
Bremsstr. norm	$1.54^{+0.16}_{-0.18}$	$[10^{-4}]$
Γ	$1.72^{+0.12}_{-0.10}$	
$N_{\mathrm{H},1}$ (intrinisic)	31 ± 5	$[10^{22}\,\mathrm{cm^{-2}}]$
C (Cov. Fac.)	0.78 ± 0.04	
$N_{\mathrm{H},2}$ (intrinisic)	5.3 ± 1.0	$[10^{22}\,\mathrm{cm^{-2}}]$
$S_{\mathrm{Fe\,K}\alpha}$	1.03 ± 0.15	$[\mathrm{ph\,cm^{-2}\,s^{-1}}]$
Fe Kα center	$6.379^{+0.014}_{-0.013}$	[keV]
$\sigma_{\mathrm{Fe\,K}\alpha}$	≤ 0.06	[keV]
χ^2/dof	1.00	

spectral fit of the data from the *Suzaku* observation are shown in Table 3.2. The data at higher energies of this observations are very helpful for constraining the continuum emission. It is difficult to determine the spectral index of the power law with high precision based on only the CCD data below 10 keV. In this lower energy regime the power law emission is strongly curved by absorption and other components contribute. At higher energies the absorption affects the spectral shape less and the other components are negligible, thus the continuum component of the nucleus dominates the emission. Its spectrum is well-described by a power law spectrum.

Using this model, data from all X-ray observations could be modeled consistently. Parameter values obtained from modeling the *XMM-Newton* data are shown in Table 3.3.

No evidence for a relativistically broadened Fe Kα line The usage of two strong absorbers is probably the reason, why no relativistically broadened iron line is required here. As it is obvious from Fig. 3.10, the usage of only one absorber instead of two would yield a column density inbetween the values obtained with two absorbers. Given the large contribution of the strongly absorbed component, this would lead to an underestimation of the iron K edge (slightly above 7 keV) and thus to an excess of emission below this value. This excess can be removed by adding an additional emission component at these energies, such as an relativistically broadened iron line. The model with such a partial covering is more likely than the interpretation with an iron line for the following reasons. Partially covered absorption has been observed in many AGN that are observed at high inclinations. For slightly extended sources it is expected that the material in the line of sight does not cover the complete source homogeneously. In addition to geometrical effects, temporal variation of the absorbing column density have been observed in numerous sources (e.g., Risaliti et al., 2002; Maiolino et al., 2010). On the other hand relativistically broadened iron lines have been observed in AGN (see, e.g., Mushotzky et al., 1995; Fabian et al., 2000; Nandra et al., 2007, and references therein). Strong Fe Kα fluorescence line from an accretion disk are typically not seen in radio-loud AGN, thus such a discovery in NGC 1052 would be a highlight. However, the obtained results from modeling such a component to the data include parameter configurations which are

Table 3.3: Same as Table 3.2, but for the four *XMM-Newton* observations.

Parameter	Value_1	Value_2	Value_3	Value_4	Unit
Obs. Date	2001-08-15	2006-01-12	2009-01-14	2009-08-12	
EPIC-PN Exp.	11.77	46.75	43.68	49.26	ks
$S_{2-10\,\text{keV}}$	$3.58^{+0.17}_{-0.31}$	4.18 ± 0.09	$4.78^{+0.09}_{-0.10}$	4.94 ± 0.09	$[10^{-12}\,\text{erg}\,\text{cm}^{-2}\,\text{s}^{-1}]$
APEC_2 norm	$3.6^{+1.3}_{-1.0}$	2.6 ± 0.6	3.0 ± 0.6	$2.5^{+0.8}_{-0.6}$	$[10^{-5}]$
$T_{\text{APEC},2}$	$0.81^{+0.10}_{-0.09}$	$0.82^{+0.10}_{-0.06}$	$0.84^{+0.10}_{-0.06}$	0.78 ± 0.06	[keV]
Bremsstr. norm	$1.06^{+0.23}_{-0.30}$	$1.30^{+0.10}_{-0.13}$	$1.26^{+0.12}_{-0.13}$	$1.29^{+0.13}_{-0.22}$	$[10^{-4}]$
Γ	$1.8^{+0.4}_{-0.6}$	$1.52^{+0.17}_{-0.16}$	$1.63^{+0.15}_{-0.14}$	$1.52^{+0.13}_{-0.12}$	
$N_{\text{H},1}$ (intrinisic)	44^{+13}_{-19}	31^{+9}_{-7}	25^{+6}_{-5}	18^{+6}_{-4}	$[10^{22}\,\text{cm}^{-2}]$
C (Cov. Fac.)	$0.86^{+0.05}_{-0.13}$	$0.71^{+0.07}_{-0.08}$	$0.72^{+0.08}_{-0.09}$	$0.83^{+0.08}_{-0.13}$	
$N_{\text{H},2}$ (intrinisic)	$4.5^{+1.8}_{-2.0}$	6.0 ± 1.4	$6.1^{+1.3}_{-1.4}$	4.7 ± 2.2	$[10^{22}\,\text{cm}^{-2}]$
$S_{\text{Fe K}\alpha}$	$1.2^{+2.5}_{-0.6}$	0.77 ± 0.17	$0.81^{+0.29}_{-0.20}$	$1.10^{+0.26}_{-0.24}$	$[10^{-5}\,\text{ph}\,\text{cm}^{-2}\,\text{s}^{-1}]$
Fe Kα center	$6.31^{+0.06}_{-0.17}$	$6.378^{+0.012}_{-0.019}$	6.39 ± 0.04	$6.349^{+0.026}_{-0.027}$	[keV]
$\sigma_{\text{Fe K}\alpha}$	$0.12^{+0.44}_{-0.11}$	≤ 0.07	$0.06^{+0.07}_{-0.06}$	$0.08^{+0.05}_{-0.04}$	[keV]
χ^2/dof	1.13	1.00	1.20	1.05	

very unlikely. One of the main problems is given by the intensity of the line. Starting from the initial continuum X-ray emission, the line profile arises from the reflection of the emission from the accretion disk (see Sect. 1.3.2). The intensity of the reflection line depends on how much of the continuum emission hits the disk. The equivalent width of the line obtained from modeling the NGC 1052 X-ray data is in the range of several hundreds of eV up to above one keV. Such unusually high values would require an extreme covering of the initial X-ray emission by the accretion disk. It would be necessary that the initial emission is focused mainly on the disk. An extremely strong reflection component from the disk is furthermore excluded by studies of the hard X-ray emission of NGC 1052, in which Brenneman et al. (2009) did not find indications of a Compton reflection hump. Another discrepancy of the model with the strong broad Fe Kα line is the variability of its shape between different observations. The line shape depends on the inclination of the accretion disk and the black hole spin, which are both not expected to vary over observational time scales. Other factors influencing the line shape are the irradiation of the disk and its ionization profile, as well as its inner radius. Various different cases have to be constructed in order to explain the different line shapes with this model, whereas in the partial covering model variations of the column densities, the covering factor, and the continuum spectrum explain the different shapes naturally and very well.

Averaged Spectra Besides using the X-ray monitoring observations for a study of the temporal variability, it is possible as well to study the average spectral properties of the source during the monitoring interval. Whereas data from the individual *RXTE* observations are not sufficient to model spectral details, the signal-to-noise ratio can be increased by adding all observations. In this way the spectral slope at higher energies can be studied, as *RXTE*/PCA data was used from about 3.5 keV up to ∼20 keV. In addition to these data the *Swift*/BAT spectrum from the 58 month catalog has been used. Starting in 2004, November, a similar observation interval as with *RXTE* is covered. With an energy range of 14–195 keV, the average X-ray spectrum is extended to higher energies. At the energies covered with *RXTE*/PCA and *Swift*/BAT a partially absorbed power

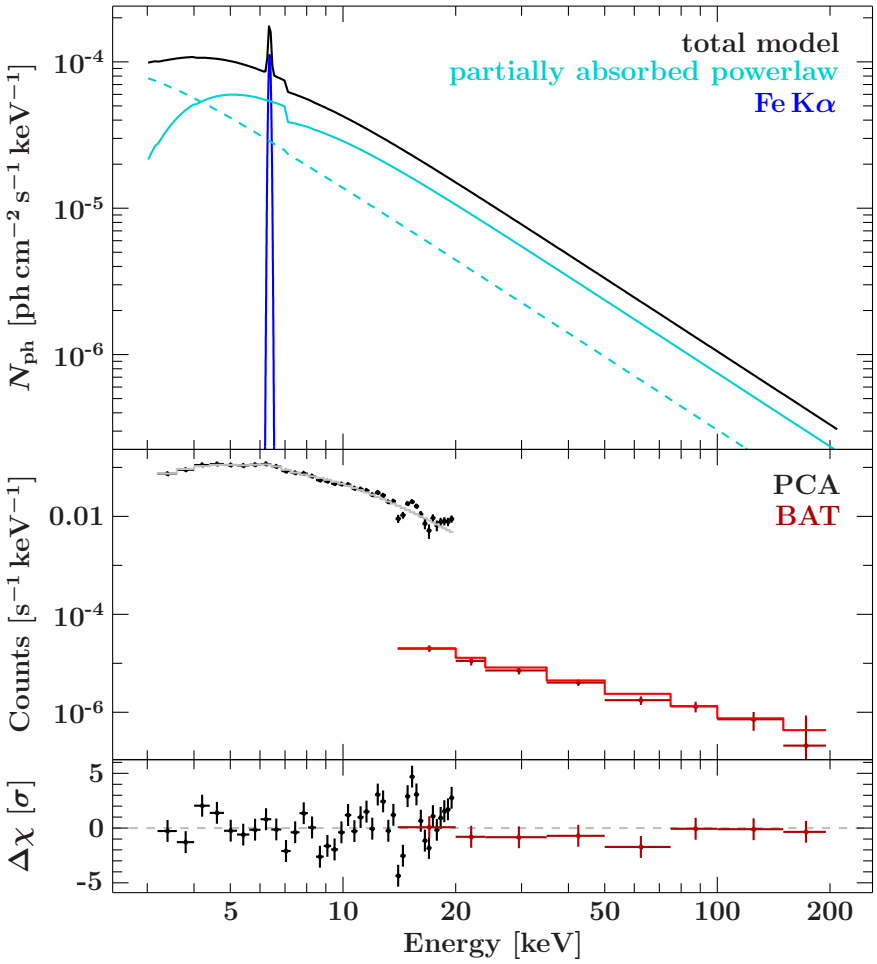

Figure 3.11: Averaged spectrum using the *Swift*/BAT 58 month spectrum and sum of all PCA observations from the monitoring campaign. The iron line width has been increased for illustration, otherwise it is a delta function.

Table 3.4: Results from spectral fitting of the averaged PCA and *Swift*/BAT 58 month data.

Parameter	Value	Unit
$S_{2-10\,\mathrm{keV}}$	$5.49^{+0.19}_{-0.26}$	$[10^{-12}\,\mathrm{erg\,cm^{-2}\,s^{-1}}]$
Γ	1.66 ± 0.10	
$N_{\mathrm{H},1}$	25^{+16}_{-13}	$[10^{22}\,\mathrm{cm^{-2}}]$
$S_{\mathrm{Fe\,K}\alpha}$	1.4 ± 0.5	$[10^{-5}\,\mathrm{photons\,s^{-1}\,cm^{-2}}]$
$\sigma_{\mathrm{Fe\,K}\alpha}$	$< 2.0 \times 10^{-1}$	[keV]
EW(Fe Kα)	$(1.7 \pm 0.6) \times 10^2$	[eV]
χ^2/dof	3.34	

law and the Gaussian profile for the narrow iron line were sufficient for a good description of the spectrum. The data, model, and residuals of the spectral fit are shown in Fig. 3.11 and the obtained parameters in Table 3.4. In the spectrum there are no strong indications for spectral curvature in this energy regime. No strong reflection hump or high-energy cutoff is clearly visible. The power law is sufficient to describe the data. The average spectra, however, have to be handled with care, as there could be significant variability of the spectrum during the years over which the spectrum is averaged. It is, e.g., obvious from the *RXTE*/PCA spectrum that problems arise from the averaging process. Above 10 keV this spectrum shows strange residual features, which are even stronger at the higher energies, where they are not seen in the *Swift*/BAT spectrum and thus ignored in the

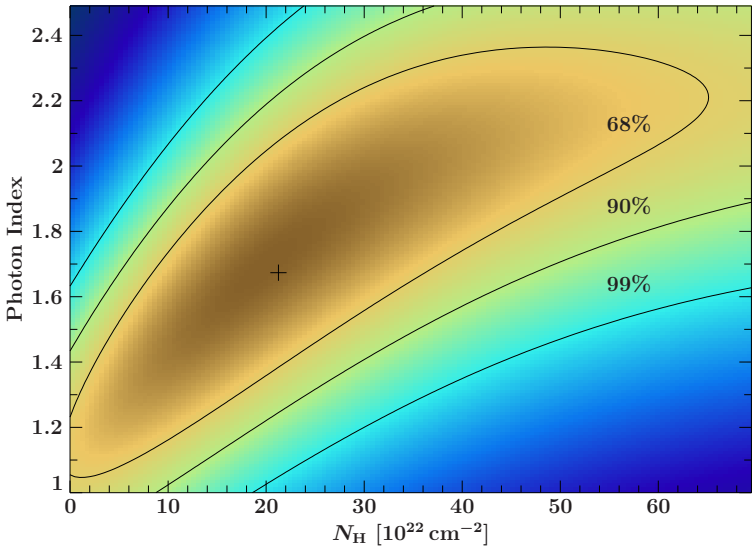

Figure 3.12: Typical confidence region for the photon index and the hydrogen column density for a single *RXTE* observation (ObsID 94148-01-23-00). The cross marks the position of the best fit.

analysis. Most likely these problems arise due to averaging of data with different spectral shapes and the enhancement of included background features. The χ^2 value is large, because of the features in the averaged PCA spectrum.

3.3.4 Monitoring X-ray Variability

Besides the X-ray properties found in the previously mentioned pointed observations with *Chandra*, *Suzaku*, and *XMM-Newton*, the main information on the X-ray variability of NGC 1052 is obtained from the monitoring campaign with *RXTE* from June 2005 until the end of 2009. The observations with average exposures of 2.7 ks (minimum 1.28 ks, maximum 3.26 ks) are suitable to determine the overall X-ray variability. As typical count rates of NGC 1052 in the total PCA of *RXTE* are even below 1 count per second, the spectra obtained in these monitoring observations cannot be used to study spectral features in detail, but provide information on the source brightness. Using the model previously determined from the deep observations with *Chandra*, *Suzaku* and *XMM-Newton* and freezing the parameters which are expected to be constant, such as the properties of the extended thermal emission, the total X-ray flux of the source was determined. The only parameters that were left variable for fitting are the spectral index of the absorbed power law, its flux in the 2–10 keV band, and the column density, $N_{\mathrm{H},1}$, of the primary absorber. The flux in this band has been modeled with the `enflux` model, which is described in Sect. 2.2.2. The flux is determined for the absorbed power law component. Although the unabsorbed flux is an important intrinsic quantity that provides insights in the emission processes, there is a large risk for obtaining wrong results when correcting for the absorption, unless the continuum and absorption parameters are known with high precision. Given the small number of detected photons in the *RXTE* spectra, it is more reasonable to use the absorbed flux. Especially the correlation between the photon index and the column density in the parameter estimation from *RXTE*/PCA data is a problem for using unabsorbed flux, whereas the absorbed flux is well-defined directly from by data. As shown in Fig. 3.12, it is not possible to accurately determine both the photon index and the column density of the primary absorber from an individual *RXTE* observation. The confidence map of the photon index and the column density shows a strong correlation. Lower values of the photon index (harder spectra) can be compensated with lower values of the column density and vice versa. It is also obvious that both parameters cannot even be well-determined individually. Based on the small number of events measured during the observation, the confidence intervals cover almost the complete allowed parameter range. For the determination of the total X-ray variability from the *RXTE* observations, the column density $N_{\mathrm{H},1}$ was therefore limited to the

range of (15–45) $\times 10^{22}\,\mathrm{cm}^{-2}$. That is the maximal range obtained from estimating this parameter with temporary close *XMM-Newton* and *Suzaku* observations. Setting these reasonable limits for the *RXTE* analysis yields proper uncertainty estimation of the flux without introducing a bias by fixing the column density.

In order to optimize the precision of the determination of the free parameters, the Cash statistic has been applied. As described in Sect. 2.2.2, it is suitable for the analysis of data with a small number of events, contrary to the Gaussian approximation used with χ^2 statistics. In addition, the number of free parameters has been reduced to only two important ones, as mentioned above. The source intrinsic absorbing column density has been frozen to the values obtained from temporary close deep observations.

The data obtained with *Swift*/XRT observations have been analyzed in a similar way as the *RXTE*/PCA ones. Due to their scheduling, the observations could be added to blocks of about 10 ks of exposure. With the resulting data sets more free parameters could be determined than with the *RXTE*/PCA data. For that reason the column density of the intrinsic absorber and the flux of the narrow Fe Kα line were left as variable parameters in addition to the photon index and the flux in the 2–10 keV energy band. The spectra were grouped to a signal-to-noise ratio of one and then fitted based on the Cash statistic. The grouping in this way essentially yields at least one count in each detector bin. The default binning of the instrument is by default relatively narrow, and over-sampling the detector resolution. At the given count rates and exposures, without grouping a large fraction of the original detector bins remained empty. As no narrow spectral features were modeled with the free parameters the grouping did not yield a notable loss of information, but yielded several advantages instead. For example the used gradient fitting algorithms converged more smoothly. In addition, the fitting process was faster due to the reduced number of bins.

Evolution of Parameters Using all the monitoring observations with *RXTE* and *Swift*, and including the pointed deep observations, the temporal evolution of the parameters can be tracked. It is shown in Fig. 3.13. Additionally to the pointed observations with *Chandra*, *Suzaku*, and *XMM-Newton*, archival data sets obtained with *ASCA* and *BeppoSAX* were analyzed and the resulting parameters included. Figure 3.13 is an overview on the results from an analysis of the entire X-ray data set. It includes all available X-ray spectra, which allow for spectral modeling, that have been obtained from NGC 1052 so far.

It is clearly visible that NGC 1052 is strongly variable in the 2–10 keV band. The flux in this band changed from below $3 \times 10^{-12}\,\mathrm{erg\,s^{-1}\,cm^{-2}}$ to almost $10 \times 10^{-12}\,\mathrm{erg\,s^{-1}\,cm^{-2}}$. Significant variability is seen on time scales of months. The photon index is not precisely constrained, but shows indications of slight variability.

3.4 Radio Analysis

Complementary to the numerous X-ray observations, NGC 1052 is well-sampled in the radio regime, too. The main reason for the good sampling is the multiwavelength monitoring campaign (Sect. 3.2). In Sect. 3.4.1 an overview on the available radio observations is given. Light curves obtained with single dish observations are described in Sect. 3.4.2. The results of an analysis of the numerous VLBI observations are presented in Sect. 3.4.3, including a full study of the jet kinematics.

3.4.1 Radio observations of NGC 1052

In order to obtain information on the total radio variability and spectral properties, single dish observations have been used. The VLBI technique has been applied for studies of the properties of the radio jet at sub-parsec scales. In this section, an overview on the used data is given. Figure 3.14 shows the temporal sampling of NGC 1052 with observations used in this work.

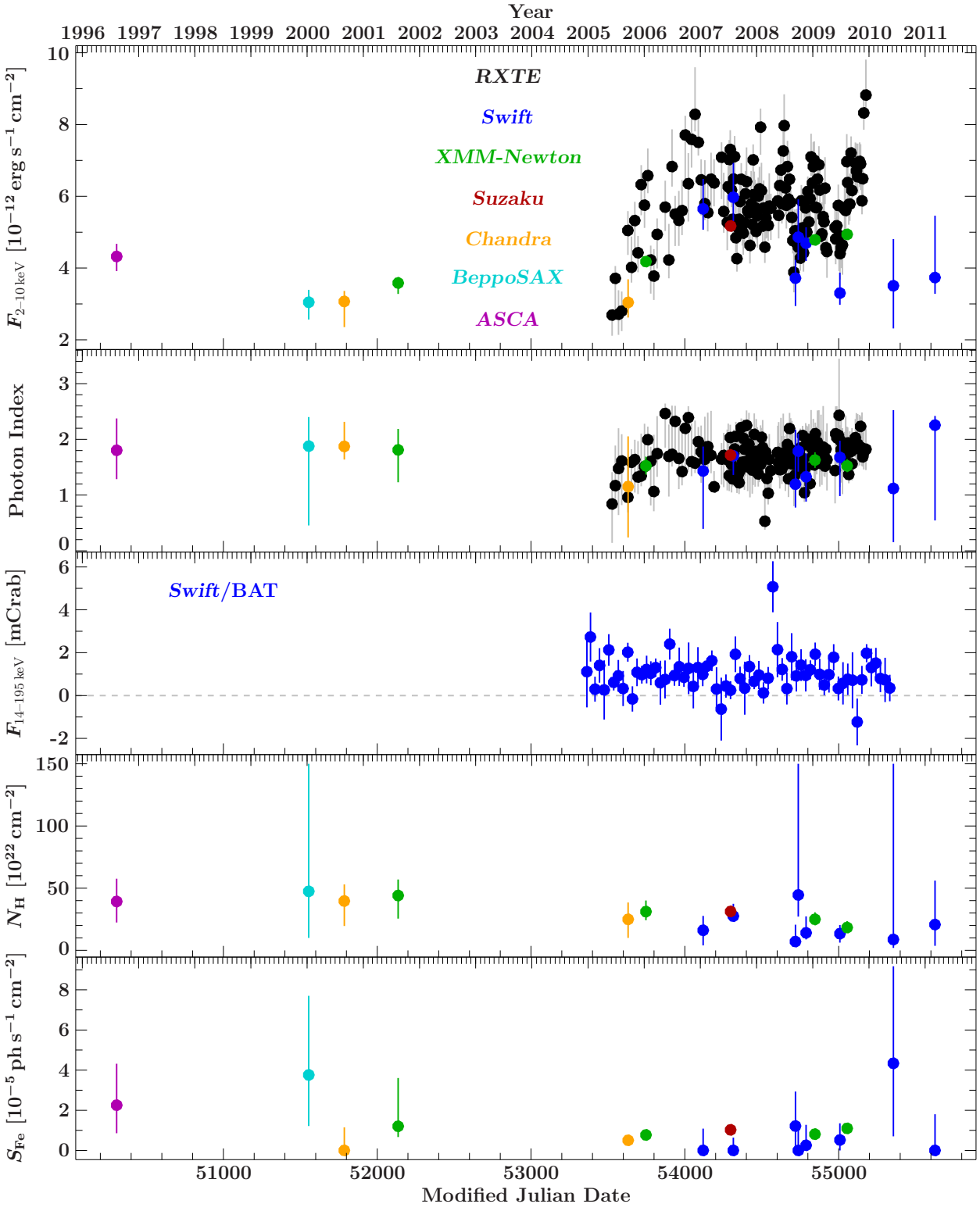

Figure 3.13: Temporal variability of NGC 1052. In the top panel the 2–10 keV light curve of the absorbed power law component is shown. The following panels show the photon index (second panel), the *Swift*/BAT light curve (third panel), the column density of the intrinsic absorber (fourth panel), and the flux of the Fe Kα line (bottom panel).

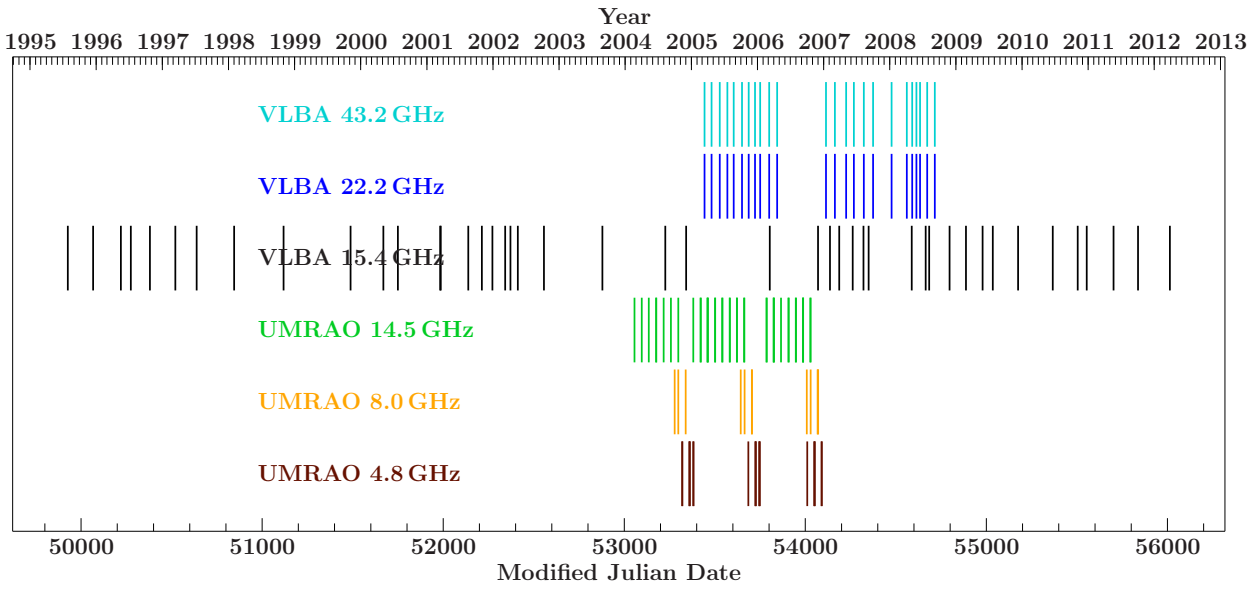

Figure 3.14: Sampling of NGC 1052 with radio observations with the VLBA and UMRAO.

In order to track the total variability of the source at different frequencies, it has been observed with different single dish instruments. Observations at 4.8 GHz, 8.0 GHz and 14.5 GHz have been performed with the University of Michigan Radio Astronomy Observatory (UMRAO; see, e.g., Hughes et al., 1992; Aller et al., 1996). In addition, data at ∼1–22 Ghz have been obtained with RATAN-600 (e.g., Pariiski et al., 1991, and references therein) are available. Higher frequencies are covered with data obtained with the 100 m Effelsberg radio telescope (which is operated by the Max-Planck-Institut für Radioastronomie, for more information see, e.g., the review by Wielebinski et al., 2011, and references therein). Light curves at cm and mm-wavelengths were obtained within the F-GAMMA program (e.g., Angelakis et al., 2010) since the middle of 2005.

Numerous VLBI observations are available at 15 GHz. NGC 1052 has been observed at this frequency since 1995 with the VLBA within the scope of the 2cm Survey and the MOJAVE program (these programs are described in Sect. 4.2). The 10 first epochs were studied in detail by Vermeulen et al. (2003) including a kinematic analysis. In addition to these data, a VLBA monitoring campaign has been performed between 2005 and 2009, where NGC 1052 has been simultaneously observed at 22 GHz and 43 GHz.

3.4.2 Single dish radio observations

The evolution of the flux density of NGC 1052 has been monitored with the UMRAO at 4.8 GHz. 8.0 GHz, and 14.5 GHz. The obtained light curves are shown in Fig. 3.15. The source shows variability at these frequencies during the covered time interval from 2004 to 2007. The highest flux density at 14.5 GHz (which is the best covered band) is observed in mid-2005. At all three frequencies, the flux density exceeds 1 Jy in all observations.

The variability from 2007 on is shown in Fig. 3.16. These light curves, which have been obtained within the scope of the F-GAMMA program, cover nine frequencies from 2.64 GHz up to 145 GHz. As visible in the shown light curves from 2007 to 2012, the characteristic variability time scales depend on the frequency. They are largest at the lowest frequencies, where only a smooth variation of the intensity is seen over the years. With increasing frequency, more variability appears at shorter time scales. At intermediate frequencies (e.g., 10.45 GHz and 14.60 GHz) several broad modulations are seen. Maxima are, e.g., seen in the end of 2008, beginnings of 2010 and 2011. Before these dates, the intensity increased over several months, and afterwards it decreased on comparable time

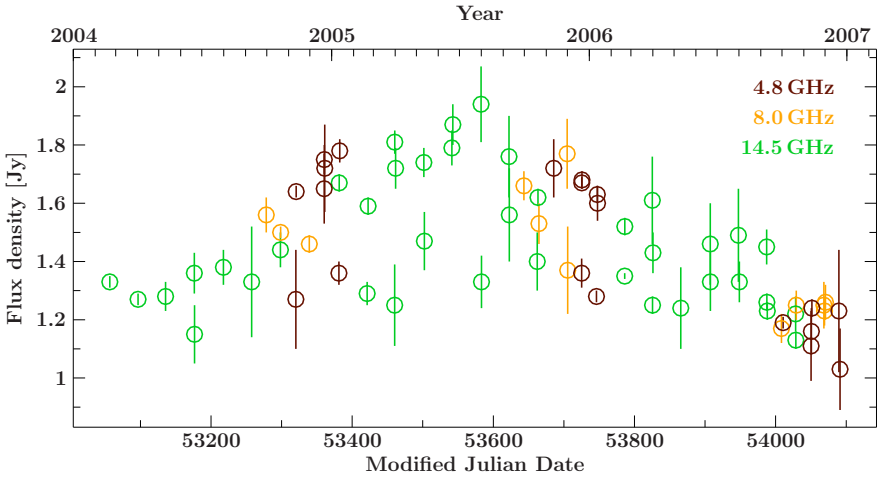

Figure 3.15: Radio light curves of NGC 1052 obtained with UMRAO at 4.8 GHz, 8.0 GHz, and 14.5 GHz. (Data provided by M. Aller)

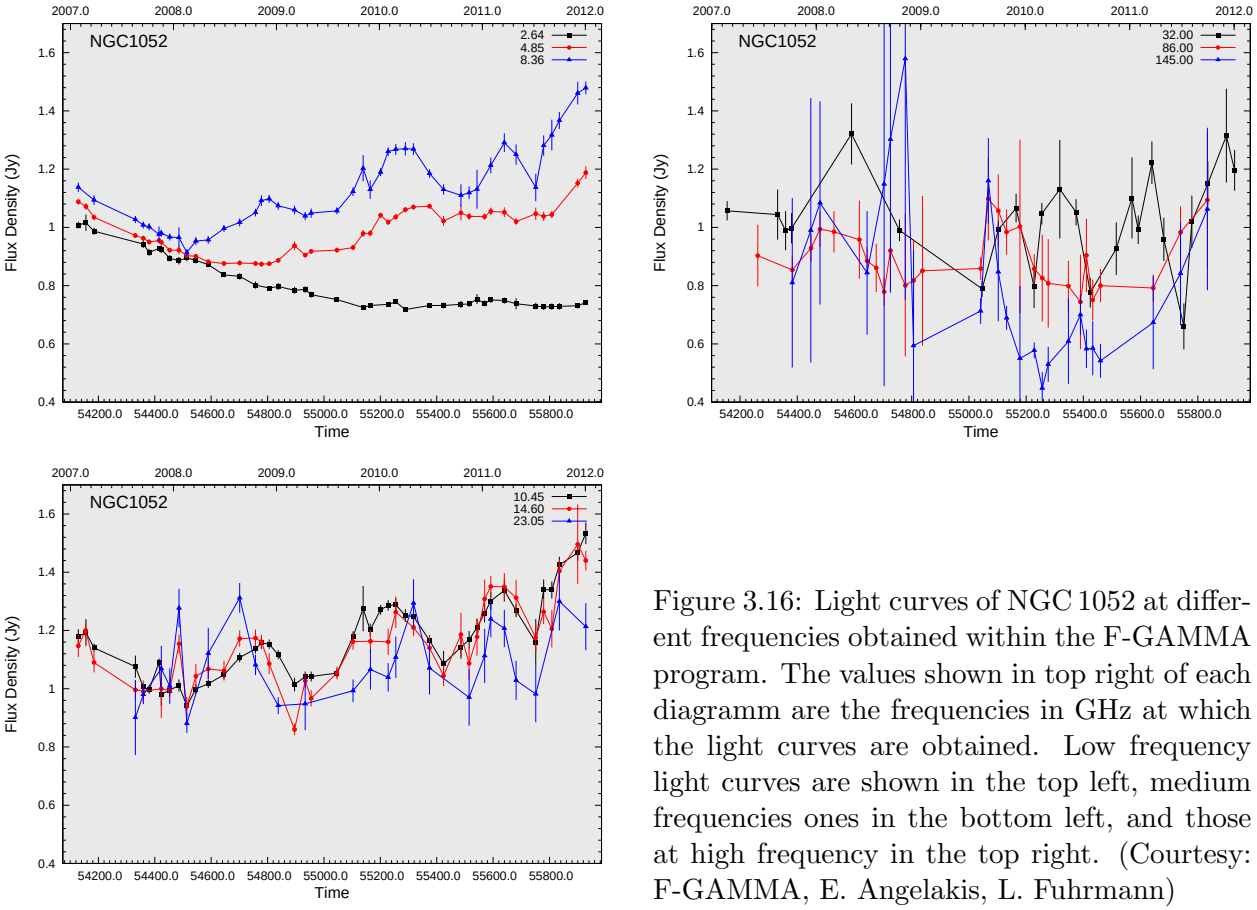

Figure 3.16: Light curves of NGC 1052 at different frequencies obtained within the F-GAMMA program. The values shown in top right of each diagramm are the frequencies in GHz at which the light curves are obtained. Low frequency light curves are shown in the top left, medium frequencies ones in the bottom left, and those at high frequency in the top right. (Courtesy: F-GAMMA, E. Angelakis, L. Fuhrmann)

scales. At high frequencies, these peaks appear to be narrower. Especially the two earlier peaks seem to have prior flares at the highest frequencies. An explanation of this behavior could be the spectral and intensity evolution of components in the radio jet. Newly ejected components in the radio jets are typically first visible at high frequencies, due to absorption of lower frequencies. When moving downstream in the jet, the intensity of the components typically decreases, due to expansion and cooling. For a detailed view on the evolution of the radio jet and its components, it is crucial to spatially resolve and track them. In this way it is possible to determine the ejection times of components and compare their kinematics and flux evolution with the radio light curves and the X-ray variability. For this purpose, VLBI observations are required, which are discussed in the following section.

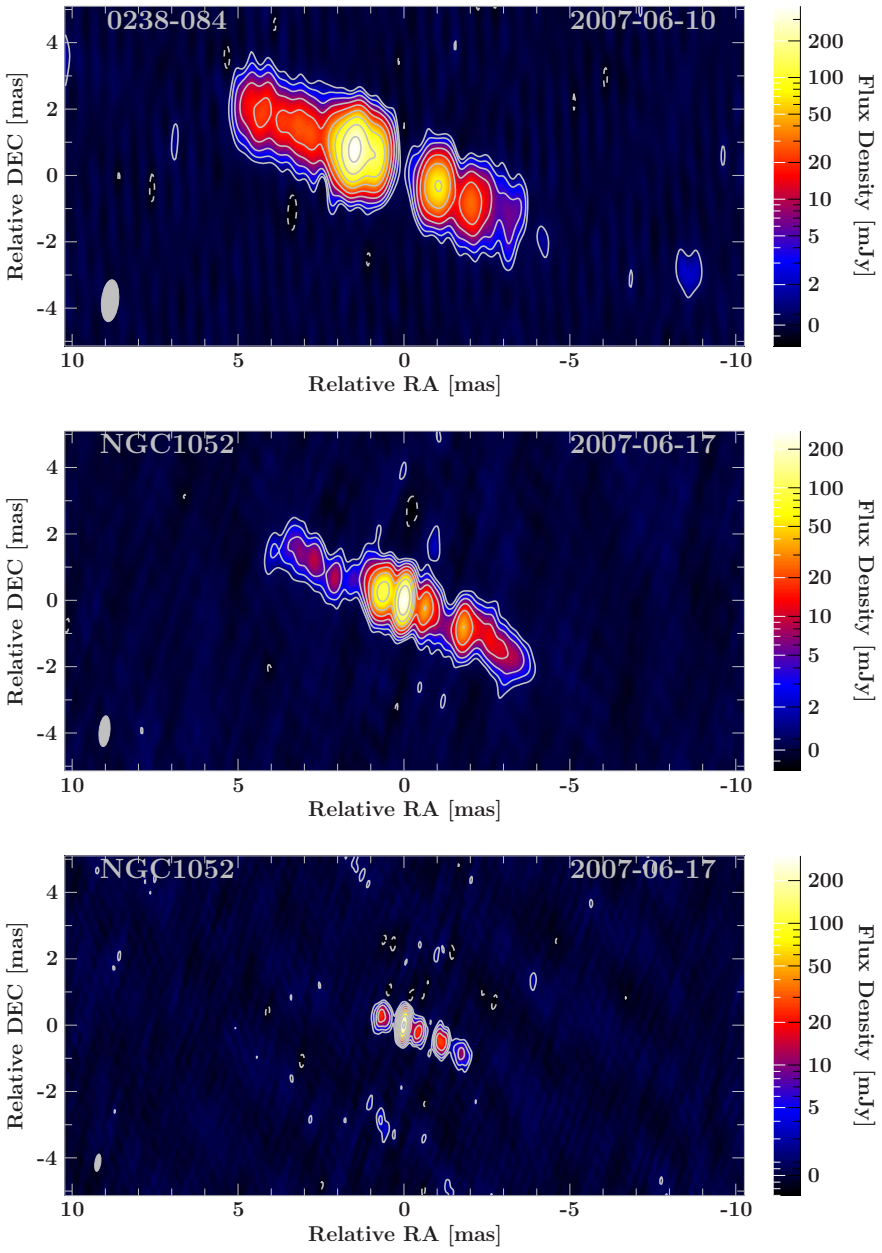

Figure 3.17: VLBI images of NGC 1052 at different frequencies. All images show the same region for better comparision. The top image is obtained from a VLBI observation at 15.4 GHz on 2007, June 10. The images at higher frequencies of 22.2 GHz (middle) and 43.2 GHz (bottom) have both been obtained one week later on 2007, June 17.

3.4.3 VLBI observations of NGC 1052

VLBI images As described previously, the goal of the VLBI observations is to monitor the evolution of the structure of the radio jet. Observations with the VLBA at 15 GHz are available since 1995. With this data set, the long-term evolution of the radio jet can be studied on parsec scales over about 17 years.

VLBA images of NGC 1052 at three different frequencies are shown in Fig. 3.17. The characteristic structure of the source consists of a jet and a counter-jet. The inclination is large, i.e., the jets are orientated close to the plane of the sky. Vermeulen et al. (2003) determine a lower limit on the inclination angle of 57 degrees. The approaching jet is pointing eastward with a position angle of about 67° (measured from the north). It is slightly brighter than the opposed counter-jet. In between of the jet and the counter-jet, there is a clear emission gap. At higher frequencies, the observed emission gap is smaller and parts of the jets closer to the black hole are visible (see, e.g., Kellermann et al., 1999; Kameno et al., 2003; Kadler et al., 2004b). This observation agrees with expected opacity effects in jets (see, e.g., Königl, 1981; Lobanov, 1998, for information on

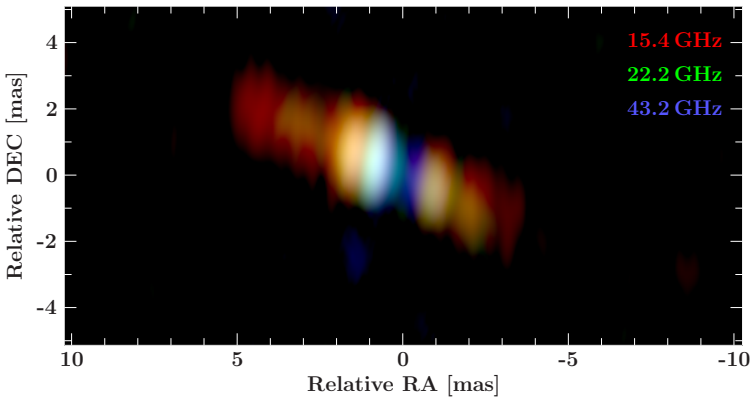

Figure 3.18: Superposition of VLBI images at different frequencies shown in Fig. 3.17. The images have been created the same resolution. In the color overlay, red corresponds to 15.4 GHz, green to 22.2 GHz, and blue to 43.2 GHz.

the frequency-dependent "core shift"). In addition, the angular resolution is better at higher frequencies (see Eq. 2.1), because the same telescope array is used with a comparable *uv*-coverage. The smaller emission gap in NGC 1052 and the increased angular resolution at high frquency can be seen on the example of three (almost) simultaneous VLBI observations at different frequencies shown in Fig 3.17. The full width at half maximum of the beam in the image obtained at 15 GHz is 1.28 mas × 0.50 mas (major and minor axis of the Gaussian approximation). The beam is smaller at 22 GHz, with values of 0.95 mas × 0.33 mas. The highest resolution of 0.52 mas × 0.17 mas is obtained at 43 GHz. In the analyzed VLBA observations, the major axis of the beam is typically orientated with a position angle of a few degrees to the west. The minor axis of the beam is therefore close to the jet axis allowing for a high resolution along the jet. The projected distances in the source corresponding to the highest angular resolutions at the frequencies of 15 GHz, 22 GHz, and 43 GHz are about 48 mpc, 31 mpc, and 16 mpc, respectively. Given in light days (ld), these values are 56 ld, 37 ld, and 19 ld. Figure 3.18 shows a color image of the NGC 1052 jet using the VLBA images of Fig. 3.17. For this overlay, the individual VLBA images have been created with the angular resolution at the lowest frequency. Different colors represent the intensity at different frequencies. It is clearly visible that emission at high frequencies is located closer to the center of the system and that low frequencies extend further downstream of the jet (see, e.g., Kameno et al., 2001).

Model fitting and kinematic analysis The VLBI jet images of NGC 1052 (Fig. 3.17) show individual features at all frequencies. In order to parameterize them, models consisting of two-dimensional Gaussian profiles were used to describe the spatial flux distribution of the source. The model parameters were obtained from fits to the interferometric data (the visibility) using the program DIFMAP. Each model component is characterized by the following set of parameters: The component's position, which is given by two sky coordinates, the flux density, and the FWHM. In this work, circular Gaussian components are used, therefore the width of the emission profile is characterized by only one parameter instead of three required for elliptical components (semimajor axis, semiminor axis, and position angle). The restriction to circular components has been used in order avoid divergences of the axis ratio and to reduce the number of free parameters, since it turned out that the data can be described well with the usage of circular components. An example of a model fit to a VLBA observation at 22 GHz is shown in Fig. 3.19. The distribution of the flux density on the sky can be described by separated circular Gaussian components. In the fitting process, a compromise between describing the data reasonably and not over-parametrizing the model has to be found. One the one hand, the model describes the data the better the more model components are used. On the other hand, it is easier for tracking properties of jet features over different observation epochs when they are uniquely described with one component in each epoch. The model for each VLBI image has been developed iteratively, by adding a component at the position close to the jet axis where the largest residuals are found. After fitting of the

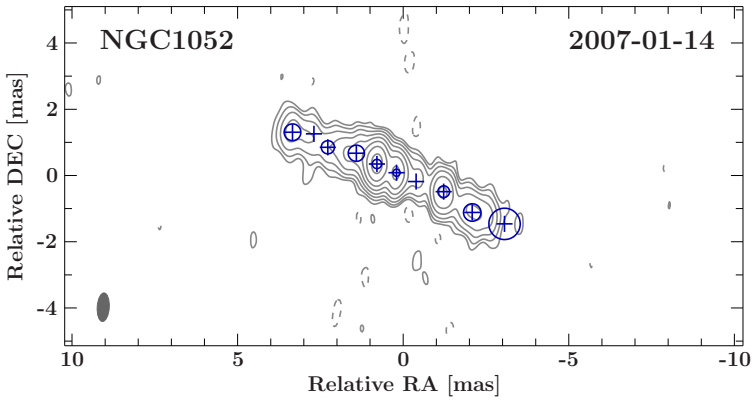

Figure 3.19: Exemplary model fit to the VLBA observation of NGC 1052 at 22 GHz on 2007, January 14. Contour lines (at logarithmically scaled intensity levels starting at three sigma above the image noise) indicate the flux distribution in the clean image. The blue crosses show the positions of model components and the circles represent their size (FWHM).

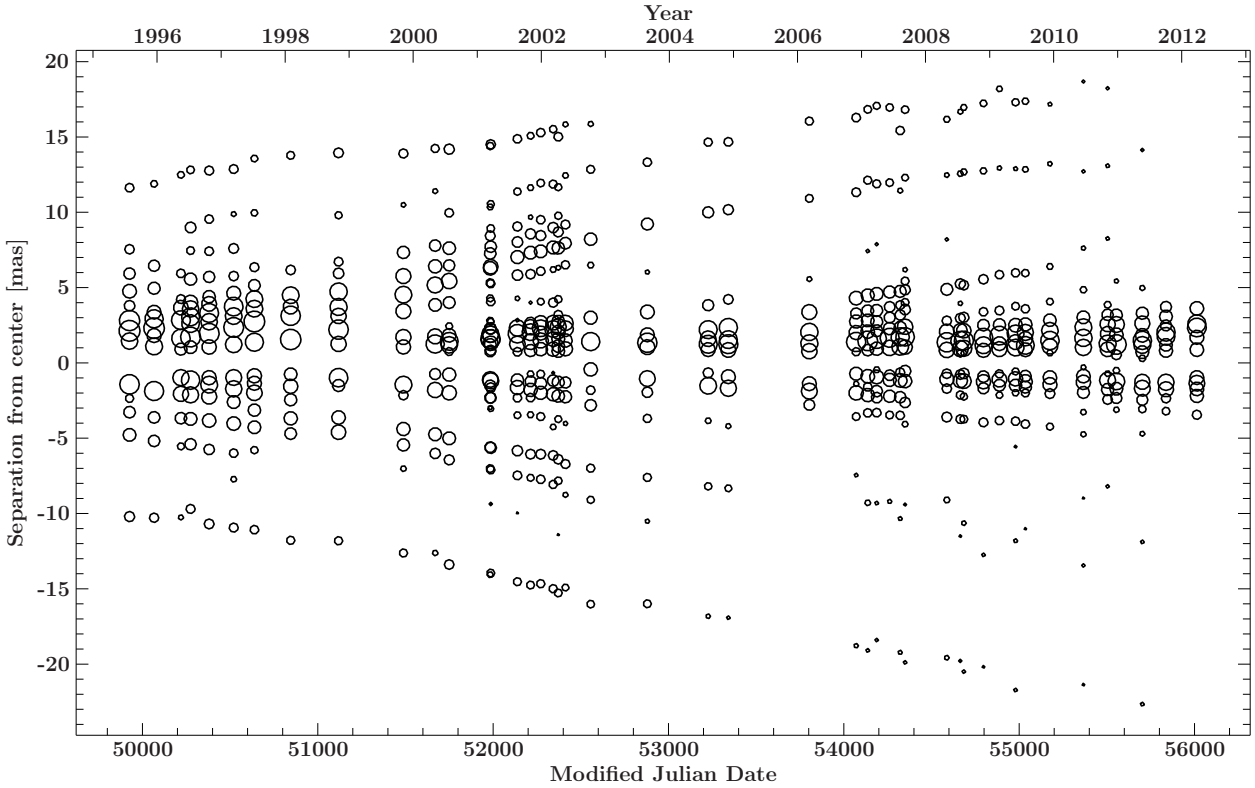

Figure 3.20: Separation of the jet components from the center at 15 GHz. A negative sign is asigned to the separation of components in the counter-jet. The symbol sizes scale logarithmically with the components' flux densities.

model parameters, another component has been added. Model fitting has been performed for each VLBA observation of NGC 1052, which were 45 epochs at 15 GHz and 24 epochs at 22 GHz, and at 43 GHz. This process was done independently at all three frequencies. In total, slightly more than a thousand model components were used for all epochs. The separation from the center of components at 15 GHz is shown in Fig. 3.20 as a function of time. The center is defined here as the middle of the emission gap between jet and counter-jet. This position, where the central supermassive black hole is expected, is assumed to remain constant over time. These VLBA images were aligned according to this "center". Per default, the VLBI images were centered on the brightest feature in DIFMAP and had thus to be shifted for further analysis. It is obvious from Fig. 3.20 that there are several jet components whose distance to the center increases with time. In addition, there is also a dependence of the components brightness on time. While large flux densities are found close to the

center, i.e., close to the emission gap where the jet becomes visible, the intensities of components further away are lower.

For a detailed study of the velocity of components moving away from the center and the temporal evolution of their brightness, it is necessary to associate the components throughout the different epochs. The identification process is difficult due to several reasons. For example, a proper alignment of the epochs is required. Because of the self-calibration of the phase, no absolute positions of the images can be obtained. The images are shifted in order to obtain a likely evolution from one epoch to the following one. The objective approach of aligning the 15 GHz images according to the emission gap (Fig. 3.20) yields already relatively good results, and a large number of components could be uniquely identified over many epochs. Besides the image alignment, problems can arise from multiple nearby components. Given the possible slight differences of the calibration and the *uv*-coverage from one epoch to another, it can happen that weak components are seen in some epochs, but not in others. Furthermore, it occured several times that a jet feature required more than one model component in one epoch, but only one in the previous or following epoch. In these cases, it had to be decided how the evolution of the feature should be tracked. For a study of the evolution of the feature, it is, e.g., possible to modify the model in an iterative process of component association and model fitting of neighboring epochs. In order to avoid a subjective bias, the models of the different epochs have been developed independently in this work. However, in the following association process ambiguities were checked. In the cases in which the same feature was modeled with a different number of components in different epochs, it was tried to modify the model accordingly. In order to track only the most significant and clearly associated features, the number of weak and redundant model components was reduced. Features modeled with two components in one epoch and only one component in the other epochs, were still treated as one feature. It is not a severe problem for the determination of the kinematics, but the "splitting" of components has to be considered, e.g., in the evolution of the features' flux distribution. Furthermore, the association of components at different frequencies is difficult, as more details can be resolved at higher frequencies and components are visible closer to the center of the system. As mentioned previously, opacity effects such as the core shift influence the observation of components in the inner milliarcseconds of the jet, while opacity is not a problem for optically thin components farther out in the jet.

The final identification of the components is shown in Fig. 3.21. Here, the components at all epochs at the three frequencies are shown. In order to determine the proper motion of the features in the jet, linear fits to the features' separation from center as a function of time have been performed. As most components are located on the jet axis, it is a valid approximation to model their proper motion in one dimension using the separation from the center. In order to model the jet kinematics properly, a dynamic and flexible fit function has been developed within the scope of this work. The function is implemented in ISIS (Sect. 2.2.2) using its intrinsic fitting algorithms for the estimation of model parameters and the determination of uncertainties. Given the data structure containing component positions and their uncertainties in each observation epoch, as well as the identification of each epoch, the model with the corresponding set of parameters is created automatically.[9] As linear functions were used to describe the proper motion of the components (more complex functions can be easily implemented), two parameters are available for each component. Firstly the ejection time of the component, i.e., the time at which the component was located in the center, and secondly the velocity of the component. In addition to the two parameters per component, two parameters for each epoch have been implemented allowing for shifts of the image. If the position angle of the jet is specified, the parametrization of the shifts is such that one parameter describes shifts along the jet axis and the other one orthogonal shifts. As the components are mainly located on the jet axis, there is only one free parameter required per epoch accounting for the shifts along

[9] This function, which is called `init_jet_fit`, is available in the `isisscripts` maintained at the Dr. Karl Remeis-Sternwarte.

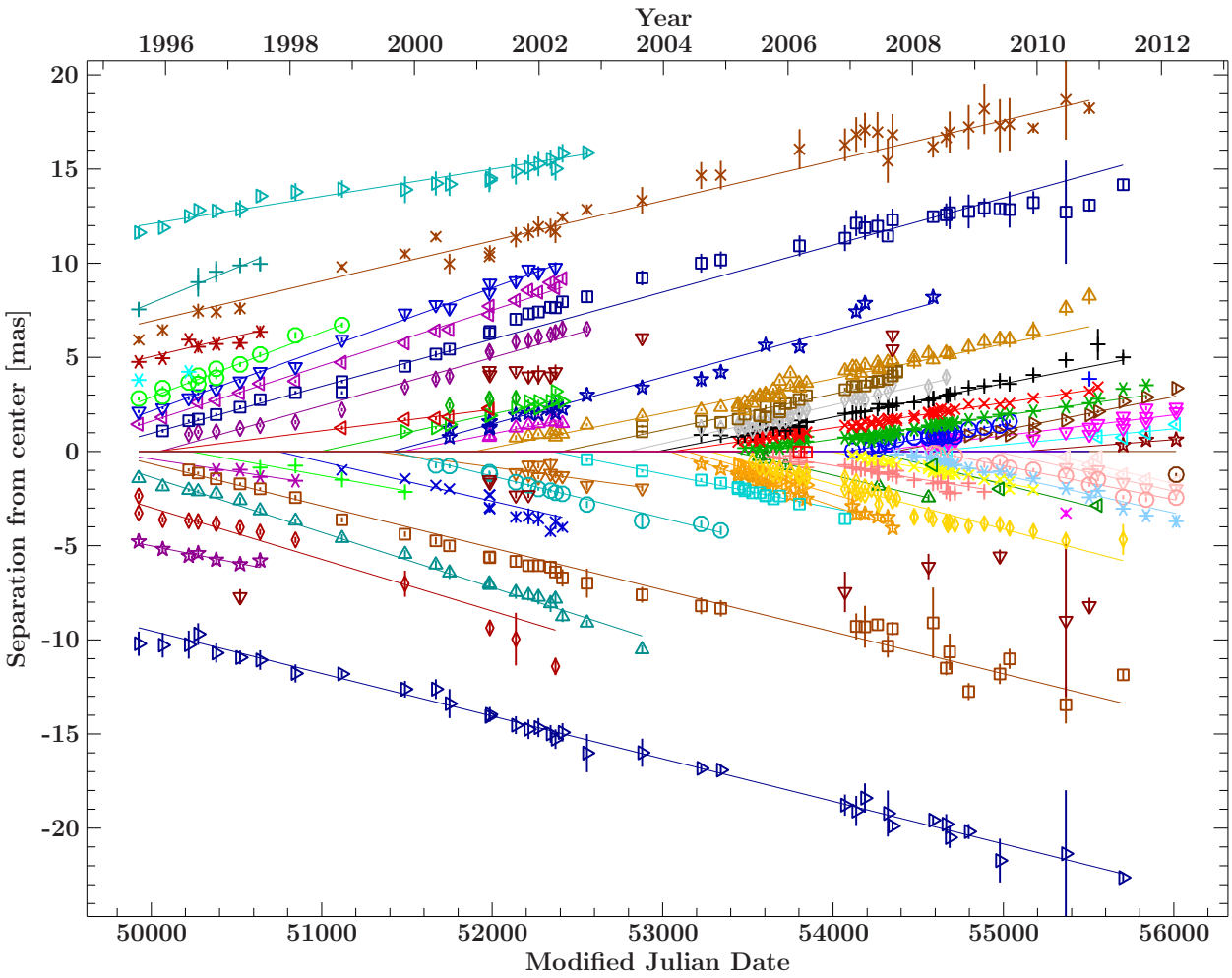

Figure 3.21: Separation of jet components as a function of time. The individual components are characterized by colors and symbols. The shown uncertainties of the separation depend on the width of the model profile and its flux density.

the jet axis.

The average of the determined component velocities is $0.74 \pm 0.06\,\mathrm{mas\,yr^{-1}}$. This value corresponds to a projected velocity of $0.230 \pm 0.011\,c$ and is consistent with that obtained by Vermeulen et al. (2003, who measured $0.78 \pm 0.12\,\mathrm{mas\,yr^{-1}}$). No significant difference between the velocities of the jet ($0.73 \pm 0.06\,\mathrm{mas\,yr^{-1}}$) and the counter-jet ($0.76 \pm 0.04\,\mathrm{mas\,yr^{-1}}$) is found. The given uncertainty is the standard deviation of the mean. The lowest and highest measured component velocities are $0.08\,c$ and $0.42\,c$, respectively.

Component trajectories Given the identification of the components in the jet it is possible to track their movement on the sky. Figure 3.22 shows the projected positions of the components on the sky for all observation epochs. All components are close to the jet axis. In a few cases the position of a component scatters from one observation to the next. This effect becomes stronger with increasing distance of the component from the center. The reason is that the size of the components typically increases and their total flux density decreases as they move away from the center. It is thus more difficult to constrain the central position of the outer components. The uncertainties are comparable to the scattering, thus it is not significant. It is, however, worth noting that the expanded outer features often indicate substructures in the clean images, thus it can be difficult to properly define their center positions. Less scatterings of the positions occur

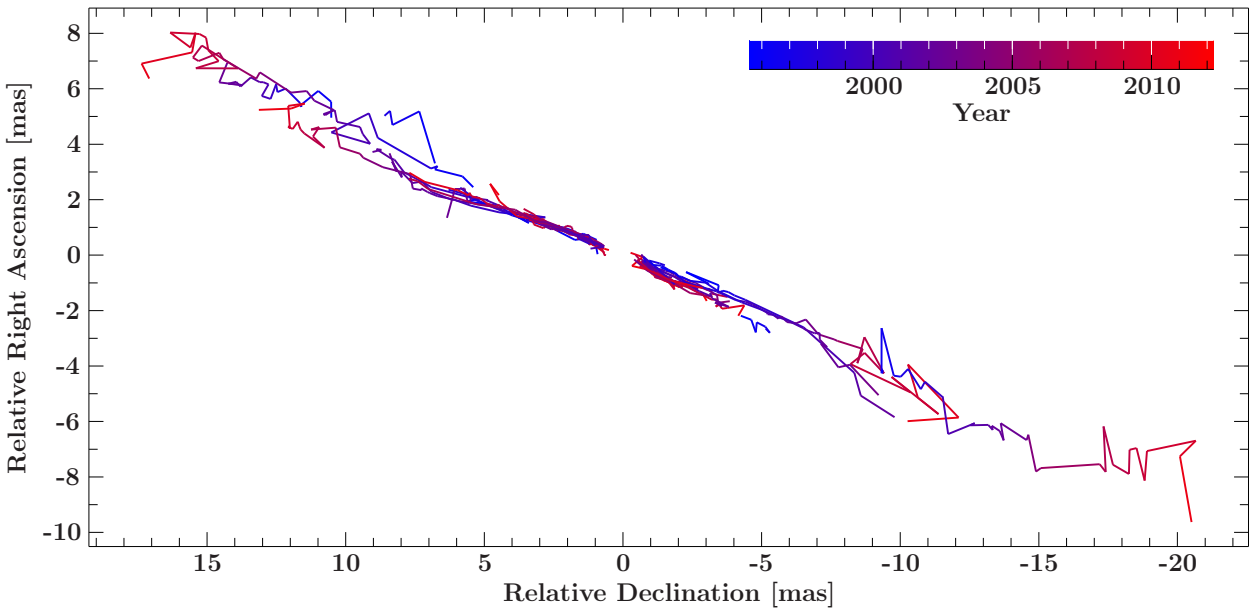

Figure 3.22: Trajectories of the jet components projected on the sky.

closer to the center, where the components are smaller, the approximation of their shape with circular Gaussian profiles works well, and their positions can be determined more precisely. The trajectories of the components in this region are, however, not completely linear either. A few components clearly show curved trajectories. In the western counter-jet, a southward curvature is seen at about −5 mas from the center. Curvature at the same distance is also seen in the eastern jet. There seems to be point symmetry with respect to the center.

Flux evolution of components As already indicated in Fig. 3.20, the flux density of a component decreases with time as it moves downstream the jet. This relation is shown in detail in Fig. 3.23 for all three frequencies. The flux distribution depends strongly on the position in the jet. At 15 GHz the prominent central emission gap is clearly visible, where no components are seen. Components travelling outward become visible and increase in brightness until they reach a maximum about 2 mas away from the center. From then on, the flux density decreases with larger distance from the center. Here, the components are most likely in the optically thin regime. A feature in the flux distribution is indicated in the counter-jet: At a separation of about 2–4 mas from the center, several components show an intensity dip. This angular separation corresponds to a projected distance from the nucleus of about 0.19–0.38 pc. This finding agrees very well the with free-free absorption in addition to the central synchrotron self absorption. The absorption excess was found by Kadler et al. (2004b), who determined a hydrogen column density of the absorbing material of $\sim 2.2 \times 10^{22}\,\mathrm{cm}^{-2}$ based on multi-frequency VLBI observations. They interpreted it as a clear sign of *"free-free absorption in a circumnuclear torus"*.

The charactistic profile of the flux distribution as a function of the separation from the center is seen at higher frequencies as well. Intensity is lower at the center, increases outward until a maximum, and decreases again farther out. The frequency bands of 22 GHz and 43 GHz indicate that with increasing frequency emission closer to the center is seen, the intensity maxima are found closer to the center, and fades out at smaller separation such that it is not detectable anymore.

Inclination angle of the jet With the apparent speed of the jet and that of the counter-jet the inclination angle and the intrinsic component velocity can be calculated. The similar speeds indicate that the jet axis is orientated close to the plane of the sky. The apparent jet speeds, β_1

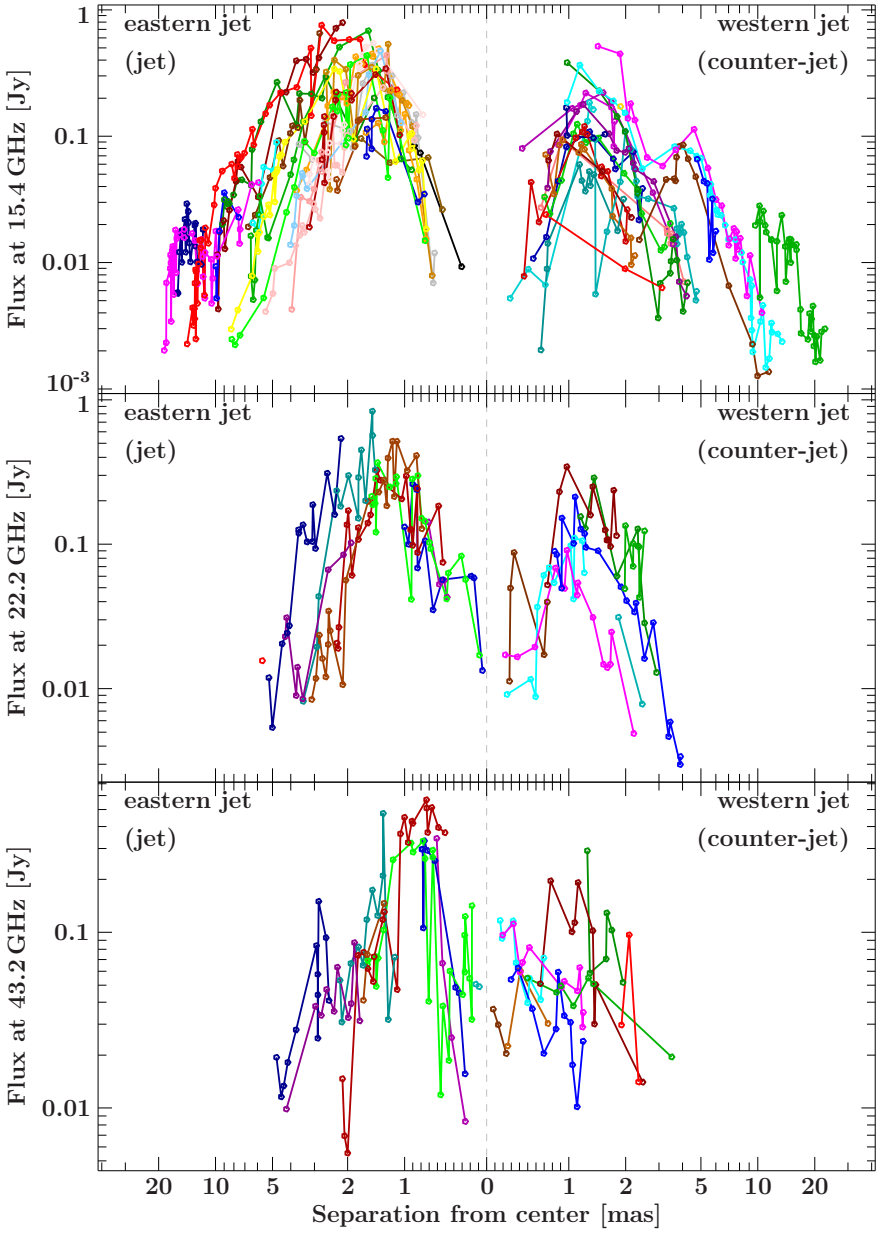

Figure 3.23: Dependence of the components' flux densities at different frequencies on the separation from the center. The three shown frequencies are 15.4 GHz (top), 22.2 GHz (middle), and 43.2 GHz (bottom). To guide the eye, the positions of individual components are chronologically connected with lines. The x-axis is scaled linearly in the central two milliarcseconds and logarithmically at larger distances.

and β_2, of the jet and the counter-jet depend on the intrinsic jet speed β and the inclination angle θ as follows (Eq. 1.10):

$$\beta_1 = \frac{\beta \sin\theta}{1 - \beta\cos\theta} \tag{3.3}$$

$$\beta_2 = \frac{\beta \sin(\pi - \theta)}{1 - \beta\cos(\pi - \theta)} = \frac{\beta \sin\theta}{1 + \beta\cos\theta}. \tag{3.4}$$

Here, a symmetric jet is assumed, i.e., jet and counter-jet and have the same speed, β, and they are pointing in opposite directions. The ratio of both equations yields:

$$\frac{\beta_1}{\beta_2} = \frac{1 + \beta\cos\theta}{1 - \beta\cos\theta} \quad \Rightarrow \quad \beta\cos\theta = 1 - \frac{2\beta_2}{\beta_1 + \beta_2}, \tag{3.5}$$

the product yields:

$$\beta_1\beta_2 = \frac{\beta^2 \sin^2\theta}{1 - \beta^2\cos^2\theta} \quad \Rightarrow \quad \beta^2\cos^2\theta = 1 - \frac{1 - \beta^2}{1 - \beta_1\beta_2}. \tag{3.6}$$

By combining both equations, β and θ can be calculated:

$$\beta = \sqrt{1 - \frac{4\beta_1\beta_2\left(1-\beta_1\beta_2\right)}{\left(\beta_1+\beta_2\right)^2}} = \frac{\sqrt{(\beta_1-\beta_2)^2+4\beta_1^2\beta_2^2}}{\beta_1+\beta_2} \tag{3.7}$$

$$\cos\theta = \sqrt{\frac{\left(\beta_1-\beta_2\right)^2}{\beta_1^2-2\beta_1\beta_2+\beta_2^2+4\beta_1^2\beta_2^2}} = \frac{|\beta_1-\beta_2|}{\sqrt{(\beta_1-\beta_2)^2+4\beta_1^2\beta_2^2}} \tag{3.8}$$

With the obtained apparent jet speed of NGC 1052, the intrinsic speed and the inclination angle are given. The similar, mildly relativistic velocities of jet and counter-jet indicates that both are orientated close to the plane of the sky. Following the approach of Vermeulen et al. (2003), a lower limit on the inclination angle can be obtained. In their work, a velocity for all components (jet and counter-jet) of $0.78 \pm 12\,\mathrm{mas\,yr^{-1}}$ has been obtained. Using the 1σ-uncertainty, they determined $\theta \geq 57°$ from a maximal velocity of the jet ($0.90\,\mathrm{mas\,yr^{-1}}$) and a minimal velocity of the counter-jet ($0.66\,\mathrm{mas\,yr^{-1}}$). Due to the smaller uncertainties of the velocities determined here, the inclination angle of the jet can be constrained better. The values $\beta_{\mathrm{app,max,j}} = 0.245$ and $\beta_{\mathrm{app,min,cj}} = 0.223$ yield $\theta \geq 78.8°$, with a corresponding $\beta = 0.238$.

Considering only the distribution of component velocities, it is not possible to differentiate between jet and counter-jet in the case of NGC 1052. The natural identification of the eastern jet as the approaching jet and the western jet as the receding jet, which is commonly used, is based on their brightness. Using the ratio between the brightness temperatures of individual components (in a single observation epoch, including different frequencies), Kadler et al. (2004b) obtained an upper limit on the inclination of $\sim 72°$. Assuming that the intrinsic brightness of the jet and the counter-jet are identical, Doppler boosting can be considered to further constrain the inclination angle from the intensity ratio of jet and counter-jet. The influence of the Doppler factor, D (Eq. 1.16), on the observed luminosity is given by:

$$L_{\mathrm{obs}} = L_{\mathrm{intrinsic}} D^{3-\alpha}, \tag{3.9}$$

where α is the spectral index ($S_\nu \propto \nu^\alpha$) of the component. A limit on the inclination can be obtained from the ratio of the brightness of the jet (j) and the counter-jet (cj):

$$\frac{L_{\mathrm{j}}}{L_{\mathrm{cj}}} = \left(\frac{D_{\mathrm{j}}}{D_{\mathrm{cj}}}\right)^{3-\alpha} = \left(\frac{1+\beta\cos\theta}{1-\beta\cos\theta}\right)^{3-\alpha} \tag{3.10}$$

$$\Rightarrow \beta\cos\theta = 1 - \frac{2}{1+(L_{\mathrm{j}}/L_{\mathrm{cj}})^{1/(3-\alpha)}} \tag{3.11}$$

The easiest way to obtain the brightness ratio between jet and counter-jet is to use the mean values of all components. At all three frequencies the ratio of the mean component brightness between jet and counter-jet is in the range of 2.00 to 2.15. Due to large number of epochs and components, problems, such as the change of the mean value by splitting one component into two, are expected to cancel out. More complicated methods, e.g., mean or median values of quantiles and the consideration of certain distances only, yield typical values of 2–3. The most conservative upper limit on θ is thus given by substituting $L_{\mathrm{j}}/L_{\mathrm{cj}} = 2$ and $\beta = 1$ in Eq. 3.11. The obtained result is $\theta \leq 85°$. From the analysis of the jet speeds it is, however, obvious that $\beta \lesssim 0.25$. Using this value in Eq. 3.11 yields $\theta \leq 70°$, which contradicts the result of the kinematic study $\theta \geq 78.8°$. The discrepancy is further increased when a larger brightness ratio between jet and counter-jet is used. This result can be interpreted in the following ways. On the one hand the obtained limits on the inclination angle could be wrong. However, the large number of components and epochs, and the consistently modeled speeds of numerous jet components at different frequencies do not indicate an error in the analysis. On the other hand, if the result is correct, physical explanations are required. One possibility is that the seen brightness ratio between jet and counter-jet is influenced

by free-free absorption, which falsifies the true ratio. Additionally, one or more of the assumptions used to obtain these results might be wrong, e.g., the intrinsic luminosity or the speed in the jet and counter-jet might be different. Furthermore, this result could be an indication for multiple velocities in a jet. In this case, the mildly relativistic velocity of the jet components (bulk velocity or propagating shocks) is smaller than that of the radiating relativistic particles. The upper limit $\theta \leq 85°$ for $\beta \approx 1$ is consistent with the lower limit obtained in the kinematic analysis ($\theta \geq 78.8°$).

3.5 Combined X-ray Radio Analysis

For a comparison of the radio and X-ray properties of NGC 1052, light curves in both energy regimes are shown in Fig. 3.24. The X-ray variability in the energy range 2–10 keV has been obtained from the available observations with different instruments, as described in Sect. 3.3. The temporal evolution of the radio flux density at different frequencies is studied based on the single-dish observations (Sect. 3.4.2). In addition, the total flux density of the VLBI observations is shown in Fig. 3.24. For this purpose the flux density of all model components are summed in each VLBI observation. As the emission regions might be different in the X-ray and the radio regime, both light curves cannot be understood as a simultaneous observation of the underlying processes. Assuming that the X-ray emission is dominated from the contribution originating close to the supermassive black hole, significant time delays between emission in both energy bands can be expected. Considering the average component speed of 0.74 mas/yr (Sect. 3.4.3) and the typical flux density evolution of a component as function of the separation from the center, these time delays can be estimated. At the constant velocity of 0.74 mas/yr it takes about one year from the ejection of a component at the nuclues until it becomes visible at 15 GHz and about 2–3 years to reach the maximal observed flux density (at a separation of about 2 mas). In order to obtain information on the jet close to the nuclues, the ejection times of the components were determined as discussed in the previous section. The obtained ejection times are shown in the third panel of Fig. 3.24, where the probability distribution for an ejection is shown. For each component, this distribution is a normal distribution centered at the ejection time obtained from the fit with a width corresponding to the uncertainty. In this way, however, all components are weighted equally, which is not very helpful for a direct comparison with the X-ray variability. In order to characterize the intensity of the ejection, the characteristic flux evolution as a function of the separation from the center (Fig. 3.23) is used. With this characteristic profile, the brightness of a component at a given separation from the center can be scaled. In this way the ejected radio flux of different components seen at different separations can be normalized with respect to each other allowing for a comparison. As individual components are observed over several epochs and radii, their scaled flux can be averaged. The ejection times of each component scaled with their corresponding flux determined in this way is shown in the bottom panel of Fig. 3.24.

Given the number of ejection events and the typical time scales of radio variability, comparisions of X-ray properties and the ejection of jet features are best possible in the time interval that is covered with the dense *RXTE* monitoring. In this period NGC 1052 showed strong variability in the 2–10 keV band with a flux of $(3–10) \times 10^{-12}\,\mathrm{erg\,s^{-1}\,cm^{-2}}$. Flares and dips in the X-ray light curves on time scales of weeks and months show nearby ejection events. Because of the uncertainties of the ejections, it is in most cases not clear if the ejection is correlated with the dip or the flare, or if the complete dip-flare pattern is typical for the ejection. One of the most prominent events is the strong radio ejection at the beginning of the *RXTE* monitoring. At this time, the X-ray flux is relatively low and from then on an increasing trend occurs for almost two years. Close to the maximum, where the intensity scatters, new ejections occur again. As described in the beginning of Sect. 3, the connection of X-ray dips and flares with ejection events in the radio jet can be, e.g., interpreted as the ejection of parts of a hot corona.

During the period of low X-ray intensity in the beginning of the X-ray monitoring, increased

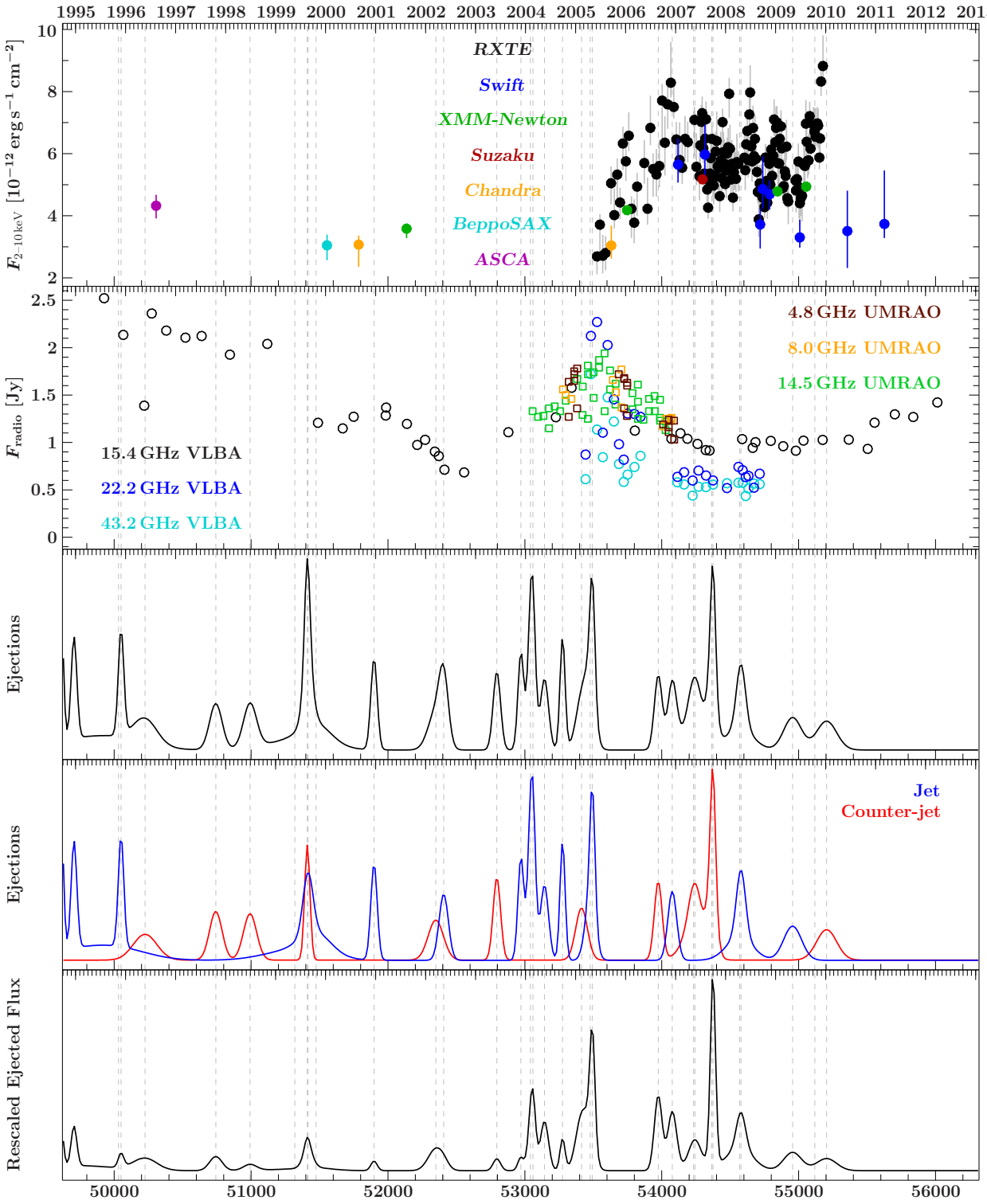

Figure 3.24: Light curves and ejection times of features in the radio jet. The top panel shows the light curve of the NGC 1052 in the 2–10 keV X-ray band (more information is provided in Sect. 3.3, see also Fig. 3.13). Radio light curves at different frequencies are shown in the second panel. The third panel indicates ejection epochs as determined from the kinematic fitting (Sect. 3.4.3), below jet and counter-jet ejections are separated. Each ejection is represented by a normal distribution characterizing the temporal uncertainty. In the bottom panel the ejections are weighted with the corresponding flux density (see text). The best fit ejection times of the components are indicated with vertical dashed lines.

radio brightness is seen in the long-term radio light curve in the second panel of Fig. 3.24. The 43.2 GHz and 22.2 GHz light curves peak after the ejection event, while an increasing trend is seen already before the ejection at 15.4 GHz. The most likely explanation for this finding is that the earlier brightening at 15.4 GHz is related to the previous ejection event.

Features seen in the radio light curves obtained within the F-GAMMA program can be tentatively associated with the ejection events. The above mentioned ejection in the beginning of the X-ray monitoring is not covered by the F-GAMMA light curves shown in Fig. 3.16, but the radio light curves at low and medium frequencies show a rising brightness trend starting in the end of 2007, which includes four peaks around the end of 2008 and in the beginnings of 2010, 2011, and 2012. Considering the time delay from the ejection time to the intensity brightening and peaking at these frequencies due to opacity effects, the seen peaks are related to the ejection events in the years before.

Another observation, which is worth noting, is a hard X-ray flare seen with *Swift*/BAT in spring 2008 (Fig. 3.13). Consistent with this time a radio ejection event is seen. However, this finding has to be handled with care as the *Swift*/BAT light curve shows scattering and NGC 1052 seems to be close to the detection limit. Additionally, no other hard X-ray flares are seen that might be correlated with ejections. For a firm discussion of this event, ascertained ejection times and more information on the *Swift*/BAT light curve are required, e.g., about the temporal coverage of the source and the uncertainties.

Chapter 4

Radio VLBI Monitoring Campaigns

For a more complete understanding of AGN, the consideration of large samples of sources is crucial in addition to studies of individual sources. In this chapter a general introduction to the TANAMI and MOJAVE programs is given. Goals of the programs and used methods are described. Additionally, contributitions to these programs, which were part of this work, are discussed.

4.1 TANAMI Program

The Tracking Active Galactic Nuclei with Austral Milliarcsecond Interferometry (TANAMI) program is a radio VLBI monitoring program of AGN in the Southern Hemisphere. Only sources with a declination below -30 degrees are included in the sample. Two different frequencies are used for the observations, namely 8.4 GHz and 22 GHz. TANAMI started in 2007. One of the main goals of the program is to gain information about the connection between γ-ray emission and radio jet properties of AGN. A central issue of this work was the γ-ray analysis of these sources (Sect. 5.5), but additionally detailed information on the sample selection and the radio properties are required. The description of the TANAMI sample and results of the first radio epochs are presented in this section following Ojha et al. (2010).

The goals of the TANAMI program are discussed in Sect. 4.1.1. Information on the sample selection are given in Sect. 4.1.2, the standard object classification scheme is described in Sect. 4.1.3, and the observations and the used facilities are presented in Sect. 4.1.4. The brightness temperature is introduced in Sect. 4.1.5. Scripts, which were developed within this work, for visualizing VLBI images and spectral index maps are described in Sects. 4.1.6 and 4.1.7, respectively. Contributions to studies of individual sources are the subject of Sect. 4.1.8. Finally, the goal of the TANAMI program to contribute to neutrino astronomy is outlined in Sect. 4.1.9.

4.1.1 Goals of the TANAMI program

Studying jets with simultaneous dual-frequency VLBI monitoring The TANAMI program aims to study a sample of southern AGN using radio VLBI observations at 8.4 GHz and 22 GHz. Radio telescopes in Australia, New Zealand , South Africa, Chile, and Antarctica are used (see Sect. 4.1.4 for more information). The VLBI technique is the only technique to determine, e.g., the morphology of the extragalactic jets on mas-scales, jet inclination, and the collimation angle. Due to the monitoring – observations are performed approximately every two months – temporal information is available in addition. Studying the structural temporal evolution, intrinsic jet properties, such as the jet speed and the Doppler factors, can be determined. As the VLBI observations are performed in two frequency bands, spectral index maps can be obtained. The two-dimensional information allows to calculate spectral indices for individual components in the jet, such as the core and extended features.

The properties discussed above are important for the understanding of the jet physics. There are still several mechanisms and properties of jets which are not completely understood so far, such as the formation, collimation, and propagation of jets, as well as their composition (see Sect. 1.4).

Connection with γ-ray observations One of the central goals for the TANAMI program is to gain information on the connection between jet properties and the high-energy emission in AGN. After the discovery of γ-ray emission from blazars with the EGRET detector (Hartman et al., 1992, see also Sect. 5.1.3), several theoretical models were developed trying to explain the γ-ray emission. As described in Sect. 1.4.3 there are indications that γ-ray emission is connected to the radio emission. For a better understanding of the underlying physics and in order to figure out which models described them best, simultaneous multiwavelength observations are required. In this way possible correlations between flares or spectral changes in different wavebands can be studied. The evolution of broadband spectral energy distributions covering the complete electromagnetic spectrum help to discriminate between different models. VLBI observations are important as they can be used to image the relativistic jets at parsec-scales. Due to the propagation of material and the different emission components in AGN, it is obvious that the total emission does not have to originate from the same region, thus there can be temporal delays between the emission at different wavelengths, which is another reason for the requirement of monitoring observations.

The launch of the *Fermi*/LAT instrument in June 2008 was the main reason for starting the TANAMI program (*Fermi*/LAT is described in detail in Sect. 5.2.2). Since the start of its operation, *Fermi*/LAT monitors the complete γ-ray sky quasi-continuously providing light curves and spectral information for numerous γ-ray sources including hundreds of AGN. The performance of *Fermi*/LAT exceeds that of all previous γ-ray instruments by far (see Sect. 5.2). With the improved sensitivity and broad energy coverage, spectra and their features, such as high-energy cutoffs, can be measured in greater detail, allowing to constrain physical mechanisms, e.g., acceleration mechanisms. For the reasons described above, VLBI monitoring of AGN is a crucial complement for these γ-ray data. TANAMI is the only program with which VLBI observations South of a declination of -30 degrees are possible. It thus completes VLBI monitoring programs covering the northern sky, such as the MOJAVE program including sources north of declination $-20°$. The MOJAVE program is discussed in detail in Sect. 4.2. Due to the previous lack of VLBI monitoring on the Southern Hemisphere, several of the sources in the TANAMI sample have not been imaged with milliarcsecond resolution before. There is, however, a number of TANAMI sources which have been studied extensively with VLBI before (see, e.g., Tingay et al., 1996a; Shen et al., 1997, 1998b; Tingay et al., 2002; Ojha et al., 2004a, 2005; Scott et al., 2004; Horiuchi et al., 2004; Dodson et al., 2008), but typically TANAMI observations provide images with higher resolution and better image quality for these sources, due to the unique array configuration.

In order to determine the required observations intervals for the sources in the TANAMI sample, TANAMI observations have been started already several months before the launch of *Fermi*. The observation intervals depend on the structural changes in the VLBI images from one epoch to the next. In order to determine correct jet kinematics, the sampling has to be high enough to track the components in an unique way. On the other hand an over-sampling has to be avoided, as the available observation time is limited and thus has to distributed carefully over the sample. In each observation epoch only about 25 out of $\sim$80 sources can be observed.

X-ray Monitoring In order to study the broad band spectra of the AGN in the sample, the TANAMI team includes simultaneous X-ray data. These data are complementary to the radio and γ-ray data and constrain the SED. For sources that are well sampled with X-ray observations it is possible to study the multiwavelength variability and study the temporal changes of simultaneous SEDs.

A first step for the broad band analysis is to determine the spectral shape and brightness in the

X-ray regime of each TANAMI AGN. For this purpose a list of the X-ray observations of sources in the sample with current X-ray instruments was collected within this work. The list is shown in Table A.2. Based on the X-ray coverage of the TANAMI sources the TANAMI team planned future observations. On the one hand Swift fill in proposals were used to observe TANAMI AGN, which have not been observed before in the X-ray regime. Some sources are detected in the *ROSAT all-sky survey bright source catalog* (Voges et al., 1999) or the *ROSAT all-sky survey faint source catalog* (Voges et al., 2000).[1] However the spectral information in these catalogs is strongly limited. For the studies of the TANAMI team more recent data is required, as well as better spectral information. The values of the *ROSAT* catalogs were nevertheless very helpful for the estimation of the required observation time, or at least a limit for them. For sources being to faint for *Swift* observations with reasonable exposure, the TANAMI proposed *XMM-Newton* observations, which were approved. Multiwavelength studies by the TANAMI team are in progress (lead be F. Krauss).

Multimessenger astronomy Besides combining the results of the TANAMI dual-frequency observations with γ-ray and X-ray data, other promising studies are possible. For example a combined study with neutrino astronomy is one of the goals of the TANAMI program. AGN jets are possible sources of cosmic neutrinos (Waxman, 2007). As their relativistic flows contain charged particles with a possible fraction of hadrons, γ-rays as well as neutrinos could be produced via pions (see Sect. 4.1.9 for more information). A combined study of AGN with TANAMI and the ANTARES and KM3NeT neutrino telescopes is interesting, because their optimal field of view is the Southern sky. Epochs of high jet activity, such as the ejection of new jet components or flares in the γ-ray regime are promising time periods for the search of correlated neutrino signals.

Public availability Information on the TANAMI program, the sample, and images are available on the TANAMI web page: `http://pulsar.sternwarte.uni-erlangen.de/tanami/`. One of the purposes of the web page is to make TANAMI data available for scientists.

4.1.2 Definition of the TANAMI Sample

The TANAMI sample is an evolving sample. Starting with an initial selection of 44 AGN, additional sources have been added since the start of the operation of *Fermi*/LAT. On the other hand there are sources in the sample which have been observed less frequently or even have even been removed completely from the sample. In this work a set of 75 TANAMI sources has been studied, which will be considered as "the TANAMI sample" throughout this work. The position of these 75 source in the sky are shown in Fig. 4.1 and 4.2, in right ascension and declination and in Galactic coordinates, respectively. As it can be seen in these figures, only sources with a declination below $-30°$ are included in the sample. Further selection criteria of the sample are summarized in the following. More details on the sample are given in Sect. 2 of Ojha et al. (2010).

The initial TANAMI sample is a hybrid sample mainly consisting of radio and γ-ray selected sub-samples.

Radio Selected Sub-Sample TANAMI contains a flux limited radio sample, which is based on the following selection criteria: The source has to have a flux density above 2 Jy at 5 GHz in the catalog of Stickel et al. (1994) and a flat or even inverted spectrum in the frequency range from 2.7 GHz to 5 GHz. The exact criterion for the latter is that the spectral index has to be larger than -0.5. In the selected declination range, 21 AGN fulfill these requirements and thus form the the radio selected sub-sample. These sources can be understood as a southern extension of

[1] The *ROSAT* mission was in operation from 1990 until 1999 (a mission overview is, e.g., provided by Trümper, 1982). The instrument was used for an all-sky survey in the 0.1–2.5 keV energy range with good angular resolution.

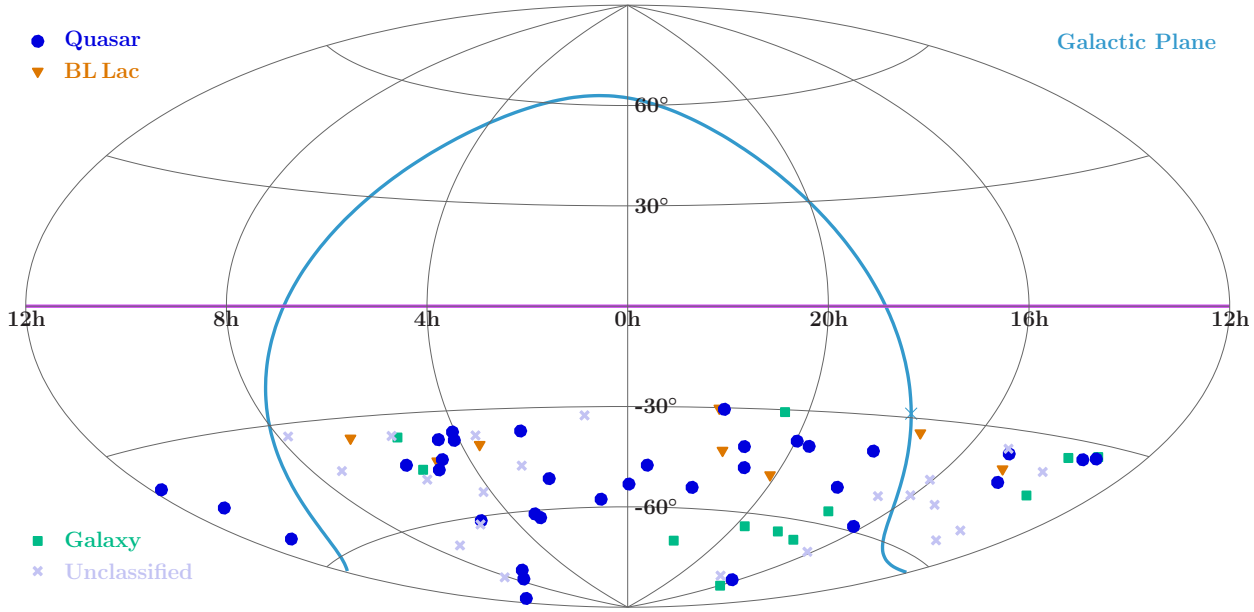

Figure 4.1: Distribution of the TANAMI sources in the sky. Aitoff projection of the sky using right ascension and declination. The blue line marks the Galactic plane and the blue cross the Galactic center.

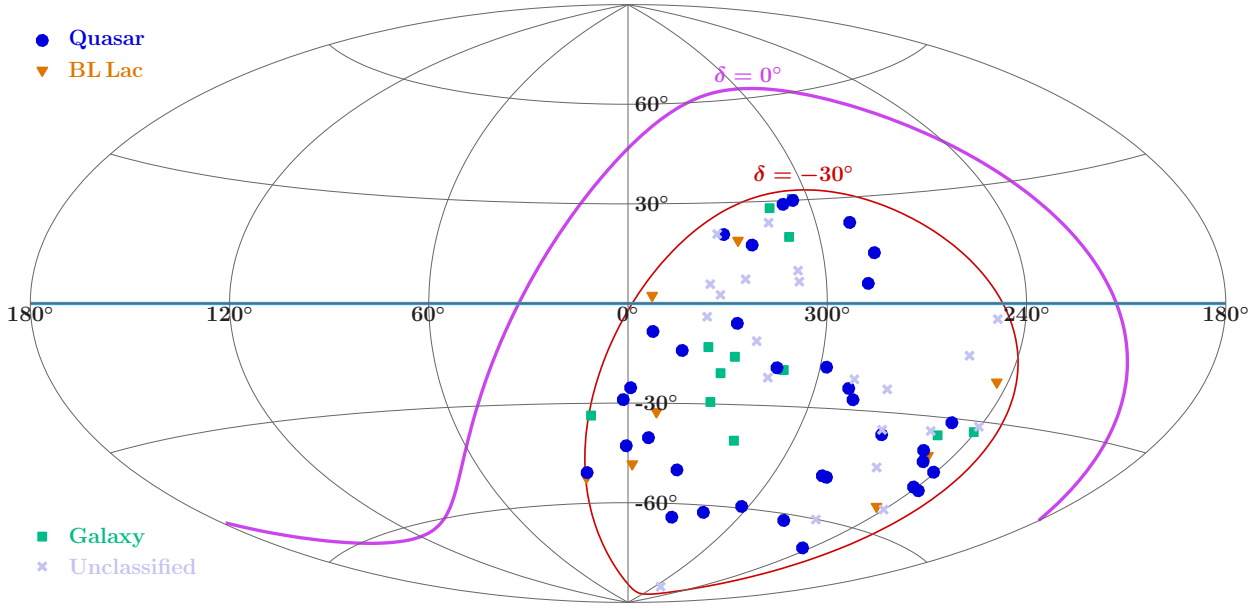

Figure 4.2: Distribution of the TANAMI sources in the sky. Aitoff projection of the sky in Galactic coordinates. The equatorial plane of the Earth (declination 0°) is shown in purple, and the limit declination for the sample of −30° is shown in red.

the MOJAVE 1 sample (Lister et al., 2009a, see also see Sect. 4.2.2 for more information), which follows the same flux-density limit at a frequency of 15 GHz.

Gamma-ray Selected Sub-Sample The γ-ray selected sub-sample includes all AGN (in the required declination range) detected with *CGRO*/EGRET. Besides the high-confidence associations of AGN with EGRET sources, also low-confidence and thus γ-ray sources candidates were selected as TANAMI sources. The associations of EGRET sources are discussed by Hartman et al. (1999),

Tornikoski et al. (2002), Sowards-Emmerd et al. (2004) and Bignall et al. (2008).

Additional Interesting Sources In addition to the radio and γ-ray selected sub-samples a number of further interesting sources, which are promising to be studied within a VLBI monitoring, have been included into the sample. In particular these are 8 sources which have the same radio properties (based on pre-TANAMI observations) than AGN detected with EGRET, but were not picked up in the radio selected part of the sample, as their flux densities were below the flux limit of 2 Jy. Furthermore 4 intra-day variable (IDV; see, e.g., Quirrenbach et al., 2000, and the references therein) sources have been included in the sample (0405−385, 1144−379, 1257−326, and 1323−526). The study of IDV sources is important, as radio variability on such short time scales is either a indication of extreme Doppler boosting or of interstellar scintillation. Finally, Pictor A (0518−458) has been added as an example of a bright nearby radio galaxy (additionally to Cen A, which is included in the γ-ray selected sub-sample), as well as NGC 6328 (1718−649), which is a gigahertz peaked spectrum (GPS) source.

Sources added due to *Fermi*/LAT detection Already during the first months of *Fermi*/LAT operations a significant number of TANAMI sources have been detected with this γ-ray instrument. The first list of bright γ-ray emitting AGN is published by (Abdo et al., 2009b). A detailed discussion of γ-ray properties of the TANAMI sources based on *Fermi*/LAT data is given in Sect. 5.5. Although the TANAMI sample has been selected in a way to include many γ-ray bright sources, there was however a number of sources included in the *Fermi*/LAT bright γ-ray source list (Abdo et al., 2009a), which were possibly AGN in the TANAMI declination range, but which were not included in the TANAMI sample. The radio brightest of these sources have then been included in the sample. Müller et al. (2012) given an overview on AGN included in the sample based on the *Fermi*/LAT detection and present results of first TANAMI radio observations.

75 Source Sample As mentioned above, the "TANAMI sample" studied in this work consist of 75 sources, including all the sources in the initial sample and the ones added due to a *Fermi*/LAT detection. A complete list of these 75 sources is given in Table A.1. The individual sources (of the initial TANAMI sample) are discussed in detail in Sect. A.1.2. This collection of information on the initial TANAMI sample has been contributed to the first epoch TANAMI paper (Ojha et al., 2010).

4.1.3 Object classification

For comparisons of properties between source classes, especially the γ-ray analysis in Sect. 5.5, it is required to use a classification scheme. As detailed classifications are often not unique and there are numerous subclasses, a strongly simplified classification scheme is used, which is mainly based on optical properties. Source in the TANAMI sample are divided in three classes, namely radio galaxies (G), BL Lac objects (B), and quasars (Q). The classifications of the objects in the sample are taken from Véron-Cetty & Véron (2006). As discussed by Böck et al. (2012) a few of these classifications have been modified due to further observations, which indicated other source classes. In the following an overview on these modification and the underlying findings is given. The full list of AGN in the TANAMI sample and the used classifications is shown in Table A.1.

0208−512 In the optical spectrum of 0208−512 Wilkes (1986) find a clear MgII line. Due to its equivalent width of 18 Å the previous BL Lac classification is changed to that of a quasar.

0302−623 According to Healey et al. (2008) the AGN 0302−623 is classified as a quasar. For the BL Lac object 0332−403 another value for the redshift is used. Instead of the redshift of 1.445

published by Hewitt & Burbidge (1987) the value $z = 1.351$ is used. The first value was not firm and doubted. The latter value has been measured by Bergeron et al. (2011) using a single weak line in the optical spectrum. Due to the lack of clear lines in the spectra of this source the redshift determination is difficult, although its optical brightness (∼18 mag). Drinkwater et al. (1997) could not determine a robust redshift for this AGN. The above listed values should be handled with care.

0521−365 The classification of 0521−365 is difficult. There are different properties that indicate it as a BL Lac object as well as a radio galaxy or further subclasses. The host galaxy of this AGN is a giant elliptical galaxy (Lauberts, 1982; Falomo et al., 1994). In the optical spectrum strong emission lines, broad as well as narrow ones, are found (see, e.g., Falomo et al., 1994), including even variable lines (Scarpa et al., 1995). Based on the observations the source is even classified as a Seyfert 1 galaxy (Véron-Cetty & Véron, 2006). In the radio regime this source has a hybrid FR 1 and FR 2 morphology on large scales (Krishna & Wiita, 2000). In the following the galaxy classification if used for this AGN. There are, however, indications for a BL Lac classification, i.e., that the jet is orientated closer to the line of sight on smaller scales. This AGN was detected with EGRET and *Fermi*/LAT.

0625−354 A very good example for a misaligned radio galaxy is the AGN 0625−354. While it has a large scale FR I radio morphology and it has been classified as a LINER (Lewis et al., 2003; Véron-Cetty & Véron, 2006), the optical spectrum of this source yields a BL Lac classification (Wills et al., 2004). The latter classification is strengthened by the γ-ray properties with a hard spectrum and a high luminosity. It is included as one of 5 misaligned radio galaxies in the first catalog of AGN detected by *Fermi*/LAT (Abdo et al., 2010b). The assumption of an inner parsec-scale jet being orientated close to the line of sight is confirmed by the TANAMI VLBI observations, which show a single-sided jet structure with a strong core component. For further studies the BL Lac classification is used in the following.

1057−797 The AGN 1057−797 is classified as a quasar in the following according to by Healey et al. (2007).

1258−321 For the object 1258−321 the classification as a radio galaxy is used, as it is the brightest galaxy in the cluster ACO 3537 (Hudson et al., 2001). This sources has, however, blazar properties as well.

1440−389 Another source with radio galaxy classification (according to Véron-Cetty & Véron, 2006) that is changed to a BL Lac classification (see, e.g., Jackson et al., 2002; Mao, 2011) is 1440−389.

4.1.4 Observations and Data Reduction

Telescopes As the TANAMI program monitors the Southern Sky, obviously southern radio telescopes are required. The core instruments for TANAMI observations are located in Australia. The Australian Long Baseline Array (LBA; see, e.g., Ojha et al., 2004b, for more information) is used.[2] The LBA includes telescopes of the Australia Telescope National Facility (ATNF), which are the 64-meter Parkes radio telescope, the 22-meter Mopra telescope and the Australia Telescope Compact Array (ATCA). ATCA is an array of six radio telescopes. Each of these radio antennas has a diameter of 22 m. One of the six telescopes is not equipped for high-frequency observations. Besides the ATNF telescopes, the LBA uses two radio telescopes operated by the University of

[2]Further information on the LBA can be found, e.g., on the LBA wiki pages http://www.atnf.csiro.au/vlbi/wiki/

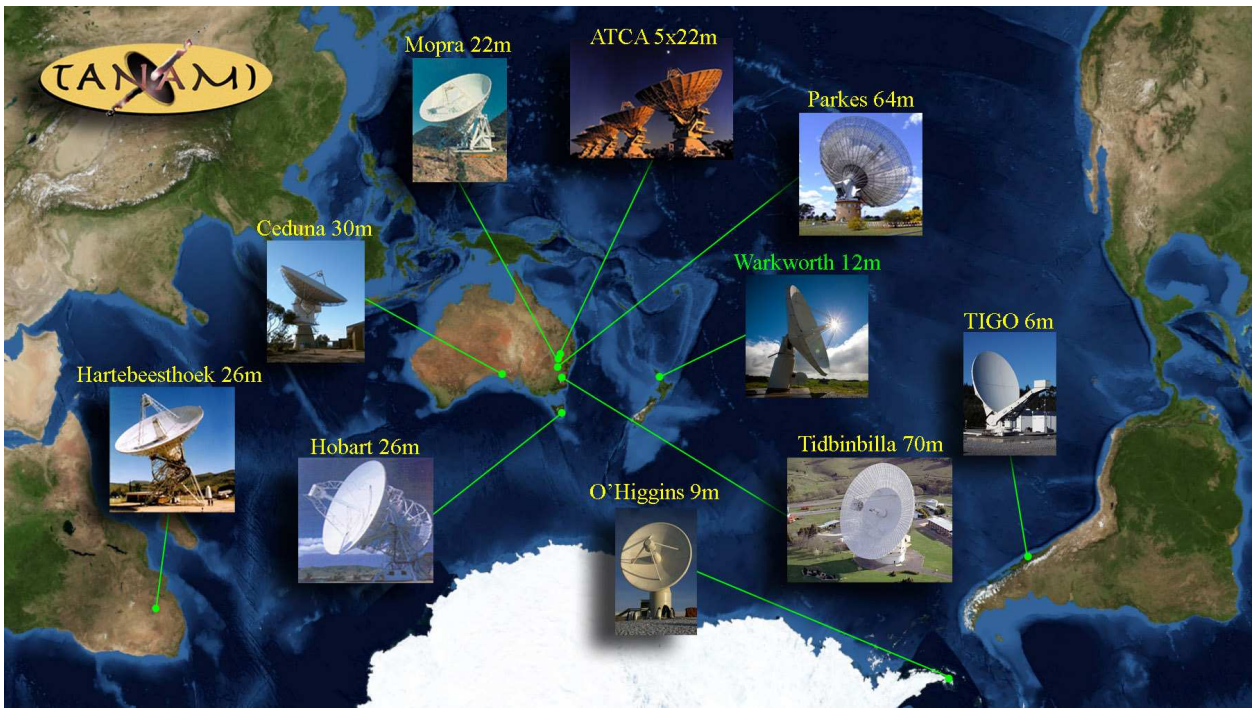

Figure 4.3: Telescopes used for TANAMI observations. An image of the radio telescopes and their antenna diameter is shown. The position of the telescopes are indicated on the projection of the Earth centered around Australia. (Courtesy: TANAMI team, Kadler, Wilms)

Tasmania: The Hobart and Ceduna antennas. The diameter of these antennas is 26 m and 30 m, respectively.

In addition, the Tidbinbilla 70 m and 34 m radio telescopes NASA's Deep Space Network can be accessed frequently. The usage of these telescopes improves the *uv*-coverage and the sensitivity of TANAMI observations.

Intercontinental baselines with the Australian telescopes have been provided by the usage of the 26 m telescope in Hartebeesthoek in South Africa. Unfortunately a major failure with the polar shaft bearing of the telescope occurred in October 2008. Since then the telescope could not be used for observations anymore until 2011.

The loss of long baselines could be partially compensated with including two smaller radio telescopes. Access to these telescopes, which are operated by the Bundesamt für Kartographie and Gedäsie (BKG[3]), became available due to a successful International VLBI Service (IVS) proposal. Although both telescope are significantly smaller than the one in Hartebeesthoek, they provide very good resolution for TANAMI observations due to their location. The 9 m telescope O'Higgins is located in Antarctica and the 6 m telescope TIGO (Transportable Integrated Geodetic Observatory) is located in Chile.

Since 2011 the 12 m Warkworth VLBI station (WARK12M) in New Zealand is ready for observations (Gulyaev et al., 2011). It is operated by the Auckland University of Technology.

An overview on all the telescopes used for TANAMI observations is given in Table 4.1 and their locations are shown in Fig. 4.3. The array configuration can vary with the observation epochs due to availability.

Data Analysis The TANAMI data analysis procedure is described in detail by Ojha et al. (2010). Following this publication of the TANAMI team an overview on the data analysis is given in the

[3]The BKG is the German federal agency for cartography and geodesy.

Table 4.1: Size and location of radio telescopes used for TANAMI observations. With O'Higgins and TIGO no 22 GHz observations are possible.

Telescope	Diameter [meter]	Location
Parkes	64	Parkes, Australia (New South Wales)
ATCA	6×22	Narrabri, Australia (New South Wales)
Mopra	22	Coonabarabran, Australia (New South Wales)
Hobart	26	Mt. Pleasant, Australia (Tasmania)
Ceduna	30	Ceduna, Australia (South Australia)
DSS43	70	Tidbinbilla, Australia (ACT)
DSS45	34	Tidbinbilla, Australia (ACT)
Hartebeesthoek	26	Hartebeesthoek, South Africa
O'Higgins	9	O'Higgins, Antarctica
TIGO	6	Concepcion, Chile
WARK12M	12	Warkworth, New Zealand

following. Using the telescope array described above each source in an observation epoch is observed in several scans for about 10 minutes per scan. The typical number of scans per source is 6. The data are recorded on disks. Afterwards the data are correlated the DiFX software correlator (Deller et al., 2007) at Swinburne University and since November 2008 at Curtin University.

After correlation the data have been loaded into *AIPS*. Using *AIPS* the data are calibrated and processed in the standard manner. Observations of known compact sources are used for the amplitude calibration. The compact sources (sources with a low flux contribution of extended emission) are fitted with a Gaussian component in order to obtain gain corrections for each telescope. Ojha et al. (2010) conservatively estimate the "accuracy of the absolute amplitude calibration [...] to be 20%".

The final imaging of TANAMI sources is done with the program DIFMAP (Shepherd, 1997). In this procedure the data were averaged into 30 second bins. As described by Ojha et al. (2010) the data were imaged using the standard CLEAN algorithm (Sect. 2.1.3), and iteratively decreasing self-calibration intervals. Images are usually created using natural weighting providing the best image sensitivity. In order to study diffuse large scale emission better, often tapers are used to give less weight to the long baselines.

Typical Observation Properties In the TANAMI program two observing frequencies are used: 8.4 GHz and 22 GHz. The X-band (8.4 GHz) has been chosen as a TANAMI observation frequency, as it is high enough to provide high-resolution images of the inner jet structure and it is low enough to detect diffuse emission of extended structures, which usually have steep spectra. With observations at the K-band (22 GHz) jet emission closer to the core can be observed (see, e.g., Tingay et al., 2003, for more information on observations using 22 GHz). Of course, the chosen frequencies depend also on the used instruments and their receivers. For example the O'Higgins and TIGO telescopes cannot be used for observations at 22 GHz. With the telescope array used for TANAMI observations. the typical obtained angular resolution is in the range of 1.5–4 mas in north-east and 0.5–1.0 mas in east-west direction at 8.4 GHz.

The dual-frequency observations of the TANAMI program provide spectral information on the sources. Two-dimensional spectral index maps with mas resolution can be obtained (Sect. 4.1.7).

4.1.5 Brightness Temperature

In order to determine the brightness temperature of a component, the flux density associated with the component and its angular size is required. A typical method, which has been also used by the TANAMI team to determine the brightness temperatures of the core component, is to model the component with a two-dimensional Gaussian profile. As discussed by Kovalev et al. (2005), the brightness temperature of a component is then given by:

$$T_B = \frac{2\ln 2}{\pi k_{\mathrm{B}}} \frac{S\lambda^2(1+z)}{\theta_{\mathrm{maj}}\theta_{\mathrm{min}}} \tag{4.1}$$

where S is the flux density of the component and θ_{maj} and θ_{min} are the major and minor axis of the Gaussian model, respectively, λ is the observing frequency, z the source's redshift and k_{B} is the Boltzmann constant.

For several studies, especially for a comparison with γ-ray properties, the brightness temperature of the radio core is important. Values of the core brightness temperatures of TANAMI sources are presented, e.g., by Ojha et al. (2010) and Böck et al. (2012). In order to determine the brightness temperature of the core, the core component has to be identified. For the identification the TANAMI uses mainly the morphology of the map and the flux distribution. In all cases the core was identified as the brightest component in the map, which is either located at the end of single-sided jets, or in the case of two-sided jets, it is centered in the double-sided jet structure. Using DIFMAP an elliptical Gaussian component is fitted to this component after removing the clean components in the corresponding region and the brightness temperature calculated as described above.

As it is immediately visible in Eq. 4.1, the calculated brightness temperature diverges if the corresponding component is unresolved, and thus one of the axis of the two-dimensional Gaussian profile approaches 0. In such cases it is more reasonable to determine a lower limit on the brightness temperature using the theoretical resolution limit of the observation. According to Kovalev et al. (2005, see Eq. 2) the resolution limit of a component depends on its signal-to-noise radio and the beam size of the observation. For an elliptical beam the resolution limit is calculated using the geometric mean of the minor and major axis of the beam. Component sizes falling below this resolution limit are considered as unresolved. A lower limit of their brightness temperature is then obtained by using the resolution limit instead of the fitted size for the calculation.

It is, however, necessary to note that due to the limited resolution of VLBI observations unresolved substructures in the "core" might contribute to the observed emission. Depending on the true flux distribution in the corresponding region, the calculated brightness temperature is averaged over that region. Depending on the distance and the orientation of the source, additional flux can be added in the given region and the measured brightness temperature could thus overestimate that of the "true core" of the jet.

There is a number of theoretical limits on the brightness temperature. Readhead (1994) discuss an equipartion limit of 10^{11} K. An inverse Compton limit of 10^{12} K is described by Kellermann & Pauliny-Toth (1969). Values exceeding this limit can be caused by Doppler boosting, which can strongly increase the observed flux density. It is possible as well to exceed these limits by considering non-standard mechanisms beyond the assumptions used in the calculation of the limits. Possible examples are, e.g., a large proton fraction in the jet, coherent emission, and complex geometries (Kellermann et al., 2004).

4.1.6 VLBI Images

To illustrate the jet images resulting from the fitting algorithm described above a routine was developed. The aim was to obtain a reasonable color scaling and color scheme. The difficulties for the scale is that on the hand the core of the jet is in general orders of magnitudes brighter than

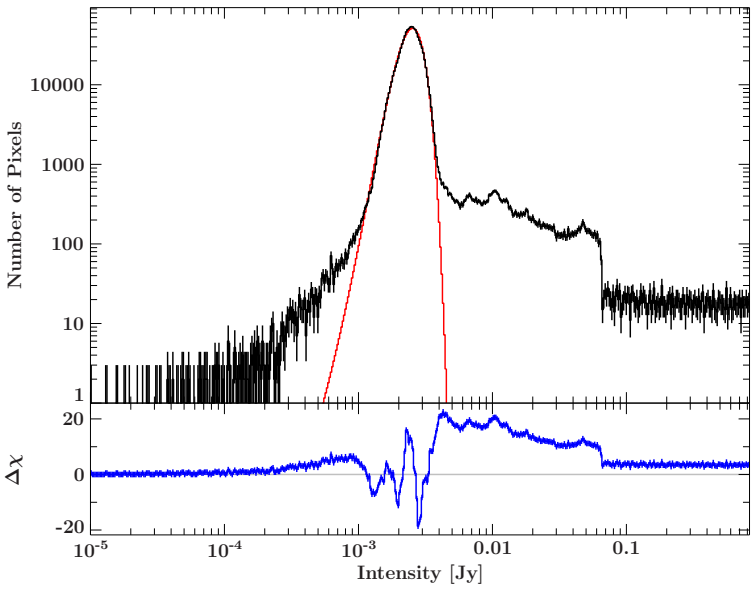

Figure 4.4: Intensity distribution of the pixels in a VLBI map. The noise distribution in the image is model with a Gaussian profile. (The intensity values are shifted such that the minimum is 10^{-5} Jy. This procedure is used for fitting on a logarithmic grid and is inverted afterward).

the emission of weaker components in the jet, thus a linear color scaling cannot be applied. On the other hand the noise in the image, which usually has weak structures due to the image creation process, a logarithmic color scaling is inappropriate as it highlights the noise structure is too much. For the color images the illustration of significant jet components is important. The brightness of these structures is only slightly above the noise level, thus the noise level has to be considered for the scaling. But the core of the jet, which usually dominates the flux density in the map, shall be color scaled as well and not saturated. The brightness of the core and the noise level can depend strongly on the source and the observation. In addition, the last step of the cleaning algorithm to compensate the small statistic effects yields small negative flux values below the noise level.

In order to obtain a useful scaling of the VLBI map for a colored image the applied process will be described here. At first a histogram of the distribution of the pixel brightnesses was created (Fig. 4.4). The histogram clearly shows the main components in the image. The main contribution to the pixel brightness distribution is the noise, which can be modeled with a Gaussian profile. Above the noise level the extended emission or the emission of weak jet components starts. There are only a few very bright pixels which correspond to the core of the jet. To obtain the noise level and its width, a Gaussian profile is fitted to the pixel distribution, which is dominated by the noise. The uncertainties in the pixel distribution are set to the square root of the value in each bin. The advantage of determining the parameters of the noise with the Gaussian fit is that in doing so, the resulting parameters are less influenced by the bright flux values of the core or the negative flux values caused by the cleaning process, as this would be the case by simply considering the mean value or the median and the standard deviation of the image. An alternative method used by DIFMAP is to calculate the mean value width of the noise by selecting a region in the image which only includes noise, but in this case it would have been necessary to make sure that no jet components are included in the selected region. The residuals of the Gaussian fit to the noise indicate that the noise has no Gaussian distribution, which is probably due to the structure of the noise caused by image creation process in which the model is folded by the beam.

Knowing the noise level and its width, the image can be scaled such that a linear color scheme can be applied. For the highlighting of components the color scaling starts at 3σ above the noise level, as components exceeding these flux values can be considered as "real" (no artifacts due to incomplete *uv*-coverage). Fluctuations with such a brightness are expected only with a probability of 0.27%. In this way jet features with a significance of several σ are clearly visible, whereas fluctuations in the noise can be suppressed or completely ignored. Above 3σ the values in the

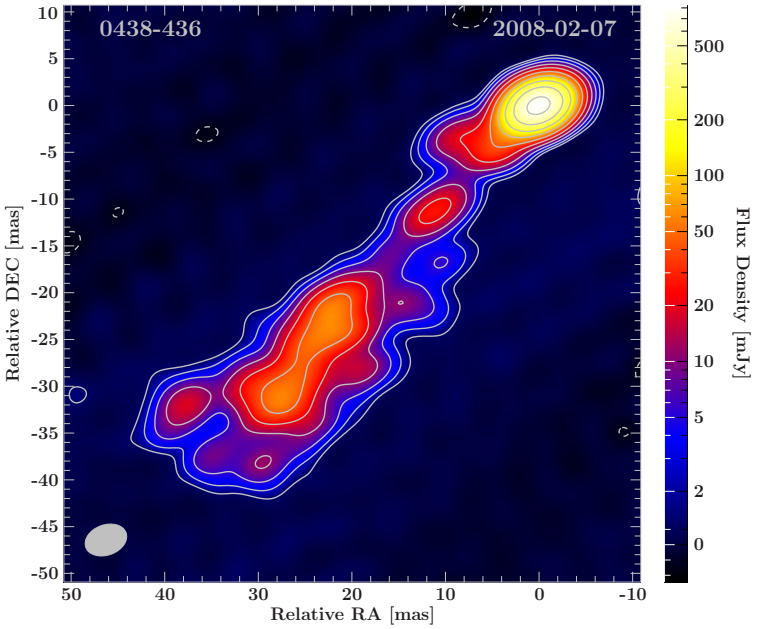

Figure 4.5: Final TANAMI image of PKS 0438−436 at 8.4 GHz. The color-scale represent the intensity distribution on the sky. The lowest contour line is at 3σ above the noise level. The image has been created with the algorithm described in Sect. 4.1.6

image are transformed with the logarithm of the significance:

$$I'_{\mathrm{xy}} = \log\left(\frac{I_{\mathrm{xy}} - \mu}{\sigma}\right) \tag{4.2}$$

where I'_{xy} is the intensity in each pixel and μ the noise level.

An example of a final image is shown in Fig. 4.5. The shown source is the distant quasar PKS 0438-436 (with redshift $z = 2.863$). The corresponding distribution of intensities in each pixel is shown in Fig. 4.4. Figure 4.5 is, however, clipped to a smaller field of view in which source emission is visible. It is better to determine the noise level and the width of the noise in the intensity distribution before clipping the image. The reason is that in this case the number of pixels which show noise is larger and with them dominating the distribution the noise can be modeled better.

4.1.7 Spectral Index Studies

One of the advantages of the TANAMI program are the simultaneous dual-frequency observations at 8.4 GHz and 22 GHz. With the high-resolution images at both frequencies it is possible to create spectral index maps and thus to study the spectral index distribution spatially resolved. Analyses of the 22 GHz TANAMI observations and a discussion of the spectral index maps are in preparation for publication by the TANAMI team. As a major contribution to this project, algorithms for the visualization and creation of spectral index maps were developed within the scope of the current work. The spectral index $\alpha(x, y)$ at each position $(x,\ y)$ can be determined from the intensity at both frequencies assuming a power law flux density:

$$S(x, y; \nu) = C(x, y)\, \nu^{\alpha(x,y)} \tag{4.3}$$

where $C(x, y)$ is the normalization. Given the intensity in both frequencies $S(x, y; \nu_1)$ and $S(x, y; \nu_2)$ the spectral index can be obtained with:

$$\alpha(x, y) = \frac{\ln S(x, y; \nu_2) - \ln S(x, y; \nu_1)}{\ln(\nu_2) - \ln(\nu_1)}. \tag{4.4}$$

The spectral index map can thus be directly obtained from the difference of the logarithms of the images (and normalizing with the frequencies as in Eq. 4.4). For this method a number of

requirements have to be fulfilled. The images have to be aligned, such that the positions (x, y) correspond to the same sky coordinates at each frequency. Technically this also implies that the pixel increment has to be identical in both images, otherwise rebinning is required. As the final images at each frequency are compared, instead of the models, it is necessary that both images have the same angular resolution. Convolving the flux distribution model at each frequency with a different beam obviously induces features in the spectral index map. In general the resolutions in images at two different frequencies are different. On the one hand the resolution depends directly on the frequency as shown in Eq. 2.1. On the other hand different configurations of telescopes may have been used, e.g., for the TANAMI observations not all telescopes are equipped with receivers operating at 22 GHz. Additionally the *uv*-coverage is typically not identical due to the scheduling of the observations.

The standard method used here for obtaining the spectral index map was to obtain images at both frequencies with the same beam, to align them and to calculate the spectral index map.[4]

Enclosing Ellipse In order to obtain a common beam for the images at both frequencies the two individual beams have to be considered. Using a common beam, which is smaller than one of the original beams is difficult, as it would require additional information that is not included in the observation (problem of "over-resolution"). On the other hand it is trivial to select a beam which is large enough to include both beams, e.g., a circle could be used with a radius equal to largest semimajor axis of both beams. In order not to lose information, the common beam should be as small as possible but still large enough to contain both original beams. As the beams are typically approximated with ellipses (characterizing a two-dimensional Gaussian profile), the determination of common beam corresponds to finding the smallest ellipse enclosing two ellipses (which have a common center). This method is explained in the following.

The procedure to obtain the enclosing ellipse, which was introduced in this work, is simply based on linear transformations. It can be shown that the linear transformation of an ellipse yields an ellipse. It is obvious that an ellipse remains an ellipse under rotations and translations. For compressions of ellipses it can be considered that they can be transformed to circles by scaling along an axis of the ellipse, which is a helpful step in combinations of transformations. A mathematical discussion is, e.g., given by Kalman (2008, in the outline of the mathematical background).

As a first step, the parameters of the ellipse resulting from the compression of an initial ellipse are calculated analytically. A general ellipse centered at the origin is given in parameter form:

$$e(a, b, \phi; t) = \begin{pmatrix} a\cos(t)\cos(\phi) - b\sin(t)\sin(\phi) \\ a\cos(t)\sin(\phi) + b\sin(t)\cos(\phi) \end{pmatrix} \tag{4.5}$$

where a is the semimajor axis, b the semiminor axis and ϕ the position angle. Compressing the ellipse in one dimension with a factor x yields an ellipse e':

$$e'(t) = e(t) \begin{pmatrix} 1 & 0 \\ 0 & x \end{pmatrix} \tag{4.6}$$

In order to obtain the new semimajor and semiminor axis, the minima and maxima of the distance

[4] The development of such scripts for spectral index maps was done within a DAAD RISE project (http://www.daad.de/rise/en/). RISE (Research Internships in Science and Engineering) is a program offered by the DAAD ("Deutscher Akademischer Austausch Dienst", the German Academic Exchange Service), in which *undergraduate students from the United States, Canada and the UK* can work *at universities and top research institutions across Germany for a period of 2 to 3 months* (from DAAD RISE description) and are supervised by a local doctoral student. Such a project was proposed within the scope of this work and awarded with funding. In this way, the undergraduate student Sherwood Andrew Richers from the University of Virginia (USA) stayed at the Dr. Karl-Remeis-Observatory for three months in 2010 and contributed to the development of spectral index map scripts.

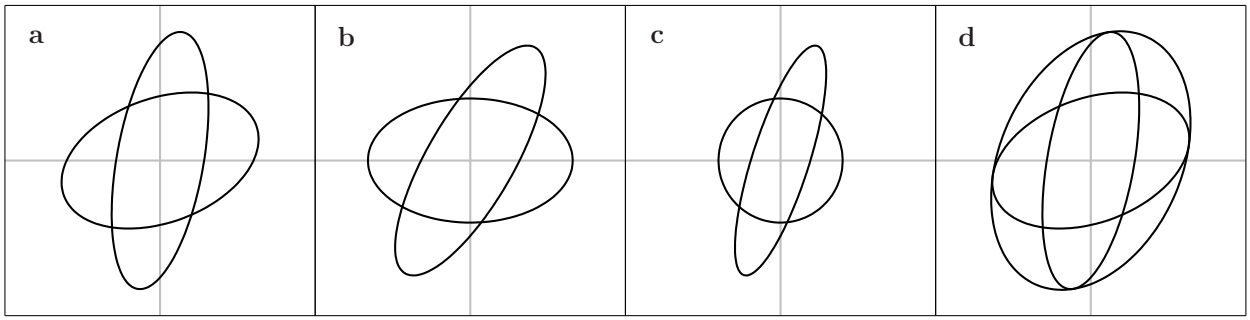

Figure 4.6: Process for finding the ellipse enclosing two ellipses. The two initial ellipses are transformed such that the definition of the enclosing ellipse is trivial. After that the inverse transformations are applied to the result. More information is given in the text.

to the origin of $e'(t)$ can be calculated. For that purpose, $e'^2(t)$ can be used, which is given by

$$\begin{aligned} e'^2(t) =& a^2\cos^2(t)\left(\cos^2(\phi) + x^2\sin^2(\phi)\right) && (4.7)\\ &+ b^2\sin^2(t)\left(x^2\cos^2(\phi) + \sin^2(\phi)\right) && (4.8)\\ &+ 2ab\sin(t)\cos(t)\left(x^2-1\right)\cos(t)\sin(t). && (4.9)\end{aligned}$$

The derivative can be calculated

$$\begin{aligned} \frac{\partial e'^2(t)}{\partial t} =& \sin(2t)\left[-a^2\left(\cos^2(\phi) + x\sin^2(\phi)\right) + b^2\left(x^2\cos^2(\phi) + \sin^2(\phi)\right)\right] && (4.10)\\ &+ \cos(2t)2ab\left(x^2-1\right)\cos(\phi)\sin(\phi) && (4.11)\end{aligned}$$

and the extrema can then be obtained via

$$\begin{aligned} \frac{\partial e'^2(t)}{\partial t} &= 0 && (4.12)\\ \Rightarrow \tan(2t_m) &= \frac{2ab\cos(\phi)\sin(\phi)\left(x^2-1\right)}{a^2\left(\cos^2(\phi) + x^2\sin^2(\phi)\right) - b^2\left(x^2\cos^2(\phi) + \sin^2(\phi)\right)}. && (4.13)\end{aligned}$$

where t_m is the parameter of the ellipse $e'(t)$ yielding the extremum. The semimajor and semiminor axes (a', b') and the position angle ϕ' of the new ellipse $e'(t)$ are then given by:

$$\begin{aligned} a' &= \sqrt{e'^2(t_m)} && (4.14)\\ b' &= \sqrt{e'^2(t_m + \pi/2)} && (4.15)\\ \phi' &= \arctan2\left(e'_y(t_m), e'_x(t_m)\right). && (4.16)\end{aligned}$$

The ellipse E enclosing two arbitrary ellipses e_1 and e_2, which are centered at the origin (Fig. 4.6 a), can be obtained in the following way. A trivial case occurs if the semimajor axis of one ellipse is smaller than the semiminor axis of the other ellipse, as then the enclosing ellipse is equal to the large one. In the non-trivial case, a sequence of transformations is applied on the ellipses in the same . Both ellipses are first rotated by the negative position angle of the ellipse with the smaller semimajor axis (it is assumed that $a_1 \leq a_2$). It is then orientated with its major and minor axes along the coordinate axes (Fig. 4.6 b). The next step is to compress this ellipse by the ratio of the semimajor and semiminor axis along the coordinate axis, such that it becomes a circle (Fig. 4.6 c). The situation is now a circle and an ellipse both centered at the origin. In this case the enclosing ellipse has the same position angle as the remaining ellipse and the same semimajor axis. Its semiminor axis is given by the radius of the circle, or the semiminor axis of the

remaining ellipse if it is larger. From this transformed system, in which the enclosing ellipse E' is obvious, the enclosing ellipse in the original system can then be obtained by applying the inverse transformations on E'.

Given the common beam for the observations, the images at each frequency can be created with this beam. The next step is to align the images.

Image alignment While relative distances in VLBI images can be measured with high precision, the accuracy of absolute positions is lower. Due to the usage of self-calibration, the absolute phase and thus the absolute position of the VLBI image is lost. Unless phase reference observations are used, where the phase in the interferometry observation is obtained relative to a reference source, there might be significant positional shifts included in the images (see, e.g., Thompson et al., 2001, and the references therein for information on VLBI phase referencing observations). In order to obtain a correct spectral index map, it is necessary that the images at both frequencies are properly aligned. For TANAMI observations typically no phase reference observations are available, as alternate observations between the target and the nearby reference calibrator are needed for this technique. Typical periods of switching are on timescales of minutes, in order to be able to account for atmospheric effects (e.g., Ros et al., 1999); the timescales depend on the observing frequency. This procedure is not possible for a monitoring program, as it is difficult to observe a large number of sources during the observation run with a good coverage. Phase referencing observations would strongly increase the observation time and make the scheduling more difficult. For that reason other methods are required for aligning the TANAMI images. A simple solution is a cross-correlation of the images. Calculating a cross-correlation coefficient map yields the shift between two images leading to best agreement. Typically the strongest feature in the VLBI images of AGN is the radio core, which dominates the emission. For that reason, a standard cross-corrlation mainly aligns the radio cores at both frequencies. That is, however, a problem as well, as typically frequency-dependent core shifts are expected in radio images of jets (see, e.g., Sokolovsky et al., 2011, and the references therein). The reason is the self-absorption in a steady jet. At higher frequencies the core is therefore visible closer to the central engine. If more components are visible in the jet, it is possible to align the images according to the optically thin components. An objective possibility for this alignment is to exclude the core region in both images for the cross-correlation.[5]

Visualization Using the aligned images which were created with the same beams the spectral index maps can be calculated according to Eq. 4.4. A selection of exemplary spectral index maps of TANAMI AGN is shown in Fig. 4.7. The shown examples include PKS 0047−579, which is a quasar with a single-sided radio jet, and the BL Lac object PKS 0332−403, where only a compact core is visible in the radio images at both frequencies. In addition the spectral index map of the nearby radio galaxy PKS 1322−428 (Cen A) is shown. A jet and the counter-jet, which both include numerous resolved components in both frequencies, is clearly visible. In all cases flat radio spectra are observed for the cores, whereas the outer components typically show soft, steep spectra. Often these components are undetected in the high-frequency image. The spectral indices at these positions can thus be only considered as limits according to the noise level. One possibility to determine the uncertainty and thus the robustness of the spectral index, which was implemented here, is the consideration of the distribution of spectral indices at each position obtained from generating a set of spectral index maps. The uncertainty of the intensity can be included in the generation of spectral index maps, as well as the uncertainty of the image alignment, e.g., by using different shifts which are weighted for example according to the cross-correlation coefficient corresponding to the shift.

[5] In order to weight different features in the image in the same way, it is possible to use normalized cross-correlations. This method as well as similar algorithms have been implemented by Christoph Grossberger at the Dr. Karl-Remeis-Observatory and will be discussed in detail in his PhD thesis, which is currently in preparation.

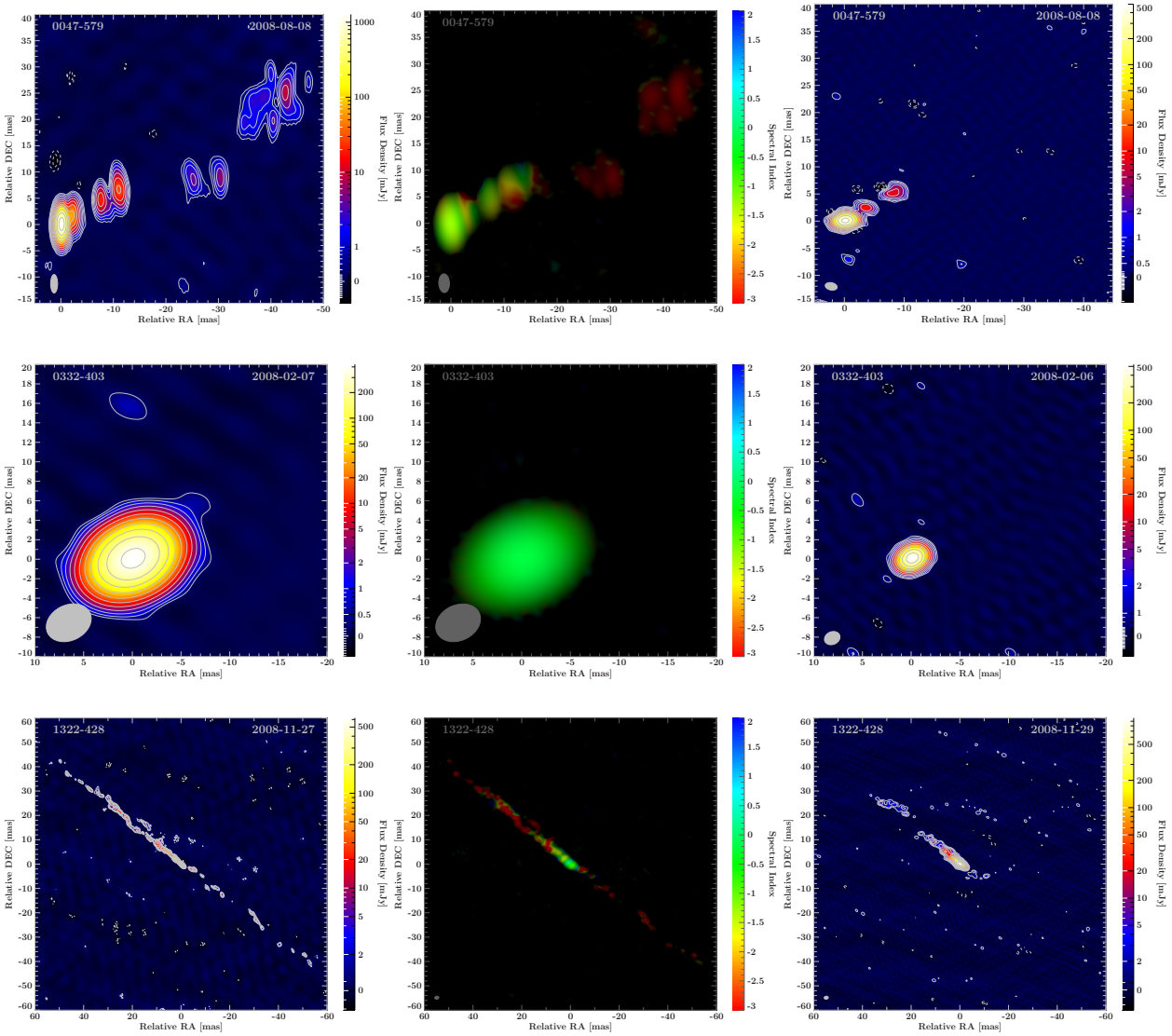

Figure 4.7: Selection of spectral index maps of TANAMI AGN. The left column shows the images at 8.4 GHz, the right column the images at 22 GHz, and in the middle the spectral index maps are shown. Source name and observation date are shown in the top of each image. The values of the spectral index are shown with the colors (hue) and the lightness indicates the intensity, i.e., the sum of the intensity of both initial images.

In Fig. 4.7 the images at both frequencies were not shifted before creating the spectral images. For that reason they are aligned according to the brightest feature, i.e., the radio core. Possible core shifts are not included, thus the alignment might be slightly incorrect. The images are mainly shown to demonstrate the visualization method. Contrary to standard spectral index maps, in which only the spectral index is characterized with a color-code, additional information on the brightness at each position is included here.

4.1.8 Individual Sources

The TANAMI sample includes numerous interesting sources, a selection of them are studied in dedicated analyses by the TANAMI team. A few sources, which are currently studied, are introduced in the following. A list of individual properties of a majority of TANAMI AGN is provided in Sect. A.1.2.

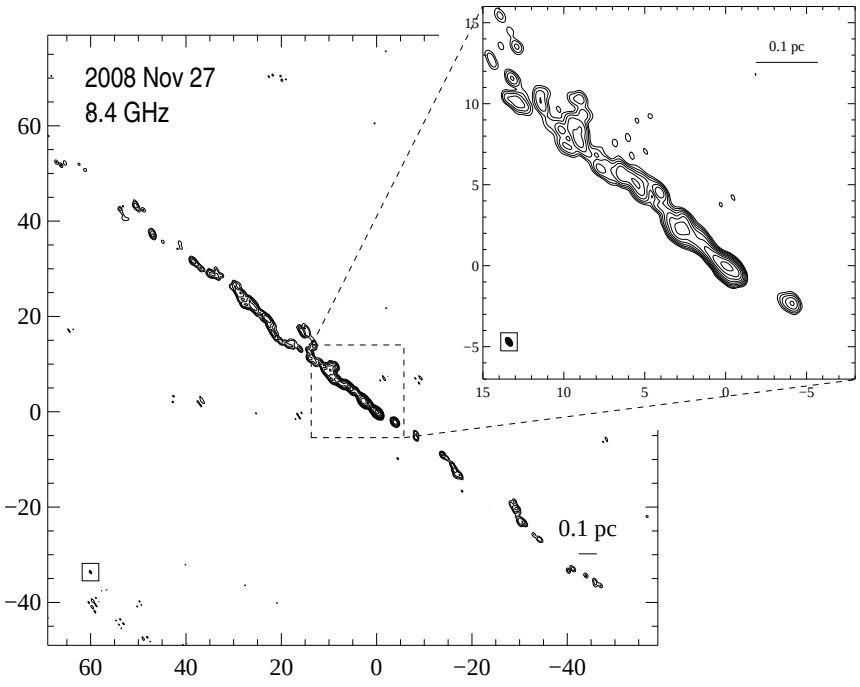

Figure 4.8: VLBI image of Cen A at 8.4 GHz. The coordinates are given in milliarcseconds relative to the phase center. The image has been created by the TANAMI team using natural weighting (Müller et al., 2011, Fig. 2). For the zoom-in with the highest resolution uniform weighting has been used.

Centaurus A One of the highlights in the TANAMI sample is PKS 1322−428, which is better known as Centaurus A. Located in a giant elliptical host galaxy with a distance of 3.8 ± 0.1 Mpc (Harris et al., 2010), it is the closest observable AGN. At this distance an angular resolution of 1 milliarcsecond corresponds to distances of 3.8×10^3 astronomical units in the source frame, which are about 0.018 pc. The mass of central black hole in Cen A is estimated to be $M = (5.5 \pm 3.0)\ 10^7\ M_\odot$ (Israel, 1998; Neumayer, 2010). The Schwarzschild radius of a black hole with such a mass is $R_S = (1.6 \pm 0.9)\ 10^{11}$ m, which is about one astronomical unit. The resolution of up to 0.5 mas in the VLBI image presented by Müller et al. (2011) corresponds thus to about $(3.1 \pm 1.7) \times 10^3$ Schwarzschild radii. There are only a few sources where a higher resolution in units of Schwarzschild radii is possible, such as M87 and the supermassive black hole in the Galactic center (see Sect. 1.2.2).

Figure 4.8 shows a high-resolution VLBI image of Cen A at 8.4 GHz. Images are shown using uniform and natural weighting. With optimized, different weighting of short and long baselines, higher resolutions or a better detection of extended larger structures are possible (Sect. 2.1.2). The image clearly reveals numerous features in the jet at both frequencies. Based on different observation epochs, the jet kinematic of this source is studied in detail and currently in preparation for publication by the TANAMI team. Given the large number of features visible in its radio jet, it is interesting to study the spectral index map of Cen A, which is shown in Fig. 4.9. Additionally the intensity profiles along the jet axis are shown at 8.4 GHz and 22 GHz, as well as the corresponding spectral index. The intensity profile at both frequencies shows clear structures and different values of the spectral index are found. Structures downstream the jet do not only have steep spectral indices, but also flat and even inverted spectra are observed at these positions.

The γ-ray properties of Cen A will be described in Sect. 5.5.1.

PMN J1603−4904 This source, which is also know as PKS 1600−489, is very interesting. It was added to the TANAMI sample based on the bright γ-ray source 1FGL J1603.8−4903, which has been detected with *Fermi*/LAT. The γ-ray spectrum of the source is very hard (see, e.g., Table 5.1). When AGN were searched for inclusion in the TANAMI sample within the scope of this work, there was a good radio association found for this γ-ray source. The position of PKS 1600−489 clearly agreed with the *Fermi*/LAT confidence region, and no further known radio source

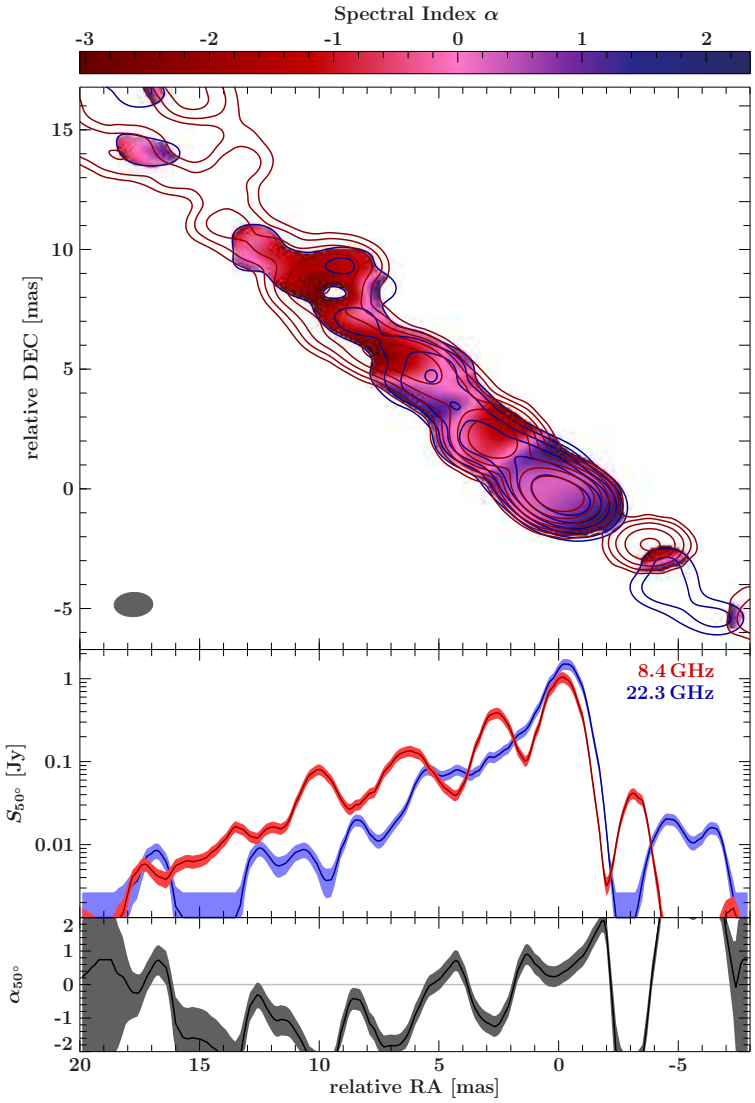

Figure 4.9: VLBI spectral index map of Cen A at 8.4 and 22 GHz. The spectral index is shown only at positions where significant emission is detected at both frequencies (at other positions only limits on the index are possible). The middle panel shows the intensity distribution along the jet axis, which is exactly the diagonal of the top panel. The bottom panel shows the spectral index along this axis (additional information is provided by Müller et al., 2011, Fig. 3).

could be a possible counterpart. A large scale radio image and the *Fermi*/LAT confidence region of this source are shown in Fig. 4.10. The interesting point is that the TANAMI VLBI image at 8.4 GHz of the radio source clearly reveals a compact symmetric structure without strong variations over different epochs. Compact Symmetric Objects (CSOs; see, e.g., O'Dea, 1998) that are small ($\lesssim 1$ kpc) are often considered as young radio galaxies. Such objects are no blazars, but are seen at relatively large inclinations. γ-ray emission is therefore not expected to originate from a relativistic jet that is orientated close to the line of sight of the observer. A detailed interpretation of the source is difficult and several possibilities have been considered and checked by the TANAMI team. For example the radio images have to be studied at both frequencies, in order to figure out if the observed morphology is indeed inconsistent with a blazar. A spectral index map could provide an identification of the core and thus allow differentiate between a blazar and a CSO object.

The crucial question is if the radio and the γ-ray source are indeed the correct counterparts. Given the good position coincidence and the lack of other sources with suitable properties in both energy regimes, the probability for a wrong association are low. If the γ-ray source is an AGN a significant radio counterpart is expected. Most γ-ray bright AGN have bright radio jets (see, e.g., the references and results in Sect. 5). If there is another bright radio source in this region, it should have already been detected (unless the separation to PMN J1603−4904 is in between the resolution limit of previous surveys and the high-resolution of the VLBI images). As the distance

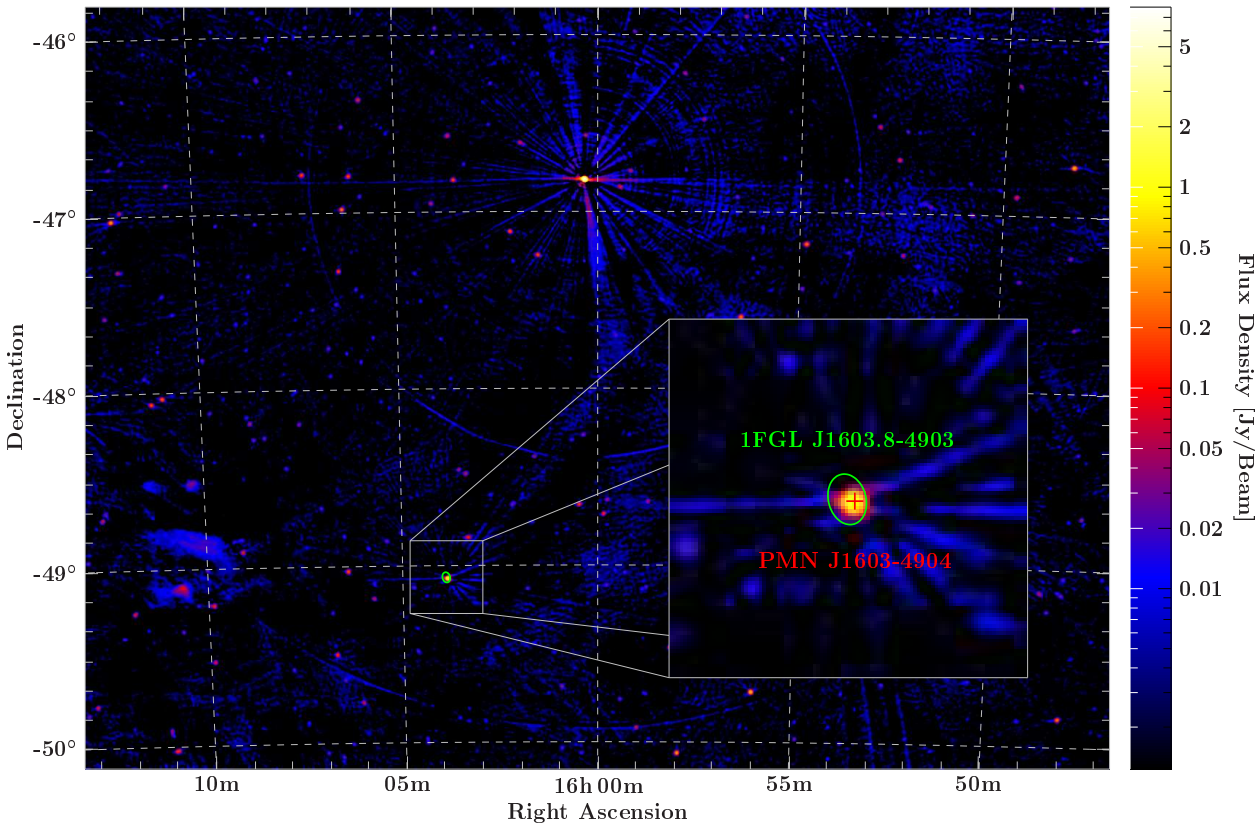

Figure 4.10: Association by positional coincidence. The color scale shows a radio image at 843 MHz from the Sydney University Molonglo Sky Survey. The radio source PMN J1603−4904 (red cross) lies inside of the 95% confidence ellipse (shown in green) of 1FGL J1603.8−4903, which is the only *Fermi*/LAT source in that field of view. (The geometric features in the background image are artifacts based on the radio observation.)

to the radio and γ-ray sources are not known, it was even considered that both sources, or at least the γ-ray source, could be of Galactic origin. That agrees with the position of the sources, which are located close to the Galactic plane. The Galactic longitude and latitude are $l \approx 332.15°$ and $b \approx 2.57°$. The γ-ray spectrum of the source is, however, untypical for pulsars, which usually reveal an exponential cutoff in this energy regime. In the case of a microquasar, significant X-ray emission is expected. Archival X-ray observations of this region do not show strong X-ray sources. No clear X-ray counterpart has been detected so far. Additionally, no unique optical counterpart is detected either, which is the reason why no redshift could be determined and the distance remained unknown. Given the bright γ-ray emission, large redshifts can be excluded as otherwise the source would have the highest γ-ray luminosity of all AGN detected with *Fermi*/LAT.

The TANAMI team proposed deep X-ray and optical observations of the region in order to figure out the true nature of this object. A detailed study led be C. Müller is in preparation for publication.

4.1.9 Multimessenger astronomy – Neutrinos

In addition to multiwavelength studies throughout the complete electromagnetic spectrum, the TANAMI program aims to include other forms of radiation. Multimessenger astronomy contributes to a more complete understanding of processes in the universe. A promising source of information are cosmic neutrinos. Based on their weak interaction they travel almost unaffected through the universe. Reviews on high-energy neutrino astronomy are, e.g., given by Learned & Mannheim

(2000) and Halzen & Hooper (2002). In particular blazars are promising candidates for neutrino sources (see, e.g., Mannheim et al., 1992; Atoyan & Dermer, 2001). Hadronic processes in jets can produce neutrinos, for example the scattering of suffienctly accelerated protons with nuclei, protons, and even photons. The mass of the neutral pion π^0 is $\sim$135 MeV/c^2 and that of charged pions $\pi^\pm$ is $\sim$140 MeV/c^2 (see Beringer et al., 2012, for the currently most accurate values). While the neutral pion decays into two γ-rays, the decay of charged pions yields neutrinos (and antineutrinos). Their dominating decay modes are (details on the decay are again provided by Beringer et al., 2012):

$$\pi^- \rightarrow \mu^- \overline{\nu}_\mu \quad \text{and} \quad \mu^- \rightarrow e^- \overline{\nu}_e \nu_\mu \tag{4.17}$$

and the corresponding charge conjugate:

$$\pi^+ \rightarrow \mu^+ \nu_\mu \quad \text{and} \quad \mu^+ \rightarrow e^+ \nu_e \overline{\nu}_\mu \tag{4.18}$$

where μ^- is the muon (μ^+ its antiparticle), e^- is the electron (e^+ the positron) and ν are neutrinos and $\overline{\nu}$ antineutrinos. The indices of the neutrinos characterize electron and muon neutrinos.

As neutrinos are extremly difficult to detect and thus require advanced detectors, neutrino astronomy is a very young part of astronomy, which started to develop in the last decades. The first (and so far the only) firmly detected celestial neutrino sources were the Sun and the supernova 1987A (see, e.g., Arnett et al., 1989). One method to detect neutrinos are Cherenkov telescopes. With this technique neutrinos can be measured indirectly. Albeit the extremely low cross section it can happen that a neutrino weakly interacts with matter. In this interaction leptons can be produced (typically muons). For high-energy neutrinos, the lepton will have a large energy. Cherenkov light is emitted from charged particles that travel faster than the speed of light in a (dielectric) medium. By measuring the pattern of the Cherenkov light, e.g., with an array of photomultipliers, properties of the incident neutrino, such as its energy and incident angle, can be reconstructed. These neutrino telescopes are typically located underground in order to minimize contamination of cosmic rays. As the Earth is used as detector material for the neutrino interaction, the field of view of such instruments is centered opposite to the zenith. Examples of neutrino telescopes of this class are ANTARES (Circella et al., 2009) and IceCube (Resconi et al., 2009). ANTARES is located in the Mediterranean Sea and is thus constructed to detect neutrinos from the Southern hemisphere. It uses the water in the sea as medium for the Cherenkov light. IceCube is located in Antarctica in the ice, which is used as detector medium, and it searches for neutrinos originating from the Northern hemisphere.

The TANAMI team is collaboration with the ANTARES team. As the sources in the TANAMI sample are located in the Southern hemisphere, they are in the field of view of the ANTARES neutrino telescope. The TANAMI team can contribute to the selection of possible neutrino sources. Based on the γ-ray brightness and variability, and events obtained from the radio monitoring of the AGN jets, periods of possibly high neutrino fluxes can be estimated. The TANAMI results are therefore important for constraints on the positions and time intervals for the search of significant detections of neutrinos from AGN. Figure 4.11 shows an example positions on the sky of a TANAMI source. The sky coordinates of the source have been calculated in azimut and elevation at the location of the ANTARES detector. As many TANAMI sources, the shown source PKS 0208−512 does not rise above the horizon at this position. Most of the γ-ray bright TANAMI sources spend a large amount of time in ANTARES' field of view and are suitable targets. A detailed description of TANAMI AGN as possible sources of neutrino is presented by Fritsch (2013).

More detailed observations of cosmic neutrinos require a higher sensitivity. The sensitivity of IceCube exceeds that of ANTARES. The highest sensitivity of a neutrino telescope is achieved by KM3NeT, which covers a volume of 3 km^3 (see, e.g., Katz et al., 2009, and the references therein).[6] Future results of neutrino astronomy will provide important insights in the emission processes in

[6] An overview on the KM3NeT project is proved online at http://www.km3net.org.

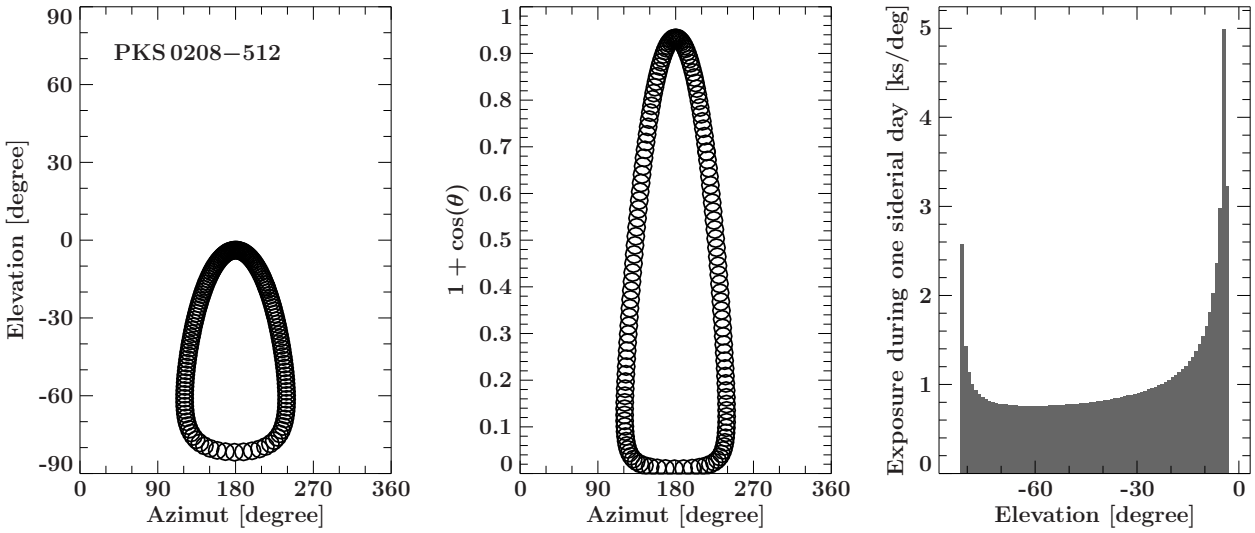

Figure 4.11: Visibility of PKS 0208−512 (its J2000 coordinates are: right ascension of 02h 10m 46.2004s and a declination of −51d 01m 01.891s) for ANTARES during one siderial day. *Left:* Azimut and elevation of the source determined for the position of the telescope. *Middle:* As the telescope is sensitive in the diretion contrary to the zenith, the visibility is often characterized by $1 + \cos(\theta)$, where θ is the angle measured from the zenith. *Right:* Time that the source spends at a given elevation.

relativistic jets. They will help to determine the hardonic contribution to the emission in relativistic AGN jets and yield constraints for the underlying accelaration mechanisms.

4.2 MOJAVE Program

Monitoring Of Jets in Active galactic nuclei with VLBA Experiments (MOJAVE) is a radio VLBI monitoring program of AGN. A detailed description of the MOJAVE program and its observations is given by Lister & Homan (2005) and Lister et al. (2009a). An overview on the program, list of the sources in the sample, and data access is provided online at the MOJAVE website: `http://www.physics.purdue.edu/astro/MOJAVE`. MOJAVE is a VLBA long-term monitoring program with a observation frequency of 15 GHz. A large fraction of the sources in the sample are monitored since 1994 within the VLBA 2 cm Survey (Kellermann et al., 1998). Since the VLBA is located in the USA, mainly sources on the northern sky can be observed. Currently almost 300 AGN with a declination larger than −30° are included in the MOJAVE program. Relevant for the current work is the MOJAVE 1 sample, which is described in Sect. 4.2.2.

4.2.1 Scientific Goals

The main goals of the MOJAVE program are different insights into the properties of relativistic jets from AGN. The long-term VLBI monitoring allows to measure several jet properties. The analyses of the large sample allow for statistical analyses, distribution and population studies. One of the main points addressed by the MOJAVE program is obtaining jet kinematics, i.e., to determine the intrinsic velocities and to study the distribution of speeds in jet sample. The distribution of the velocities of individual components and their trajectories can be analyzed within individual jets. In this way it is possible to study if different components have different velocities and if and where accelerations and decelerations occur in jets. From these studies, insights in the acceleration, collimation, and structure of relativistic flows can be obtained, e.g., to distinguish between the

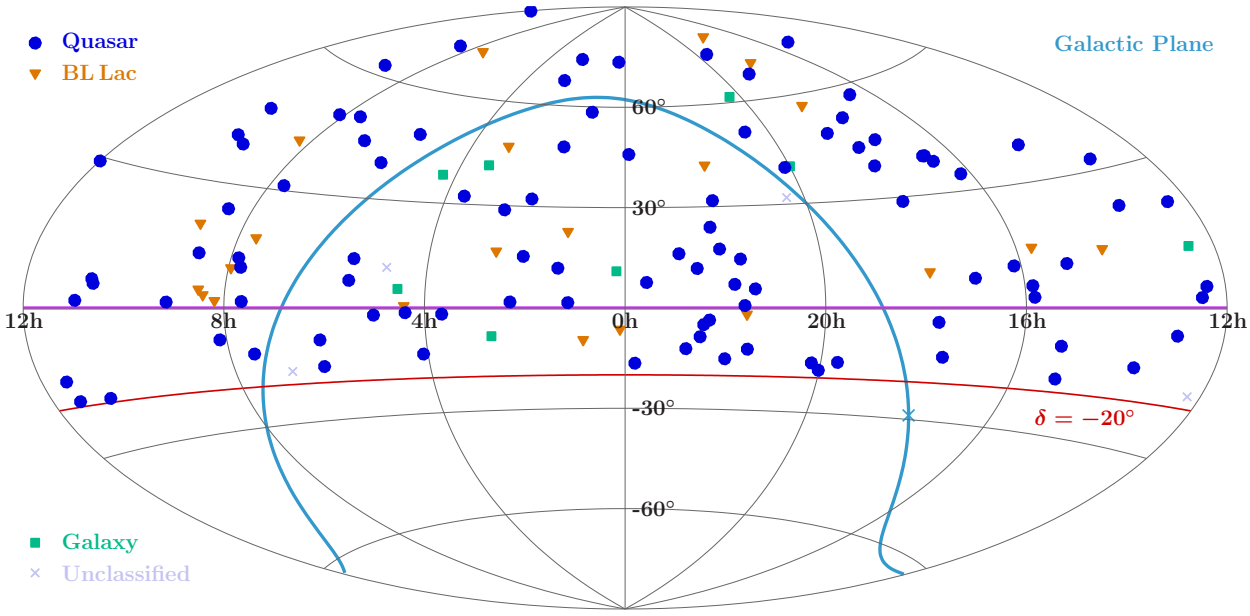

Figure 4.12: Distribution of the MOJAVE sources in the sky. Aitoff projection of the sky using right ascension and declination. As in Fig. 4.1, the blue line marks the Galactic plane and the blue cross the Galactic center. The colors indicate different object classes.

propagation of shocks in the jet and the bulk movement. Besides the kinematic studies, the analysis of polarization properties is important in the MOJAVE program. For example variations of the jet polarization and the underlying mechanisms are studied, as well as the search for circular polarization and its origin in jets. Very important are multiwavelength studies, as comparisons of the previous mentioned properties with those at other wavelengths and further properties of the AGN are crucial for a complete understanding of these systems. Especially the connection between the radio jet and γ-ray emission is currently studied in detail by the MOJAVE team.

4.2.2 MOJAVE 1 Sample

The MOJAVE 1 sample is a flux-limited sample consisting of 135 AGN. The objects in the sample were included based on the following selection criteria. As the observations are performed with the VLBA, there is a limit on the declination of the sources. In order to allow reasonable visibility of the sources, only objects with a declination above -20 degrees were included in this sample. Another positional constraint on the sources is given by the Galactic plane. Only sources above and below the Galactic plane, at a Galactic latitude $|b| > 2.5$ degrees, are included. The final criterion is the flux limit: only sources that exceeded a certain flux at 15 GHz (in at least one observation epoch with the VLBA between 1994 and 2004) are included in the sample. For southern sources (with negative declination), the flux limit is 2 Jy, whereas it is 1.5 Jy for nothern sources (with positive declination). The sky positions of the AGN in the MOJAVE 1 sample are shown in Figs. 4.12 and 4.13. A complete list is given in Table A.3.

4.3 Source Identification

For multiwavelength studies data obtained with different instruments are required. Every instrument is limited to specific energy regimes and has individual properties. Depending on the instrument for example different angular resolutions are possible. In order to study a source in different energy bands using data obtained with different instruments, it is necessary to ensure that the data

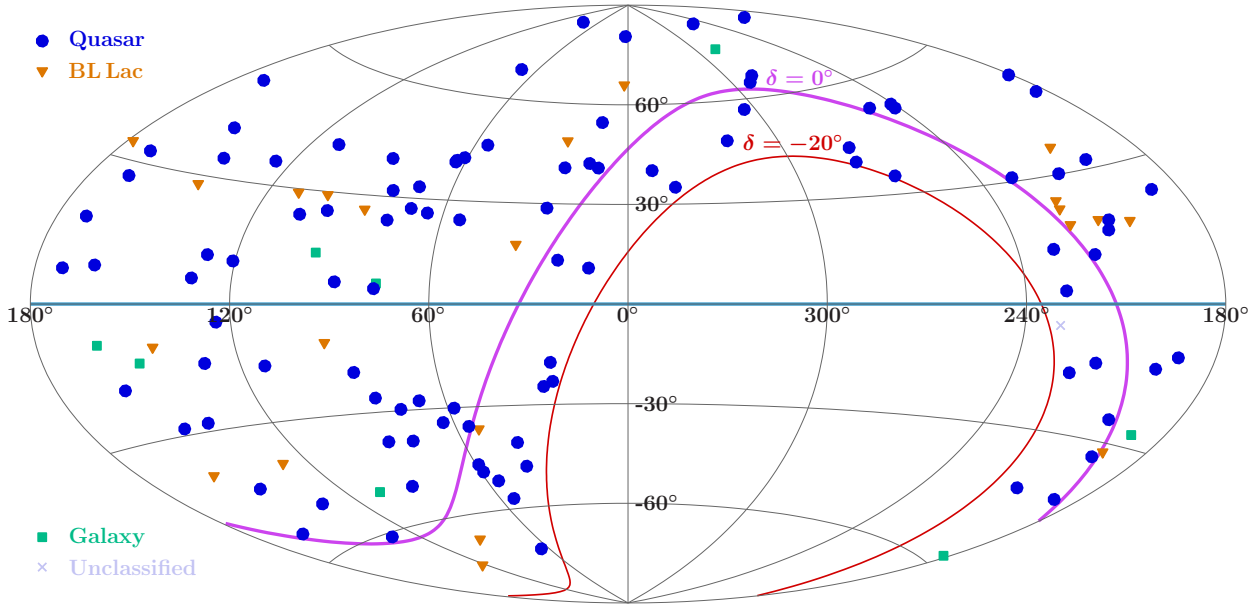

Figure 4.13: Aitoff projection of the positions of MOJAVE sources in the sky in Galactic coordinates. The equatorial plane of the Earth (declination 0°) is shown in purple and the limit declination for the sample of −20° in red.

obtained with each instrument characterize the same source. The better the angular resolutions of the instruments are, the lower is the probability of source confusion. Similar instrument properties, such as overlapping energy ranges simplify the source association of different observations as well. The basis of source association is positional coincidence. For firm identifications of sources in different energy bands, the positional agreement is not sufficient. In addition correlated variability is required. For example pulsars can often be identified based on their characteristic frequencies.

In this work it is especially important to find radio associations for γ-ray sources (Sect. 5.5.1). While the positions of the radio sources are known with high accuracy (up to milliarcsecond precision), those of the γ-ray sources are only known with a precision of several arcminutes down to a degree. As both energy bands are significantly separated and the sources are typically variable on different timescales in both bands, the main association criteria are the positions. An example for positional agreement is PMN J1603−4904 and 1FGL J1603.8−4903, which are discussed in Sect. 4.1.8 and shown in Fig. 4.10.

The probability for the correct identification includes the measured positions, the physical expectations according to properties of the sources in both bands, as well as the number of alternatives, i.e., other possible counterparts in the reason. In the following a method to quantify the association probability based on the source positions alone is discussed. The probability to measure a separation angle ϕ between two point sources S_1 and S_2 is given by

$$w(\phi) = \int_0^{2\pi} \mathrm{d}\alpha_1 \int_{-\pi/2}^{+\pi/2} \mathrm{d}\delta_1 \int_0^{2\pi} \mathrm{d}\alpha_2 \int_{-\pi/2}^{+\pi/2} \mathrm{d}\delta_2 \; P_1(\alpha_1, \delta_1) \; P_2(\alpha_2, \delta_2) \; \delta(\phi - \Phi(\alpha_1, \delta_1, \alpha_2, \delta_2)) \tag{4.19}$$

where $P_i(\alpha_i, \delta_i)$ is the probability that the source S_i is located at the position (α_i, δ_i) (e.g., right ascension and declination) and Φ is the angular distance between (α_1, δ_1) and (α_2, δ_2). For small separation angles ϕ and narrow localizations P_1 and P_2 it is justified to use a planar approximation:

$$w(\phi) = \int_{-\infty}^{\infty} \int_{-\infty}^{\infty} \int_{-\infty}^{\infty} \int_{-\infty}^{\infty} \mathrm{d}x_1 \mathrm{d}y_1 \mathrm{d}x_2 \mathrm{d}y_2 P_1(x_1, y_1) P_2(x_2, y_2) \delta(\phi - \Phi(x_1, y_1, x_2, y_2)). \tag{4.20}$$

The probability distributions of the positions are typically approximated with Gaussian profiles. A circular profile with a 1σ-uncertainty of σ_i of the source position (x_i, y_i) is given by:

$$P_i(x,y) = \frac{1}{2\pi\sigma_i^2} \exp\left(-\frac{(x-x_i)^2 + (y-y_i)^2}{2\sigma_i^2}\right). \tag{4.21}$$

As mentioned previously, source positions measured with radio interferometry have very small uncertainties ($\ll$ arcsec), which can be neglected with respect to the γ-ray position. Assuming that S_2 is the radio source, which is for simplicity located at the origin ($x_2 = 0$, $y_2 = 0$), its position probability distribution can be approximated as a δ distribution:

$$P_2(x,y) \rightarrow \delta(x)\,\delta(y) \tag{4.22}$$

The separation between the source positions is then given by:

$$\Phi(x_1, y_1, 0, 0) = \sqrt{x_1^2 + y_1^2} \tag{4.23}$$

Assuming that S_1 and S_2 are the same object (both located at the origin), the probability w to measure angular separation ϕ between the determined source positions is:

$$w(\phi) = \frac{1}{2\pi\sigma_1^2} \int_{-\infty}^{\infty} \mathrm{d}x_1 \int_{-\infty}^{\infty} \mathrm{d}y_1 \exp\left(-\frac{x_1^2 + y_1^2}{2\sigma_1^2}\right) \delta\left(\phi - \sqrt{x_1^2 + y_1^2}\right), \tag{4.24}$$

which can be expressed in polar coordinates (r_1, ϕ_1):

$$\begin{aligned} w(\phi) &= \frac{1}{2\pi\sigma_1^2} \int_0^{\infty} \mathrm{d}r_1 \int_0^{2\pi} \mathrm{d}\phi_1 r_1 \exp\left(-\frac{r_1^2}{2\sigma_1^2}\right) \delta(\phi - r_1) \\ &= \frac{\phi}{\sigma_1^2} \exp\left(-\frac{\phi^2}{2\sigma_1^2}\right). \end{aligned} \tag{4.25}$$

If the the two point sources are identical, the probability to measure an anglur separation larger than ϕ is:

$$W(\phi) = \int_{\phi}^{\infty} w(\phi')d\phi' = \exp\left(-\frac{\phi^2}{2\sigma^2}\right). \tag{4.26}$$

4.4 Broad band modelling

4.4.1 SED catalog

There are already several (self-consistent) physical models available, which describe broad band spectra of AGN (see Sect. 1.5). Many of these models are, however, computationally intensive. Detailed simulations and modelling of the involved radiation processes is typical difficult. Depending on the complexity of the model, a single model evaluation, i.e., the determination of the model spectrum for a given set of parameters requires time scales from seconds to several hours. In addition only a few models are available for fitting in XSPEC or ISIS (e.g., the jet model of Markoff et al., 2005).

For certain studies it is reasonable to use strongly simplified models. An example for such a study is the SED catalog of MOJAVE sources (see Chang et al., 2010b, for preliminary results). In this work the broad band spectra of source in the MOJAVE sample are modelled with polynomials

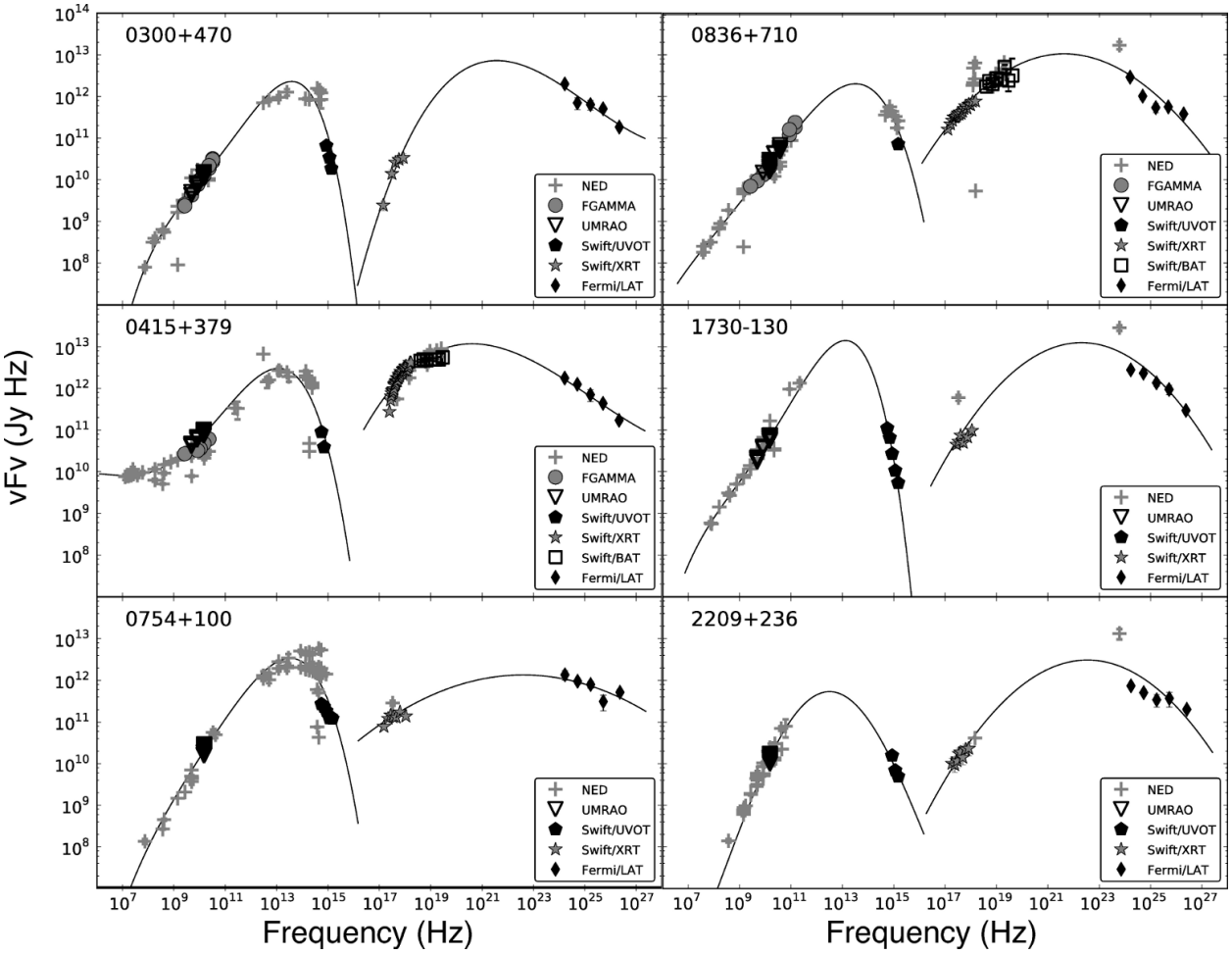

Figure 4.14: SEDs of a selection of MOJAVE sources by Chang et al. (2010a, Fig. 1). The multi-wavelength data have been fitted with polynomials (in $\log \nu$-$\log(\nu F_\nu)$ space).

(of forth order, in $\log \nu$-$\log(\nu F_\nu)$ space). This method provides a quick description of the SED shape and yields peak frequencies for the two humps in the SED. A selection of these fits is shown in Fig. 4.14. The obtained results, such as the SED peak frequencies, can then be compared with intrinsic jet properties, which are determined from the VLBI monitoring of these sources within the MOJAVE program. Relations between these properties provide insights on jet physics, and could, e.g., help to understand the origin of the high-energy emission better. The final results of this study are in preparation for publication by the MOJAVE team.

In the study described above, polynomials have been applied for broad band fitting in $\log \nu$-$\log(\nu F \nu)$ space. In this case the data had to be transfered from counts in detector space to real flux, which is a problem in the X-ray regime (Sect. 3.3) as this requires an inversion of the response matrix. In addition it is necessary to correct X-ray data for absorption before starting the fitting process. This procedure is generally not easily possible, the propagation of uncertainies almost impossible, and even significant errors can be induced. Especially in the X-ray regime spectral fitting should thus be done in the detector count space. All firmly measured fluxes can trivially be included in the count space by assigning a diagonal response matrix. This method then allows a proper estimation of parameter values and confidence intervals.

4.4.2 Implementation of the LogParabola

Strongly simplified models for fitting are typically affine linear functions, i.e., functions of the form $f(x) = a\ x + b$, as well as polynomials of higher orders. However, the electromagnetic spectra of many emission components of celestial sources, which often cover several orders of magnitude, can be typically approximated partially with power laws $f(x) = b\,x^a$ (see Sect. 1.4.3 for a description of astrophysical radiation processes). Power laws are affine linear functions in the double logarithmic space ($\log(x)$, $\log(f(x))$). A polynomial of second order in this double logarithmic space is called "LogParabola" in the following and will be discussed in this section.

The LogParabola is given by using a second order polynomial of $\ln(E)$ as the argument of the exponential function, which can be written as:

$$P_{\log}(E) = k \exp\left(a \ln^2(E/E_0)\right), \tag{4.27}$$

where k is a normalization constant, it defines the extremum of the LogParabola, E_0 is the abscissa of the extremum, and the factor a describes the curvature of the parabola.

For fitting binned data, an integrated version of the LogParabola is required. The integrated flux in one bin is then given by:

$$F_{\text{bin}} = \int_{E_1}^{E_2} P_{\log}(E) dE \tag{4.28}$$

where E_1 and E_2 are the lower and upper borders of the bin.

$$F_{\text{bin}} = kE_0 \int_{\ln(E_1/E_0)}^{\ln(E_2/E_0)} \exp\left[ay^2 + y\right] dy \tag{4.29}$$

$$= kE_0 \frac{e^{-\frac{1}{4a}}}{\sqrt{-a}} \int_{\sqrt{-a}\left(\ln(E_1/E_0)+\frac{1}{2a}\right)}^{\sqrt{-a}\left(\ln(E_2/E_0)+\frac{1}{2a}\right)} \exp\left[-t^2\right] dt \tag{4.30}$$

$$\tag{4.31}$$

Depending on the value of a, the integral can be solved analytically. For $a = 0$ we get the trivial solution for Eq. 4.28:

$$F_{\text{bin}} = k\,(E_2 - E_1) \tag{4.32}$$

In the case $a < 0$, the solution is given by:

$$F_{\text{bin}} = \frac{kE_0\sqrt{\pi}e^{-\frac{1}{4a}}}{2\sqrt{-a}} \left[\text{erf}\left(\sqrt{-a}\left(\ln\left(\frac{E_2}{E_0}\right) + \frac{1}{2a}\right)\right) - \text{erf}\left(\sqrt{-a}\left(\ln\left(\frac{E_1}{E_0}\right) + \frac{1}{2a}\right)\right)\right] \tag{4.33}$$

Where erf(x) is the error function, which is defined by:

$$\text{erf}(x) = \frac{2}{\sqrt{\pi}} \int_0^x e^{-t^2} dt \tag{4.34}$$

For $a > 0$, the solution can be expressed as:

$$F_{\text{bin}} = \frac{-\mathrm{i}kE_0\sqrt{\pi}e^{-\frac{1}{4a}}}{2\sqrt{a}} \left\{ w\left(-\sqrt{a}\left(\ln\left(\frac{E_1}{E_0}\right) + \frac{1}{2a}\right)\right) \exp\left[a\left(\ln\left(\frac{E_1}{E_0}\right) + \frac{1}{2a}\right)^2\right] \right.$$
$$\left. - w\left(-\sqrt{a}\left(\ln\left(\frac{E_2}{E_0}\right) + \frac{1}{2a}\right)\right) \exp\left[a\left(\ln\left(\frac{E_2}{E_0}\right) + \frac{1}{2a}\right)^2\right] \right\} \tag{4.35}$$

where $w(x)$ is the Faddeeva function given by:

$$w(x) = e^{-x^2}\left(1 - \mathrm{erf}(-\mathrm{i}x)\right) \tag{4.36}$$

An alternative method to determine the integrated value F_{bin} is the application of a Taylor expansion of Eq. 4.28 around E_1 in units of $\ln(E/E_1)$:

$$F_{\mathrm{bin}} = \int_{E_1}^{E_2} k \exp\left[a \ln^2\left(\frac{E}{E_0}\right)\right] \mathrm{d}E \tag{4.37}$$

$$= k\ E_1 \exp\left[a \ln^2\left(\frac{E_1}{E_0}\right)\right] \int_0^{\ln\left(\frac{E_2}{E_1}\right)} \exp\left[ax^2 + \left(1 + a \ln^2\left(\frac{E_1}{E_0}\right)\right) x\right] \mathrm{d}x \tag{4.38}$$

$$= k\ E_1 \exp\left[a \ln^2\left(\frac{E_1}{E_0}\right)\right] \sum_{n=1}^{\infty} \frac{c_n}{n!} \left(\ln\left(\frac{E_2}{E_1}\right)\right)^n. \tag{4.39}$$

The coefficients are given by

$$c_n = \left[\left(\frac{\partial}{\partial x}\right)^{(n-1)} \exp\left(ax^2 + \left(1 + a \ln^2\left(\frac{E_1}{E_0}\right)\right) x\right)\right]_{x=0} \quad \forall n \geq 1. \tag{4.40}$$

The trival case $a = 0$ yields obviously again the result of Eq. 4.32:

$$F_{\mathrm{bin}} = k\ E_1 \sum_{n=1}^{\infty} \frac{1}{n!} \left(\ln\left(\frac{E_2}{E_1}\right)\right)^n = k\ E_1 \left[\exp\left(\ln\left(\frac{E_2}{E_1}\right)\right) - 1\right] = k(E_2 - E_1). \tag{4.41}$$

The highest precision of the Taylor expansion is achieved in the case of small bins, i.e. $\ln(E_2/E_1) \ll 1$. The coefficients for the first orders (Eq. 4.4.2) can be determined easily.

Chapter 5

Gamma-ray Emission of AGN

Studies of cosmic γ-rays provide information on the most energetic phenomena in the universe. AGN jets being cosmic particle accelerators are interesting objects to study at these high energies.

In this chapter an introduction to γ-ray astronomy is given (Sect. 5.1) including its history with the early difficulties of detecting celestial γ-rays and the subsequently improved γ-ray instruments. In the following the *Fermi Gamma-Ray Space Telescope* is discussed in Sect. 5.2, as well as the difficulties of analyzing γ-ray data in Sect. 5.3. After this introduction, the analyses of the γ-ray properties of the TANAMI and MOJAVE samples, which are a major part of this work, and the obtained results are presented in Sects. 5.5 and 5.6, respectively.

5.1 Gamma-ray Astronomy

5.1.1 Prediction of Cosmic Gamma-rays

The discovery of cosmic rays in the begin of the 20th century revealed that there are high-energy phenomena in the universe. Based on the existence of energetic cosmic rays the production of cosmic γ-rays had been discussed. Production theories included electro-magnetic (Bremsstrahlung, Compton scattering) and annihilation processes (see, e.g., the review of γ-ray astronomy by Fazio, 1970, and references therein). Suggested mechanisms were interactions of high-energy particles (such as electron, protons, and cosmic nuclei) with stellar photons or interstellar matter (e.g., Feenberg & Primakoff, 1948; Hayakawa, 1952; Ginzburg & Syrovatskii, 1964). It was considered as well that pions can be produced in hadronic collisions, where the π^0-meson decays into two γ-ray photons.

Observing and studying γ-rays was promising for several reasons. Comparisons of measurements with the predicted γ-ray fluxes were required to support or to rule out certain theories. γ-ray observations were also important for cosmology and the structure of the universe. For example constraints on the distribution of antimatter could be found by observing emission caused by annihilation. Concerning this motivation, Fazio (1970) wrote: "The proposal that the radio source Cygnus A could be matter-antimatter galaxies in collision acted as a spur to the experimentalist". In addition, the trajectories of γ-rays are not influenced by magnetic fields, contrary to charged particles, thus their paths could be traced back to figure out the sources of high-energy emission in the universe helping to explain the origin of cosmic rays.

Although there was a lot of interest in observing cosmic γ-rays, it took several decades after the discovery of cosmic rays until they could be detected, because of experimental difficulties. In laboratories and particle accelerators there were detectors available which could detect the predicted γ-ray fluxes. However, direct ground-based observations were not possible, as the γ-rays interact with the Earth's atmosphere and do not reach the ground.[1] The problem was to construct

[1]There is, however, an indirect ground based observation technique using the interaction of high-energy γ-rays with

detectors, which are compact enough to be brought into high altitudes with balloons or rockets, or to be mounted on satellites, but which are nonetheless sensitive enough for measuring the cosmic γ-ray flux.

5.1.2 Early Gamma-ray Missions

As reviewed by Kraushaar et al. (1972), the first experiments trying to detected celestial γ-rays were using counter systems on balloons and a B-29 aircraft (Hulsizer & Rossi, 1948; Rossi, 1949, tried to detect high-energy electrons and photons in cosmic rays), balloon-borne cloud chambers (Critchfield et al., 1952), and Geiger counters in V-2 rocket flights (Perlow & Kissinger, 1951). With these experiments, however, only upper limits on the flux were obtained. A first indication of a γ-ray flux at $\sim$1 MeV, which seemed to be isotropic, had been obtained with a detector on the *Ranger 3* spacecraft (Arnold et al., 1962).[2] Further experiments on balloons and satellites followed, as well as the first dedicated cosmic γ-ray satellite experiment onboard *Explorer 11*. The results of these missions were again upper limits. Based on the previous results an instrument for the *3rd Orbiting Solar Observatory* (*OSO-3*) had been designed. The technical improvements of the spacecraft and the instrument (larger payload, higher telemetry, and increase in effective exposure; see Kraushaar et al., 1972, for a more detailed description) yielded the first certain measurements of cosmic γ-rays. Having used data which had been obtained in 1967–1968 with the detector onboard *OSO-3*, Kraushaar et al. (1972) discussed the discovery of cosmic γ-rays with energies above $\sim$50 MeV. They found that the emission is not isotropic, but could be separated into two components. The emission of one of them was concentrated in a band along the Galactic plane with a maximal intensity at the Galactic center, while the analysis showed that the second component was isotropic, had a softer energy spectrum, and was interpreted to be of extragalactic origin. More detailed studies were possible with a 32-level wire spark-chamber onboard of the second NASA *Small Astronomy Satellite* (*SAS-2*), which covered the energy range of 20 MeV to 1 GeV. Based on observations with this instrument, Fichtel et al. (1975) confirmed the uniform γ-ray component and associated the flux distribution of the Galactic component with structural features, such as arm segments, of the Galaxy. With a large γ-ray telescope carried onboard the mission *COS-B*, which operated in the years 1975–1982, a complete γ-ray map of the Galaxy had been obtained. Its "magnetic-core, wire-matrix, spark chamber γ-ray detector" (Bignami et al., 1975) provided data of γ-ray pulsars, especially the GEMINGA pulsar was studied in detail. Using *COS-B* data Swanenburg et al. (1978) detected the quasar 3C 273 as a γ-ray source.

5.1.3 Compton Gamma-Ray Observatory

Based on the scientific insights, which had been obtained with the *SAS-2* and *COS-B* missions, a new instrument with improved performance was constructed: The Energetic Gamma Ray Experiment Telescope (EGRET; Thompson et al., 1993b) onboard of the *Compton Gamma-Ray Observatory (CGRO)*. After its launch on April 5, 1991, the mission had a lifetime of nine years, until it was deorbited on June 4, 2000.[3] With its four instruments, of which each had an im-

the Earth's atmosphere. The underlying method is to measure the Cherenkov light of particle showers caused by the interaction of γ-rays in the air and reconstruct the trajectory of the incident γ-ray (e.g., Catanese & Weekes, 1999, and references therein). Cherenkov telescopes can be used to detect photons with energies $\gtrsim$100 GeV. Current missions are HESS, MAGIC, and VERITAS (e.g., Hinton, 2004; Baixeras et al., 2004; Weekes et al., 2002, respectively).

[2] The *Ranger 3* spacecraft had been launched on January 26, 1962. Its mission included impacting on the Moon, "rough-landing" a seismometer capsule on the Moon, and measuring γ-ray data during flight to gain information for future missions. Due to several malfunctions the spacecraft missed the Moon significantly. More information on *Ranger 3* can be found on: http://nssdc.gsfc.nasa.gov/nmc/spacecraftDisplay.do?id=1962-001A

[3] More information on the deorbit of *CGRO*, which was "NASA's first intentional controlled deorbit of a satellite" can be found in a review by R. Mrozinski (http://ntrs.nasa.gov/archive/nasa/casi.ntrs.nasa.gov/20010084992_2001127597.pdf, Mission Operations Directorate, NASA Johnson Space Center), and is provided by Gehrels & Shrader (2001). After one of the satellite's gyroscopes failed, NASA decided for a controlled reentry instead of an

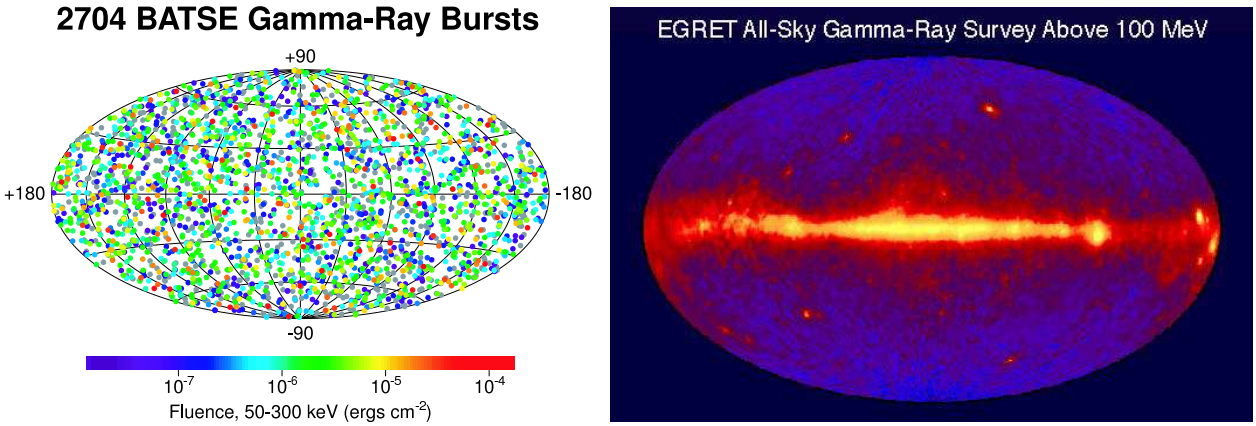

Figure 5.1: Two of the scientific highlights obtained with *CGRO*: Isotropic distribution of gamma-ray bursts (left) and an all-sky map in the high-energy regime (right). Both images are projections in Galactic coordinates. (Credit: BATSE and EGRET teams, NASA)

provement in sensitivity of more than a factor of ten compared to precious missions and which covered in combination the energy range of 30 keV to about 30 GeV, *CGRO* led to several new discoveries in the high-energy regime (see, e.g., Gehrels & Shrader, 2001, for a *CGRO* review). The Burst and Transient Spectrometer Experiment (BATSE) was an all-sky monitor of the energy band 20–600 keV with the scientific goal of studying gamma-ray bursts.[4] It revealed the isotropic distribution of gamma-ray bursts on the sky indicating their extragalactic origin (see Fig. 5.1, left). Maps at 511 keV (the energy of the electron-positron annihilation line) of the Galactic center region were obtained with the Oriented Scintillation Spectrometer Experiment (OSSE). The Imaging Compton Telescope (COMPTEL) provided an all-sky map using the emission of ^{26}Al, revealing clear structures in the Galaxy.

The instrument related the most to the present work is EGRET (for a detailed description, see Thompson et al., 1993b). It determined the direction and energy of incident γ-rays using tantalum foils, spark chambers, and a NaI(Tl) calorimeter. The electron-positron pairs produced in the foils could be tracked and measured by subsequent devices. The energy range was about 20 MeV to 30 GeV. Using data collected within several years, an all-sky map in this energy regime had been created (see Fig 5.1, right), which clearly shows the Galactic diffuse emission and several point sources. One of the scientific highlights of EGRET was the measurement of γ-ray emission from blazars (Hartman et al., 1992). The γ-ray sources found by this instrument are given in the Third EGRET Catalog (3EG; Hartman et al., 1999), which includes 271 sources. A majority of 170 sources remained unidentified. Most of the identified sources were AGN: 66 high-confidence and 27 possible blazar associations, as well as the radio galaxy Cen A. The remaining associations include five pulsars, the Large Magellanic Cloud, and a solar flare.

In order to solve the mystery of the large number of unidentified EGRET sources, and to the study the identified source types in much greater detail, the *Fermi Gamma-ray Space Telescope* had been developed.[5] This mission is subject of the following section.

uncontrolled crash of the 15 900 kg spacecraft endangering public safety. Mrozinski et al. (2002) point out an U.S. guideline stating that the entries should be controlled if the "casualty expectation" is larger than 1 in 10 000. The deorbiting operation of *CGRO* succeeded without problems and the fragments of the spacecraft, which survived the reentry in Earth's atmosphere, impacted in the Pacific Ocean about 3 500 km southeast of Hawaii (Gehrels & Shrader, 2001).

[4] Gamma-ray bursts are extremely luminous events associated with core-collapse supernovae. A discussion of the current understanding of the physics of gamma-ray bursts is, e.g., given by Piran (2004).

[5] Another current γ-ray mission is *Astro-rivelatore Gamma a Immagini Leggero* (AGILE; Tavani et al., 2008).

5.2 Fermi Gamma-ray Space Telescope

The *Fermi Gamma-ray Space Telescope* (*Fermi*) has been launched on June 11, 2008 by NASA, with a goal of 10 years of operation. The mission had been know as the *Gamma-ray Large Area Space Telescope* (*GLAST*), but was renamed after Enrico Fermi honoring his work in high-energy astrophysics.[6] Onboard *Fermi* there is the Large Area Telescope, which is the primary instrument, and the Gamma-ray Burst Monitor. Both instruments and their scientific objectives are discussed in the following Sects. 5.2.1 and 5.2.2.

5.2.1 Gamma-ray Burst Monitor

The Gamma-ray Burst Monitor (GBM; von Kienlin et al., 2004; Meegan et al., 2007), is the secondary instrument onboard *Fermi*. GBM is designed to detect γ-ray burst and high-energy transients. As short γ-ray bursts can occur in time scales of microseconds, a high temporal resolution is required. The accomplished instrument's time resolution is about 2 μs. Due to the isotropic distribution of γ-ray bursts in the sky and their short duration (microseconds to thousands of seconds), a maximal field of view of the instrument is desired. A complete view of the unocculted sky is achieved permanently by the positioning of 12 Sodium Iodide (NaI) scintillation detectors and 2 Bismuth Germanate (BGO) detectors around the spacecraft. The arrangement is such that a γ-ray burst is typically detected by at least three NaI and one BGO detectors (Meegan et al., 2007). The energy range covered by the NaI detectors is ~8 keV to 1 MeV, and that of the BGOs 150 keV to ~30 MeV. The energy resolution $\Delta E/E$ is about 10% (~14% at 100 keV and ~9% at 1 MeV). GBM's broad energy coverage connects the energy ranges of current and previous X-ray instruments with that of LAT.

Besides measuring transient events, GBM is used as well to provide light curves and spectra of bright persistent sources. As the field of view of GBM covers a large fraction of the sky and has almost no spatial resolution, no pointed or imaging observations are possible. In order to separate the flux of different sources, the Earth occultation method is applied. The brightness of known sources is obtained by studying changes in the detector's count rates, which occur when the Earth occults the position of the source. Details of this technique and its results are presented by Case et al. (2011). Within the GBM Pulsar Project the frequencies of the pulsed emission of detected persistent and transient pulsars are measured and monitored. In this way changes in the frequency of the pulsars' periods can be measured, allowing for studying torques (see, e.g., Camero-Arranz et al., 2010).[7] Besides analyzing celestial γ-rays, GBM can be used as well to study Terrestrial Gamma-ray Flashes (TGFs), which are events on time scales of milliseconds in Earth's atmosphere (Briggs et al., 2010). A possible origin of these flashes are thunderstorms and lightnings, where electrons can be accelerated to high-energies in a relativistic runaway process.

5.2.2 Large Area Telescope

The principal scientific instrument onboard *Fermi* is the Large Area Telescope (LAT; Atwood et al., 2009). It is an imaging γ-ray telescope, which covers the energy range from about 20 MeV to more than 300 GeV. "More than" means here that in principle photons up to TeV energies can be measured, however the effective area at such high energies is too small to obtain reasonable count rates. To study the low γ-ray flux in detail, the instrument requires a large effective area. In order

[6] On August 26, 2008, NASA announced the change of the mission's name (see, e.g., NASA's science news of that day: http://science.nasa.gov/science-news/science-at-nasa/2008/26aug_firstlight/). According to NASA's Science Mission Directorate chief scientist Paul Hertz "Enrico Fermi was the first person to suggest how cosmic particles could be accelerated to high speeds" and "His theory provides the foundation for understanding the new phenomena his namesake telescope will discover."

[7] The histories of pulse frequencies and pulsed fluxes of the studied pulsars are available at the GBM Pulsar Project (http://gammaray.msfc.nasa.gov/gbm/science/pulsars/).

to identify and analyze individual sources, a high angular resolution is needed, as well as a large field of view for monitoring the large number of variable sources. In the following the scientific objectives and the performance of LAT are discussed in more detail.

5.2.3 Scientific objectives of LAT

The key science objectives of LAT are discussed in detail by Atwood et al. (2009) in Sect. 3 of their work. Following the structure of their publication, a brief summary is given in the next paragraphs (for more information see Atwood et al., 2009, and the references therein):

Resolve the γ-ray Sky: the Origins of Diffuse Emission and the Nature of Unidentified Sources. This objective includes the following three scientific targets:

1. Identification of the numerous unidentified EGRET sources.

2. Studying the diffuse emission of our Galaxy and nearby galaxies, which is assumed to originate from processes in the interstellar medium.

3. Analysis of the extragalactic diffuse emission.

For a more detailed understanding of these sources, it is required to separate the emission of discrete sources from the structures of the diffuse emission, which is especially strong in the Galactic plane. In order find associations for the unidentified EGRET sources, the superior performance of LAT comes into play (the performance of the instrument is discussed in detail in the following Sect. 5.2.4). A better γ-ray source localization simplifies the search for counterparts and thus the source identification. Compared to EGRET, the confidence region is smaller by a factor of about 6 (depending on the spectrum the 68% confidence region is in the range of 2 arcmin to less than 0.4 arcmin for a source detected on the 5σ level; Atwood et al., 2009, Sect. 3.1.1.). The better source localization provides more accurate positions for identified EGRET sources and thus allows for example to confirm associations or reveal misidentifications. In addition to a better determination of positional agreement, source identifications are more reliable with LAT due to an improved measurement of spectra covering a broad range of energy and light curves covering a broad range of timescales. For example the pulsed emission of pulsars allows undoubted associations with counterparts at other wavelengths.

For sources with no or weak temporal variability, that are located close the Galactic plane, identifications are highly complicated, as the diffuse Galactic emission is dominating the γ-ray sky. The latter is, however, an interesting source itself to study. As the diffuse emission is connected to the interaction of the interstellar medium with energetic particles, it can be used to gain information on both. On the one hand the distribution of interstellar gas can be studied, while on the other hand spectra of cosmic rays can be obtained, as well as insights to their acceleration and propagation in the Galaxy.

Another part of this science objective is to obtain a better understanding of the extragalactic diffuse emission. There are still several open questions concerning the origin of this emission component (see Sect. 3.1.3. of Atwood et al., 2009, and the references therein, for a detailed discussion). The extragalactic γ-ray background probably includes a superposition of unresolved sources, such as blazars, other kinds of active galactic nuclei, and the diffuse contribution of normal galaxies, as well as distant γ-ray bursts. In addition it could include emission of galaxy clusters and emission due to cascades of ultra high-energy cosmic rays and γ-rays. Even more exotic components such as annihilation processes of dark matter particles, evaporation of primordial black holes, annihilation of baryons and anti-baryons after the Big Bang, and further ideas have been discussed.

Understand the Mechanisms of Particle Acceleration in Celestial Sources. This science objective of LAT is discussed in detail in Sect. 3.2 of (Atwood et al., 2009). To study the mechanisms of particle acceleration and γ-ray emission processes, the following sources types are brought into focus:

1. Blazar AGN jets
2. Pulsars, pulsar wind nebulae, and supernova remnants
3. γ-ray emission from the Sun and solar system bodies

With its quasi-continuous monitoring and good spectral resolution LAT provides an excellent data base for studying processes in these sources. Besides studies of individual bright sources LAT allows population studies with good statistics. During its life time LAT is expected to detect about thousand (or up to a few thousand) AGN. The γ-ray emission of AGN Jets is an important part of this work and is discussed in detail in Sect. 1.4.3. Ideal laboratories for studying particle acceleration are pulsars and supernova remnants (Atwood et al., 2009, Sect. 3.2.2). *Fermi*/LAT data allows for studies of the Solar System as well. Promising objects are the Sun with solar flares and the interaction of cosmic rays with the Moon's surface, objects in the Asteroid Belt, and the Earth's atmosphere, which is the brightest source of γ-rays for the LAT instrument.

Study the High-Energy Behavior of GRBs and Transients. Observing and studying transient events such as γ-ray bursts is an important goal of the *Fermi* mission. With its large field of view and monitoring mode LAT can detect numerous of these events and allows measuring their high-energy behavior, which is important to quantify delays to the prompt emission. In this way LAT strongly contributes to the understanding of the underlying acceleration mechanisms, interaction with the environment such as shocks, and geometrical details. A more detailed discussion is given in Sect. 3.3 of the work by Atwood et al. (2009) and the references therein.

Probe the Nature of Dark Matter. One of the more exotic science objectives of LAT is the search for signatures of weakly interacting massive particles (WIMPs) (Atwood et al., 2009, Sect. 3.4). The hypothetical WIMPs are candidates for the explanation of dark matter. LAT data are used for determining constraints on the existence and intensity of mono-energetic γ-ray lines and continuous flux caused directly by annihilation of WIMPs or subsequent decays in fragmentation processes.

Use High-Energy γ-rays to Probe the Early Universe. The final scientific goal of the instrument being listed by Atwood et al. (2009, Sect. 3.5) is the study of the extragalactic background light (EBL). The EBL includes emission from structure and star formation, and starlight at wavelengths from infra red to ultra violet. Obviously these wave bands cannot be measured directly with a γ-ray instrument, but can be studied indirectly due to absorption of γ-rays via pair production. The cross section for two photons yielding a electron positron pair has a clear maximum when the product of the photon energies is about $8 \times 10^{11}\,\mathrm{eV}^2$. Using γ-ray sources at different distances including high-redshift quasars the EBL and its evolution can be probed.

5.2.4 Large Array Telescope and its Performance

In order to fulfill its scientific goals, a large number of requirements are demanded of the instrument:

- large field of view to cover the variability of the numerous sources
- good angular resolution in order to localize and identify sources accurately

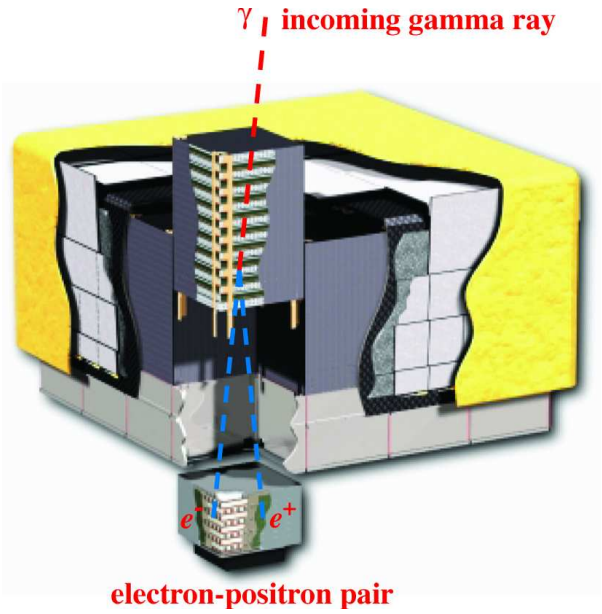

Figure 5.2: Schematic diagram of LAT. A pair conversion of the incident γ-ray is induced in one of the 16 tracker modules, in which the trajectory of the pair is tracked as well. Its energy is measured in the calorimeter modules below. The system is covered with a segmented anticoincidence detector. (Origin of the image: Atwood et al., 2009, Fig. 1)

- broad energy coverage and good spectral resolution
- capability of measurements in short time scales for studying transient or highly variable events, such as γ-ray bursts
- long operation time in order to provide long exposures for weak sources as well as to allow long-term studies of sources
- good background rejection

The functional principle and performance of LAT discussed in the current section follows the full technical description of LAT by Atwood et al. (2009).[8] As the energy of γ-ray photons is too high to reflect or refract them in a reasonable way, efficient γ-ray telescopes require the usage other mechanisms. LAT is a pair conversion telescope, i.e., direction and energy of an incident γ-ray photon are determined via an electron positron pair, whose production is induced by the γ-ray in the telescope. The track and the energy of the pair is measured in a tracker and a calorimeter. Figure 5.2 shows a schematic diagram of the LAT instrument. It consists of an array of tracker modules located above the calorimeter modules. The system is covered with a segmented anticoincidence detector.

Precision Converter-Tracker The purpose of this instrument is to convert an incident γ-ray photon into an electron-positron pair and to track the trajectory of the pair. Its functionality and properties are discussed by Atwood et al. (2009, Sect. 2.2.1) and in even more detail by Atwood et al. (2007). The converter-tracker consists of 16 modules which are aligned in a 4×4-array (see Fig. 5.2). As indicated in Fig. 5.2 each tracker module includes several layers. In every module there are 18 tracking planes, which can measure the position of charged particles passing through the plane. Each plane consists of two layers of silicon strip detectors, where each of them can determine the penetration point of the particle in one dimension of the plane. Due to their orientation the complete position in the plane is obtained. In front of each of the top 16 tracking planes one layer

[8] William B. Atwood was awarded with the 2012 American Physical Society's W. H. K. Panofsky Prize in Elementary Particle Physics "For his leading work on the design, construction, and use of the Large Area Telescope on the Fermi Gamma-Ray Satellite, enabling numerous new results in gamma-ray astrophysics and fundamental physics." (http://www.aps.org/programs/honors/prizes/panofsky.cfm).

of a conversion-foil is located. The foils are made out of tungsten. As tungsten is a dense metal with a high nuclear charge, it is suitable to induce a pair-conversion of incident γ-rays.

Based on the penetration points of the electron and the positron through the layers, the incident angle of the γ-ray can be determined. The uncertainty of the reconstructed direction can be characterized by the telescope's point spread function (PSF). The PSF is given by the instrument's response to a point source. The accuracy of the reconstructed incident angle can be influenced by several effects. The path of the electron-positron pair can be distorted due to multiple scattering and bremsstrahlung. In order to avoid these processes and to measure the pair as soon as possible after the conversion the tracking planes are located directly behind the conversion-foils. The foils are thin to reduce multiple scattering. The thinner the foils are, the smaller is the effective area for conversion of a γ-ray. To obtain a sufficiently large effective area for high-energy γ-rays the converter-tracker modules are split into a so-called "front" and "back" region. The "front" region are the first twelve conversion layers, with thin conversion-foils. The following four converters are thicker by a factor of about 6 and form the "back" region. A further effect which increases the PSF is the possibility that the pair conversion occurs within the silicon tracking plane or in the space between the layers, which can cause uncertainties due to the distance before the first tracking measurement. Although the conversion-foils do not cover inactive parts of the silicon layers, it can happen that the passage of the pair through one silicon layer (in one of the following planes) is missed, which further negatively affects the PSF.

Additional information on the tracker including readout electronics and background rejection is given by Atwood et al. (2007) and Atwood et al. (2009). Fine segmentation of the silicon drift detectors allows to measure the electron and positron separately. In this case it is more simple to distinguish the signature of a pair from other signals.

Calorimeter Each converter-tracker is followed by a calorimeter module, which is used to measured the energy of the electron-positron pair via the resulting particle shower. Another purpose of the calorimeter is to image the development profile of the shower in order to identify signals, and thus contributing to the background rejection. A determination of the incident direction is possible with the calorimeter due to its segmentation. A calorimeter module consists of 96 CsI(Tl) crystals (of the size $2.7\,\mathrm{cm} \times 2.0\,\mathrm{cm} \times 32.6\,\mathrm{cm}$), which are aligned in eight layers of twelve parallel crystals. The crystals in each layer are orientated orthogonally to the ones in the following layer. More information on the calorimeter is given in Sect. 2.2.2 of Atwood et al. (2009) and the references therein.

Anticoincidence Detector The anticoincidence detector (ACD) is discussed in detail in Sect. 2.2.3 of the technical description of LAT by Atwood et al. (2009). It is used for the background rejection. The ACD is located around the converter-tracker array with the purpose detect charge particles. As the cosmic-ray flux is dominating the γ-ray flux, an efficient rejection of signals in the detectors caused by charged particles is required. For that reason charged particles entering the instrument have to be detected with the ACD with a 0.9997 efficiency. The background rejection is a difficult part of the data processing. It is even not possible to reject all events measured in the converter-tracker and calorimeter, which are correlated with a signal in the ACD. The reason for that is that true γ-ray events can cause major signatures in the ACD due to back splash from their showers in the calorimeter modules. On the other hand it has to be considered that background events can appear as a true γ-ray event. For example it is possible that a background particle hits the outer part of the instrument and interacts such that a γ-ray photon enters the detector, while no charged particle is detected in the ACD. An example for this reaction are positrons annihilating in the inactive parts of the ACD yielding to photons. It is possible as well that a π^0 enters the detector and decays into two γ-rays. The π^0 can originate from a hadronic interaction in the inactive ACD parts. In order to not to be detected by the ACD charged products of this interaction have to be

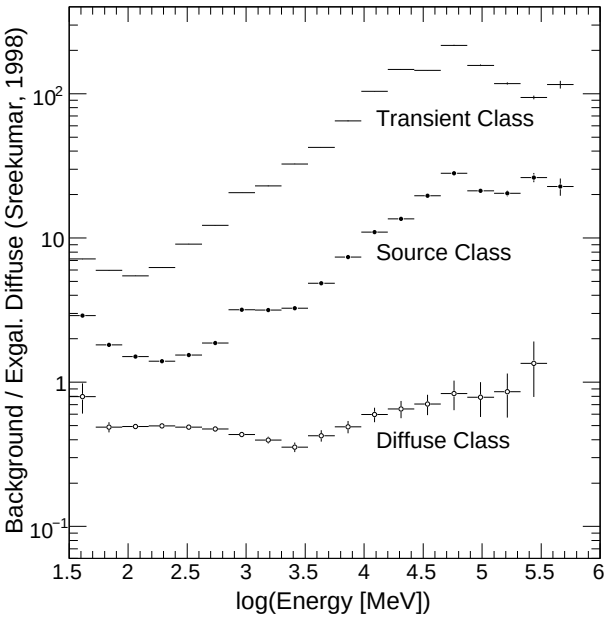

Figure 5.3: Ratio of the background to the extragalactic diffuse emission for different event classes. The values for the diffuse emission were estimated according to Sreekumar et al. (1998). (Origin of the image: Atwood et al., 2009, Fig. 13)

aimed away from the detector.

Instrument Operations The instrument's electronics and mechanics concerning the triggering systems, track reconstruction, energy reconstruction, and background rejection are not discussed in detail in this work, but extensive information is provided by Atwood et al. (2009). In Sect. 2.6.1 of their work a description of the onboard science processing, pipeline and data products, and automated science processing is given. The instrument's measured data is transferred to the LAT Instrument Science Operation Center every two satellite orbits, corresponding to about three hours. A typical amount of downlinked data is about 1.5 GB. In order to process the data before the next block arrives two orbits later, 100 computing cores are used. As processing and reconstruction increases the size of the stored data significantly, about 150 TB of disk space are required for each year of mission operations. To provide rapid information on γ-ray transients, primarily γ-ray bursts but also solar flares and related events, there is automated processing of data onboard the satellite. Of course the methods are significantly simpler than the ground-based analysis. The purpose is to select γ-ray burst candidate events and to search for a preliminary localization. The accuracy of the onboard localization is better than 10 arcminutes for a γ-ray burst with more than 100 counts within less than 20 s (most γ-ray bursts are much shorter). The spacecraft notification after the detection of the γ-ray burst is about 5 s.

Event Classes Important for the analysis of LAT data are the event classes. Depending on the expected backgrounds and the property of the event, it is classified into a structure of three hierarchical classes. The class with the highest requirements is the so-called "diffuse" class. The class "source" has lower requirements and includes all events of the "diffuse" class. The least cuts are applied to the "transient" class, which again contains all the previous classes. In all classes the charged particle background is rejected. As described in Table 6 of Atwood et al. (2009), the "transient" events are suitable for studying localized transient sources, as this class is optimized for a large effective area, but has the highest background rate. The "source" class has a lower background rate and is suitable for analyzing localized sources. For studying weak diffuse sources the highest signal to noise ratio is required, for this purpose the "diffuse" class is optimized. Figure 5.3 shows the ratio of the background to the extragalactic diffuse emission for the different event classes. As more information on the instrument response becomes available during operation, in-flight improvements, which concern data filtering and analysis, are possible. After the first year of

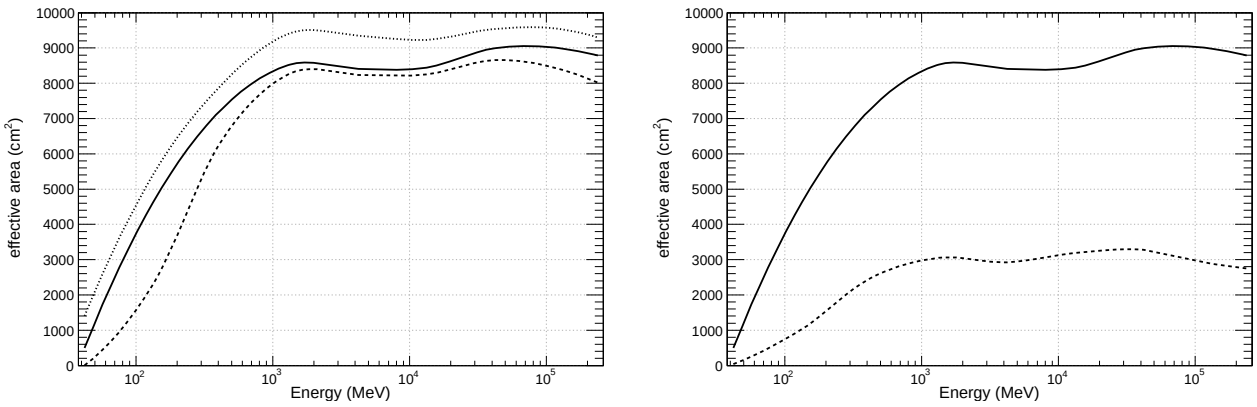

Figure 5.4: Effective area of the LAT. (Atwood et al., 2009, Fig. 14 and 15)

operation the analysis classifications have been optimized as well. The previous three event classes have been replaced in an updated data set (Pass 7) by a finer structure of four classes. The current classes are named "transient", "source", "clean", and ultraclean".

LAT Performance In order to achieve an excellent performance of the instrument, the LAT design of the LAT has been optimized before launch using theoretical and experimental methods. Monte Carlo simulations have been used to estimate and optimize the instruments sensitivity, the back ground rejection, and its other properties. Components of LAT, including a calibration unit consisting of several tracker and calorimeters have been tested with beams at various accelerator laboratories. In the following the performance and measurement capability of LAT will be discussed. Both characteristics are dominated by the instrument's construction, i.e., its hardware, but as discussed before there is an important contribution of the software and the understanding of the instrument. Among others, the background rejection, event classification, reconstruction of the event's direction and energy are improved continuously. New instrument response functions including in-flight improvements are published. The latest information on the LAT performance are provided here: `http://www-glast.slac.stanford.edu/software/IS/glast_lat_performance.htm`. Figures 5.4 and 5.5 were shown in the technical description of LAT by Atwood et al. (2009), and thus do not include the slight post-launch improvements. Figure 5.4 shows the energy dependence of the effective area of LAT.

The instrument's angular resolution (Fig. 5.5, left) has a strong dependence on the energy. The 68% containment radius for reconstructed directions of events converted in the "thin" section of the converter-tracker is almost 10° for 30 MeV events. It decreases at higher energies. At 200 GeV it is about 0.4°. The containment radius is larger for off-axis events. For events converted in the "thick" section of the instrument the containment radius is about twice as large as for conversion in the "thin" section. AS the reconstruction is more difficult due to an increased possibility of multiple scatterings. In Fig. 5.5 (right) the energy resolution is shown for source class events.

Orbit and Sky-Survey Mode An important goal of *Fermi*/LAT is to observe the complete sky in an uniform way within short time scales. To achieve such a challenging goal, an efficient scanning mode is required additionally to the instrument's large field of view. As described by Atwood et al. (2009) the sky coverage is optimized by a rocking movement of the telescope. In an altitude of about 565 km, the duration of an orbit is about 1.5 hours. The orbit is inclined by 25.°5. In two subsequent orbits the pointing position of the instrument alternates between about +35° from the zenith towards north and south, respectively. In this way almost uniform exposure on the complete sky can be obtained within only two satellite orbits, i.e. within three hours. During

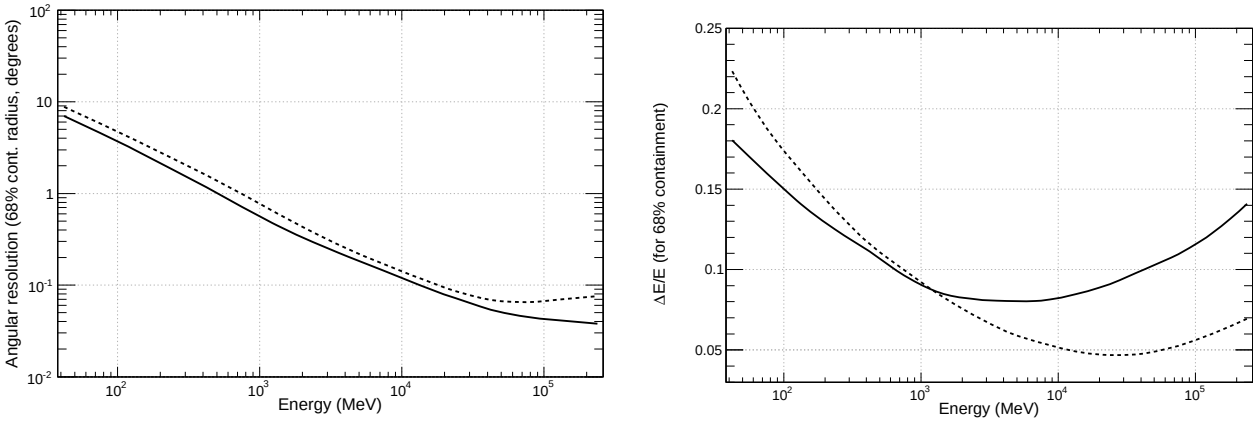

Figure 5.5: *Left:* Angular resolution of LAT as a function of the energy. It is shown as the 68% containment radius of events converted in the "thin" section of the tracker-converter. *Right:* Energy resolution $\Delta E/E$ as a function of the energy. In both plots the solid line is valid for events with normal incident angle, whereas the dashed line corresponds to 60° off-axis events. (Origin of the image: Atwood et al., 2009, Fig. 17 and 18)

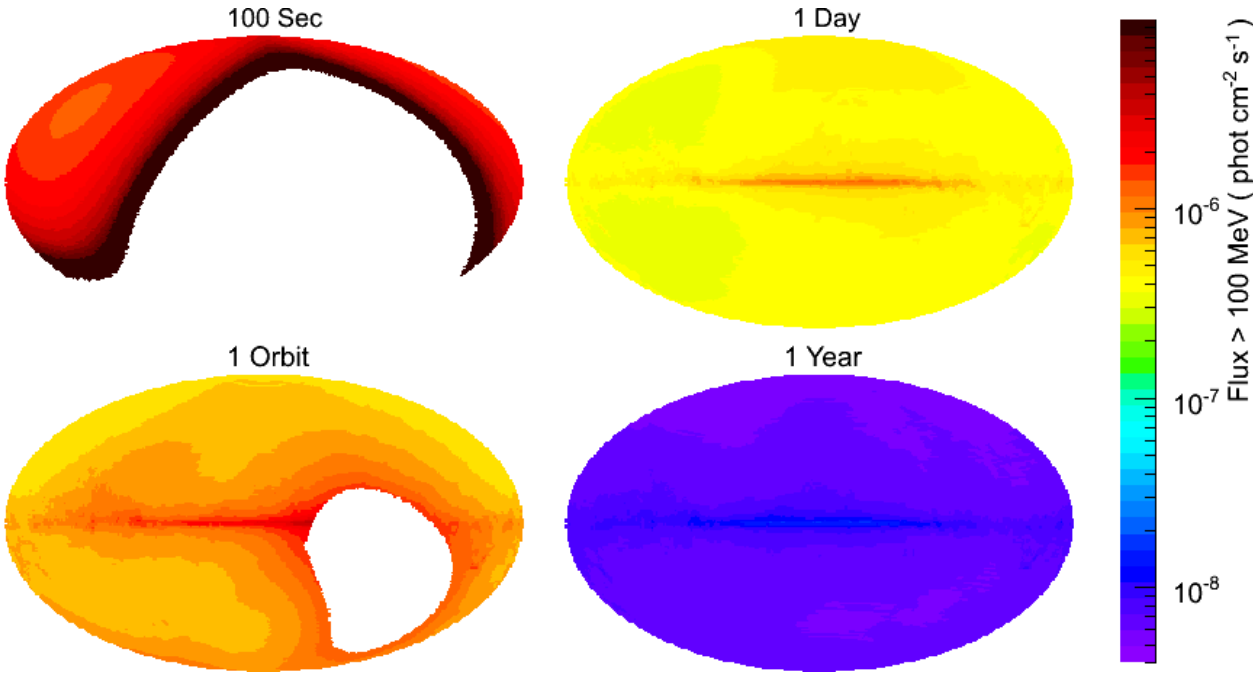

Figure 5.6: Aitoff projection in Galactic coordinates of the *Fermi*/LAT sensitivity for different exposure times. Due to the sky-survey scanning mode of the instrument almost uniform exposure is obtained every two orbits (origin of the image: Atwood et al., 2009, Fig. 2).

that time interval each position in the sky is observed for about 30 minutes. Figure 5.6 shows the resulting sensitivity for different exposures in the standard sky-survey mode. In addition to this observing mode, which has the goal to provide uniform exposure, pointed observations are possible as well.

5.3 Analysis of Gamma-ray data

The aim of data analysis is to obtain source characteristics based on the quantities measured with the instrument. The searched characteristics are here the flux distribution on the sky, which should be disentangled into individual sources. Spectral information and temporal variability of the sources are of interest as well. These quantities have to be inferred from detected photons. For each event the incident time, the reconstructed incident angle, the estimated photon energy, and the event class are available. Data processing methods yielding these values are not discussed here. In addition the orientation of the instrument is recorded during its operation. Given the above mentioned measured values, it is however not possible to obtain the searched source characteristics easily. A complicated analysis is required because of reasons which will be described in the following.

5.3.1 Instrumental Difficulties

One of the main challenges of LAT data analysis arises from the instrument's low angular resolution with a 68% containment radius of several degrees at low energies (Fig. 5.5). A large point spread function means that the reconstructed incident angle of detected photons originating from a point source are distributed in a large region around the true position of the source. As this effect is especially strong at low energies, it is difficult to localize weak sources with a soft γ-ray spectrum, i.e., sources with small number of high-energy photons compared to that of low-energy photons. Sources are mainly localized based on the high-energy events, which have a small containment radius. The brighter the sources are the better they can be localized, as in the case of large counts the point spread function can be models the observed count maps more accurately. For that reason sources can be localize much better than the 68% containment region of single high-energy photons.

Orientation of the instrument comes into play, which makes the analysis even more complicated. As the LAT performance depends on the incident angle of the events, its orientation during an event detection has to be considered. For that reason each event has to be studied individually. Due to the dependence of the performance on the photons incident angle and energy an individual response is required for individual events. This effect is taken into account in the calculation of the exposure map for the analysis. This map is obtained by integrating the sensitivity in each direction given by the instruments response function over the analyzed time of operation considering the instrument's orientation at each time. For that reason information on the spacecraft orientation is required during analysis in addition to the event file. As described above the instrument response function depends on energy and incident angle in order to improve the instrument's performance, however photons of the same energy entering the detector with the same incident angle can still have different uncertainties of their reconstructed origin in sky coordinates due to their interaction within the detector. Depending on where the conversion occurred in the converter-tracker and in how many tracking layers the event could be recorded the photons incident angle can be constrained differently. The different event classes provide thus different IRFs for a given data quality. This IRFs are however average for each event class. For that reason the analysis of weak extended sources can be theoretically improved further by considering the complete measuring process of each event individually.

5.3.2 *Fermi*/LAT Science Tools and Data Access

In the following the typical analysis procedure of *Fermi*/LAT data is described. The *Fermi*/LAT team provides software (*Fermi*/LAT ScienceTools) for the standard and high-level analysis, which is based on the maximum likelihood method. Detailed information on the ScienceTools and their application is provided online at `http://fermi.gsfc.nasa.gov/ssc/data/analysis/`, the *Cicerone* (`http://fermi.gsfc.nasa.gov/ssc/data/analysis/documentation/Cicerone/`). The analysis methods are also described on the basis of individual studies of sources (see, e.g., Abdo et al.,

2010c). The *Fermi*/LAT team frequently provides new versions of the ScienceTools. Changes and the current versions are listed in the online documentation.

In this section a brief overview on the analysis of *Fermi*/LAT data is presented, which follows the references listed above. For the data analysis the following files are required:

1. event data file
2. spacecraft data file
3. current background models

The event data file is essential for the analysis. It includes information on the properties of measured photons, such as the detection time, the measured energy, the determined incident angle and the reconstructed origin in sky coordinates. Among other information the spacecraft data file includes the orientation of the space at each time (the file is typically available with 30 s binning). The information on the spacecraft's orientation is required for the analysis as the *Fermi*/LAT performance depends on the incident angle of the events. In principle each photon, which is determined to originate from a certain region in the sky, could be detected during different pointing positions of the instrument and have different energies. For that reason each single photon has its individual detector response and uncertainty of its properties. In the analysis process it is therefore required to consider the spacecraft's orientation for each detected event. The event data and the spacecraft file are provided on the *Fermi*/LAT data server (see, e.g., http://fermi.gsfc.nasa.gov/ssc/data/access/ for information on data access). Here, custom data files can be obtained, where certain time intervals, energy ranges, and further filters can be selected.

The *Fermi*/LAT science tools offer two methods: the binned and the unbinned analysis. In the unbinned analysis the events are treated individually, whereas for the binned analysis the events are binned in sky coordinates and energy. When large time ranges are analyzed and large numbers of photons are included, the calculation times for the determination of source parameters are obviously smaller for the binned analysis. In this work only the unbinned analysis has been used, therefore the following description is more focused on the unbinned analysis.

5.3.3 Data Preparation

Given the event and the spacecraft file *Fermi*/LAT data can be analyzed. The first step of the data analysis is selection and filtering of data. Obviously a time range has to be given. Data is available since the start of *Fermi*/LAT operations and almost up to latest observations. Besides the selection of the analyzed time interval the energy range can be specified. The *Fermi* Science Support Center recommends to use events with energies above 100 MeV with the Pass 7 event selection. The recommended event class is 2 for the analysis of point sources, and 3 for extragalactic diffuse analysis. For studies of short time intervals (< 200 s), which are, e.g., used for the study of γ-ray bursts, event class 0 for transients can be used. Additionally to the selection of time and energy ranges, the analyzed region should be specified. Due to the large PSF photons can be detected up to several degrees away from the true source position, thus large region of interest around the studied source or region is required. The studied position can include events originating from surrounding sources, which are again influenced from nearby sources. In order to study one position in detail, it would therefore be necessary to model data from the complete sky simultaneously. This is however not practicable, as already the analysis of regions of several degrees in radius is very time consuming when a time interval of several months or years is considered. For that reason models for the surrounding sources are used, which are based on the *Fermi*/LAT catalogs, and the region of interest around the studied position or source is selected such that all events originating from that position are included in the region of interest. Typical regions of interest have thus radii in the range of 10–20 degrees. Programs to filter *Fermi*/LAT data for time, energy, and position

are included in the *Fermi*/LAT ScienceTools. Another important filter criterion is the maximal zenith angle. Given its orbit, the zenith angle of the Earth's limb is 113 degrees. The Earth's limb is a bright source of atmospheric γ-ray. In order to avoid the contamination of these photons, a maximal zenith angle of 100 degrees is recommended from the *Fermi* Science Support Center. Data which have been obtained while parts of the region of interested exceed the maximal zenith angle are excluded from the analysis.

In addition to the selection of the total time range for data, good time intervals (GTIs) within that specified time range have to be determined. GTIs provide information if data at a given time are "good", i.e., if they are valid an can be used for analysis. The studied object is usually not in the field of view permanently, and there can be further reasons why certain periods should not be used in the analysis. For example *Fermi*/LAT is not taking data during the passage of the South Atlantic Anomaly (SAA)[9], or during maneuvers of the spacecraft and software updates (the latter events are usually rare). Times in which the quality of *Fermi*/LAT data are decreased are excluded as well with GTIs. The GTIs are crucial for the calculation of the exposure time.

5.3.4 Source Model

As the instrument response function cannot be inverted easily, the flux distribution on the sky cannot be obtained directly from the measured counts. As in X-ray astronomy (Sect. 2.2.2) the true flux distribution on the sky is determined via a source model, which is folded with the detector response, compared with the data, and varied to achieve the best possible agreement. The flux density distribution on the sky, $S(E, \hat{p}, t)$, depends on the energy, E, and the position, $\hat{p}$, in addition it can be variable with time t. The model can be separated into different components. Two obvious diffuse background components are the extragalactic diffuse emission $S_{EG}(E, \hat{p})$ and the Galactic diffuse emission $S_G(E, \hat{p})$ (see, e.g., Moskalenko et al., 2004, for a review of diffuse γ-ray emission). Both models do not depend on t, as they are considered to be invariable on the studied time scales. The Galactic diffuse emission has a strong spatial dependence, as this emission is originating from interactions in the material of the Galaxy (e.g., cosmic rays interacting with interstellar gas). This model has been developed using the distribution of interstellar gas. The distribution has been derived from spectral line observations. In particular the used lines were the HI line at 1420.406 MHz (which is a tracer of molecular hydrogen) and a carbon monoxide (CO) line at 806.652 GHz. A detailed description of the production of γ-rays in the interstellar medium is given for example by Dermer (1986) and Hunter & Kanbach (1990). The extragalactic diffuse emission is considered to be isotropic and is discussed in detail by, e.g., Sreekumar et al. (1998). Both background models are provided and updated by the *Fermi*/LAT team.

Besides the background models the source model includes point sources $S_i(E, t)$ located at positions $\hat{p}_i$. In addition there are further sources $S_i(E, \hat{p}, t)$, such as the Sun, the Moon, supernova remnants, etc., which can be extended (i.e. resolved by *Fermi*/LAT) and possibly variable with time or moving.

The complete source model can be written in the following form:

$$S(E, \hat{p}, t) = \sum_i s_i(E, t)\delta(\hat{p} - \hat{p}_i) + S_G(E, \hat{p}) + S_{EG}(E, \hat{p}) + \sum_i S_i(E, \hat{p}, t) \tag{5.1}$$

In the standard analysis the sources are assumed to be constant during the studied time range. For that reason the time-dependence is neglected and the determined model parameters, such as the spectral shape or the intensity are averaged over the time interval. A standard method to study

[9]The South Atlantic Anomaly is a region located above South America and the southern Atlantic, in which the density of energetic charged particles is strongly increased. Because of the significantly larger background radiation most instruments onboard satellites are switched of during SAA transits. The reason for the larger particle flux is that due to the shape of Earth's magnetic field, the inner Van Allen radiation belts are closer to the surface of the Earth in that region. More information on the SAA is, e.g., provided by Fürst et al. (2009)

variability, e.g., to obtain a light curve, is to cut the time range of interest into bins, in which the spectrum and intensity of the sources can be considered as constant.

As mentioned above the diffuse models are provided by the *Fermi*/LAT team, in addition models for extended sources are available. For the point sources the *Fermi*/LAT catalogs can be used. The *Fermi*/LAT team studied the complete data in order to obtain all sources in the sky, which are detected with a significance above a certain threshold. Updated catalogs are published with increasing observation times. Currently (at the time when this work has been written) the most important *Fermi*/LAT catalogs cover the first year (1FGL catalog) and the first two years of *Fermi*/LAT operation. More information on these catalogs is provided in Sect. 5.4. The determination of the positions of the catalog sources and their spectral properties was an iterative process. The complete sky has been modeled starting with initially putting sources at the positions with the highest count excesses. The steps have been repeated until a final model converged.

The components listed above can be used to obtain an initial model for the analysis. Although the sources and their parameters in the *Fermi*/LAT catalogs have been averaged over certain time ranges, they provide an excellent initial model for user-defined analyses. Tools to generated a source model for a given region are provided by the *Fermi*/LAT team. For the analysis of a position on the sky (or a given source) the parameters of the model components in the region of interest (ROI), which is centered around the analyzed position, are left variable during the analysis process. The reason for that is that these source can still influence the position of the studied due to the large PSF. Sources around the region of interest are considered as well, but their parameters are usually frozen, as they do not directly influence the central position. However their flux can contribute to the outer parts of the region of interest. This method is a compromise. On the one hand the influence of surrounding source on the analyzed region is considered and on the other hand the computation time required for the analysis is reasonable, as it would not be the case when varying all sources in the complete sky during the analysis of a single position.

5.3.5 Lifetime Cubes and Exposure Maps

As described previously the response of the *Fermi*/LAT depends on the inclination angle of the γ-rays relative to the orientation of the instrument. Here, this angle can be defined as the angle between the *Fermi*/LAT normal and the incident angle of the photon. As the instrument changes its pointing position during the orbits in scanning mode, this angle changes as well. Due to the angle-dependent sensitivity the measured counts of a source depend on the times which the instrument spends at each angle with respect to the source. These times are defined as the "lifetimes". Using the spacecraft file and the filters described above the lifetime is determined for each position in the sky and for each inclination angle. For practicable usage these quantities are determined in binned form, i.e., on an inclination grid and a two-dimensional healpix grid on the sky. The array of lifetimes in this three-dimensional grid is called "lifetime cube". As noted by the *Fermi* Science Support Center, lifetime cubes are calculated for the complete sky and thus do not have to be recalculated for different analyses of the same time interval, such as different sources during one time period. Lifetime cubes are additive.

Using the response function of *Fermi*/LAT, an exposure map and the expected count distribution corresponding to the model can be determined. The total response R is given in the following simplified and factorized way

$$R(E', \hat{p}'; E, \hat{p}, t) = A(E, \hat{p}, \vec{L}(t))\ D(E'; E, \hat{p}, \vec{L}(t))\ P(\hat{p}; E, \hat{p}, \vec{L}(t)) \tag{5.2}$$

where E is the energy of a γ-ray photon and $\hat{E}$ its incident direction. The quantities E' and $\hat{p}'$ are the corresponding measured values. The dependence on the time t mainly characterizes the orientation of the instrument at each time $\vec{L}(t)$. Additionally to the orientation internal degrees of freedom can be included here. The angular dependence of the *Fermi*/LAT response is mainly

characterized by the incident angle of the photon with respect to the current orientation and not independently on both directions. The components of the factorized instrument response function are the effective area A, the energy dispersion D, and the PSF P.

Given a source model and the response, an expected count map corresponding to the model can be obtained by folding the model with the response:

$$M(E', \hat{p}') = \int \mathrm{d}E \int\limits_{\text{exposure}} \mathrm{d}t \int\limits_{\text{Sky}} \mathrm{d}\hat{p}\; R(E', \hat{p}'; E, \hat{p}, t) S(E, \hat{p}, t) \tag{5.3}$$

The predicted total number N_{pred} of counts in the region of interest is then given by the integration of the expression above:

$$N_{\text{pred}} = \int \mathrm{d}E' \int\limits_{\text{ROI}} \mathrm{d}\hat{p}' M(E', \hat{p}'). \tag{5.4}$$

In order to save computation time during the analysis a quantity similar to a exposure map can be calculated:

$$\epsilon(E, \hat{p}) = \int \mathrm{d}E' \int\limits_{\text{exposure}} \mathrm{d}t \int\limits_{\text{ROI}} \mathrm{d}\hat{p}'\; R(E', \hat{p}'; E, \hat{p}, t) S(E, \hat{p}, t). \tag{5.5}$$

As E' and $\hat{p}'$ are the measured energies and directions, respectively, this "exposure map" gives the exposure "for a given position on the sky producing counts" in the ROI (*Fermi* Science Support Center, see above mentioned references for more information). Using the exposure map the predicted number of counts can be determined via:

$$N_{\text{pred}} = \int \mathrm{d}E \int\limits_{\text{ROI}} \mathrm{d}\hat{p}\; S(E, \hat{p})\; \epsilon(E, \hat{p}) \tag{5.6}$$

5.3.6 Likelihood Analysis

As noted at the beginning of Sect. 5.3 the aim of the data analysis is to obtain the best possible estimation of the properties of observed sources, such as intensity, spectral information, spatial flux distribution, and variability. In high-energy astronomy typically individual photon events can be measured, which are then binned to data grids for the parameter estimation. The parameter estimation using the likelihood ratio is described in detail by Cash (1979) and is summarized in the following. The likelihood ratio is especially useful in the case of a small number of counts. If the number of counts in each bin is high enough, the χ^2 statistic is valid for modeling the data:

$$\chi^2 = \sum_{i=0}^{N} \frac{(n_i - \theta_i)^2}{\theta_i} \tag{5.7}$$

where n_i is the observed number of counts, θ_i the expected number of counts from the correct model in each bin i. N is the number of bins. In this case the distribution of the differences between measured and expected counts can be approximated with a Gaussian distribution. The quality of the model be measured easily. With σ of the Gaussian distribution being the square root of the number of counts in each bin, a good fit is characterized by $\chi^2/N \approx 1$. In the case of few counts the situation is more difficult. A method which had been successfully used for the analysis of γ-ray data, e.g., for EGRET data, is the maximum likelihood analysis. It is used for the analysis of *Fermi*/LAT data as well. For a measured data set the likelihood of a model is the probability of obtaining the given data set under the assumption that the model is correct. With Poisson statistics the probability L to obtain a set of n_i events in the bin i, given the predicted counts θ_i from the correct model (Cash, 1979, Eq. 2):

$$\mathcal{L} = \prod_{i=0}^{N} \frac{\theta_i^{n_i} e^{-\theta_i}}{n_i!} \tag{5.8}$$

L is thus the likelihood of the model yielding the set of θ_i, where the θ_i depend on the model and its parameters. The set of parameters which maximizes the statistic in Eq. 5.8 the is maximum likelihood estimate. How to obtain confidence levels for the parameters using the likelihood ratio is described by Cash (1979). For that purpose the following statistic is formed:

$$C = -2\ln(\mathcal{L}) = -2\sum_{i=0}^{N}(n_i \ln(\theta_i) - \theta_i - \ln(n_i!)). \tag{5.9}$$

It can be studied how different values of the model parameters change the statistic. Improvements can be measured with the difference between the statistic corresponding to the different configurations. As mainly relative changes of the statistic and not its absolute value are used, the term $\ln(n_i!)$ can be neglected. It is independent of the model and thus cancels out in the subtraction.

A value which is frequently used by the *Fermi*/LAT team, as well as in this work, is the test statistic (TS):

$$\mathrm{TS} = -2\ln(\mathcal{L}_{\mathrm{max},0}/\mathcal{L}_{\mathrm{max}}) \tag{5.10}$$

With this expression the significance of a source can be calculated. In this case $\mathcal{L}_{\mathrm{max},0}$ is the maximum likelihood of the null hypothesis, i.e. the model without the source, and $\mathcal{L}_{\mathrm{max}}$ is the maximum likelihood of the model in which the source has been included. According to Wilks' theorem (Wilks, 1938) the logarithm of the likelihood ratio multiplied by -2 has a probability distribution which is asymptotically like a χ^2 distribution with the degrees of freedom being given by the difference of the number of free parameters. In the example of determining the significance of a source, the degrees of freedom correspond to the number of parameters characterizing the additional source. A simplified estimate is that $\sqrt{\mathrm{TS}}$ is comparable to the significance in σ.

For the analysis of EGRET data the maximum likelihood method was successfully applied (Mattox et al., 1996). The analysis of *Fermi*/LAT data is based on this technique as well. There are, however, differences in the detailed application. Whereas in the EGRET data analysis (for energies above 100 MeV) the source detection and localization was decoupled from the spectral analysis and only a single energy-independent PSF had been used, the analysis of *Fermi*/LAT data is more advanced. Here the estimation of all source parameters is coupled, because basically an individual response is required for each event (see Sects. 5.3.1 and 5.3.5). An obvious example for the necessity of coupled estimation parameters, such as spectral properties, total flux, and position, are nearby sources. Here, there can be strong energy-dependent overlaps of counts. The degree of source confusion depends on the source spectra.

For binned data Eq. 5.8 can be applied. Data can be binned, e.g., in sky coordinates and energy. Using the logarithm of the likelihood (as in Eq. 5.9) and neglecting the model-independent term yields:

$$\ln(\mathcal{L}) = \sum_{i=0}^{N} n_i \ln(\theta_i) - \sum_{i=0}^{N} \theta_i. \tag{5.11}$$

The sum of the θ_i gives the total number of predicted counts N_{pred}. For the region of interest this quantity is given by Eq. 5.4. In the case of unbinned analysis the first sum over the bins in Eq. 5.11 can be replaced by the sum of the detected events in the region of interest. The reason for that is the following: If the size of the bins is decreased, the counts are distributed into more bins, and thus the number of counts per bin decreases. In the limit of infinitely small bins, the number of counts in the bins n_i is either 0 or 1. Considering the estimated number of counts at the measured energy E' and position $\hat{p}'$, which is given in Eq. 5.3, yields:

$$\ln(\mathcal{L}) = \sum_{j} \ln\left(M(E'_j, \hat{p}'_j)\right) - N_{\mathrm{pred}} \tag{5.12}$$

where the sum runs over all measured events in the region of interest.

The function in Eq. 5.12 is used in the *Fermi*/LAT science tools has been applied in the *Fermi*/LAT data analysis presented in this work, such as the upper limit calculations and parameters estimations of spectral models.

5.4 Source catalogs obtained with *Fermi*/LAT

Since its launch the *Fermi* instrument provided numerous scientific results and new insights in high-energy astronomy. A review of the results obtained in the first year of *Fermi*/LAT is provided by Michelson et al. (2010). In the following an overview on the *Fermi*/LAT source catalogs, which are required for this work, is given.

In its scanning mode *Fermi*/LAT obtains almost uniform exposure on the sky, which is important for the monitoring of the complete sky and sample analyses. Figure 5.7 shows all-sky projections of events which have been measured during the first three years of *Fermi*/LAT operations. The two shown images contain events with energies above 1 GeV and above 10 GeV, respectively. The Galactic plane is clearly visible in both images. It consists of several point sources and the Galactic diffuse emission. In addition there are numerous sources which are located outside of the Galactic plane. The extragalactic sources are mainly AGN.

The sources and their properties have been analyzed and published by the *Fermi*/LAT team. In the following an overview on the current catalogs is given. Based on the first three months of *Fermi*/LAT operation, the most significant sources have been presented by Abdo et al. (2009a). This *Fermi*/LAT bright γ-ray source list includes all sources which have been detected in the data collected in that time range with a TS above 100, which corresponds to a significance of $\gtrsim 10\sigma$. This catalog contains 205 sources and is also know as the 0FGL catalog.

1FGL catalog The "*Fermi* Large Area Telescope First Source Catalog", which is called 1FGL catalog, contains sources detected in the first 11 months of *Fermi*/LAT operation. It is discussed in great detail by Abdo et al. (2010a). The exact time interval of the data ranges from 2008 August 4 until 2009 July 4. Or given in mission elapsed time (MET) the interval is 239557414–268411953. For many satellite missions the observation times are typically given in MET, which is defined as the time in seconds since a mission reference data. For *Fermi* the MET is given in seconds since 00:00 UTC on 2001, January 1. The energy band used for the 1FGL catalog extends from 100 MeV to 100 GeV. Using this time and energy range sources have been detected, localized, and their spectral characteristics determined. As the developed model in the standard *Fermi*/LAT data analysis is time-independent, effectively the obtained source properties are averaged over the selected time interval. However, after sources had been localized and averaged, their variability has been studied as well. For each source, the public 1FGL catalog includes the intensity with monthly binning in addition to the averaged properties. The 1FGL catalog contains all sources which are detected in the total 11 month time range with TS > 25 (which corresponds to a statistical significance $\gtrsim 4\sigma$). The minimal flux for a point source (with spectral index of 2.2), which is required to exceed a TS of 25, is shown in Fig. 5.8 for each position on the sky. This limiting flux depends on the spectral index of the source, because of *Fermi*/LAT's IRF. This relation is shown in Fig. 5.9.

The total number of sources in the 1FGL catalog is 1451. The majority of these sources are associated with counterparts at other wavelengths, but 630 sources remained without a plausible counterpart. As pointed out by the *Fermi*/LAT team there are only a few unique identifications, which are based on timing signals or correlated variability in other energy bands of the counterpart candidate. Especially most pulsars can be identified due to the period of the pulsed emission. Unless there is further temporal information leading to an identification, there are only associations based on positional coincidence. Although all sources in the 1FGL catalog are localized relatively well, there are typically several known sources at other energy bands (radio, infrared, optical, X-ray, etc.) within the γ-ray source region, such as stars, and galaxies. On average the semimajor axis of

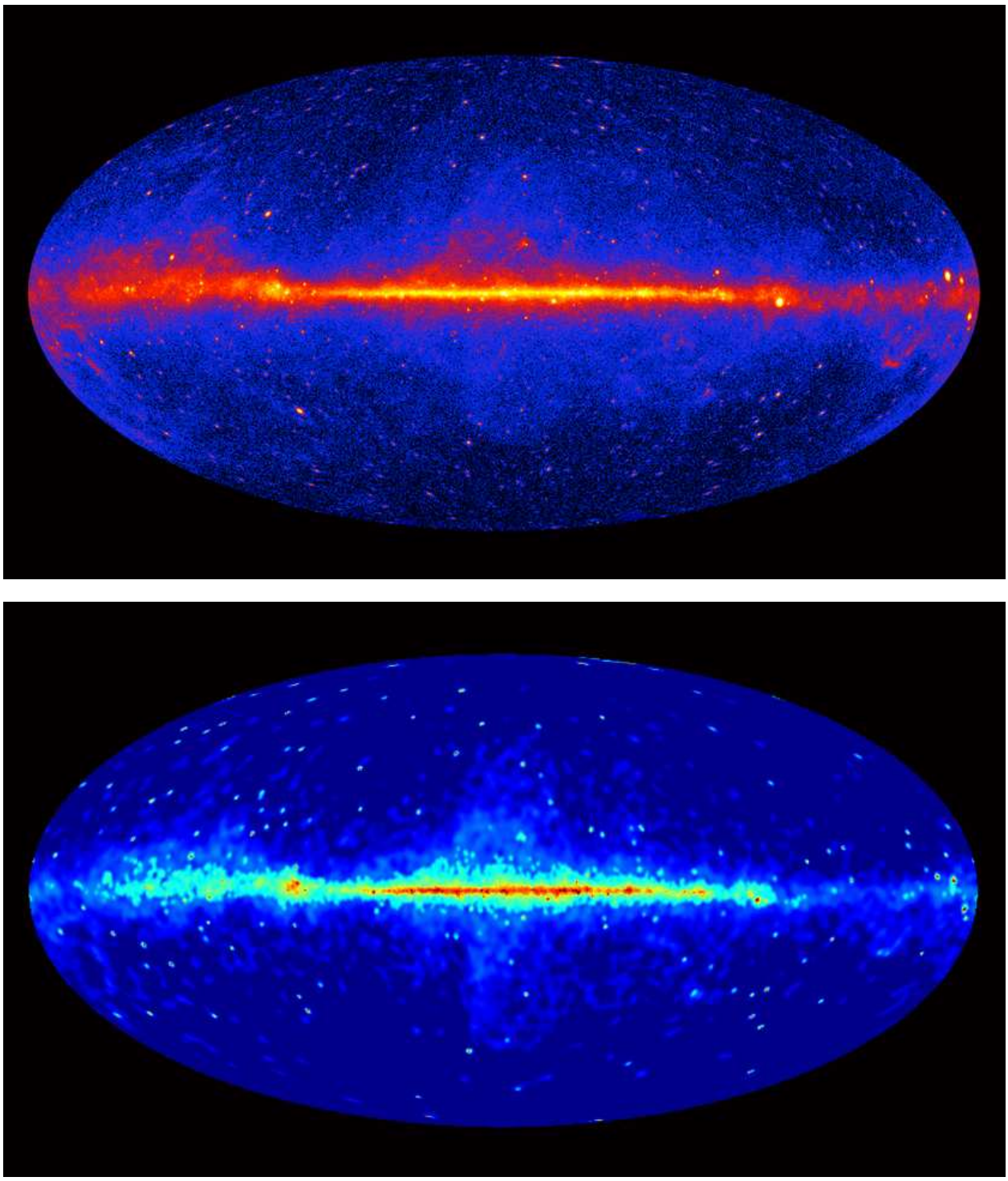

Figure 5.7: The γ-ray sky as seen by *Fermi*/LAT. Both images are projections of the complete sky in Galactic coordinates with an exposure of three years. The top image includes events above 1 GeV, whereas only photons with energies above 10 GeV are used in the bottom image. (Credit: NASA, DOE, *Fermi*/LAT Collaboration)

the 95% confidence region of the 1FGL sources is 0.13 degrees and for the best localized source it is about 0.5 arcminutes. Considering, e.g., the broad band spectra of the counterpart candidates, the probability that the associations are true counterparts is, however, large in many cases. For

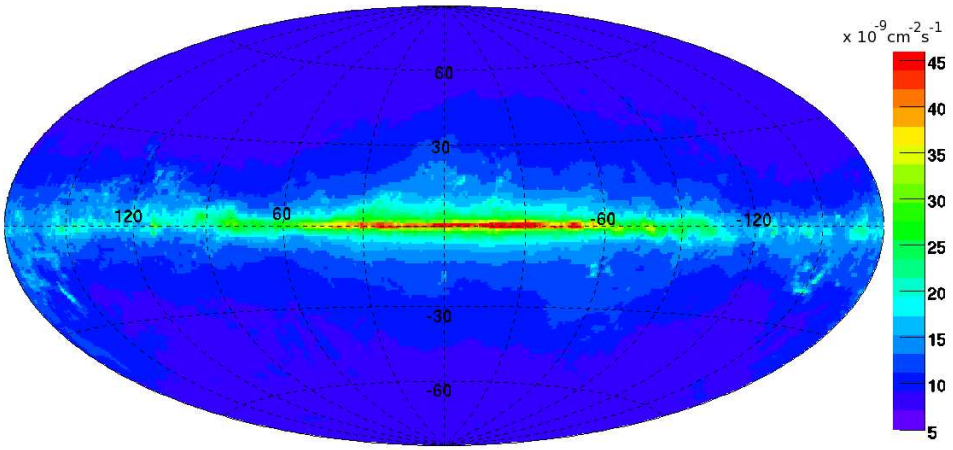

Figure 5.8: All-sky projection in Galactic coordinates of the sensitivity limit of *Fermi*/LAT (determined by the *Fermi*/LAT team, Abdo et al., 2010a, Fig. 19). The color code represents the flux (in photons $\mathrm{cm}^{-2}\,\mathrm{s}^{-1}$) of a point source with spectral index 2.2, which is required (based on the diffuse background model) such that the source is detected with TS = 25 in the 1FGL period.

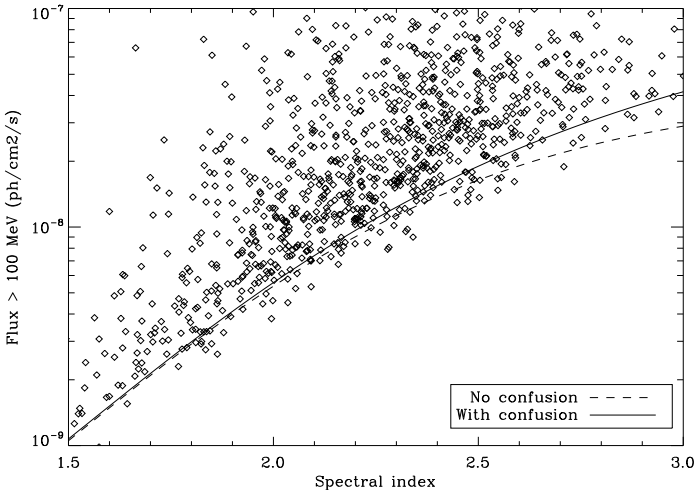

Figure 5.9: Spectral indices and fluxes of the 1FGL sources. As the source localization depends on the spectral index, the significance of a source depends on the flux and the spectral index. The lines indicate the TS = 25 limit for the 1FGL period (as determined by the *Fermi*/LAT team, Abdo et al., 2010a, Fig. 20).

example bright AGN, which are clearly detected from the radio to the X-ray regime, are obviously more plausible counterparts of γ-ray sources, than faint stars.

2FGL catalog The "*Fermi*/LAT Second Source Catalog" (2FGL) is based on the first 24 months of *Fermi*/LAT data. A detailed discussion of the catalog and its construction is given by Nolan et al. (2012). The used time range begins at the same as the 1FGL catalog (2008, August 4, 15:43 UTC), but it extends until 2010 August 1 (01:17 UTC), which corresponds to MET 302318220. The 2FGL catalog has been created in a similar way as the 1FGL catalog. In total 1873 sources are detected above the TS > 25 criterion. Contrary to the 1FGL catalog, in which only power law spectra have been used to model the sources, slightly more complicated spectral models have been included in the 2FGL catalog. The longer exposure revealed stronger deviations from simple power laws. The spectra of many sources showed clear curvature (in the $\log(E)$-$\log(S)$ space). The additionally used models were a exponentially cut off power law, which describes numerous pulsar spectra very well, and the so-called LogParabola (which is a parabola in the $\log(E)$-$\log(S)$ space). These models were applied in the cases in which they were significant. The criterion was TS > 16. Given the additional parameter for the curvature this corresponds to a 4σ significance.

5.5 Gamma-ray Properties of TANAMI Sample

In this section the γ-ray properties of the TANAMI sample are discussed. Results of this study are published by the TANAMI team (Böck et al., 2012).[10] An overview on the analysis and the results is given in the following. In this study the γ-ray properties of the sources are compared with other source properties such as the classification and in particular the radio properties, which have been obtained from TANAMI VLBI observations. As AGN are variable – especially in the γ-ray regime – it is important to select corresponding time intervals for observations in different energy bands. The selected time interval for this analysis was the 1FGL period (which is described in Sect. 5.4). This choice allows to use the results of the 1FGL catalog, with the source properties firmly determined by the *Fermi*/LAT team. The main reason for this selection is the fact that for this time interval the TANAMI team finalized the calibration and analysis of VLBI observations. For the majority of TANAMI AGN, at least one VLBI image at 8.4 GHz is available and the core flux has been determined. The radio properties in this time interval can thus be compared with the γ-ray properties during the corresponding period.

The γ-ray analysis of the TANAMI sample consists of two separated parts. On the one hand it had to be checked which sources are γ-ray bright, i.e., if they are detected significantly with *Fermi*/LAT during the first eleven months of *Fermi* operation. The search for 1FGL counterparts for objects in the TANAMI sample is described in Sect. 5.5.1. On the other hand, upper limits on the γ-ray flux were required for AGN which could not be detected in the *Fermi*/LAT data (Sect. 5.5.2).

5.5.1 Gamma-ray Counterparts of TANAMI AGN

Source Association The association of the objects in the TANAMI sample with 1FGL sources is based on positional coincidence. The counterparts were searched in the following simple way. For each object in the TANAMI sample the radio position was used and the angular separation between this position and the positions of the objects in the 1FGL calculated. In this way the closest γ-ray source was obtained for each TANAMI AGN. Given the separation and the uncertainties of the position measurements a probability for the positional coincidence can be calculated (Sect. 4.3). Here, the uncertainty of the radio position can be neglected, as it is significantly smaller than arcseconds. In contrast, the *Fermi*/LAT detected γ-ray sources are localized only with a fraction of a degree (Sect. 5.4). Using the *Fermi*/LAT 95% confidence region as criteria for the source association works well. A number of TANAMI AGN clearly remain without γ-ray counterpart as they lie several degrees outside of the confidence region of the closest *Fermi*/LAT sources. There are only a small number of objects which are located close to the edge of the confidence region, while a large number of sources have a very good positional agreement (automatized scripts for this procedure have been implemented in local software packages within the scope of this work). The association turned out to be unique in all cases. There were no TANAMI AGN which were associated with the same γ-ray sources and the other way around it did not occur that a TANAMI AGN was located inside of more than one confidence regions of γ-ray sources. For the association of the sources it has to be considered as well how many other possible counterparts are located in the corresponding region. For that reason the preliminary associations were checked for consistency with the results of the automatic source association pipeline for γ-ray sources of the LAT team Abdo et al. (2009a). In addition to the simple positional agreement, an association probability can be determined considering the counterpart candidate's class and physical expectations of the association. Healey et al. (2008) discuss such a figure-of-merit approach for finding AGN associations. The results of these methods were consistent with the above mentioned simple positional comparison. The resulting list of associated objects in the sample and their properties is shown in Table 5.1. The associations

[10] Prelimanary results have been published earlier by Böck et al. (2009, 2010b).

Table 5.1: List of TANAMI AGN associated with 1FGL sources.

Source	Name[a]	Common name	1FGL Association	TS	Flux (0.1–100 GeV) [10^{-8} ph cm^{-2} s^{-1}]	LAT Γ	L (0.1–100 GeV) [erg s^{-1}]	$S_{\rm core}$ (8.4 GHz) Jy	T_B K	ID[b]	z
J0049-5738	0047-579	[HB89] 0047-579	1FGL J0049.8-5738	80.2	2.3 ± 0.7	2.42 ± 0.17	$(0.39 \pm 0.16) \times 10^{48}$	1.35 ± 0.20	4.8×10^{11}	Q	1.797
J0058-3234	0055-328	PKS 0055-328	1FGL J0058.4-3235	60.7	1.6 ± 0.5	2.31 ± 0.16		0.060 ± 0.009			
J0210-5101	0208-512	[HB89] 0208-512	1FGL J0210.6-5101	1175.4	14.6 ± 1.0	2.37 ± 0.05	$(0.48 \pm 0.04) \times 10^{48}$	1.39 ± 0.20	2.3×10^{11}	Q	0.999
J0229-3643	0227-369	PKS 0227-369	1FGL J0229.3-3644	375.7	8.0 ± 0.8	2.60 ± 0.08	$(2.10 \pm 0.22) \times 10^{48}$	0.38 ± 0.06	2.9×10^{12}	Q	2.115
J0246-4651	0244-470	PKS 0244-470	1FGL J0245.9-4652	570.7	9.4 ± 0.8	2.52 ± 0.07		0.193 ± 0.029			
J0303-6211	0302-623	PKS 0302-623	1FGL J0303.4-6209	116.7	5.1 ± 1.0	2.59 ± 0.13	$(3.8 \pm 0.9) \times 10^{47}$	0.77 ± 0.12	5.4×10^{11}	Q	1.351
J0309-6058	0308-611	PKS 0308-611	1FGL J0310.1-6058	104.2	4.2 ± 1.0	2.53 ± 0.15	$(3.1 \pm 1.0) \times 10^{47}$	0.38 ± 0.06	1.1×10^{12}	Q	1.480
J0334-3725	0332-376	PMN J0334-3725	1FGL J0334.4-3727	226.2	2.8 ± 0.5	2.10 ± 0.09		0.23 ± 0.04			
J0334-4008	0332-403	[HB89] 0332-403	1FGL J0334.2-4010	675.3	8.2 ± 0.7	2.35 ± 0.06	$(0.74 \pm 0.08) \times 10^{48}$	0.95 ± 0.15	1.8×10^{11}	B	1.445
J0403-3605	0402-362	PKS 0402-362	1FGL J0403.9-3603	685.1	10.9 ± 0.9	2.56 ± 0.06	$(0.89 \pm 0.08) \times 10^{48}$	0.24 ± 0.04	3.6×10^{12}	Q	1.417
J0406-3826	0405-385	[HB89] 0405-385	1FGL J0407.4-3827	338.8	6.1 ± 0.8	2.40 ± 0.08	$(3.9 \pm 0.6) \times 10^{47}$	1.38 ± 0.20	1.4×10^{11}	Q	1.285
J0413-5332	0412-536	PMN J0413-5332	1FGL J0413.4-5334	351.7	7.4 ± 0.9	2.55 ± 0.09					
J0428-3756	0426-380	PKS 0426-380	1FGL J0428.6-3756	7749.7	31.5 ± 0.9	2.127 ± 0.020	$(1.72 \pm 0.07) \times 10^{48}$	1.45 ± 0.22	8.6×10^{12}	Q	1.110
J0449-4350	0447-439	PKS 0447-439	1FGL J0449.5-4350	2221.4	9.7 ± 0.7	1.95 ± 0.04	$(3.37 \pm 0.25) \times 10^{47}$	0.069 ± 0.010	$>2.9 \times 10^{11}$	B	0.107
J0455-4615	0454-463	[HB89] 0454-463	1FGL J0455.6-4618	213.9	6.2 ± 0.9	2.57 ± 0.10	$(1.30 \pm 0.20) \times 10^{47}$	3.2 ± 0.5	4.2×10^{11}	Q	0.853
J0506-6109	0506-612	[HB89] 0506-612	1FGL J0507.3-6103	162.5	7.6 ± 1.3	2.73 ± 0.12	$(2.8 \pm 0.6) \times 10^{47}$	1.12 ± 0.17	3.3×10^{11}	Q	1.093
J0516-6207	0516-621	PKS 0516-621	1FGL J0516.7-6207	327.7	5.8 ± 1.0	2.28 ± 0.10		0.48 ± 0.08			
J0522-3627	0521-365	ESO 362- G 021	1FGL J0522.8-3632	604.8	11.5 ± 0.9	2.60 ± 0.07	$(3.34 \pm 0.26) \times 10^{44}$	1.52 ± 0.23	2.9×10^{11}	G	0.055
J0526-4830	0524-485	PKS 0524-485	1FGL J0526.3-4829	137.2	3.6 ± 0.7	2.37 ± 0.12		0.40 ± 0.07			
J0538-4405	0537-441	[HB89] 0537-441	1FGL J0538.8-4404	6494.3	37.8 ± 1.0	2.271 ± 0.022	$(1.01 \pm 0.04) \times 10^{48}$	4.7 ± 0.8	5.6×10^{12}	Q	0.894
J0627-3529	0625-354	PKS 0625-35	1FGL J0627.3-3530	50.4	0.7 ± 0.4	1.86 ± 0.18	$(0.7 \pm 0.4) \times 10^{44}$	0.35 ± 0.06	1.2×10^{11}	B	0.055
J0635-7516	0637-752	[HB89] 0637-752	1FGL J0636.1-7521	109.8	5.1 ± 1.0	2.49 ± 0.13	$(0.43 \pm 0.12) \times 10^{47}$	3.0 ± 0.5	2.0×10^{11}	Q	0.653
J0700-6610	0700-661	PKS 0700-661	1FGL J0700.4-6611	485.5	6.0 ± 0.8	2.15 ± 0.07		0.088 ± 0.014			
J0718-4319	0717-432	PMN J0718-4319	1FGL J0718.7-4320	247.8	1.9 ± 0.4	1.83 ± 0.09		0.0174 ± 0.0027			
J0734-7711	0736-770	PKS 0736-770	1FGL J0734.1-7715	87.6	7.2 ± 1.3	2.75 ± 0.13				Q	
J0747-3310	0745-330	PKS 0745-330	1FGL J0747.4-3303	130.5	8.9 ± 1.4	2.38 ± 0.08					
J0811-7530	0812-736	PMN J0810-7530	1FGL J0811.1-7527	150.9	1.4 ± 0.4	1.80 ± 0.12		0.0107 ± 0.0017			
J1058-8003	1057-797	PKS 1057-79	1FGL J1058.1-8006	154.0	6.3 ± 1.0	2.45 ± 0.10	$(0.46 \pm 0.09) \times 10^{47}$	1.44 ± 0.22	5.1×10^{13}	Q	0.581
J1103-5357	1101-536	PKS 1101-536	1FGL J1103.9-5355	396.4	6.7 ± 0.9	2.05 ± 0.06		0.192 ± 0.029		Q	
J1147-3812	1144-379	[HB89] 1144-379	1FGL J1146.9-3812	220.9	4.9 ± 0.8	2.31 ± 0.09	$(1.9 \pm 0.4) \times 10^{47}$	1.91 ± 0.29	5.9×10^{11}	Q	1.048
J1316-3338	1313-333	[HB89] 1313-333	1FGL J1316.1-3341	321.0	8.1 ± 1.0	2.34 ± 0.08	$(0.48 \pm 0.07) \times 10^{48}$	1.33 ± 0.20	3.7×10^{12}	Q	1.210
J1325-4301	1322-428	Cen A	1FGL J1325.6-4300	627.8	20.4 ± 1.5	2.71 ± 0.06	$(1.27 \pm 0.10) \times 10^{41}$	0.72 ± 0.10	8.6×10^{10}	G	0.002
J1326-5256	1323-526	PMN J1326-5256	1FGL J1327.0-5257	387.0	11.4 ± 1.3	2.33 ± 0.07		1.19 ± 0.18			
J1329-5608	1325-558	PMN J1329-5608	1FGL J1329.2-5605	244.4	13.9 ± 1.6	2.56 ± 0.08		0.24 ± 0.04			
J1347-3750	1344-376	PMN J1347-3750	1FGL J1347.8-3751	73.0	5.0 ± 1.0	2.70 ± 0.15		0.093 ± 0.014			
J1427-4206	1424-418	[HB89] 1424-418	1FGL J1428.2-4204	240.9	6.7 ± 0.9	2.31 ± 0.08	$(0.59 \pm 0.09) \times 10^{48}$	1.47 ± 0.23	1.1×10^{12}	Q	1.522
J1443-3908	1440-389	PKS 1440-389	1FGL J1444.0-3906	288.6	2.3 ± 0.5	1.83 ± 0.08	$(3.6 \pm 0.7) \times 10^{44}$	0.052 ± 0.008	3.4×10^{10}	B	0.065
J1457-3539	1454-354	PKS 1454-354	1FGL J1457.5-3540	3706.9	33.3 ± 1.2	2.274 ± 0.025	$(3.09 \pm 0.12) \times 10^{48}$	0.70 ± 0.10	1.7×10^{11}	Q	1.424
J1505-3432	1501-343	PMN J1505-3432	1FGL J1505.1-3435	48.9	1.1 ± 0.6	2.02 ± 0.19		0.136 ± 0.020			
J1604-4441	1600-445	PMN J1604-4441	1FGL J1604.7-4443	508.8	21.9 ± 1.8	2.46 ± 0.05		0.41 ± 0.07			
J1603-4904	1600-489	PMN J1603-4904	1FGL J1603.8-4903	737.3	19.0 ± 1.8	2.12 ± 0.05		0.128 ± 0.020			
J1610-6649	1606-667	PMN J1610-6649	1FGL J1610.6-6649	266.0	1.18 ± 0.28	1.60 ± 0.10		0.026 ± 0.004			
J1617-7717	1610-771	[HB89] 1610-771	1FGL J1617.9-7716	338.7	10.7 ± 1.2	2.53 ± 0.08	$(1.55 \pm 0.16) \times 10^{48}$	1.38 ± 0.20	9.6×10^{10}	Q	1.710
J1617-5848	1613-586	PMN J1617-5848	1FGL J1617.7-5843	117.6	11.2 ± 1.7	2.72 ± 0.10		0.71 ± 0.10		Q	
J1650-5044	1646-506	PMN J1650-5044	1FGL J1650.4-5042	252.0	18.4 ± 2.2	2.55 ± 0.07		1.09 ± 0.17			
J1717-3342	1714-336	PMN J1717-3342	1FGL J1717.9-3343	208.8	22.2 ± 2.8	2.42 ± 0.06		0.54 ± 0.09		B	
J1802-3940	1759-396	PMN J1802-3940	1FGL J1802.5-3939	1207.3	19.6 ± 1.2	2.25 ± 0.04	$(3.19 \pm 0.20) \times 10^{46}$	0.89 ± 0.14	2.1×10^{11}	Q	0.296
J1937-3958	1933-400	PKS 1933-400	1FGL J1938.2-3957	145.1	6.0 ± 0.9	2.45 ± 0.09	$(1.66 \pm 0.27) \times 10^{47}$	1.40 ± 0.20	2.5×10^{13}	Q	0.965
J1957-3845	1954-388	[HB89] 1954-388	1FGL J1958.4-3847	273.4	7.6 ± 0.9	2.47 ± 0.08	$(0.70 \pm 0.09) \times 10^{47}$	1.57 ± 0.24	2.2×10^{11}	Q	0.630
J2009-4849	2005-489	[HB89] 2005-489	1FGL J2009.5-4849	532.7	3.9 ± 0.5	1.90 ± 0.07	$(0.66 \pm 0.08) \times 10^{45}$	0.76 ± 0.12	2.5×10^{10}	B	0.071
J2056-4714	2052-474	[HB89] 2052-474	1FGL J2056.3-4714	1052.0	17.0 ± 1.0	2.54 ± 0.05	$(1.68 \pm 0.12) \times 10^{48}$	1.74 ± 0.27	1.5×10^{12}	Q	1.489
J2139-4235	2136-428	PMN J2139-4235	1FGL J2139.3-4235	1263.4	9.0 ± 0.7	2.08 ± 0.05				B	
J2158-3013	2155-304	[HB89] 2155-304	1FGL J2158.8-3013	7310.2	21.4 ± 0.8	1.907 ± 0.020	$(1.00 \pm 0.05) \times 10^{46}$	0.38 ± 0.06	7.7×10^{10}	B	0.116
J2207-5346	2204-540	[HB89] 2204-540	1FGL J2207.8-5344	186.0	5.2 ± 0.8	2.50 ± 0.10	$(2.3 \pm 0.5) \times 10^{47}$	0.71 ± 0.10	2.2×10^{11}	Q	1.206

[a] Name in B 1950.0 IAU format, [b] Classifications from Véron-Cetty & Véron (2006): Q: Quasar, B: BL Lac, G: galaxy. (including changes of classification as described in Sect. 4.1.3)

are consistent with those in the 1FGL catalog and "The First Catalog of Active Galactic Nuclei Detected by the Fermi Large Area Telescope" (1LAC; Abdo et al., 2010b).

Detection Rates From previous γ-ray studies and the underlying models for high-energy emission from AGN, clear dependencies of the γ-ray brightness on the AGN classification are expected (see Sects. 1.1.3 and 1.4.3). Studies of the γ-ray detection rates of different sources types in the TANAMI sample have to be handled with care, as the results are biased by the selection of the sample. The sample is neither statistically complete, nor defined with consistent selection criteria. As discussed in Sect. 4.1.2 and by Ojha et al. (2010), the sample contains a flux-limited radio sub-sample and a γ-ray selected sub-sample, as well as a selection of further interesting AGN (intra-day variable sources and gigahertz peaked spectrum sources). As the sample includes known and candidate EGRET sources and candidate counterparts for *Fermi*/LAT sources detected in the first months of *Fermi* operation, the γ-ray detection rates in the sample are modified directly by the construction of the sample.

Based on the AGN classifications of Véron-Cetty & Véron (2006) and including the changed classifications discussed in Sect. 4.1.3, the following numbers of TANAMI AGN were found to have a *Fermi*/LAT detected γ-ray counterpart. The total number of AGN from the TANAMI sample that can be associated with γ-ray sources from the 1FGL catalog are 54 out of the 75. It turned out that all of the BL Lac objects in the sample (8/8) are significantly detected with *Fermi*/LAT. The detection rate is lower for quasars, but with 26 out of 34 quasars it is still high. The lowest detection rate in the sample is found for the radio galaxies, where only 2 out of 12 have strong enough γ-ray emission to be detected with LAT.

Radio Galaxies detected with *Fermi*/LAT The two radio galaxies in the TANAMI sample that can be associated with sources in the 1FGL catalog are PKS 0521−365 (ESO 362- G 021) and PKS 1322−428 (Cen A). Cen A, which is the closest AGN (more information on this object is provided in Sect. 4.1.8), has already been detected with EGRET. With *Fermi*/LAT not only emission from its nucleus is detected (Abdo et al., 2010e), but in addition a comparable intensity of γ-ray emission originates from the Cen A's giant radio lobes (γ-ray images of Cen A are presented by Abdo et al., 2010d). The second *Fermi*/LAT detected galaxy in the TANAMI sample, PKS 0521−365, is a luminous giant elliptical galaxy with strong emission lines (see, e.g., Falomo et al., 1994). Given some properties of its nucleus a BL Lac classification of this object has been suggested (see, e.g., Danziger et al., 1979). PKS 0521−365 is therefore considered as an example of a misaligned radio galaxy, in which the inner jet on milliarcsecond-scales is aligned with a small angle to the line of sight, whereas the large scale structure has larger inclination. Two similar examples are PKS 0625−354 (OH-342) and PKS 1440−389. On large scales PKS 0625−354 exhibits an FR I radio-galaxy morphology, but some properties, e.g., its optical spectrum, are similar to that of BL Lac objects (Wills et al., 2004). In the first AGN catalog of the *Fermi*/LAT team, PKS 0625−354 is is included as a misaligned radio galaxy (Abdo et al., 2010b, discuss 5 objects of this class in total). For the three latter sources, the TANAMI radio VLBI observations show a milliarcsecond morphology of a single-sided jet with a strong core component. This morphology indicates that the inner parsec-scale jet is orientated close to the line of sight. A unique classification of these sources is not possible, but as in this work especially the inner parts of the jet are important, the blazar classification has been used for PKS 0625−354 and PKS 1440−389. PKS 0521−365 is still considered as a galaxy. Further TANAMI observations will help to classify these sources better, as they will allow to determine the inner jet properties better by measuring the kinematics and determining the inclination angle of the jet. It has to be noted that the classification scheme of galaxy, BL Lac object, and quasar is a strong simplification and that there are intermediate objects. This classification will, however, be used in the following to characterize the main properties of the objects in the sample and to allow for comparisons.

The detection of the above mentioned galaxies agrees with the unification scheme and the γ-ray emission models, in which the inclination of the jet and thus the relativistic beaming effects are considered. In this model radio galaxies, where the jet has a relatively large angle to the line

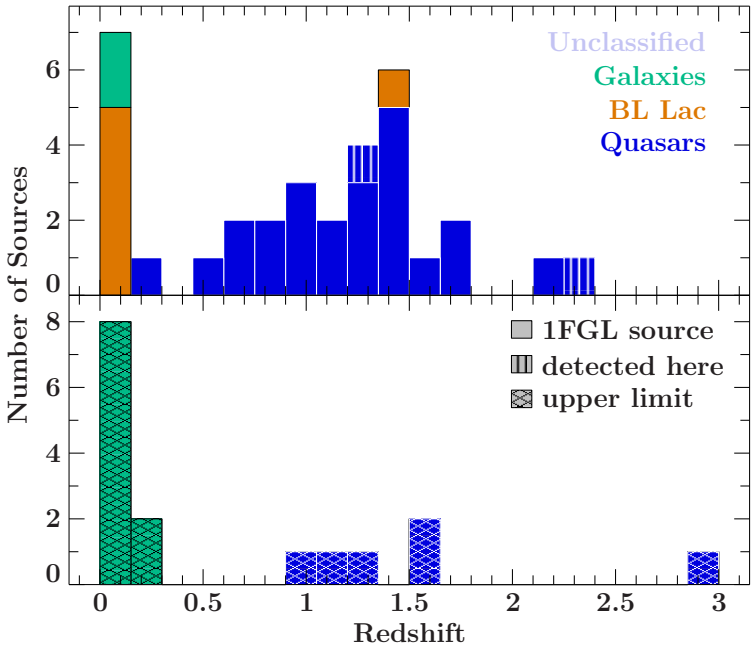

Figure 5.10: Redshift distribution of TANAMI AGN which are *Fermi*/LAT-detected (top panel) and non-detected (bottom panel). The colors represent different source classes. The fill style indicates 1FGl sources (plain), new detections (vertical hatching), and upper limits (cross hatched). The latter cases are discussed in Sect. 5.5.2.

of sight, are not γ-ray bright. Due to its vicinity Cen A, as the closest AGN, is detectable with *Fermi*/LAT. Using the distance and the measured flux, the sources luminosities can be calculated. The luminosity of Cen A is the lowest one of all associated detected objects in the sample. The other detected AGN, which show properties similar to radio galaxies, have larger luminosities, but also exhibit properties similar to BL Lac objects. It is thus likely that these sources are misaligned, i.e., that the inner jet is orientated with a small angle to line of sight, while the large scale structure has a different inclination.

Redshift distribution of *Fermi*/LAT-detected sources The redshift distribution of TANAMI AGN that are detected and un-detected with *Fermi*/LAT is shown in Fig. 5.10. Within each object class the *Fermi*/LAT γ-ray detection rates do not show a clear dependence on the object's redshift. All galaxies in the sample are located at low redshifts. This finding is simply based on the selection of the sample. Due to the selection criteria only nearby objects of this class, which have relatively low intrinsic luminosities, are included in the sample. Due to their high luminosities quasars up to high redshifts are included in the sample. Most of the BL Lac objects, which have lower luminosities on average, are nearby. The AGN PKS 0332−403 is an exception of higher redshift, due to its properties it might be classified as a flat-spectrum radio quasar as well.

5.5.2 Upper limits on the gamma-ray flux

Upper limit analysis For a study of the full sample it is important to have information on the γ-ray properties of all TANAMI AGN. For a better understanding of the high-energy emission it is important to figure out why certain AGN are γ-ray bright and others are not. As discussed in the previous section a large fraction of the objects in the sample are associated with sources in the 1FGL catalog. A number of sources remain, which have not significantly been detected in the data obtained during the first eleven months of *Fermi*/LAT operations. To understand if these sources are not detected because they have different intrinsic properties or if their properties are consistent with the detected sources, but the non-detection is based on other parameters, e.g., that they are too distant, it is necessary to calculate upper limits on the γ-ray flux for these sources.

For TANAMI AGN without an association in the 1FGL catalog, upper limits on the γ-ray flux were calculated following the standard analysis method using a maximum likelihood analysis (Cash,

1979; Mattox et al., 1996), as it is outlined in Sect. 5.3. The selected data and software configuration will be described in the following. For the analysis the standard *Fermi*/LAT *ScienceTools* software package[11] (version v9r23p1) was used with the "P7CLEAN_V6" set of instrument response functions. The same time interval as for the 1FGL catalog was used. Photons with the "source" event class were considered in an energy range of 100 MeV–100 GeV. Upper limits on the γ-ray flux were calculated in this energy band as well as in the 1–100 GeV energy band. All photons with a zenith angle larger than 100° were excluded from the analysis in order to minimize the contamination from limb photons.

For the upper limit calculation the radio position was used. A region of interest (RoI) with a radius of 10° around the radio position was selected. A source model for the region was constructed using all sources from the 1FGL catalog in this region. The parameters of sources located inside of the RoI remained variable during the analysis. Additionally sources around the RoI were included, which contribute due to the large PSF of *Fermi*/LAT to the events in the RoI. The parameters of the outer sources remained fixed during the analysis. The source models included the Galactic diffuse emission and the isotropic diffuse emission as well[12]. Finally a model for the source, for which the upper limit should be calculated, was added to the model at the radio position. The used model was a point source with a simple power law spectrum ($dN/dE = K(E/E_0)^{-\Gamma}$, where Γ is the spectral index). The spectral index of the source was set to 2.4, which is an average value for the *Fermi*/LAT-detected TANAMI AGN. Using the complete model the parameters were varied in order to estimate the parameters' best fit values and their uncertainties. In this way the TS (significance) and the upper limit for the sources were determined. The upper limit is obtained by increasing the flux until a certain $\Delta \ln(\mathcal{L})$ is obtained (per default a value of 4). In cases where the TS of the studied source is below 1 the upper limit obtained with this method can be underestimated (see, e.g., Abdo et al., 2010a, Sec. 4.4), thus a Bayesian method (as proposed by Helene, 1983) is applied in these cases.

Long computation time As described in Sect. 5.3, the analysis process of *Fermi*/LAT data is computationally intensive, especially the Bayesian upper limit calculation requires a lot of time. Given the large used time interval of almost a year, in which data were collected, a large number of events were included and the unbinned analysis was time-consuming. Typical computation times for one source were about 40 to 500 hours on a typical CPU (∼3 GHz processor, 4 GB RAM). Additionally it often occurred that the fitting process did not converge in the first run and iterative runs were required.[13] Upper limits were calculated not only for the TANAMI sample but for the MOJAVE sample as well (Sect. 5.6), thus for about 70 sources in total. Given the large computation time it is obvious that the analysis is not possible on a typical individual computer. The analysis has been run parallelized using the High Performance Computing at SLAC[14] and on the computers available at the Dr. Karl Remeis-Sternwarte.[15]

Possible new detections In the above described upper limit analysis the TS for the sources was calculated. For relatively significant sources it was possible to model the source and to determine the flux and the spectral index. According to the criteria of the *Fermi*/LAT team, sources with TS $\geq$ 25 were modeled and considered as a detection. For less significant sources upper limits were determined. A list of the sources for which a γ-ray source was detected at radio position is shown in Table 5.2. It includes the determined γ-ray properties. The additionally detected γ-ray sources

[11] http://fermi.gsfc.nasa.gov/ssc/data/analysis/documentation/Cicerone/
[12] http://fermi.gsfc.nasa.gov/ssc/data/access/lat/BackgroundModels.html
[13] The *Fermi*/LAT team used several iterative runs to obtain the final all-sky model yielding the 1FGL and 2FGL catalogs.
[14] High Performance Computing at SLAC: http://www.slac.stanford.edu/comp/unix/public-machines.html
[15] The available computing system includes two machines with 4 × AMD Opteron Twelve-Cores with 2.2 GHz and 64 and 96 GB RAM, respectively

Table 5.2: Properties of tentative new detections of the unassociated sources in the sample.

Source	Name[a]	Common name	TS	S (0.1–100 GeV) [10^{-8} ph cm^{-2} s^{-1}]	LAT Γ	L (0.1–100 GeV) [erg s^{-1}]
J1508-4953	1505-496	PMN J1508-4953	67.9	4.0 ± 0.9	2.18 ± 0.09	
J2151-3027	2149-306	PKS 2149-306	60.7	5.1 ± 0.9	2.99 ± 0.16	$(2.3 \pm 0.5) \times 10^{48}$
J2329-4730	2326-477	[HB89] 2326-477	27.2	3.0 ± 1.0	3.0 ± 0.4	$(2.3 \pm 0.9) \times 10^{47}$

Source	Name[a]	Common name	$S_{\rm core}$ (8.4 GHz) Jy	T_B K	ID[b]	z	Sep.[c] [degree]	Conf95$_\gamma$[d] [degree]
J1508-4953	1505-496	PMN J1508-4953	0.29 ± 0.05				0.8931	0.0486
J2151-3027	2149-306	PKS 2149-306	1.27 ± 0.20	1.4×10^{12}	Q	2.345	1.5138	0.0156
J2329-4730	2326-477	[HB89] 2326-477	0.81 ± 0.13	9.7×10^{10}	Q	1.299	0.3164	0.1608

[a] Name in B 1950.0 IAU format, [b] Classifications from Véron-Cetty & Véron (2006): Q: Quasar, B: BL Lac, G: galaxy. (including changes of classification as described in Sect. 4.1.3), [c] Angular separation of the radio position of the TANAMI source and the closest 1FGL source, [d] Semimajor axis of the 95% confidence region of the position of the closest 1FGL source

are not included in the 1FGL catalog. The detection was simplified by the usage of the improved IRF and galactic and extragalactic background models. For the final results presented here the IRF and background models, which were obtained by the *Fermi*/LAT team from two years of *Fermi* operations, were used in the analysis. The two most significant detections (PKS 1505−496 and PKS 2149−306) were, however, detected with the same significance, when the models of the 1FGL catalog were used.

All three sources that are detected in this work in the 1FGL data with a TS above 25 were also detected in the 2FGL data set. The corresponding association of PKS 1505−496 is 2FGL J1508.5−4957. This source has TS = 70.1, a flux of $S_{\rm ph} = (5.5 \pm 0.9)\, 10^{-8}$ ph cm^{-2} s^{-1} in the 0.1–100 GeV range and a spectral index of 2.61 ± 0.09. The counterpart of PKS 2149−306 (2FGL J2151.5−3021) even has TS = 168.0 averaged over the 24 month 2FGL period, a flux of $S_{\rm ph} = (6.4 \pm 0.7)\, 10^{-8}$ ph cm^{-2} s^{-1}, and a spectral index of 3.00 ± 0.09. The increased significance and flux shows that this source became brighter after the 1FGL period. PKS 2326−477 is associated with a source in the 2FGL catalog (2FGL J2329.7−4744) that slightly exceeds the significance limit with TS = 25.3, a flux of $S_{\rm ph} = (1.6 \pm 0.7)\, 10^{-8}$ ph cm^{-2} s^{-1}, and a spectral index of 2.58 ± 0.22.

The full list of the remaining *Fermi*/LAT-undetected TANAMI sources is shown in Table 5.3. The table lists the source properties and the determined upper limits on the γ-ray flux.

5.5.3 Gamma-ray properties of the TANAMI sample

Flux and index distribution The distribution of the γ-ray flux of the AGN in the TANAMI sample that are associated with 1FGL sources is shown in Fig. 5.11. The used values for the flux are taken from the 1FGL catalog. The measured photon flux of these source does not show an obvious dependence on the AGN classes. A large fraction of these sources is unclassified. The reason for that is the sample selection. The γ-ray selected sub-sample includes a large number of unclassified objects. Many of these objects have not been studied in detail at other wavelengths. The distribution of the photons fluxes are dominated by the different distances of the individual sources. Clearer relations are expected for the distribution of intrinsic luminosities.

Figure 5.12 shows the distribution of photon spectral indices (1FGL values) for the sources included in the TANAMI sample. A slight asymmetry in this distribution might be induced by a detector effect. Weak γ-ray sources are difficult to detect with *Fermi*/LAT as they are difficult to localize due to the instrument's large point spread function at low energies. For this reason the *Fermi*/LAT 1FGL catalog includes only few weak sources with a soft spectrum (Fig. 5.9). Figure 5.12 indicates a slight asymmetry, but the has to be handled with care as the uncertainties of the spectral indices are on the order of the bin width for several sources. The distribution of spectral indices of BL Lac objects is different from that of quasars. On average the γ-ray spectra of BL Lacs are harder than those of quasars. A Kolmogorov-Smirnov two sample test yields a probability of

Table 5.3: Upper limits on the γ-ray emission of TANAMI sources not associated with 1FGL.

Source	Name[a]	Common name	TS	F (0.1–100 GeV) [10^{-8} ph cm^{-2} s^{-1}]	L (0.1–100 GeV) [erg s^{-1}]	$S_{\rm core}$ (8.4 GHz) Jy	T_B K	ID[b]	z	Sep.[c] [degree]	Conf95$_\gamma$[d] [degree]
J0440-4333	0438-436	[HB89] 0438-436	1.9	$\leq$ 1.1	$\leq 7.0 \times 10^{47}$	0.59 ± 0.09	1.4×10^{11}	Q	2.863	1.6920	0.0219
J0519-4546	0518-458	PICTOR A	10.7	$\leq$ 1.8	$\leq 2.8 \times 10^{43}$	0.55 ± 0.09	2.7×10^{10}	G	0.035	1.8580	0.2466
J0529-3555	0527-359	PMN J0529-3555	0.4	$\leq$ 1.1						1.5076	0.0950
J1107-4449	1104-445	[HB89] 1104-445	1.5	$\leq$ 1.4	$\leq 1.8 \times 10^{47}$	1.41 ± 0.22	2.7×10^{11}	Q	1.598	0.7664	0.2073
J1300-3253	1257-326	PKS 1257-326	2.0	$\leq$ 2.1	$\leq 1.4 \times 10^{47}$	0.129 ± 0.020	3.9×10^{10}	Q	1.256	0.3506	0.1305
J1301-3226	1258-321	ESO 443- G 024	18.2	$\leq$ 2.4	$\leq 8.6 \times 10^{42}$			G	0.017	0.5554	0.1305
J1336-3357	1333-337	IC 4296	0.1	$\leq$ 0.9	$\leq 1.6 \times 10^{42}$	0.22 ± 0.04	6.2×10^{9}	G	0.012	4.2696	0.0713
J1556-7914	1549-790	PKS 1549-79	4.8	$\leq$ 2.2	$\leq 7.5 \times 10^{44}$	0.36 ± 0.06	1.6×10^{10}	G	0.150	2.2313	0.0906
J1723-7713	1716-771	PKS 1716-771	9.4	$\leq$ 2.0		0.43 ± 0.07				1.4471	0.0785
J1723-6500	1718-649	NGC 6328	4.1	$\leq$ 0.8	$\leq 2.0 \times 10^{42}$			G	0.014	3.5705	0.1657
J1737-5634	1733-565	PKS 1733-56	0.2	$\leq$ 0.8	$\leq 1.0 \times 10^{44}$	0.181 ± 0.028	4.9×10^{10}	G	0.098	4.8296	0.1041
J1808-5011	1804-502	PMN J1808-5011	22.8	$\leq$ 2.2	$\leq 3.0 \times 10^{47}$	0.45 ± 0.07	5.9×10^{12}	Q	1.606	2.2818	0.1517
J1819-6345	1814-637	PKS 1814-63	5.4	$\leq$ 2.1	$\leq 1.1 \times 10^{44}$	0.32 ± 0.05	6.5×10^{10}	G	0.063	1.9539	0.1807
J1939-6342	1934-638	PKS 1934-63	0.0	$\leq$ 0.9	$\leq 4.8 \times 10^{44}$			G	0.183	5.7365	0.3974
J2030-3040	2027-308	ESO 462- G 027	5.3	$\leq$ 1.8	$\leq 8.7 \times 10^{42}$			G	0.020	2.0886	0.1401
J2109-4110	2106-413	[HB89] 2106-413	-0.0	$\leq$ 0.6	$\leq 2.5 \times 10^{46}$	1.04 ± 0.16	1.6×10^{11}	Q	1.058	2.9350	0.1200
J2157-6941	2152-699	ESO 075- G 041	4.8	$\leq$ 1.7	$\leq 1.7 \times 10^{43}$	0.43 ± 0.07	4.1×10^{10}	G	0.028	2.4547	0.2082
J2357-5311	2355-534	[HB89] 2355-534	2.2	$\leq$ 1.7	$\leq 6.4 \times 10^{46}$	1.53 ± 0.23	5.0×10^{11}	Q	1.006	0.4018	0.2791

[a] Name in B 1950.0 IAU format, [b] Classifications from Véron-Cetty & Véron (2006): Q: Quasar, B: BL Lac, G: galaxy. (including changes of classification as described in Sect. 4.1.3) [c] Angular separation of the radio position of the TANAMI source and the closest 1FGL source, [d] Semimajor axis of the 95% confidence region of the position of the closest 1FGL source

0.2% that both source classes have the same distribution. This finding is consistent with the results from the first *Fermi*/LAT AGN catalog (Abdo et al., 2010b, Fig. 12). The larger sample studied by the *Fermi*/LAT team even allows to study the spectral index distribution for BL Lac subclasses. As shown in Fig. 14 of Abdo et al. (2010b) there is trend for harder γ-ray spectra in the sequence of flat-spectrum radio quasars, LSP-BL Lacs, ISP-BL Lacs, and HSP-BL Lacs objects. The abbreviations

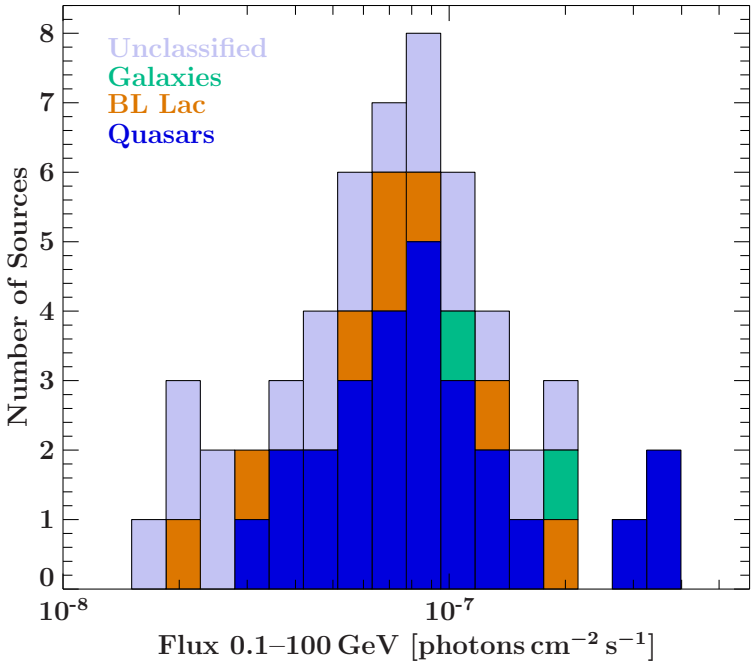

Figure 5.11: Distribution of the γ-ray flux of TANAMI AGN associated with 1FGL sources. The colors represent the source classes. Fluxes are given in units of photons cm^{-2} s^{-1} in the 0.1–100 GeV energy range.

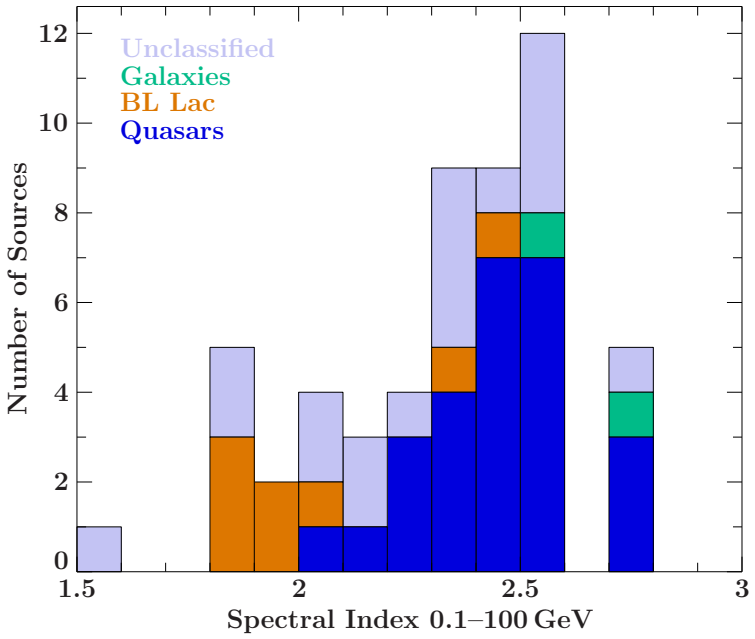

Figure 5.12: Distribution of the spectral indices Γ of the associated sources in the TANAMI sample color-coded with the object classification.

stand for low, intermediate and high synchrotron-peaking BL Lac, which characterizes the peak frequency of the synchrotron component in the SED.

Gamma-ray luminosities A comparison of the intrinsic source brightness in the γ-ray regime requires to correct for the distance. The calculation of the γ-ray luminosities requires the measured energy flux, the luminosity distance, and the spectral index (see Sect. 1.6 for a discussion of cosmological effects which have to be accounted for).

If the energy flux in a certain energy band is not available directly it can be determined from the photon flux if a model for the flux density is available (see first paragraph of Sect. 1.6). In this work the γ-ray spectra were mainly modeled with power laws $\mathrm{d}N/\mathrm{d}E \propto E^{-\alpha}$. In this case the photon flux S_{ph} (with the units photons cm^{-2} s^{-1}) in an energy band from E_{min} to E_{max} and the

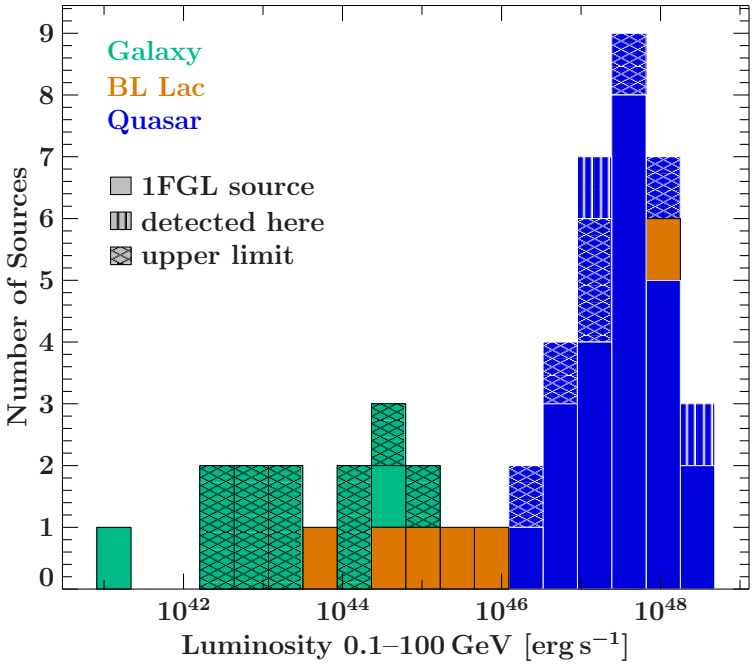

Figure 5.13: Distribution of γ-ray luminosities of the AGN in the TANAMI sample. The colors represent the object classification. The fill style indicates 1FGL catalog sources and sources, which have been studied in this work.

photon spectral index α yield the exact version of the photon spectrum:

$$N_{\mathrm{ph}}(E) = S_{\mathrm{ph}} \frac{1-\alpha}{E_0} \left(\left(\frac{E_{\mathrm{max}}}{E_0} \right)^{1-\alpha} - \left(\frac{E_{\mathrm{min}}}{E_0} \right)^{1-\alpha} \right)^{-1} \left(\frac{E}{E_0} \right)^{-\alpha}. \tag{5.13}$$

The energy flux S_{E} in this band is then given by integrating $N_{\mathrm{ph}}(E) \times E$ from E_{min} to E_{max}:

$$S_{\mathrm{E}} = \int_{E_{\mathrm{min}}}^{E_{\mathrm{max}}} E\, N_{\mathrm{ph}}(E)\, \mathrm{d}E = \begin{cases} S_{\mathrm{ph}} \frac{E_{\mathrm{max}} - E_{\mathrm{min}}}{\log(E_{\mathrm{max}}/E_{\mathrm{min}})} & \text{for} \quad \alpha = 1 \\ S_{\mathrm{ph}} \frac{\log(E_{\mathrm{max}}/E_{\mathrm{min}}) E_{\mathrm{max}} E_{\mathrm{min}}}{E_{\mathrm{max}} - E_{\mathrm{min}}} & \text{for} \quad \alpha = 2 \\ S_{\mathrm{ph}} \frac{1-\alpha}{2-\alpha} E_0 \frac{(E_{\mathrm{max}}/E_0)^{2-\alpha} - (E_{\mathrm{min}}/E_0)^{2-\alpha}}{(E_{\mathrm{max}}/E_0)^{1-\alpha} - (E_{\mathrm{min}}/E_0)^{1-\alpha}} & \text{else} \end{cases} \tag{5.14}$$

As described in Sect. 1.6 the luminosity L_E is then given by:

$$L_E = 4\pi d_{\mathrm{L}}^2 \frac{S_{\mathrm{E}}}{(1+z)^{2-\alpha}} \tag{5.15}$$

where d_{L} is the luminosity distance. In this way the luminosity can be determined for all sources with known redshift. For the nearby AGN Cen A, redshift-independent distance determinations were used. The measured redshift of this source is not dominated by the cosmological expansion of space thus the luminosity distance cannot be derived from the redshift. In the above described way, upper limits on the γ-ray flux can be transferred in an upper limit on the luminosity.

The calculated luminosities of all sources, for which a luminosity distance could be derived, are shown in Fig. 5.13. The luminosities are strongly dependent on the AGN class. Luminosities are low for the radio galaxies, larger for the BL Lac objects, and highest for quasars. Within each object class, there is no obvious difference between the distributions of the γ-ray luminosities of sources with 1FGL counterpart and the distribution of upper limits on the luminosity. The probability that the underlying distributions are the same is 40.6% according to a Kolmogorov-Smirnov two sample test. The consistent distributions of upper limits and measured values shows that there are no significant source intrinsic differences required to explain why some sources of

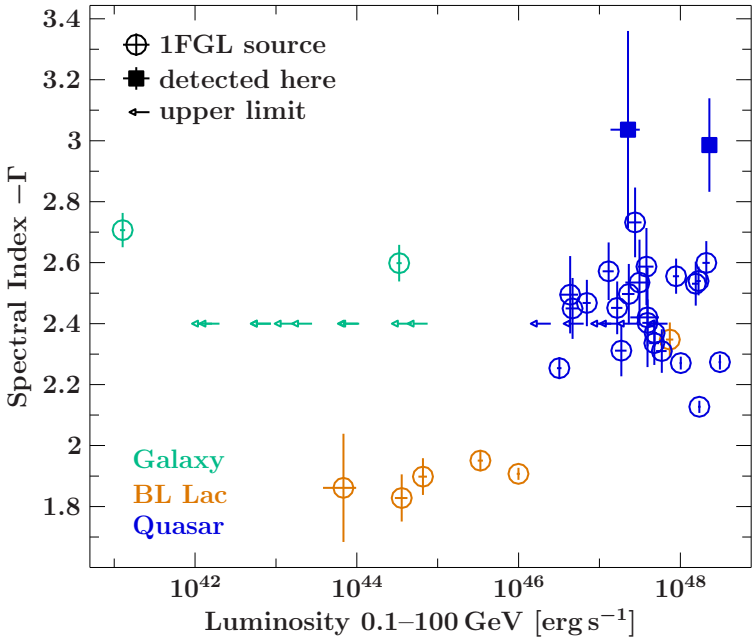

Figure 5.14: Relation between γ-ray luminosities and spectral indices for TANAMI AGN. Colors characterize different source classes. Symbols represent 1FGL sources, sources detected in this work and upper limits.

a class are *Fermi*/LAT-detected and others not. If several of the true luminosities of the sources, for which only upper limits are available, are significantly below the value of the upper limit, the distributions would not agree anymore. It is thus likely that a few of these sources are close to detection and might become visible with the continuously increasing exposure with *Fermi*/LAT, due to the improving sensitivity or upcoming flares.

Figure 5.14 shows the relation between the γ-ray luminosities and the spectral indices. It combines the information of Figs. 5.12 and 5.13. Radio galaxies have low γ-ray luminosities and quasars high luminosities, while that of BL Lac objects is in between and harder γ-ray spectra are found on average for this class. The upper limits are shown at the average spectral index of 2.4 in this plot. The two sources detected in this work (that have a known redshift) have relatively soft γ-ray spectra, but these values are consistent with the relation between γ-ray luminosities and spectral indices for all AGN detected in the 1FGL period with *Fermi*/LAT (as shown in Fig. 24 of Abdo et al., 2010b).

5.5.4 Radio Gamma-ray Relations

Brightness relations A goal of the TANAMI project is to gain insights in the mechanisms of γ-ray emission of AGN by studying the relations between radio and γ-ray properties. Figure 5.15 shows the relation between the γ-ray flux discussed above and the flux density of the radio core measured with TANAMI observations at 8.4 GHz. The fluxes in both energy bands seem to be weakly correlated. The γ-ray bright sources in the sample have a strong radio flux as well. The correlation is quantified with a Kendall's τ rank correlation coefficient of 0.22. The consideration of the upper limits can be done with the Kendall's τ rank correlation coefficient for censored data (as described by Akritas & Siebert, 1996, and summarized in Sect. 2.3). The resulting coefficient is 0.20.

Figure 5.16 shows the relation between the radio and the γ-ray luminosities. At first sight there seems to be a clear correlation between both luminosities, but it is mainly induced by scaling the radio and γ-ray fluxes of each source with the square of the (source-dependent) luminosity distance in order to obtain the luminosities. In order to obtain the partial correlation between the luminosities the given redshift (which is isomorphic to the luminosity distance in the used ranges) has to be accounted for, as discussed in Sect. 2.3. The resulting partial Kendall's τ rank correlation

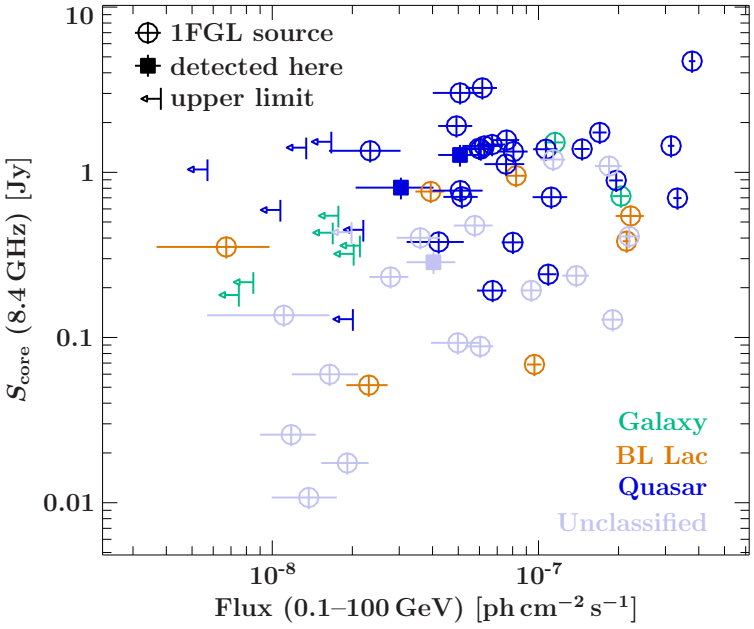

Figure 5.15: Relation between the γ-ray and the flux of the radio core at 8.4 GHz. Different object classes in the sample are highlighted with different colors.

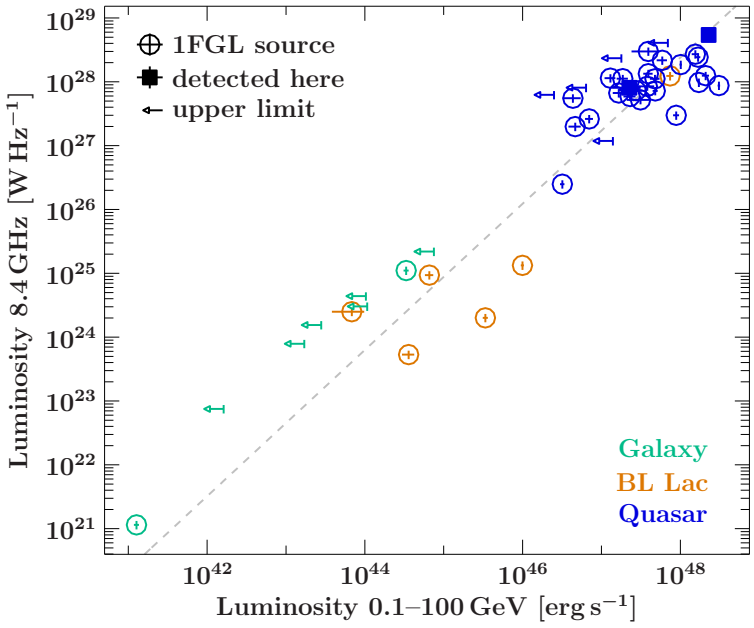

Figure 5.16: Relation between the γ-ray and the radio core luminosity measured at 8.4 GHz. The γ-ray upper limits are shown with arrows and the object classes are color-coded. The dashed line is the linear correlation described in the text.

coefficient is 0.29 and 0.24 when the upper limits are considered as censored data. As expected this result is similar to that for the correlation between the measured fluxes. Besides the usage of the partial correlation coefficient a difference is that K-correction (Sect. 1.6) has been applied in the determination of the γ-ray luminosity. The relation between the radio L_r and the γ-ray luminosity L_γ is $L_\gamma \propto L_r^{0.86\pm0.04}$, as obtained from a linear fit to the logarithms of the luminosities.

Although the distributions of upper limits and the fluxes of *Fermi*/LAT-detected sources seemed consistent in Fig. 5.13, the consideration of the radio fluxes indicate a difference between *Fermi*/LAT-detected and undetected sources. The correlation coefficients between radio and γ-ray fluxes, as well as that between the luminosities, decrease when the upper limits are considered. It can be seen in Fig. 5.15 and 5.16 that the upper limits are smaller than expected from a strong correlation between the radio and γ brightness. As the true value of a source is smaller or at equal than the upper limit, this discrepancy might even be stronger. The ratio between the γ-ray and the radio luminosity seems on average smaller for *Fermi*/LAT-undetected sources than for *Fermi*/LAT-detected

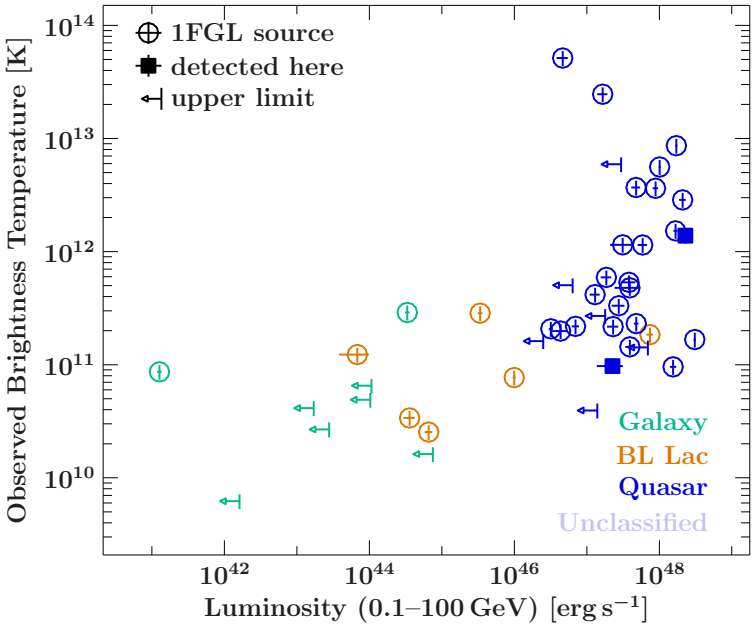

Figure 5.17: Relation between γ-ray luminosity and brightness temperature of the radio core.

ones. A Kolmogorov-Smirnov two sample test confirms this difference. It yields a probability of only 1.2% that the distribution of these ratios are the same for both cases. This value was obtained for the most conservative case, in which the flux of the undetected sources was assumed to be the upper limit and not smaller. Before concluding that the *Fermi*/LAT-undetected sources are intrinsically γ-ray fainter than the detected ones, it has to be considered that all AGN, which can be observed with a sufficient signal-to-noise ratio, are variable in both energy bands. On the one hand γ-ray flares can significantly increase the averaged flux in the *Fermi*/LAT catalog. It might be that some of the undetected sources were less active during the 1FGL period and thus remain undetected in this time interval. On the other hand the radio emission is variable as well. Several sources, for which more TANAMI observations epochs have been analyzed by the TANAMI team, are significantly variable. Comparisons between the radio and the γ-ray flux therefore requires corresponding observation intervals. Depending on the emission mechanisms and sites for the γ-rays, different time delays and more complicated relations between both energy regimes are required. With more TANAMI epochs being analyzed and increasing *Fermi*/LAT exposure times, variability studies will become possible.

Brightness temperature of the radio core As described in Sect. 4.1.5 the brightness temperature T_B is strongly influenced by the Doppler factor. It is thus interesting to compare this value with the γ-ray properties. For each source the brightness temperature of the radio core has been determined by the TANAMI team using the VLBI observations at 8.4 GHz. To determine this value a two dimensional Gaussian model had been fitted to the core in the radio image. Given the size of the axis of the component and the flux, the brightness temperature was determined according to Eq. 4.1, where also the redshift was taken into account. For unresolved components a lower limit on the brightness temperature was calculated based on the resolution limit of the radio image as described in Sect. 4.1.5. The relation between the brightness temperature and the γ-ray luminosity is shown in Figure 5.17. A weak correlation of between these quantities is indicated. Sources with a large γ-ray luminosity tend to have a large brightness temperature of the radio core on average. The partial correlation coefficient between γ-ray luminosity and brightness temperature given the redshift is 0.24 and 0.26 when the upper limits are considered. The radio galaxies and quasars in the sample for which only upper limits on the γ-ray flux are available tend to have lower brightness temperatures. The large values of the brightness temperatures, which exceed the theoretical limits (Sect. 4.1.5), such as the inverse Compton limit of 10^{12} K (Kellermann & Pauliny-Toth, 1969),

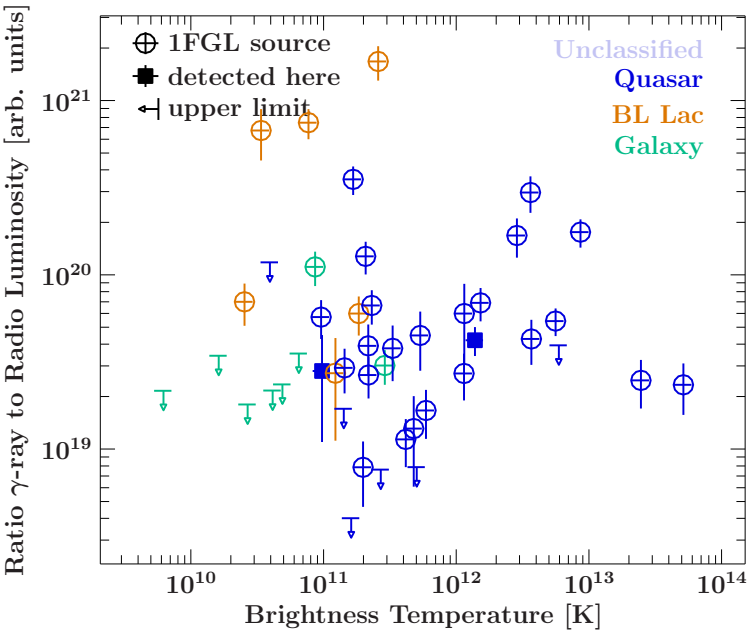

Figure 5.18: Relation between the brightness temperature of the radio core and the ratio between the γ-ray luminosity and the radio luminosity.

indicate that strong Doppler boosting occurs in the emission.

Figure 5.18 shows the dependence of the ratio between the γ-ray luminosity and that of the radio core at 8.4 GHz on the brightness temperature. As mentioned before this ratio is lower for *Fermi*/LAT-undetected sources than for the detected AGN in the TANAMI sample.

5.6 Gamma-ray properties of MOJAVE sample

Analog the analysis of the γ-ray properties of the TANAMI sample (Sect. 5.5) the γ-ray properties of the MOJAVE 1 sample were studied with *Fermi*/LAT. For simplicity the term MOJAVE sample refers to the MOJAVE 1 sample, which is studied in the following. An advantage of this sample is its definition. Contrary to the hybrid TANAMI sample, the MOJAVE sample follows consistent selection criteria as discussed in Sect. 4.2.2. For that reason the MOJAVE sample is suitable for statistical studies. As the MOJAVE program was started several years ago, numerous jet parameters are already available, such as the degree of polarization, long-term variability, and the jet speed. These quantities are especially interesting to be compared with the γ-ray properties. The connection between the radio and γ-ray properties of the MOJAVE sample are discussed by Lister et al. (2009b). The results presented in this section are in preparation for publication with the MOJAVE and *Fermi*/LAT teams.

In the first step the 1FGL counterparts for AGN in the MOJAVE sample with the method discussed in Sect. 5.5.1. Table 5.4 lists the MOJAVE AGN with 1FGL associations and their main properties. In total 87 out of 135 AGN in the MOJAVE sample can be associated with γ-ray sources in the 1FGL catalog. The fraction of *Fermi*/LAT detected AGN depends on their classification as found for the TANAMI sample. The highest detection rate in the MOJAVE sample is found for BL Lac objects, where 19 out of 22 AGN of this class are significantly detected with *Fermi*/LAT. Out of 101 quasars in the sample, 63 are detected. As for the TANAMI sample, radio galaxies have the lowest γ-ray detection rate in the sample, with only 3 out of 8. One of the *Fermi*/LAT-undetected radio galaxies is NGC 1052, which has been discussed in detail in other energy regiems in Sect. 3. A γ-ray image of the region around this object is shown in Fig. 5.19.

Analog to the analysis discussed in Sect. 5.5.2, the upper limit analysis revealed new detections (with TS $>$ 25) of γ-ray sources at the radio position of MOJAVE AGN. A list of these sources and their properties is shown in Table 5.5. A list of the upper limits on the γ-ray flux of the remaining

Table 5.4: List of MOJAVE AGN associated with 1FGL sources (sorted by right ascension).

MOJAVE Source	Common name	1FGL Association	TS	Flux (0.1–100 GeV) [10^{-8} ph cm^{-2} s^{-1}]	LAT Γ	L (0.1–100 GeV) [erg s^{-1}]	$S_{\rm core}$ (15 GHz) [Jy]	T_B [K]	ID	z
J0050-0929	PKS 0048-09	J0050.6-0928	769.8	7.4 ± 0.7	2.20 ± 0.06		1.03	13.44	B	
J0102+5824	TXS 0059+581	J0102.8+5827	280.0	9.4 ± 1.0	2.38 ± 0.07	$(0.94 \pm 0.12) \times 10^{47}$	2.92	12.49	Q	0.644
J0108+0135	4C +01.02	J0108.6+0135	1796.2	19.3 ± 1.0	2.54 ± 0.04	$(0.492 \pm 0.024) \times 10^{49}$	2.56	12.63	Q	2.099
J0112+2244	S2 0109+22	J0112.0+2247	778.1	7.8 ± 0.7	2.23 ± 0.06	$(0.99 \pm 0.09) \times 10^{46}$	0.39	11.33	B	0.265
J0136+4751	DA 55	J0137.0+4751	2037.8	20.5 ± 1.0	2.34 ± 0.04	$(4.65 \pm 0.23) \times 10^{47}$	2.72	12.66	Q	0.859
J0204+1514	4C +15.05	J0204.5+1516	29.8	1.8 ± 0.6	2.47 ± 0.19	$(0.43 \pm 0.20) \times 10^{46}$	0.38	11.65	Q	0.405
J0205+3212	B2 0202+31	J0205.3+3217	77.2	4.9 ± 1.0	2.75 ± 0.13	$(2.8 \pm 1.0) \times 10^{47}$	1.57	14.24	Q	1.466
J0217+7349	S5 0212+73	J0217.8+7353	56.1	7.2 ± 1.5	2.85 ± 0.14	$(2.1 \pm 0.8) \times 10^{48}$	0.65	13.85	Q	2.367
J0217+0144	OD 026	J0217.9+0144	1038.7	8.3 ± 0.7	2.18 ± 0.05	$(1.32 \pm 0.10) \times 10^{48}$	1.89	12.57	Q	1.715
J0237+2848	4C +28.07	J0237.9+2848	821.3	14.2 ± 1.0	2.52 ± 0.05	$(0.76 \pm 0.06) \times 10^{48}$	1.19	12.06	Q	1.207
J0238+1636	AO 0235+164	J0238.6+1637	9731.2	43.4 ± 1.0	2.143 ± 0.017	$(1.53 \pm 0.05) \times 10^{48}$	2.93	12.00	B	0.940
J0303+4716	4C +47.08	J0303.1+4711	57.0	4.0 ± 1.0	2.56 ± 0.14		0.49	12.88	B	
J0319+4130	3C 84	J0319.7+4130	3544.2	22.8 ± 1.0	2.133 ± 0.025	$(1.22 \pm 0.06) \times 10^{44}$	4.83	11.06	G	0.018
J0336+3218	NRAO 140	J0334.2+3233	50.4	6.3 ± 1.3	2.81 ± 0.14	$(4.0 \pm 0.9) \times 10^{47}$	1.04	12.05	Q	1.259
J0339-0146	CTA 26	J0339.2-0143	103.2	4.0 ± 0.7	2.50 ± 0.10	$(0.69 \pm 0.15) \times 10^{47}$	0.78	11.86	Q	0.852
J0405-1308	PKS 0403-13	J0405.6-1309	30.6	1.0 ± 0.6	2.33 ± 0.25	$(1.8 \pm 1.6) \times 10^{46}$	0.62	12.62	Q	0.571
J0418+3801	3C 111	J0419.0+3811	27.2	4.3 ± 1.2	2.61 ± 0.16	$(0.59 \pm 0.25) \times 10^{44}$	0.71	13.34	G	0.049
J0423-0120	PKS 0420-01	J0423.2-0118	1072.8	14.0 ± 1.0	2.42 ± 0.05	$(3.70 \pm 0.27) \times 10^{47}$	4.26	12.17	Q	0.914
J0424+0036	PKS 0422+00	J0424.8+0036	49.1	2.3 ± 0.8	2.38 ± 0.16		0.52	12.58	B	
J0449+1121	PKS 0446+11	J0448.6+1118	115.9	5.9 ± 0.9	2.51 ± 0.10		0.51	12.40		
J0501-0159	S3 0458-02	J0501.0-0200	101.7	3.7 ± 0.8	2.50 ± 0.12	$(1.18 \pm 0.24) \times 10^{48}$	0.79	11.79	Q	2.286
J0530+1331	PKS 0528+134	J0531.0+1331	436.6	16.9 ± 1.3	2.64 ± 0.06	$(3.8 \pm 0.4) \times 10^{48}$	1.62	12.13	Q	2.070
J0532+0732	OG 050	J0532.9+0733	340.0	9.7 ± 1.0	2.47 ± 0.07	$(0.53 \pm 0.06) \times 10^{48}$	0.70	10.40	Q	1.254
J0533+4822	TXS 0529+483	J0533.0+4825	119.7	5.5 ± 0.9	2.43 ± 0.10	$(1.9 \pm 0.5) \times 10^{47}$	0.68	13.68	Q	1.162
J0607-0834	OC -010	J0608.2-0837	90.2	5.0 ± 1.0	2.43 ± 0.12	$(0.96 \pm 0.23) \times 10^{47}$	0.99	12.41	Q	0.872
J0650-1637	PKS 0648-16	J0650.6-1635	44.5	4.2 ± 1.2	2.46 ± 0.14		2.15	11.35		
J0721+7120	S5 0716+71	J0721.9+7120	3554.3	17.3 ± 0.8	2.147 ± 0.029	$(3.98 \pm 0.20) \times 10^{46}$	0.94	12.72	B	0.310
J0730-1141	PKS 0727-11	J0730.3-1141	4593.2	44.4 ± 1.4	2.332 ± 0.022	$(0.520 \pm 0.017) \times 10^{49}$	2.79	12.89	Q	1.591
J0738+1742	OI 158	J0738.2+1741	575.5	4.6 ± 0.5	2.02 ± 0.06		0.32	11.10	B	
J0739+0137	OI 061	J0739.1+0138	466.4	11.3 ± 1.0	2.63 ± 0.07	$(0.49 \pm 0.04) \times 10^{46}$	0.71	11.71	Q	0.191
J0750+1231	OI 280	J0750.6+1235	142.6	4.1 ± 0.7	2.44 ± 0.10	$(0.94 \pm 0.17) \times 10^{47}$	1.88	12.13	Q	0.889
J0757+0956	PKS 0754+100	J0757.2+0956	259.7	4.9 ± 0.7	2.39 ± 0.09	$(0.53 \pm 0.09) \times 10^{46}$	0.99	12.13	B	0.266
J0808-0751	PKS 0805-07	J0808.2-0750	1527.4	12.8 ± 0.9	2.14 ± 0.04	$(2.47 \pm 0.17) \times 10^{48}$	1.82	13.09	Q	1.837
J0811+0146	OJ 014	J0811.2+0148	91.3	3.0 ± 0.7	2.45 ± 0.13	$(1.2 \pm 0.4) \times 10^{47}$	1.22	12.70	B	1.148
J0818+4222	OJ 425	J0818.2+4222	1686.5	11.8 ± 0.8	2.15 ± 0.04	$(1.57 \pm 0.10) \times 10^{46}$	1.53	12.08	B	0.245
J0825+0309	PKS 0823+033	J0825.9+0309	52.5	0.5 ± 0.4	1.83 ± 0.23	$(1.0 \pm 0.5) \times 10^{46}$	0.65	12.57	B	0.506
J0830+2410	OJ 248	J0830.5+2407	274.3	8.3 ± 0.9	2.79 ± 0.09	$(1.83 \pm 0.26) \times 10^{47}$	1.32	11.78	Q	0.940
J0831+0429	OJ 049	J0831.6+0429	351.1	7.4 ± 0.8	2.50 ± 0.08	$(2.4 \pm 0.4) \times 10^{45}$	0.41	10.90	B	0.174
J0841+7053	4C +71.07	J0842.2+7054	188.9	8.1 ± 1.0	2.98 ± 0.13	$(2.8 \pm 0.5) \times 10^{48}$	1.11	12.56	Q	2.218
J0840+1312	3C 207	J0840.8+1310	79.0	2.8 ± 0.7	2.44 ± 0.14	$(2.5 \pm 0.9) \times 10^{46}$	0.64	11.90	Q	0.681
J0854+2006	OJ 287	J0854.8+2006	376.1	7.0 ± 0.9	2.38 ± 0.07	$(1.16 \pm 0.16) \times 10^{46}$	4.29	12.42	B	0.306
J0909+0121	4C +01.24	J0909.0+0126	681.9	13.3 ± 1.0	2.74 ± 0.06	$(4.3 \pm 0.4) \times 10^{47}$	0.73	12.16	Q	1.024
J0921+6215	OK 630	J0919.6+6216	74.2	3.7 ± 0.9	2.70 ± 0.16	$(3.4 \pm 0.8) \times 10^{47}$	0.61	12.79	Q	1.446
J1041+0610	4C +06.41	J1040.5+0616	170.0	5.0 ± 0.8	2.56 ± 0.10	$(2.7 \pm 0.5) \times 10^{47}$	1.17	11.90	Q	1.265

Table 5.4: continued

MOJAVE Source	Common name	1FGL Association	TS	Flux (0.1–100 GeV) [10^{-8} ph cm^{-2} s^{-1}]	LAT Γ	L (0.1–100 GeV) [erg s^{-1}]	$S_{\rm core}$ (15 GHz) [Jy]	T_B [K]	ID	z
J1041+0610	4C +06.41	J1040.5+0616	170.0	5.0 ± 0.8	2.56 ± 0.10	$(2.7 \pm 0.5) \times 10^{47}$	1.17	11.90	Q	1.265
J1058+0133	4C +01.28	J1058.4+0134	1283.5	13.1 ± 0.9	2.29 ± 0.05	$(3.83 \pm 0.30) \times 10^{47}$	4.03	12.23	Q	0.890
J1127-1857	PKS 1124-186	J1126.8-1854	353.9	7.4 ± 0.8	2.45 ± 0.07	$(2.35 \pm 0.30) \times 10^{47}$	1.37	12.45	Q	1.048
J1130-1449	PKS 1127-14	J1130.2-1447	554.2	13.0 ± 1.0	2.73 ± 0.07	$(0.65 \pm 0.06) \times 10^{48}$	0.81	11.87	Q	1.184
J1159+2914	4C +29.45	J1159.4+2914	1292.4	12.2 ± 0.8	2.37 ± 0.05	$(1.80 \pm 0.14) \times 10^{47}$	1.63	12.15	Q	0.729
J1222+0413	4C +04.42	J1222.5+0415	143.5	5.7 ± 0.9	2.66 ± 0.10	$(1.21 \pm 0.30) \times 10^{47}$	1.04	12.90	Q	0.965
J1224+2122	4C +21.35	J1224.7+2121	449.6	8.1 ± 0.8	2.55 ± 0.07	$(2.60 \pm 0.27) \times 10^{46}$	0.78	11.80	Q	0.432
J1229+0203	3C 273	J1229.1+0203	5469.4	55.3 ± 1.5	2.748 ± 0.026	$(1.56 \pm 0.04) \times 10^{46}$	7.17	12.06	Q	0.158
J1230+1223	M87	J1230.8+1223	129.4	2.8 ± 0.6	2.33 ± 0.13	$(0.74 \pm 0.17) \times 10^{42}$	1.47	10.93	G	0.004
J1256-0547	3C 279	J1256.2-0547	14693.1	68.8 ± 1.4	2.321 ± 0.016	$(0.496 \pm 0.012) \times 10^{48}$	8.29	12.88	Q	0.536
J1310+3220	OP 313	J1310.6+3222	1617.2	12.9 ± 0.8	2.30 ± 0.05	$(0.481 \pm 0.028) \times 10^{48}$	2.09	12.23	Q	0.997
J1327+2210	B2 1324+22	J1326.6+2213	258.2	5.9 ± 0.8	2.44 ± 0.08	$(0.45 \pm 0.07) \times 10^{48}$	0.49	13.08	Q	1.400
J1337-1257	PKS 1335-127	J1337.7-1255	199.0	7.2 ± 1.2	2.50 ± 0.09	$(0.48 \pm 0.08) \times 10^{47}$	3.57	12.80	Q	0.539
J1504+1029	OR 103	J1504.4+1029	35641.9	$(1.104 \pm 0.015) \times 10^2$	2.221 ± 0.010	$(1.96 \pm 0.04) \times 10^{49}$	2.81	13.13	Q	1.839
J1512-0905	PKS 1510-08	J1512.8-0906	10318.5	$(1.271 \pm 0.019) \times 10^2$	2.408 ± 0.012	$(3.12 \pm 0.07) \times 10^{47}$	2.13	12.66	Q	0.360
J1549+0237	PKS 1546+027	J1549.3+0235	219.8	6.4 ± 0.9	2.46 ± 0.09	$(2.14 \pm 0.27) \times 10^{46}$	0.89	13.30	Q	0.414
J1550+0527	4C +05.64	J1550.7+0527	52.9	2.2 ± 0.7	2.36 ± 0.16	$(1.2 \pm 0.7) \times 10^{47}$	0.98	12.07	Q	1.422
J1608+1029	4C +10.45	J1609.0+1031	132.5	6.2 ± 0.9	2.72 ± 0.10	$(3.4 \pm 0.6) \times 10^{47}$	0.93	11.76	Q	1.226
J1613+3412	DA 406	J1613.5+3411	30.0	1.0 ± 0.5	2.29 ± 0.23	$(1.0 \pm 0.6) \times 10^{47}$	0.68	11.65	Q	1.397
J1635+3808	4C +38.41	J1635.0+3808	1176.2	19.2 ± 1.2	2.47 ± 0.04	$(3.17 \pm 0.25) \times 10^{48}$	1.46	13.50	Q	1.814
J1642+3948	3C 345	J1642.5+3947	1232.0	16.9 ± 1.0	2.49 ± 0.05	$(1.37 \pm 0.09) \times 10^{47}$	7.27	12.60	Q	0.593
J1727+4530	S4 1726+45	J1727.3+4525	200.6	5.7 ± 0.8	2.57 ± 0.09	$(0.60 \pm 0.10) \times 10^{47}$	1.01	12.56	Q	0.717
J1733-1304	NRAO 530	J1733.0-1308	202.2	8.7 ± 1.2	2.34 ± 0.07	$(1.72 \pm 0.29) \times 10^{47}$	2.54	12.58	Q	0.902
J1740+5211	4C +51.37	J1740.0+5209	970.4	17.2 ± 1.0	2.71 ± 0.06	$(1.28 \pm 0.09) \times 10^{48}$	0.58	12.31	Q	1.379
J1743-0350	PKS 1741-03	J1744.6-0354	29.8	1.2 ± 0.9	2.05 ± 0.20	$(1.0 \pm 1.0) \times 10^{47}$	1.82	11.67	Q	1.054
J1751+0939	4C +09.57	J1751.5+0937	721.5	12.2 ± 1.0	2.29 ± 0.05	$(2.69 \pm 0.20) \times 10^{46}$	3.95	12.68	B	0.322
J1800+7828	S5 1803+784	J1800.4+7827	439.1	6.2 ± 0.8	2.35 ± 0.07	$(0.88 \pm 0.09) \times 10^{47}$	1.62	12.14	B	0.680
J1806+6949	3C 371	J1807.0+6945	255.9	7.7 ± 1.0	2.60 ± 0.09	$(1.96 \pm 0.25) \times 10^{44}$	0.62	11.31	B	0.051
J1824+5651	4C +56.27	J1824.0+5651	345.0	6.6 ± 0.8	2.34 ± 0.07	$(0.74 \pm 0.09) \times 10^{47}$	0.72	12.46	B	0.664
J1829+4844	3C 380	J1829.8+4845	36.0	1.6 ± 0.6	2.31 ± 0.18	$(1.6 \pm 0.9) \times 10^{46}$	1.22	12.11	Q	0.692
J1849+6705	S4 1849+67	J1849.3+6705	4097.4	24.2 ± 0.9	2.252 ± 0.026	$(3.06 \pm 0.13) \times 10^{47}$	2.47	12.79	Q	0.657
J2000-1748	PKS 1958-179	J2000.9-1749	286.9	8.5 ± 1.0	2.46 ± 0.07	$(0.92 \pm 0.10) \times 10^{47}$	2.72	12.55	Q	0.650
J2134-0153	4C -02.81	J2134.0-0203	42.2	1.7 ± 0.5	2.31 ± 0.15	$(0.8 \pm 0.5) \times 10^{47}$	1.34	12.06	B	1.285
J2148+0657	4C +06.69	J2148.5+0654	27.0	1.9 ± 0.8	2.56 ± 0.20	$(0.8 \pm 0.8) \times 10^{47}$	3.62	11.79	Q	0.990
J2158-1501	PKS 2155-152	J2157.9-1503	58.6	2.8 ± 0.8	2.51 ± 0.16	$(2.6 \pm 1.0) \times 10^{46}$	0.90	11.86	Q	0.672
J2202+4216	BL Lac	J2202.8+4216	1048.6	16.8 ± 1.0	2.38 ± 0.05	$(0.93 \pm 0.06) \times 10^{45}$	1.60	12.87	B	0.069
J2203+1725	PKS 2201+171	J2203.5+1726	741.4	10.4 ± 0.8	2.39 ± 0.06	$(4.3 \pm 0.4) \times 10^{47}$	0.56	12.53	Q	1.076
J2212+2355	PKS 2209+236	J2212.1+2358	45.4	1.2 ± 0.6	2.13 ± 0.19	$(0.9 \pm 0.9) \times 10^{47}$	0.98	11.53	Q	1.125
J2225-0457	3C 446	J2225.8-0457	319.0	7.7 ± 0.8	2.53 ± 0.08	$(0.59 \pm 0.07) \times 10^{48}$	6.45	12.46	Q	1.404
J2229-0832	PHL 5225	J2229.7-0832	1534.9	21.3 ± 1.0	2.65 ± 0.05	$(2.34 \pm 0.12) \times 10^{48}$	1.75	12.84	Q	1.560
J2232+1143	CTA 102	J2232.5+1144	847.3	14.7 ± 1.0	2.56 ± 0.05	$(0.52 \pm 0.04) \times 10^{48}$	2.68	12.83	Q	1.037
J2253+1608	3C 454.3	J2253.9+1608	23787.3	$(1.368 \pm 0.018) \times 10^2$	2.466 ± 0.012	$(2.91 \pm 0.04) \times 10^{48}$	3.02	12.33	Q	0.859
J2334+0736	TXS 2331+073	J2334.3+0735	76.7	3.0 ± 0.8	2.44 ± 0.14	$(0.86 \pm 0.22) \times 10^{46}$	0.68	11.34	Q	0.401
J2348-1631	PKS 2345-16	J2348.0-1629	155.0	4.3 ± 0.8	2.39 ± 0.10	$(3.1 \pm 0.8) \times 10^{46}$	1.30	12.53	Q	0.576

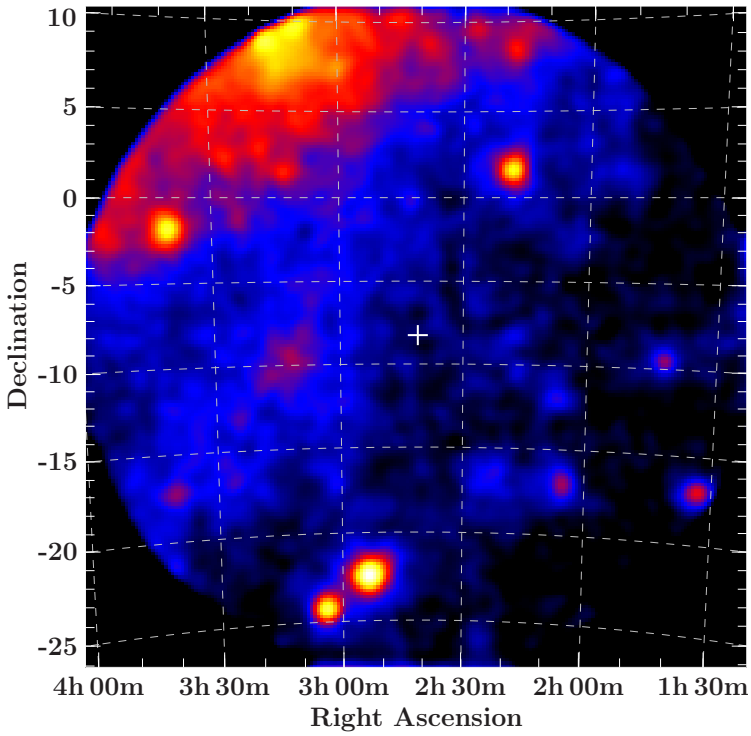

Figure 5.19: γ-ray emission from the region around NGC 1052. The position of NGC 1052 is indicated by the central cross. This image has been created using data obtained with *Fermi*/LAT before 2011, October (about 3 years integration time). For a better illustration the image has been slightly smoothed using a convolution with a Gaussian profile.

Table 5.5: Tentative new γ-ray detections of the unassociated sources in the MOJAVE sample, as shown in Table 5.2 for the TANAMI sample.

Source	Common name	TS	F (0.1–100 GeV) $[10^{-8}\,\mathrm{ph\,cm^{-2}\,s^{-1}}]$	LAT Γ	L (0.1–100 GeV) $[\mathrm{erg\,s^{-1}}]$
J0948+4039	4C +40.24	43.8	2.4 ± 0.7	2.73 ± 0.20	$(1.5 \pm 0.4) \times 10^{47}$
J1640+3946	NRAO 512	63.2	4.0 ± 1.6	2.43 ± 0.17	$(0.57 \pm 0.17) \times 10^{48}$
J1959+4044	Cygnus A	32.1	3.2 ± 0.9	2.32 ± 0.13	$(1.5 \pm 0.4) \times 10^{44}$
J2007+4029	TXS 2005+403	65.8	5.3 ± 1.0	2.29 ± 0.09	$(0.93 \pm 0.16) \times 10^{48}$

Source	Common name	S_{core} (15 GHz) Jy	T_B K	ID[b]	z	Sep.[c] [degree]	Conf95$_\gamma$[d] [degree]
J0948+4039	4C +40.24	1.12	12.14	Q	1.249	1.3846	0.1266
J1640+3946	NRAO 512	0.23	11.48	Q	1.666	0.3970	0.0564
J1959+4044	Cygnus A	0.28	10.26	G	0.056	3.1465	0.0190
J2007+4029	TXS 2005+403	2.46	11.26	Q	1.736	2.3480	0.1015

sources is shown in Table 5.6.

The redshifts of the *Fermi*/LAT-detected and undetected MOJAVE AGN are shown in Fig. 5.20. As in the TANAMI sample, for which this distribution is shown in Fig. 5.10, the closest AGN in the sample are the radio galaxies, of which the majority is not detected in the γ-ray regime. BL Lac objects are located at larger distances and the majority of them is detected with *Fermi*/LAT. The distance of the quasars reaches up to high redshifts of $z > 2$.

The distribution of the measured γ-ray flux is dominated by the different distances to the sources, thus there is no obvious source dependence expected in a histogram of the flux. This dependence changes completely when correcting for the distance and determining the luminosities as described in Sect. 5.5.3. Figure 5.21 shows the distribution of the γ-ray flux and luminosity. As in the TANAMI sample (Fig. 5.13), the radio galaxies have the lowest γ-ray luminosities. On average those of BL Lacs are higher. The highest luminosities are found for quasars.

The distribution of γ-ray photon spectral index and its relation to the luminosity is shown in Fig. 5.22. There is indication of a slight difference in this distribution and that of the TANAMI sample (Fig. 5.12) and that of all 1FGL AGN (Abdo et al., 2010b, Fig. 12 and 14). There seem

Table 5.6: List of MOJAVE AGN upper limits.

Source	Name	Common name	TS	F (0.1–100 GeV) [10^{-8} ph cm^{-2} s^{-1}]	L (0.1–100 GeV) [erg s^{-1}]	$S_{\rm core}$ (15 GHz) [Jy]	T_B [K]	ID	z	Sep. [degree]	Conf95$_\gamma$ [degree]
J0006-0623	0003-066	NRAO 005	0.8	≤ 0.7	$\leq 1.6 \times 10^{45}$	1.13	11.80	B	0.347	1.8967	0.1790
J0010+1058	0007+106	III Zw 2	1.4	≤ 1.0	$\leq 1.0 \times 10^{44}$	1.22	12.15	G	0.089	3.5228	0.1612
J0019+7327	0016+731	S5 0016+73	0.0	≤ 0.5	$\leq 8.0 \times 10^{46}$	1.40	11.86	Q	1.781	1.0031	0.0000
J0121+1149	0119+115	PKS 0119+11	2.0	≤ 0.8	$\leq 6.0 \times 10^{45}$	0.21	12.18	Q	0.570	2.4139	0.1725
J0228+6721	0224+671	4C +67.05	9.8	≤ 4	$\leq 2.4 \times 10^{46}$	0.46	12.15	Q	0.523	0.6375	0.0430
J0241-0815	0238-084	NGC 1052	0.0	≤ 0.4	$\leq 1.1 \times 10^{41}$			G	0.005	5.3826	0.1006
J0433+0521	0430+052	3C 120	19.5	≤ 2.6	$\leq 3.5 \times 10^{43}$	0.23	11.99	G	0.033	1.4150	0.2103
J0555+3948	0552+398	DA 193	18.4	≤ 4	$\leq 1.4 \times 10^{48}$	2.48	12.14	Q	2.363	1.5720	0.0737
J0609-1542	0607-157	PKS 0607-15	3.0	≤ 2.7	$\leq 5.6 \times 10^{45}$	0.89	11.24	Q	0.324	0.5317	0.0773
J0646+4451	0642+449	OH 471	0.6	≤ 1.1	$\leq 1.1 \times 10^{48}$	0.66	12.41	Q	3.396	1.4268	0.0427
J0733+5022	0730+504	TXS 0730+504	10.4	≤ 1.7	$\leq 2.6 \times 10^{46}$	0.48	11.75	Q	0.720	3.3714	0.0712
J0741+3112	0738+313	OI 363	0.0	≤ 0.6	$\leq 6.2 \times 10^{45}$	0.12	11.93	Q	0.631	3.0173	0.0697
J0745+1011	0742+103	PKS B0742+103	10.8	≤ 1.5	$\leq 7.6 \times 10^{47}$	0.42	11.81	Q	2.624	2.7117	0.1734
J0808+4950	0804+499		18.9	≤ 2.2	$\leq 2.1 \times 10^{47}$	0.50	12.05	Q	1.436	2.4782	0.0608
J0927+3902	0923+392	4C +39.25	9.0	≤ 1.9	$\leq 2.6 \times 10^{46}$	0.13	10.64	Q	0.695	1.5128	0.3222
J0958+4725	0955+476	OK 492	17.0	≤ 1.4	$\leq 2.9 \times 10^{47}$	0.25	11.19	Q	1.882	3.4524	0.0260
J1038+0512	1036+054	PKS 1036+054	0.0	≤ 0.7	$\leq 3.7 \times 10^{45}$	0.87	12.61	Q	0.473	1.1527	0.1150
J1048-1909	1045-188		1.1	≤ 0.9	$\leq 7.8 \times 10^{45}$	0.78	11.64	Q	0.595	4.4857	0.1568
J1153+8058	1150+812		10.1	≤ 2.1	$\leq 1.4 \times 10^{47}$	0.22	12.78	Q	1.250	1.2776	0.1085
J1215-1731	1213-172	PKS 1213-17	12.5	≤ 1.6		0.74	11.32			4.7839	0.0630
J1415+1320	1413+135	PKS B1413+135	8.0	≤ 1.2	$\leq 1.3 \times 10^{45}$	0.76	11.77	B	0.247	5.6213	0.0701
J1419+3821	1417+385	B3 1417+385	20.8	≤ 2.1	$\leq 4.0 \times 10^{47}$	0.15	12.28	Q	1.831	0.8663	0.1994
J1459+7140	1458+718	3C 309.1	1.1	≤ 0.7	$\leq 1.9 \times 10^{46}$	0.23	11.64	Q	0.904	4.1908	0.1059
J1507-1652	1504-166		3.6	≤ 1.6	$\leq 4.1 \times 10^{46}$	0.52	12.75	Q	0.876	1.4100	0.1177
J1540+1447	1538+149	4C +14.60	22.4	≤ 1.8	$\leq 1.7 \times 10^{46}$	0.39	12.13	B	0.605	1.8823	0.1620
J1638+5720	1637+574	OS 562	3.7	≤ 1.1	$\leq 1.8 \times 10^{46}$	0.52	13.38	Q	0.751	3.8184	0.1985
J1658+0741	1655+077	PKS 1655+077	12.0	≤ 2.4	$\leq 2.6 \times 10^{46}$	1.39	12.90	Q	0.621	3.9253	0.1081
J1753+2848	1751+288	B2 1751+28	9.0	≤ 1.9	$\leq 9.4 \times 10^{46}$	0.46	13.08	Q	1.118	3.4031	0.0691
J1800+3848	1758+388		14.8	≤ 2.3	$\leq 6.3 \times 10^{47}$	0.81	12.08	Q	2.092	5.0579	0.0603
J1801+4404	1800+440	S4 1800+44	24.0	≤ 2.5	$\leq 3.1 \times 10^{46}$	0.84	11.72	Q	0.663	2.3500	0.0603
J1927+7358	1928+738	4C +73.18	14.5	≤ 2.5	$\leq 4.3 \times 10^{45}$	2.11	12.01	Q	0.302	2.0015	0.1481
J1939-1525	1936-155		0.0	≤ 0.8	$\leq 1.1 \times 10^{47}$	0.75	12.07	Q	1.657	4.2540	0.0610
J2011-1546	2008-159	PKS 2008-159	14.1	≤ 2.9	$\leq 1.7 \times 10^{47}$	2.02	11.81	Q	1.180	1.7071	0.1199
J2023+3153	2021+317	4C +31.56	17.4	≤ 1.7		0.14	11.82			1.9369	0.0562
J2022+6136	2021+614	OW 637	2.3	≤ 1.4	$\leq 1.2 \times 10^{45}$	1.44	10.59	G	0.227	4.2931	0.0310
J2038+5119	2037+511	3C 418	3.2	≤ 2.5	$\leq 3.8 \times 10^{47}$	1.50	12.16	Q	1.686	0.8600	0.3841
J2123+0535	2121+053	PKS 2121+053	7.9	≤ 1.4	$\leq 3.1 \times 10^{47}$	1.08	11.86	Q	1.941	3.6019	0.1125
J2131-1207	2128-123	PKS 2128-12	0.2	≤ 1.0	$\leq 5.7 \times 10^{45}$	0.20	11.27	Q	0.501	2.8830	0.0359
J2136+0041	2134+004	PKS 2134+004	0.4	≤ 0.8	$\leq 1.7 \times 10^{47}$	1.44	12.39	Q	1.932	2.8311	0.2448
J2139+1423	2136+141	OX 161	0.0	≤ 0.8	$\leq 3.0 \times 10^{47}$	1.42	11.96	Q	2.427	3.4902	0.0579
J2203+3145	2201+315	4C +31.63	2.5	≤ 1.4	$\leq 2.2 \times 10^{45}$	0.48	11.95	Q	0.295	1.2581	0.1081
J2218-0335	2216-038	PKS 2216-03	5.4	≤ 1.5	$\leq 4.0 \times 10^{46}$	0.93	11.23	Q	0.901	2.2194	0.0872
J2246-1206	2243-123	PKS 2243-123	6.7	≤ 1.3	$\leq 1.4 \times 10^{46}$	1.42	12.04	Q	0.632	3.1157	0.1036
J2354+4553	2351+456	4C +45.51	2.5	≤ 1.2	$\leq 2.8 \times 10^{47}$	0.39	11.15	Q	1.986	2.3943	0.1937

to be less BL Lacs with hard γ-ray spectra in the MOJAVE sample than in the TANAMI sample. Possible reasons for that are the sample selection criteria and the blazar sequence (Sect. 1.5). As discussed by Abdo et al. (2010b), the hardness of the γ-ray spectra increases from LSP-BL Lacs over ISP-BL Lacs to HSP-BL Lacs (see also Sect. 5.5.3). The shift of the synchrotron peak also affects the radio brightness. In the MOJAVE frequency regime of 15 GHz the spectral shift to

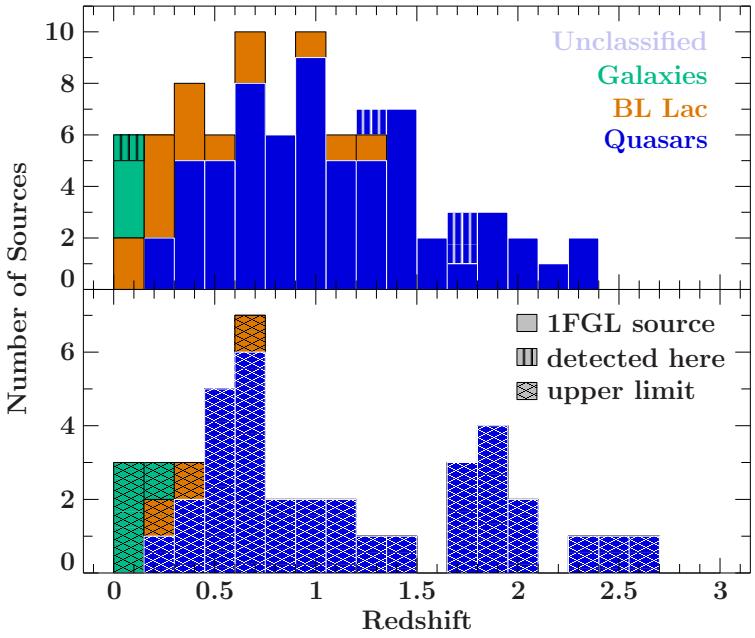

Figure 5.20: Distribution of the redshift of *Fermi*/LAT detected and undetected AGN in the MOJAVE sample. Analog to Fig. 5.10 the object classes are highlighted with colors and the *Fermi*/LAT detections with the fill style.

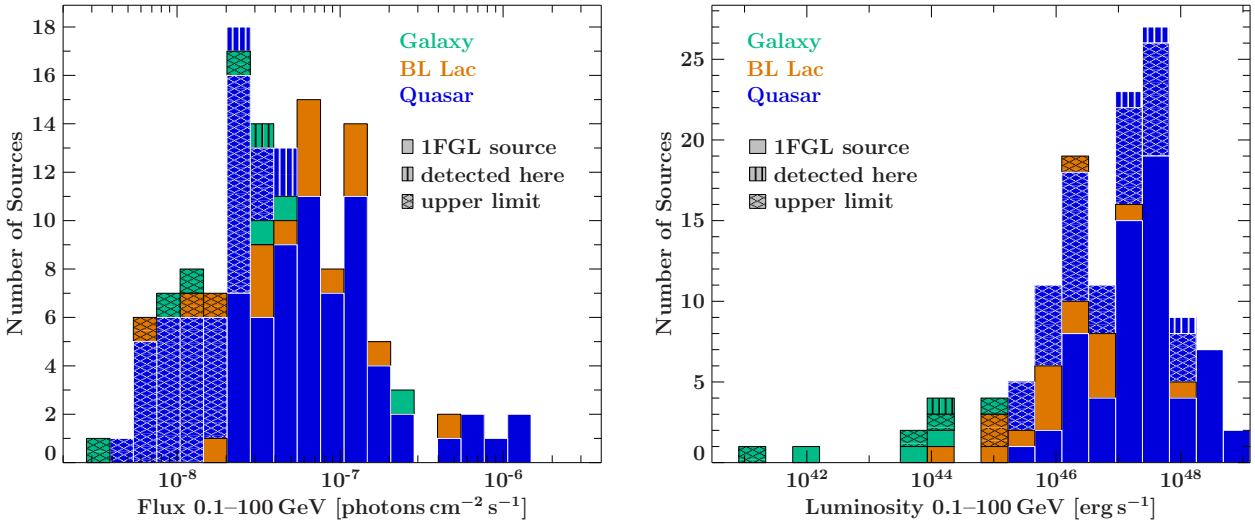

Figure 5.21: *Left:* Distribution of the γ-ray flux of the AGN in the MOJAVE sample. *Right:* Luminosity distribution of these sources. The different colors represent different object classes.

higher frequencies can decrease the radio flux, due to inverted spectra. Based on the flux limit as a selection criterion, less HSP-BL Lacs than LSP-BL Lacs are included in the MOJAVE sample. In contrast several of the γ-ray bright BL Lacs with a high synchrotron peak are included in the TANAMI sample, due to the γ-ray selected sub-sample.

The relation between the measured radio and γ-ray flux in the 1FGL period is shown in Fig. 5.23. The correlation between both fluxes is quantified by a Kendall's τ rank correlation coefficient of 0.36 without upper limits. This value is 0.35 if the method for censored data is applied and the γ-ray upper limits included.

As visible in Fig. 5.24 there is a slight correlation between the brightness temperature of the radio core and the γ-ray luminosity. This relation is included in the discussion by Lister et al. (2009b). No clear correlation is observed between the brightness temperature and the ratio between the γ-ray and radio luminosities.

Figure 5.25 shows the luminosities in the radio and the γ-ray regime. Similar properties as

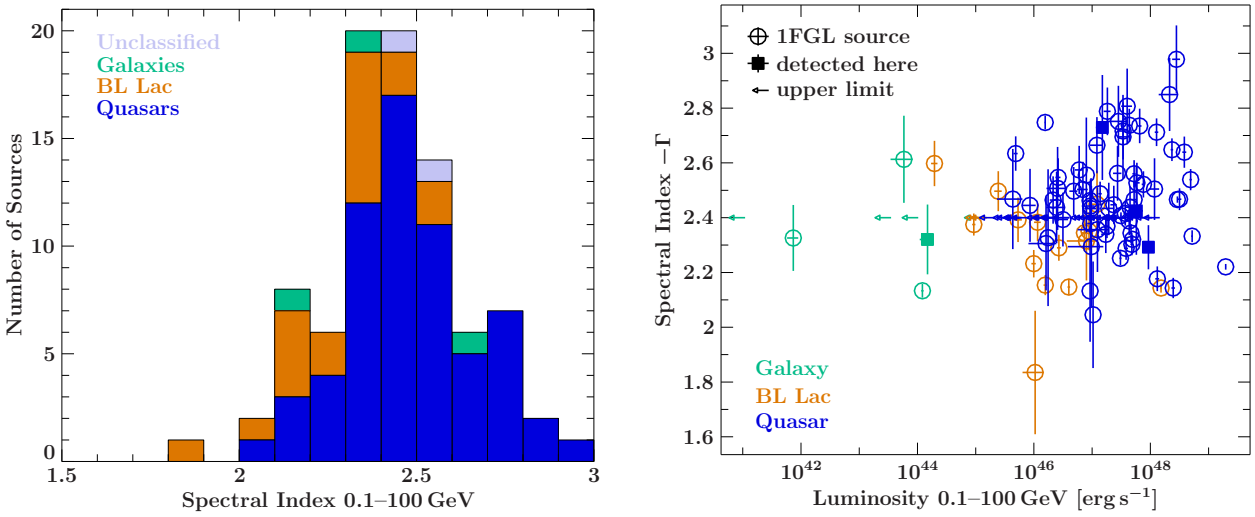

Figure 5.22: *Left:* Distribution of the indices of γ-ray photon spectra color-coded according to the object class. *Right:* Relation between the γ-ray luminosity and the spectral index (as shown left) of each source.

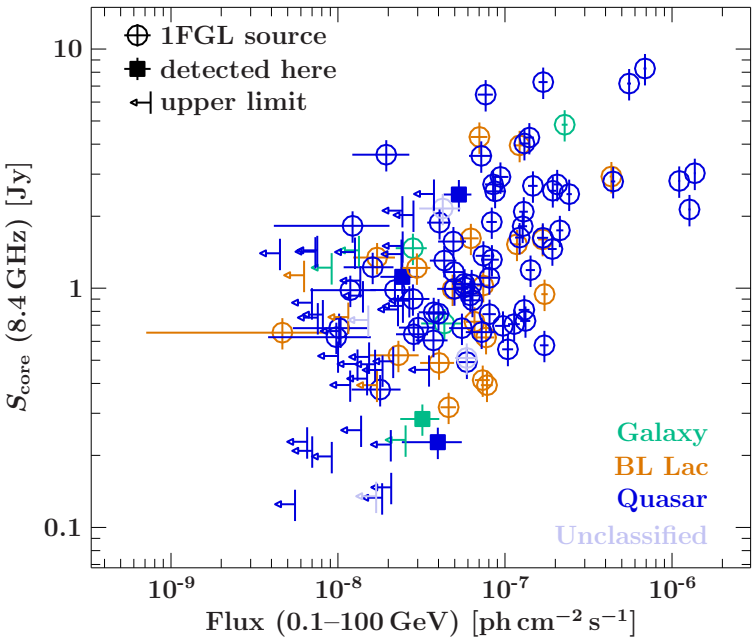

Figure 5.23: Relation between the radio and the γ-ray flux of the objects in the MOJAVE sample.

for the TANAMI sample are found (Fig. 5.16). The partial Kendall's correlation coefficient given the redshift is 0.43, and decreases to 0.33 when the upper limits are included. The values of the γ-ray upper limits seem to be smaller than expected under the assumption of a perfect correlation between radio and γ-ray luminosities, as discussed in Sect. 5.5.4.

Due to the long-term monitoring of the MOJAVE program, jet speeds have been determined by the MOJAVE team for all sources in the sample. Figure 5.26 shows the relation between the apparent jet speed $\beta_{\rm app}$ and the luminosities of the AGN in the MOJAVE sample. The figure shows the relation for the radio and the γ-ray luminosity. Both distributions are similar and seem to have a characteristic envelope. The distribution is typical if there is relativistic beaming and boosting of the emission. Cohen et al. (2007) discuss this dependence in detailed based on the radio luminosities and the apparent jet speeds of the AGN in the MOJAVE sample. The authors discuss the underlying approximations, such as the connection between the bulk velocity and the

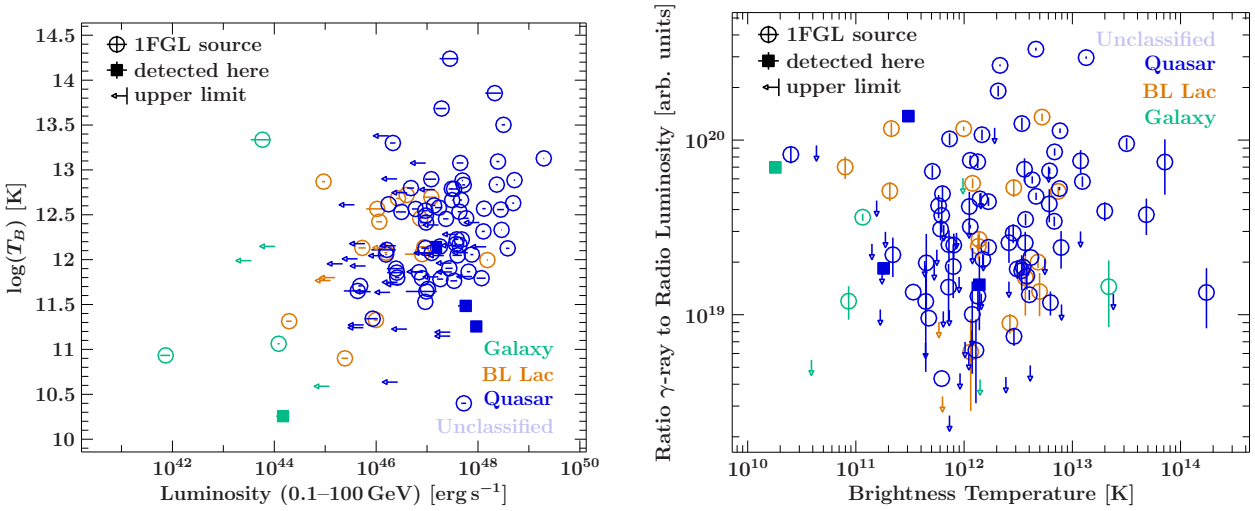

Figure 5.24: *Left:* The relation of the brightness temperature T_B of the radio core at 15 GHz and the γ-ray luminosity. *Right:* T_B as a function of the ratio between the γ-ray and the radio luminosity.

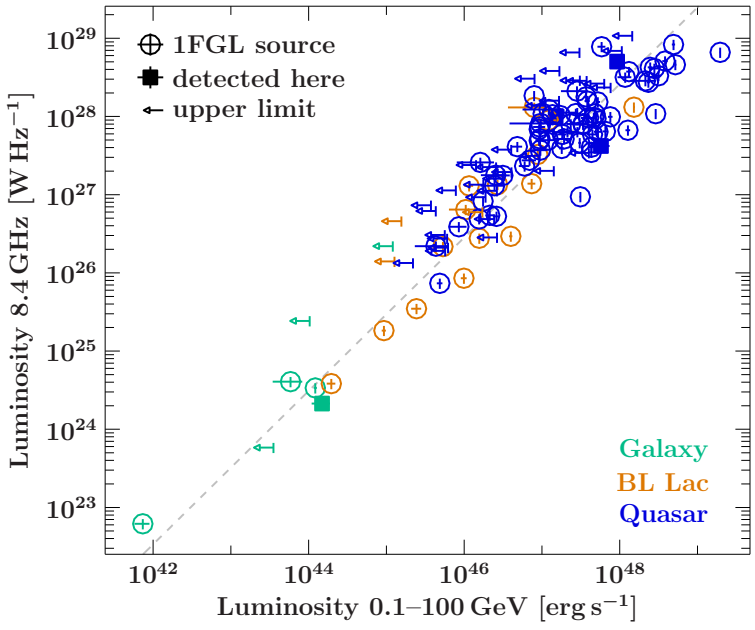

Figure 5.25: Relation between the radio and the γ-ray luminosities of the AGN in the MOJAVE sample. Object classes and the type of the determined γ-ray luminosity (upper limit, new detection, 1FGL catalog source) are highlighted as in the previous figures.

speed of the observed features and shock waves in the jet. The left plot in Fig. 5.26 is similar to Fig. 6 of their work, but includes data measured during the 1FGL period. As done by Cohen et al. (2007), aspect curves are shown in Fig. 5.26. Given the intrinsic luminosity L_0, the angle between the jet and the line of sight θ, and the Lorentz factor γ of the jet, the observed luminosity L can be obtained using the Doppler factor D:

$$L = L_0 D^n \tag{5.16}$$

where D is given from Eq. 1.16

$$D = \frac{1}{\gamma\,(1 - \beta\cos\theta)} \tag{5.17}$$

with $\beta = \sqrt{1-\gamma^{-2}}$ and $n = \alpha + p$ is the sum of the spectral index α and the Doppler boost exponent p. As discussed in Sect. 2.1 of Cohen et al. (2007) an appropriate selection for the radio

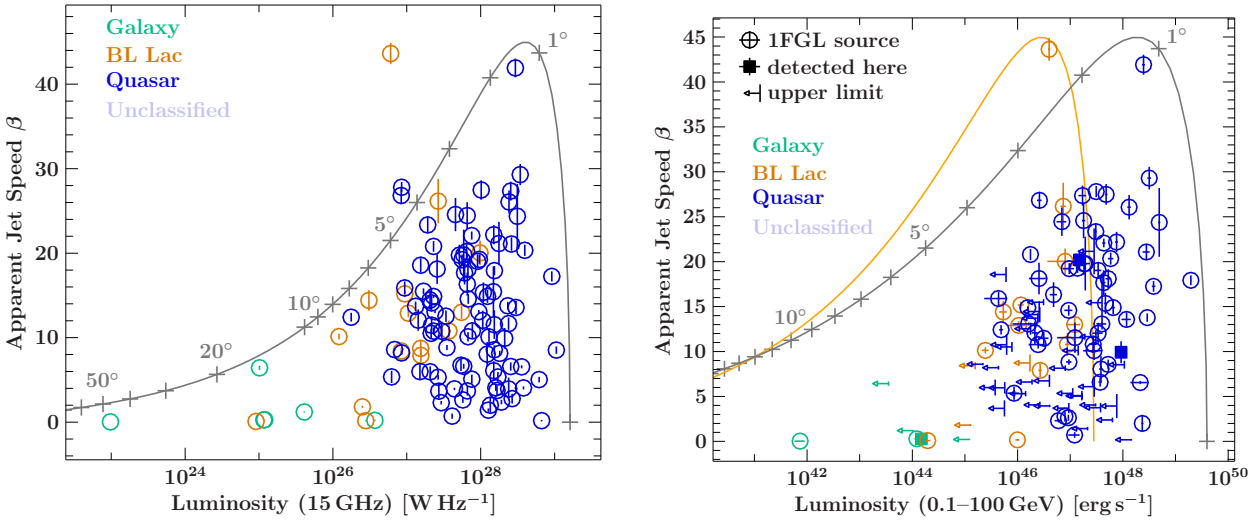

Figure 5.26: Relation between the apparent jet speed and the luminosities of MOJAVE AGN. *Left:* Relation between radio luminosity and the jet speed. As labeled in the image the color-code characterizes the source class. The gray line shows the values for an AGN with intrinsic luminosity of $L_0 = 2 \times 10^{25}\,\mathrm{W\,Hz^{-1}}$ and a Lorentz factor of 45 for different viewing angles. *Right:* Relation between jet speed and γ-ray luminosity. The gray line shows the values for an intrinsic luminosity of $L_0 = 10^{42}\,\mathrm{erg\,s^{-1}}$ at different viewing angles. The different spectral indices between the radio and γ-ray regime contribute to the different curves in both images. The orange line corresponds to a harder spectral index.

luminosity is $\alpha = 0$ and $p = 2$. This selection is based on the assumption of a flat radio spectrum ($S \propto \nu^{-\alpha}$ with $\alpha = 0$), which is a selection criterion of the MOJAVE sample ($|\alpha| < 0.5$), and a steady jet (for a moving blob the Doppler boost exponent is 3 including the time dilatation). For a given Lorentz factor and viewing angle the apparent projected jet speed can be obtained via Eq. 1.10:

$$\beta_{\mathrm{app}} = \frac{\beta \sin\theta}{1 - \beta\cos\theta}. \tag{5.18}$$

Under the assumption of a steady jet, the observed luminosity and apparent jet speed at a given line of sight can be directly obtained from the intrinsic luminosity, the Lorentz factor and the spectral index. Figure 5.26 shows the values which would be observed under different viewing angles for sources with a given Lorentz factor and luminosity. The left figure shows the radio luminosity. Here, a flat radio spectrum ($\alpha = 0$) was assumed and the intrinsic luminosity set to $L_0 = 2 \times 10^{25}\,\mathrm{W\,Hz^{-1}}$ and the Lorentz factor to $\gamma = 45$. No larger intrinsic luminosities are required to explain the large observed luminosities of the sources in the sample. For the majority of the MOJAVE AGN it is sufficient to use lower intrinsic luminosities and/or Lorentz factors to explain the observed quantities. The right plot in Figure 5.26 shows the same relation for the γ-ray luminosity. Here, the intrinsic luminosity was changed to $10^{42}\,\mathrm{erg\,s^{-1}}$ and the spectral index in the γ-ray range was changed according to $N_\gamma(\nu) \propto \nu^{-2.4}$. The orange line in Fig. 5.26 shows an example of a very hard spectrum ($N_\gamma(\nu) \propto \nu^{-1.3}$), which fits the BL Lac distribution. The more likely reason for the lower observed luminosities of BL Lac objects are lower intrinsic luminosities, as the observed spectral indices in the MOJAVE sample are similar to that of the quasars and the apparent jet speed reaches similar values as well.

Chapter 6

Summary and Outlook

6.1 Summary

In this work AGN have been studied. In order to gain insights into the emission properties of AGN, with a focus on their relativistic jets, individual sources as well as samples of AGN were considered. The multiwavelength studies include data throughout the electromagnetic spectrum, from radio to γ-rays.

An overview on the current understanding of AGN, the components expected in these systems and their emission mechanisms is given in an extended introduction (Sect. 1).

NGC 1052 – combined radio and X-ray analysis An important issue for the understanding of radio-loud AGN is the connection between accretion and outflow. In radio-loud AGN relativistic jets are typically observed, which can be studied in detail with the high angular resolution of radio VLBI observations. While information on the outflows can be gained in the radio regime, the inflow, i.e., accretion, processes can be studied well with X-ray observations. The basic analysis methods of these radio and X-ray observations are outlined in Sect. 2. An ideal source for such studies is NGC 1052 with its prominent double-sided radio jet and the clearly detectable X-ray emission. Analyses of the massive data set of this source and the obtained results are presented in detail in Sect. 3.

In the X-ray regime the source is very well sampled with deep observations providing insights in detailed spectral features, as well as monitoring observations that allow for studies of the temporal variability (Sect. 3.3). Based on a 60 ks *Chandra* observation the flux distribution of the source has been studied with arcsecond resolution in this work. Additionally to the AGN nucleus, extended X-ray emission was found in the host galaxy. Soft X-ray emission agrees with the distribution of the jet's radio emission on kpc scales indicating an origin in the jet. In combination with deep observations with *Suzaku* and *XMM-Newton*, a consistent spectral model has been developed. The soft X-ray emission is described with that of a thermal plasma and bremsstrahlung. The X-ray emission of the nucleus is modeled with a heavily absorbed power law, where a partial covering absorber is used. This model, with which all available X-ray observations can be modeled well, does not require a relativistically broadened iron line from an accretion disk as suggested in previous studies of this source. The X-ray monitoring observations reveal clear variability on time scales of weeks to years.

The radio observations of NGC 1052 include single-dish and VLBI observations at different frequencies (Sect. 3.4). The source's overall radio variability is monitored with the single-dish observations. The VLBI observations with high angular resolution are used for studying the radio jet at sub-parsec scales. In total 45 VLBA observations covering the period from 1995–2012 at 15 GHz have been analyzed in addition to 22 epochs at 22 GHz and 43 GHz. A parametrization and tracking of the features in the VLBI images allow for a kinematic study, which yields the velocity

of the components and the ejection times (Sect. 3.4.3). A characteristic flux density evolution as a function of the component's separation from the center was found. Using this flux distribution and extrapolating the average proper motion of components in the jet of $\sim$0.74 mas yr^{-1}, an ejection event in the nucleus requires about 1 year until it reaches the the position where it becomes visible at 15 GHz and even up to 2–3 years until reaching maximal observed flux density. In a comparison of the determined ejection times with the X-ray light curve indicates that ejection events occur temporally close to dips and rises of the X-ray activity. A clear strong ejection event occurred when the X-ray intensity was low. After that the X-ray intensity increased for about 2 years until further ejection events took place.

Contributions to the TANAMI program In Sect. 4 the TANAMI and the MOJAVE program are described. In both programs samples of AGN jets are monitored with the VLBI technique. Intrinsic jet properties and kinematics can be determined from the obtained data. Comparisons with properties in other energy regimes are especially important for a better understanding of the processes occurring in AGN. On the one hand this allows for studies of individual sources, such as the above case of NGC 1052. On the other hand statistical studies using the distribution of properties within the samples are possible. Contributions to the TANAMI program, such as the development of tools for the visualization of VLBI images and spectral index maps, are described in this work.

Gamma-ray emission from AGN After studies in the radio and X-ray regime, the high-energy regime is addressed. With the *Fermi*/LAT instrument detailed measurements of the γ-ray properties are possible. In the last chapter (Sect. 5) of this work a brief overview on γ-ray astronomy is given, *Fermi*/LAT is described, and the difficulties of the analysis of γ-ray data are outlined. Based on *Fermi*/LAT data, the γ-ray properties of the TANAMI and the MOJAVE sample have been studied. A large fraction of these objects have γ-ray counterparts in the *Fermi*/LAT catalogs. Almost all of the BL Lacs in the sample are detected with *Fermi*/LAT, as well as the majority of the quasars. Only a few of the radio galaxies are bright enough in the γ-ray regime to be detected with *Fermi*/LAT. For all AGN in the samples without a significant γ-ray counterpart upper limits on the γ-ray flux have been calculated. Using the distances (or redshifts) of the γ-ray sources, the fluxes were used to determine the luminosities. The objects with the lowest γ-ray luminosities in the sample are the radio galaxies. Larger values have been found for BL Lacs and the highest ones for quasars. For the MOJAVE sample, the relation of the apparent jet speeds provided by the MOJAVE team and the γ-ray luminosity could be studied. This relation is consistent with the high-energy emission being dominated strongly Doppler boosted emission originating from a relativistic jet orientated at a small angle to the line of sight. The apparent jet speeds indicate that the largest Lorentz factor of jets in the MOJAVE sample is at least $\gamma = 45$. The intrinsic luminosity is strongly increased by the boosting.

6.2 Outlook

More insights in the processes occurring in AGN will be gained in the future. An essential contribution for the development of new theories or confirmations of assumptions is provided by improved data sets and increased computational power. The latter allows for more detailed and more realistic simulations of processes in AGN and it will be possible to draw conclusions from the better description of these systems. Direct insights in the underlying mechanisms might be possible due to the increasing temporal coverage with observations and the unprecedented sensitivity of upcoming missions. Improvements of the observational capabilities will occur in all energy regimes within the next years and decades.

Radio In the radio regime several new facilities, which allow for interesting studies of AGN, are currently starting operations or will start in the next years. With mm-VLBI, extremely high angular resolutions are possible at high frequencies. In this way, radio jets can be observed even closer to the supermassive black holes, which yields additional information about the structure of jets, their formation and interaction with other components. New instruments, such as the Atacama Large Millimeter Array (ALMA) and the Square Kilometer Array (SKA), strongly increase the observational capabilities in the radio regime. On the other hand current monitoring programs such as MOJAVE and TANAMI are being continued. Currently the TANAMI program has reached enough observation epochs to start kinematic studies. As many of the AGN in this sample are bright and variable sources throughout the electromagnetic spectrum, jet speeds and ejection times are awaited for multiwavelength studies. The long-term VLBI monitoring of AGN provides data that can be used for studying several objects in a similar way as NGC 1052 has been studied in this work. For example the connection between X-ray variability and ejection events can be constrained. A larger number of such events allows for a statistical analysis and unique events could help to clarify the association and underlying processes of ejections with characteristic X-ray variations.

X-ray Several new missions are upcoming in the X-ray regime as well. Especially sensitive hard X-ray observations will be possible with missions such as the recently launched missions *NuSTAR* or *Astro-H*, which is planned to start operations in 2013. *NuSTAR* is an X-ray telescopes that is capable of imaging observations in the high-energy regime with high angular resolution. It focuses X-rays with energies of 5–80 keV. With these unprecedented possibilities, new insights in the high-energy properties of AGN can be gained. For nearby sources possible contributions to the hard X-ray emission from the jet could be resolved. In particular, detailed information on the spectral properties in this energy band are provided, which are important for modeling physical processes.

Gamma-rays With the continued all-sky survey at γ-ray energies using *Fermi*/LAT, an increasing data base is provided. Firstly, the possibilities of the sensitivity increases with larger integrations of observation times and weaker sources can be detected. Furthermore longer temporal baselines are provided, which allow for clearer correlations and more secure associations between γ-ray variability and events observed in the radio jet or at other wavelengths. In particular, correlations with jet ejection events are interesting. It is possible to search for temporal delays between emission in different energy bands. With the quasi-continuous monitoring of the complete sky, comparisons with observations of other instruments are easily possible.

Neutrinos As described in Sect. 4.1.9, it might be possible to observe neutrinos from AGN jets with upcoming neutrino telescopes, such as KM3NeT. Such detections would allow for determining the fraction of hadronic processes in jets and provide important insights into the composition of jets and underlying acceleration processes.

Appendix A

Appendix

A.1 TANAMI sources

A.1.1 List of TANAMI sources

Table A.1: List of all sources in the TANAMI sample. The listed values have been collected by the TANAMI team (see, e.g., Ojha et al., 2010)

Source	J2000 name	Common name	Opt. ID	Redshift	Right ascension	Declination
0047−579	J0049−5738	[HB89] 0047-579	Q	1.797	$00^{h}49^{m}59^{s}.473$	$-57°38'27''.339$
0055−328	J0058−3234	PKS 0055-328			$00^{h}58^{m}02^{s}.230$	$-32°34'20''.747$
0208−512	J0210−5101	[HB89] 0208-512	Q	0.999	$02^{h}10^{m}46^{s}.200$	$-51°01'01''.891$
0227−369	J0229−3643	PKS 0227-369	Q	2.115	$02^{h}29^{m}28^{s}.449$	$-36°43'56''.821$
0244−470	J0246−4651	PKS 0244-470			$02^{h}46^{m}00^{s}.110$	$-46°51'17''.400$
0302−623	J0303−6211	PKS 0302-623	Q	1.351	$03^{h}03^{m}50^{s}.631$	$-62°11'25''.549$
0308−611	J0309−6058	PKS 0308-611	Q	1.480	$03^{h}09^{m}56^{s}.099$	$-60°58'39''.055$
0332−376	J0334−3725	PMN J0334-3725			$03^{h}34^{m}15^{s}.420$	$-37°25'43''.300$
0332−403	J0334−4008	[HB89] 0332-403	B	1.445	$03^{h}34^{m}13^{s}.654$	$-40°08'25''.396$
0402−362	J0403−3605	PKS 0402-362	Q	1.417	$04^{h}03^{m}53^{s}.750$	$-36°05'01''.912$
0405−385	J0406−3826	[HB89] 0405-385	Q	1.285	$04^{h}06^{m}59^{s}.035$	$-38°26'28''.042$
0412−536	J0413−5332	PMN J0413-5332			$04^{h}13^{m}13^{s}.510$	$-53°32'01''.000$
0426−380	J0428−3756	PKS 0426-380	Q	1.110	$04^{h}28^{m}40^{s}.424$	$-37°56'19''.579$
0438−436	J0440−4333	[HB89] 0438-436	Q	2.863	$04^{h}40^{m}17^{s}.180$	$-43°33'08''.602$
0447−439	J0449−4350	PKS 0447-439	B	0.107	$04^{h}49^{m}24^{s}.690$	$-43°50'08''.900$
0454−463	J0455−4615	[HB89] 0454-463	Q	0.853	$04^{h}55^{m}50^{s}.772$	$-46°15'58''.681$
0506−612	J0506−6109	[HB89] 0506-612	Q	1.093	$05^{h}06^{m}43^{s}.989$	$-61°09'40''.993$
0516−621	J0516−6207	PKS 0516-621			$05^{h}16^{m}44^{s}.926$	$-62°07'05''.388$
0518−458	J0519−4546	PICTOR A	G	0.035	$05^{h}19^{m}49^{s}.721$	$-45°46'43''.780$
0521−365	J0522−3627	ESO 362- G 021	G	0.055	$05^{h}22^{m}57^{s}.985$	$-36°27'30''.848$
0524−485	J0526−4830	PKS 0524-485			$05^{h}26^{m}16^{s}.671$	$-48°30'36''.791$
0527−359	J0529−3555	PMN J0529-3555			$05^{h}29^{m}37^{s}.660$	$-35°55'16''.200$
0537−441	J0538−4405	[HB89] 0537-441	Q	0.894	$05^{h}38^{m}50^{s}.361$	$-44°05'08''.934$
0625−354	J0627−3529	PKS 0625-35	B	0.055	$06^{h}27^{m}06^{s}.720$	$-35°29'15''.400$
0637−752	J0635−7516	[HB89] 0637-752	Q	0.653	$06^{h}35^{m}46^{s}.508$	$-75°16'16''.814$
0700−661	J0700−6610	PKS 0700-661			$07^{h}00^{m}31^{s}.240$	$-66°10'45''.800$
0717−432	J0718−4319	PMN J0718-4319			$07^{h}18^{m}43^{s}.640$	$-43°19'49''.700$
0736−770	J0734−7711	PKS 0736-770	Q		$07^{h}34^{m}43^{s}.520$	$-77°11'12''.900$
0745−330	J0747−3310	PKS 0745-330			$07^{h}47^{m}19^{s}.683$	$-33°10'46''.972$

0812−736	J0811−7530	PMN J0810-7530			$08^{h}11^{m}03^{s}.170$	$-75°30'27''.800$
1057−797	J1058−8003	PKS 1057-79	Q	0.581	$10^{h}58^{m}43^{s}.310$	$-80°03'54''.159$
1101−536	J1103−5357	PKS 1101-536	Q		$11^{h}03^{m}52^{s}.222$	$-53°57'00''.696$
1104−445	J1107−4449	[HB89] 1104-445	Q	1.598	$11^{h}07^{m}08^{s}.693$	$-44°49'07''.567$
1144−379	J1147−3812	[HB89] 1144-379	Q	1.048	$11^{h}47^{m}01^{s}.371$	$-38°12'11''.022$
1257−326	J1300−3253	PKS 1257-326	Q	1.256	$13^{h}00^{m}42^{s}.426$	$-32°53'12''.110$
1258−321	J1301−3226	ESO 443- G 024	G	0.017	$13^{h}01^{m}00^{s}.788$	$-32°26'28''.700$
1313−333	J1316−3338	[HB89] 1313-333	Q	1.210	$13^{h}16^{m}07^{s}.986$	$-33°38'59''.171$
1322−428	J1325−4301	Cen A	G	0.002	$13^{h}25^{m}27^{s}.615$	$-43°01'08''.805$
1323−526	J1326−5256	PMN J1326-5256			$13^{h}26^{m}49^{s}.230$	$-52°56'23''.600$
1325−558	J1329−5608	PMN J1329-5608			$13^{h}29^{m}01^{s}.130$	$-56°08'02''.600$
1333−337	J1336−3357	IC 4296	G	0.012	$13^{h}36^{m}39^{s}.030$	$-33°57'57''.000$
1344−376	J1347−3750	PMN J1347-3750			$13^{h}47^{m}40^{s}.429$	$-37°50'36''.620$
1424−418	J1427−4206	[HB89] 1424-418	Q	1.522	$14^{h}27^{m}56^{s}.297$	$-42°06'19''.437$
1440−389	J1443−3908	PKS 1440-389	B	0.065	$14^{h}43^{m}57^{s}.200$	$-39°08'39''.700$
1454−354	J1457−3539	PKS 1454-354	Q	1.424	$14^{h}57^{m}26^{s}.712$	$-35°39'09''.971$
1501−343	J1505−3432	PMN J1505-3432			$15^{h}05^{m}02^{s}.360$	$-34°32'57''.200$
1505−496	J1508−4953	PMN J1508-4953			$15^{h}08^{m}38^{s}.980$	$-49°53'01''.800$
1549−790	J1556−7914	PKS 1549-79	G	0.150	$15^{h}56^{m}58^{s}.870$	$-79°14'04''.281$
1600−445	J1604−4441	PMN J1604-4441			$16^{h}04^{m}31^{s}.021$	$-44°41'31''.974$
1600−489	J1603−4904	PMN J1603-4904			$16^{h}03^{m}50^{s}.670$	$-49°04'05''.100$
1606−667	J1610−6649	PMN J1610-6649			$16^{h}10^{m}46^{s}.460$	$-66°49'01''.200$
1610−771	J1617−7717	[HB89] 1610-771	Q	1.710	$16^{h}17^{m}49^{s}.276$	$-77°17'18''.467$
1613−586	J1617−5848	PMN J1617-5848	Q		$16^{h}17^{m}17^{s}.960$	$-58°48'06''.100$
1646−506	J1650−5044	PMN J1650-5044			$16^{h}50^{m}16^{s}.490$	$-50°44'46''.200$
1714−336	J1717−3342	PMN J1717-3342	B		$17^{h}17^{m}36^{s}.029$	$-33°42'08''.829$
1716−771	J1723−7713	PKS 1716-771			$17^{h}23^{m}50^{s}.750$	$-77°13'51''.300$
1718−649	J1723−6500	NGC 6328	G	0.014	$17^{h}23^{m}41^{s}.030$	$-65°00'36''.615$
1733−565	J1737−5634	PKS 1733-56	G	0.098	$17^{h}37^{m}35^{s}.771$	$-56°34'03''.155$
1759−396	J1802−3940	PMN J1802-3940	Q	0.296	$18^{h}02^{m}42^{s}.680$	$-39°40'07''.905$
1804−502	J1808−5011	PMN J1808-5011	Q	1.606	$18^{h}08^{m}13^{s}.920$	$-50°11'53''.500$
1814−637	J1819−6345	PKS 1814-63	G	0.063	$18^{h}19^{m}35^{s}.002$	$-63°45'48''.189$
1933−400	J1937−3958	PKS 1933-400	Q	0.965	$19^{h}37^{m}16^{s}.217$	$-39°58'01''.552$
1934−638	J1939−6342	PKS 1934-63	G	0.183	$19^{h}39^{m}25^{s}.026$	$-63°42'45''.625$
1954−388	J1957−3845	[HB89] 1954-388	Q	0.630	$19^{h}57^{m}59^{s}.819$	$-38°45'06''.356$
2005−489	J2009−4849	[HB89] 2005-489	B	0.071	$20^{h}09^{m}25^{s}.391$	$-48°49'53''.720$
2027−308	J2030−3040	ESO 462- G 027	G	0.020	$20^{h}30^{m}57^{s}.590$	$-30°40'00''.900$
2052−474	J2056−4714	[HB89] 2052-474	Q	1.489	$20^{h}56^{m}16^{s}.360$	$-47°14'47''.627$
2106−413	J2109−4110	[HB89] 2106-413	Q	1.058	$21^{h}09^{m}33^{s}.188$	$-41°10'20''.605$
2136−428	J2139−4235	PMN J2139-4235	B		$21^{h}39^{m}24^{s}.160$	$-42°35'20''.400$
2149−306	J2151−3027	PKS 2149-306	Q	2.345	$21^{h}51^{m}55^{s}.524$	$-30°27'53''.697$
2152−699	J2157−6941	ESO 075- G 041	G	0.028	$21^{h}57^{m}05^{s}.981$	$-69°41'23''.685$
2155−304	J2158−3013	[HB89] 2155-304	B	0.116	$21^{h}58^{m}52^{s}.065$	$-30°13'32''.118$
2204−540	J2207−5346	[HB89] 2204-540	Q	1.206	$22^{h}07^{m}43^{s}.733$	$-53°46'33''.820$
2326−477	J2329−4730	[HB89] 2326-477	Q	1.299	$23^{h}29^{m}17^{s}.704$	$-47°30'19''.115$
2355−534	J2357−5311	[HB89] 2355-534	Q	1.006	$23^{h}57^{m}53^{s}.266$	$-53°11'13''.689$

A.1.2 Information on individual TANAMI sources

The following collection of information on TANAMI sources contains results from various studies. A large fraction of the information given here is obtained from the source notes available at the

NASA/IPAC Extragalactic Database (NED).

0046−579

- QSO with z=1.797 (Peterson et al., 1976)
- map: two components, core + component WNW, separation 20mas (Ojha et al., 2005)
- map: core extended symetrically (WNW,ESE) (Preston et al., 1989)

0208−512

- map: compact core extended to SW (Ojha et al., 2004a)
- map: compact core + additional component (slight extension to SW) superluminal candidate, from model fit parameters (1992,1993) proper motion of 0.6mas/yr, corresponding to a transverse velocity of 16.8c ($H_0 = 100$, $q_0 = 0.5$), from ROSAT measurement of 0.22 microJansky at 1 keV (Dondi & Ghisellini, 1995): lower limit of Doppler factor 10.2 (Shen et al., 1998a)
- X-ray emission of core and 4" jet to SW revealed by Chandra (Marshall et al., 2005)
- HPQ (highly polarized quasar) (Impey & Tapia, 1988, 1990)
- second southern AGN detected at gamma-ray energies (Bertsch et al., 1993; Blom et al., 1995)
- one of the hardest spectra (von Montigny et al., 1995; Chiang et al., 1995)
- γ-ray Blazar (Tavecchio et al., 2007)

0332−403

- map: compact core (no clear additional components in the mas scale) (Ojha et al., 2004a)
- map: compact core slightly extended to the east, redshift may be wrong (This value is from the Catalogue of Quasi Stellar-Objects (Barbieri et al., 1975), in which the reference was incorrect.) (Shen et al., 1998a)
- different map, small jet component to the west, separation ∼2 mas (Fomalont et al., 2000)
- HPQ ($p \approx 14\%$), redshift $z = 1.445$ is doubted strongly in several papers (see, e.g., Tornikoski et al., 2001)

0405−385

- one of three unusually strong IDV sources (other two: PKS 1257−326 and J1819+385), extreme example of intra-day variability (IDV) one of three IDV sources, possibly caused by interstellar scintillation (ISS) (Kedziora-Chudczer et al., 1996; Kedziora-Chudczer, 2006)
- component to the west at 1.5 mas, compatible with the RRFID images (Zensus et al., 2002)
- 2003 November: component to the west at 4 mas (Ojha et al., 2005)
- rapid variability in the flux density on hourly time scales, alternation between long periods (years) of quiescence and short (a few months) periods of intense activity (Cimo et al., 2004)

0438−436

- radio-loud, core-dominated, highly polarized quasar (Impey & Tapia, 1988)
- first X-ray spectrum of a high-redshift quasar ($z = 2.85$), strong soft X-ray absorption (probably intrinsic) (Wilkes et al., 1992)
- Brocksopp et al. (2004): radio-loud, high-redshift source $z = 2.852$, spectrum with redshifted absorption
- two components aligned in SE (separation 35 mas), northern component is compact (core) (Preston et al., 1989)
- with better resolution than (Preston et al., 1989), (Shen et al., 1998b) find similar structure: two components aligned in SE separation 35 mas
- core elongated to E–SE with a separation of 1 mas (Tingay et al., 2002)

0454−463

- core-dominant, flat spectrum radio source (flux 2.06 Jy at 5 GHz) (Kuehr et al., 1981)
- highly polarized quasar, measurements of 7.2% (Impey & Tapia, 1990) to 27.1% (Wills et al., 1992)
- compact core, no additional components visible (Ojha et al., 2004a)
- source detected with EGRET (Thompson et al., 1993a; Hartman et al., 1999)

0506−612

- blazar ($z = 1.093$) with a strong associated metal absorber at $z = 1.079$ (Bechtold et al., 2002)
- strong COMPTEL (1–10 MeV) source in the region close to the source, but only very weak EGRET source (above 100 MeV, $3\,\sigma$ source) (Bloemen et al., 1995)
- compact radio core (Ojha et al., 2004a)

05128−458

- PICTOR A is one of the very few nearby ($z = 0.035$) FR II-type radio galaxies (Fanaroff & Riley, 1974)
- FRII broad-line radio galaxy with a strong double-lobed radio source oriented along the east-west direction (Christiansen et al., 1977)
- extended X-ray emission coincident with the eastern radio lobe (most likely non-thermal mechanism) (Grandi et al., 2003)
- VLBI maps: jet to the west, apparent motions for three of the five parsec-scale jet components have been estimated: $0.5 \pm 0.4\,c$, $1.1 \pm 0.5\,c$ and $0.4 \pm 0.7\,c$, no parsec-scale counterjet has been detected (Tingay et al., 2000)
- double peaked Balmer line component (torus model) (Halpern & Eracleous, 1994)
- Chandra observation: X-ray emission is detected from the nucleus, a 1.”9 (110 kpc) long jet to the west of the nucleus, the western radio hot spot some 4.”2 (240 kpc) from the nucleus, and the eastern radio lobe (Wilson et al., 2001)
- counterjet in discussion

0521−365

- BL Lac with strong HI emission lines, intense broad permitted lines have appeared in the spectrum (Ulrich, 1981)
- blazar, powerful radio source, remarkable for its optical synchrotron jet (Danziger et al., 1979; Boisson et al., 1989; Scarpa et al., 1999)
- exhibits strong broad and variable nuclear optical emission lines (Scarpa et al., 1995)
- VLBI map: core jet northwestward consisting of a core and two additional components separated from the core by 3.38 and 8.27 mas (Shen et al., 1998b)
- map: core and component to NW with 3 mas separation (Ojha et al., 2004a)
- object contains a well-studied optical/radio jet extending to the northwest (see Scarpa et al., 1999, and references therein), which was recently detected in the X-rays (Birkinshaw et al., 2002; Cheung et al., 2003)
- EGRET detected and source of γ-rays above 100 GeV(Thompson et al., 1995; Tornikoski et al., 2002)

0537−441

- BL Lac ($z = 0.894$), candidate for a gravitational lensing (Stickel et al., 1988; Romero et al., 1995), but disputed by other authors Falomo et al. (1992); Lewis & Williams (1997)
- strong variable EGRET γ-ray source (Thompson et al., 1993a; Hartman et al., 1999)
- source with a GPS-type spectrum, with spectral peak at 5 GHz (Tornikoski et al., 2001)
- VLA map shows curved jet-like structure leading to the west (Cassaro et al., 1999)

0625−354

- VLBA map shows "core-jet" structure, faint component to the southeast of the core is in the direction of the larger-scale jet. correlation position was 22" north of the core position, image may have some distortion (Fomalont et al., 2000)
- optical counterpart of this FR I radio source, located at the center of the cluster Abell 3392, is a giant elliptical embedded in a rich environment. It is worth noticing the presence of a strong point source in the nucleus of this galaxy (Govoni et al., 2000)

0637−752

- peculiar emission line at 1.60 ± 0.07 keV and equivalent width 59^{+38}_{-34} eV (both in the quasar frame) in the X-ray spectrum of this radio-loud quasar (Yaqoob et al., 1998)
- VLBI map: component to the west (separation ∼5 mas) (Ojha et al., 2004a)
- map: component to the west (separation ∼1.5 mas) (Tingay et al., 2002)
- first celestial Chandra target, 100 kpc X-Ray Jet discovered by Chandra, coinciding with optical and radio contours (Tingay et al., 1998), jet to west turning to the northwest after ∼10 as and a single hot spot to the east of the core (Schwartz et al., 2000)

- Chandra observation: at least 4 knots in the jet resolved, separated from the core by a few arcseconds (Chartas et al., 2000)
- apparent superluminal speed of this jet on the parsec-scale, SSC model of an electron-positron jet with a Doppler factor of ∼10 (Edwards et al., 2006)
- proper motions are just consistent with a weighted average apparent speed of $17.8 \pm 1.0\,c$ (Schwartz et al., 2000; Lovell et al., 2000, using $H_0 = 70\,\mathrm{km/s}$ and $q_0 = 0.15$)

1104−445

- first southern VLBI compact shows core with additional component ∼17 mas ENE (Preston et al., 1989)
- map by Shen et al. (1997) shows slight jet curvature at ∼1.8 mas from the northeast to the north
- map by Tingay et al. (2002) shows structure in NE direction, core heavily resolved

1144−379

- BL Lac object, optical, infrared and rapid radio variability, featureless powerlaw spectrum (Nicolson et al., 1979)
- first VLBI map: unresolved core (Shen et al., 1997)

1257−326

- flat-spectrum, radio-loud quasar, extreme IDV source, Rapid Interstellar Scintillation (Bignall et al., 2003)
- pper limit on the distance to the scattering plasma of no more than 10 pc (Bignall et al., 2006)

1313−333

- possible EGRET detection of this flat spectrum QSO (Nolan et al., 1996)
- map by Fey et al. (1996) shows jet components to the west, separated from the core by a few mas (4.7 at 2.32 GHZ, and 0.9 and 4.5 mas at 8.55 GHz)
- source is very variable at the high radio frequencies, EGRET detections have been made at the increase of millimeter-wave activity, from the end of 1991 to the first half of 1993. The radio spectrum is extremely flat, likely counterpart of 3EG J1313-431 (Tornikoski et al., 2002)

1322−428

- better known as Centaurus A, the closest AGN, thus well-studied, large radio lobes spanning about 10° on the sky (e.g., Cooper et al., 1965, and references therein), includes inner radio lobes (Clarke et al., 1992)
- located in a giant elliptical host galaxy with a distance of 3.8 ± 0.1 Mpc (Harris et al., 2010)
- highest resolved AGN jet, with a resolution of about $(3.1 \pm 1.7) \times 10^3$ Schwarzschild radii in a VLBI image (Müller et al., 2011)

- X-ray emission originating from the jet and the lobes (e.g., Cooke et al., 1978; Mushotzky et al., 1978; Kraft et al., 2003; Hardcastle et al., 2003)
- γ-ray emission detected with EGRET, with *Fermi*/LAT the nucleus and the source's giant radio lobes are seen in the γ-ray regime (Abdo et al., 2010e,d)

1323−526

- IDV source (McCulloch et al., 2005)
- Bignall et al. (2008) suggest a tentative association of this little-studied IDV flat-spectrum radio source with the unidentified EGRET source 3EG J1316-5244

1333−334

- large scale jet: 2 outer components separated by 30 arcmin (650 kpc) and two inner components separated by 2 arcmin (45 kpc) (Goss et al., 1977)
- strong slightly-bent bridge or jet between two diffuse lobes. The bridge shows double structure (inner lobes) near the centre, but not a distinct core. The lobes are edge-brightened although it is an intrinsically weak radio source (Jones & McAdam, 1992)
- regular elliptical galaxy located at the center of cluster Abell 3565 (it is the brightest one) (Govoni et al., 2000)
- compact dust ring close to the nucleus (Jensen et al., 2001)
- on the parsec scale, a jet and a counterjet (direction NW,SE) extend out from a central unresolved core in the 8.4 GHz image, which is consistent with the large scale jet, pointlike emission from center of the galaxy, bolometric luminosity of the unresolved source: $2\,10^{-5}$ of the Eddington luminosity of a 10^9 solar mass BH, thermal soft X-ray emission frum the nucleus with a broader radial profile than the PSF (from hot gas ∼0.56 eV), northwestern jet is brighter (Doppler boosting in an intrinsically symmetric source), relativistic bulk speed (0.79 c), analysis with VLBA and Chandra by Pellegrini et al. (2003)

1424−418

- highly optically polarized quasar (Impey & Tapia, 1988, 1990), $z = 1.524$, VLBI image shows two components separated by ∼3 mas. Assuming the stronger component is the core, the position angle of the weaker component is 260°, significantly different from the reported value for the two 2.3 GHz components of 236°/284° (Preston et al., 1989)
- jet extending 1" to the west of a compact core (Marshall et al., 2005)
- unresolved core, no additional components (Ojha et al., 2004a)
- core slightly extended to the east (Tingay et al., 2002)

1454−354

- Fermi/LAT discovery of γ-ray emission from this flat-spectrum radio quasar (Abdo et al., 2009d)
- indication for weak EGRET detection, PKS 1454−354 and PKS 1501−343 are possible counterparts of the EGRET source 3EG J1500-3509 (Mattox et al., 2001; Sowards-Emmerd et al., 2004)

1501−343

- Mattox et al. (2001) and Sowards-Emmerd et al. (2004) list this source and 1454-354 as a possible counterpart for the EGRET source 3EG J1500-3509

- Petrov et al. (2007) did not detect this source at 22 GHZ in six observations with a minimum flux density limit of 170 mJy.

1549−790

- core-jet radio source of ∼400 pc (about 120 mas) in size, the [O III]lambda5007 has one of the largest widths measured in radio galaxies (Morganti et al., 2001)

- radio jets are pointing close to our line of sight (Tadhunter et al., 2001)

- Holt et al. (2006) claim that this luminous quasar observed at an early stage of its evolution, quasar and jet activity have been triggered in a major merger which has also triggered substantial star formation, accreting at close to the Eddington rate, the black hole in this system is growing rapidly and simultaneously driving relativistic jets, links together several classes of active galaxies, common properties with high-redshift AGN

- map by Ojha et al. (2005) shows two components (core and one comp. SW, separation ∼4 mas

1610−771

- strong flat spectrum radio source identified with a QSO, steep power law continuum ($nu^{-3.8}$, atmosph. correction: $nu^{-2.7}$), until then highest redshift ($z = 1.71$) QSO with steep optical continuum (Hunstead & Murdoch, 1980)

- strongly curved spectrum indicating a strong ultraviolet absorption by dust (Courbin et al., 1997)

- map by Preston et al. (1989) is modeled with a 3.8 Jy component 10 mas in extend with a 1.4 Jy halo approximately 50 mas in diameter (data with 22 mas resolution)

- map by (Tingay et al., 2002) reveal presence of extended component, small scale structure: 3 components at a position angle of -30 degree within about 3 mas (southern one is the brightest one, but not necessarily the core)

- map by Ojha et al. (2005) shows 3 components in the E-W line, separated by 40 mas each

1714−336

- possible counterpart of 3EG J1718-3313 (Sowards-Emmerd et al., 2004)

1716−771

- possible counterpart of 3EG J1720-7820, only one 90 GHz data point, very faint source (S/N less than 4), upper limit 370 Jy at 90 GHZ (Tornikoski et al., 2002)

1718−649

- NGC 6328, closest ($z = 0.014$) gigahertz-peaked spectrum radio galaxy (closest and best studied GPS source), suggestion that GPS sources arise as a consequence of galaxy merger activity (NGC 6328) (Tingay et al., 1997)
- one of the closest GPS sources (distance: 56 Mpc), closer GPS sources are: NGC 1052 (18 Mpc) and IC 1459 (PKS B2254-367, 19 Mpc) (Tingay et al., 2003)
- the object is regarded as a merger of two galaxies, at least one of which is a gas-rich spiral, in the process of forming an elliptical (Fanti et al., 2000)
- analysis of radio spectrum and variability of this source: synchrotron self-absorption or free-free absorption as the sole process responsible for the gigahertz-peaked spectrum (Tingay et al., 2003)

1733−565

- FR II radio source (Morganti et al., 1993), with emission lines in the optical spectrum (Simpson et al., 1996)
- in the kpc-scale: extended lobes, bridge and core emission. radio-lobes (in the SW and NE) separated by 4.57 arcmin (Hunstead et al., 1982)
- SPIRAL observations: emission-line gas is measured to be rotating about and extended perpendicular to the (kpc-scale) radio axis (Bryant & Hunstead, 2002)
- map: unresolved core, tiny component SW separation ∼10 mas (Ojha et al., 2004a)

1759−396

- indentified with the EGRET source 2EG J1800−4005 with 81% confidence (Mattox et al., 1997) and in the precessing catalog with 3EG J1800−3955 (Sowards-Emmerd et al., 2004)

1804−502

- possible counterpart of 3EG J1806-5005, only one 90 GHz data point, very faint source (S/N less than 4), upper limit 250 Jy at 90 GHZ (Tornikoski et al., 2002)

1814−637

- compact steep-spectrum (CSS) source with a basic double-lobed structure oriented almost north-south, no information which structures (if any) correspond to the core, (Tzioumis et al., 1996, 2002)
- the determined redshift $z = 0.645$ is problematic due to bright foreground star (Morganti et al., 2001)
- map: two components, separated by ∼90 mas, NNW (Ojha et al., 2004a)
- map: two (resolved) components, one 200–300 mas to the south, problably an additional small component in between (Tzioumis et al., 2002)

1933−400

- identified with the source 3EG J1935-4022 (Hartman et al., 1999)
- VLA observation: diffuse secondary extending from core to $r = 3.5$ arcsec in p.a. 140 degree (Perley, 1982)

1934−638

- one of the earliest known GPS sources (Kellermann, 1966; Bolton et al., 1963)
- VLBI imaging reveals the GPS source has a compact double morphology with a separation of 42 mas orientated east-west (Tzioumis et al., 1989, 1998)
- this GPS radio galaxy is significantly polarized in the UV with the polarization E-vector close to perpendicular to the radio axis (Tadhunter et al., 2002)
- Compton thick source (shown by *BeppoSAX* observations), high equivalent width of Fe Kα line (equivalent width greater 1 keV) (Risaliti et al., 2003)
- map: two components, separated in E-W direction by ∼40 mas (Ojha et al., 2004a)

1954−388

- optically violent variable (Gilmore, 1980)
- high optical polarization, up to 11% (Impey & Tapia, 1988, 1990)
- VLBI observations showed the presence of a compact core at 2.3 GHz (Preston et al., 1985)
- VLBI image shows a single compact component 0.4 mas × 0.3mas in size, with a flux density of 1.9 Jy (Shen et al., 1998b)
- noted as a new source with a GPS-type spectrum by Tornikoski et al. (2001), with turnover at ∼10 GHz, the compilation of data would suggest that the spectral peak lies closer to 8 GHz (Edwards & Tingay, 2004)
- a compact core-jet morphology (core elongated to the SSE) was revealed by the VLBA observations of (Fomalont et al., 2000)
- map: compact core (tiny component ∼3 mas to the west) (Ojha et al., 2004a)

2005−489

- one of the brightest known BL Lac sources (Wall et al., 1986)
- Discovery of VHE gamma rays, the first AGN independently discovered by HESS as an emitter of VHE photons and only the second such AGN known in the Southern Hemisphere, with $\Gamma = 4.0$ the softest VHE spectrum ever measured from a BL Lac (Aharonian et al., 2005b)
- classified as a high-frequency peaked BL Lac (HBL) due to its X-ray-to-radio flux ratio (Sambruna et al., 1995)
- source detected with EGRET (Lin et al., 1999)
- map: unresolved core, additional component to the SW with separation ∼3 mas (Ojha et al., 2005)
- map: compact core (Shen et al., 1998b)

2027−308

- probably a member of the class of very-narrow-line emission galaxies (Grandi, 1983)
- possible counterpart for 3EG 2034-3110 (Sowards-Emmerd et al., 2004)

2052−474

- quasar ($z = 1.489$) has a bright radio core and a two-sided arcsec-scale radio jet. VLBA data on this object have not revealed the presence of a milliarcsec-scale jet (Tingay et al., 1998)
- no extended X-ray emission detected with *Chandra* (Marshall et al., 2005)
- identified with the EGRET source 3EG J2055-4716 (Hartman et al., 1999)
- compact core (Ojha et al., 2004a)

2106−413

- This object has been identified as a quasar at $z = 1.055$ with several emission lines with equivalent widths of 27–55 Å(White et al., 1988)
- The radio core is moderately polarized 3.5% (Impey & Tapia, 1990)
- core slightly resolved in the VLBA image (Fomalont et al., 2000)

2149−306

- high-redshift, high-luminosity, radio-loud quasar with a strongly blueshifted Fe Kα line (at ∼17 keV in the quasar frame) (Yaqoob et al., 1999; Wang et al., 2003)
- blueshifted lines due to extremely large outflow bulk velocities of 0.6–0.75c (Basu, 2006)
- object hosts a bright X-ray source extensively observed in the past by *ROSAT* and *ASCA* (Siebert et al., 1996; Cappi et al., 1997), *BeppoSAX* (Elvis et al., 2000), *Chandra* (Fang et al., 2001), *XMM-Newton* (Ferrero & Brinkmann, 2003), and more recently by *Swift* (Sambruna et al., 2007)
- VLBI map: core and component to the W, separation 8.7 mas (Ojha et al., 2005)

2152−699

- NED note: Fosbury et al. (1990) suggest that this radio galaxy is a blazar. The radio structure shows a core, a nearby bright lobe and a more distant diffuse lobe, image of kpc-scale radio structure shows the classic double-lobed structure of FR II type.
- There is a bright extended emission-line blob to the north-east of the core (Morganti et al., 1993).
- one of the brightest sources in the sky at 2.3 GHz (Wall, 1994)
- parsec-scale radio jet aligns strongly with optical emission line features, and not with the kiloparsec-scale radio structure (Tingay et al., 1996b)
- Roughly spherical halo of hot gas extending out to 30 kpc around PKS 2153−69 seen with *Chandra* in the X-rays (Young et al., 2005).

- a system of low-ionization filaments extending out to a maximum radius of 20 arcsec and, to the north-east, a luminous cloud at a distance of 10 arcsec from the nucleus. In addition to emission lines of extremely high ionization, the cloud has a continuum that is considerably bluer than that of the underlying stellar population. The radial ionization gradient noted suggests that the nucleus provides the ionizing energy for the cloud, and the tangential ionization gradient suggests that this energy is directed toward it in an intense radiation or plasma beam. radio axis and optical emission line features on the kiloparsec-scale appear to have an obvious connection but are somewhat misaligned (most likely being due to an interaction between the radio jet and an extra-nuclear cloud of gas, the misalignment possibly caused by the deflection of the radio jet in the interaction) (Tadhunter et al., 1988)
- VLBI image: VSOP image shows a resolved core and highly linear, narrow jet approximately 6 mas in extent to the NE (Tingay et al., 2002)
- VLBI image: core with additional jet component to the NE, separation a few milliarcseconds (Ojha et al., 2004a)

2155−304

- NED note: typical X-ray-selected BL Lac object and one of the TeV γ-ray sources (Griffiths et al., 1979). This source is one of the brightest and the most intensively studied object of this class (Smith et al., 1992; Treves et al., 1989; Xie et al., 2001)
- one of the brightest extragalactic X-ray sources in the sky and as a result other X-ray satellites, including ROSAT, *BeppoSAX*, *RXTE*, and *Chandra* (Brinkmann et al., 1994; Chiappetti & Torroni, 1997; Vestrand & Sreekumar, 1999; Nicastro et al., 2002)
- compact, flat-spectrum radio source ($\sim$0.3 Jy), and exhibits an essentially featureless continuum from the radio to the X-ray regime, maximum power emitted by PKS 2155−304 is between the UV and soft X-ray range, and it is the brightest BL Lac detected in the UV regime (Wandel & Urry, 1991)
- detected by EGRET (Vestrand et al., 1995)
- VHE gamma-rays from this source were observe (Aharonian et al., 2005a)
- TeV flare observered (July 2006) (Aharonian et al., 2007)
- VLBI map: only compact core without additional components (Ojha et al., 2004a)
- measured apparent speed of the single jet component was (0.93 ± 0.31)c (Piner et al., 2008)

2204−540

- QSO with a flux of 1.3 Jy at 18.5 GHz with a polarization of 6.6 ± 0.2 % (Ricci et al., 2004)

2326−477

- Scott et al. (2004) find a compact, unresolved core structure smaller than 0.1 mas^2 of 410 mJy and a brightness temperature above 3×10^{11} K at 5 GHz.
- Tingay et al. (2003) find a substantially higher mean flux-density 5 GHz of 1.63 Jy with ATCA and a moderate variability index of 0.05, suggesting that a substantial fraction of the 5 GHz total brightness is emitted on larger scales unresolved for the space-VLBI array.
- our image shows jet-like emission peaking in two distinct components $\sim$6 mas to the east and $\sim$10 mas to the north-east of the compact core at 8.4 GHz

2355−534

- optically violent and highly polarized source (Impey & Tapia, 1988, 1990)
- VLBI image shows two components with similar size but different flux densities. The stronger component, which may be the core, has a brightness temperature of 3.5×10^{11} K. The second component is located at a distance of 4.9 mas at a position angle of 235° (Shen et al., 1998b)
- the VSOP data proved insufficient to produce an image, single-component model fit of the data (Tingay et al., 2002)

A.1.3 X-ray observations of TANAMI sources

Table A.2: List of X-ray observations with current X-ray instruments of the AGN in the TANAMI sample (Status: end of 2010). For each of the selected instruments the table shows the number of observations from the master catalog and the total exposure in ks.

Source	*Chandra* ACIS-HRC		*RXTE* PCA		*Suzaku* XIS		*Swift* XRT		*XMM-Newton* EPIC-PN	
	#	ks	#	ks	#	ks	#	ks	#	ks
0047-579							2	4.8		
0055-328							3	7.2		
0208-512	2	59.2			1	52.0	59	107.8	1	16.9
0227-369							1	12.4		
0244-470							1	5.4		
0302-623							2	12.3		
0308-611							3	7.7		
0332-376							5	33.2		
0332-403			4	20.1			3	9.5		
0402-362	1	53.7					10	36.8		
0405-385			1	1.0			3	22.1		
0412-536							1	5.1		
0426-380							7	10.2		
0438-436							2	6.7	1	12.9
0447-439			11	17.7			11	46.1		
0454-463	1	53.7					4	9.6		
0506-612							1	20.2		
0516-621							2	18.4		
0518-458	8	221.1	5	40.2					3	82.6
0521-365	3	65.3					14	33.7	2	63.0
0524-485							2	13.1		
0527-359										
0537-441			3	21.1			38	163.1	3	69.2
0625-354	1	53.7					2	5.9	3	37.3
0637-752	28	405.6					6	14.8		
0700-661							2	4.9		
0717-432							4	21.4		
0736-770							2	7.0		
0745-330							3	4.8		
0812-736							6	85.0		
1057-797							5	16.2		
1101-536							1	4.0		
1104-445										
1144-379							3	11.1		

1257-326										
1258-321	1	53.7					1	2.1		
1313-333							3	6.8		
1322-428	25	391.2	257	866.7	4	234.3	16	48.7	2	39.2
1323-526							4	16.8		
1325-558							3	3.6		
1333-337	2	59.2	1700	2343.3						
1344-376							2	3.9		
1424-418	1	53.7					12	29.7		
1440-389							1	8.4		
1454-354							2	10.7		
1501-343							2	5.1		
1505-496							2	10.3		
1549-790					1	82.2	2	18.8	2	93.5
1600-445							2	7.7		
1600-489							3	6.1		
1606-667							2	1.2		
1610-771							7	10.6		
1613-586										
1646-506										
1714-336										
1716-771										
1718-649							3	5.1		
1733-565	1	53.7								
1759-396							2	12.0		
1804-502										
1814-637	1	53.7							2	52.1
1933-400							1	5.0		
1934-638	1	53.7								
1954-388							4	7.6		
2005-489	5	121.5	158	483.2			9	47.5	3	62.1
2027-308							2	5.0		
2052-474	1	53.7					6	11.4		
2106-413										
2136-428	1	53.7					2	7.3	2	21.5
2149-306	2	59.2					10	27.0	1	24.9
2152-699	3	65.3					3	5.5	1	57.0
2155-304	75	1510.5	501	1107.3	6	263.5	67	159.0	21	1206.5
2204-540							3	15.7		
2326-477	1	53.7					2	4.4		
2355-534							3	7.4		

A.2 MOJAVE sources

Table A.3: List of all sources in the MOJAVE 1 sample. The listed values have been collected by the MOJAVE team (see, e.g., the sample list on the MOJAVE website: http://www.physics.purdue.edu/astro/MOJAVE)

Source	J2000 name	Common name	Opt. ID	Redshift	Right ascension	Declination
0003−066	J0006−0623	NRAO 005	B	0.3467	$00^{h}06^{m}13\overset{s}{.}893$	$-06°23'35\overset{''}{.}335$
0007+106	J0010+1058	III Zw 2	G	0.0893	$00^{h}10^{m}31\overset{s}{.}006$	$+10°58'29\overset{''}{.}504$
0016+731	J0019+7327	S5 0016+73	Q	1.781	$00^{h}19^{m}45\overset{s}{.}786$	$+73°27'30\overset{''}{.}018$
0048−097	J0050−0929	PKS 0048-09	B	0.635	$00^{h}50^{m}41\overset{s}{.}317$	$-09°29'05\overset{''}{.}210$
0059+581	J0102+5824	TXS 0059+581	Q	0.644	$01^{h}02^{m}45\overset{s}{.}762$	$+58°24'11\overset{''}{.}137$

0106+013	J0108+0135	4C +01.02	Q	2.099	$01^h08^m38^s.771$	$+01°35'00''.317$
0109+224	J0112+2244	S2 0109+22	B	0.265	$01^h12^m05^s.825$	$+22°44'38''.786$
0119+115	J0121+1149	PKS 0119+11	Q	0.57	$01^h21^m41^s.595$	$+11°49'50''.413$
0133+476	J0136+4751	DA 55	Q	0.859	$01^h36^m58^s.595$	$+47°51'29''.100$
0202+149	J0204+1514	4C +15.05	Q	0.405	$02^h04^m50^s.414$	$+15°14'11''.044$
0202+319	J0205+3212	B2 0202+31	Q	1.466	$02^h05^m04^s.925$	$+32°12'30''.095$
0212+735	J0217+7349	S5 0212+73	Q	2.367	$02^h17^m30^s.813$	$+73°49'32''.622$
0215+015	J0217+0144	OD 026	Q	1.715	$02^h17^m48^s.955$	$+01°44'49''.699$
0224+671	J0228+6721	4C +67.05	Q	0.523	$02^h28^m50^s.051$	$+67°21'03''.029$
0234+285	J0237+2848	4C +28.07	Q	1.206	$02^h37^m52^s.406$	$+28°48'08''.990$
0235+164	J0238+1636	AO 0235+164	B	0.94	$02^h38^m38^s.930$	$+16°36'59''.275$
0238−084	J0241−0815	NGC 1052	G	0.005037	$02^h41^m04^s.799$	$-08°15'20''.752$
0300+470	J0303+4716	4C +47.08	B		$03^h03^m35^s.242$	$+47°16'16''.276$
0316+413	J0319+4130	3C 84	G	0.0176	$03^h19^m48^s.160$	$+41°30'42''.105$
0333+321	J0336+3218	NRAO 140	Q	1.259	$03^h36^m30^s.108$	$+32°18'29''.342$
0336−019	J0339−0146	CTA 26	Q	0.852	$03^h39^m30^s.938$	$-01°46'35''.804$
0403−132	J0405−1308	PKS 0403-13	Q	0.571	$04^h05^m34^s.003$	$-13°08'13''.691$
0415+379	J0418+3801	3C 111	G	0.0491	$04^h18^m21^s.277$	$+38°01'35''.800$
0420−014	J0423−0120	PKS 0420-01	Q	0.9161	$04^h23^m15^s.801$	$-01°20'33''.065$
0422+004	J0424+0036	PKS 0422+00	B		$04^h24^m46^s.842$	$+00°36'06''.329$
0430+052	J0433+0521	3C 120	G	0.033	$04^h33^m11^s.096$	$+05°21'15''.619$
0446+112	J0449+1121	PKS 0446+11			$04^h49^m07^s.671$	$+11°21'28''.596$
0458−020	J0501−0159	S3 0458-02	Q	2.286	$05^h01^m12^s.810$	$-01°59'14''.256$
0528+134	J0530+1331	PKS 0528+134	Q	2.07	$05^h30^m56^s.417$	$+13°31'55''.150$
0529+075	J0532+0732	OG 050	Q	1.254	$05^h32^m38^s.998$	$+07°32'43''.345$
0529+483	J0533+4822	TXS 0529+483	Q	1.162	$05^h33^m15^s.866$	$+48°22'52''.808$
0552+398	J0555+3948	DA 193	Q	2.363	$05^h55^m30^s.806$	$+39°48'49''.165$
0605−085	J0607−0834	OC -010	Q	0.872	$06^h07^m59^s.699$	$-08°34'49''.978$
0607−157	J0609−1542	PKS 0607-15	Q	0.3226	$06^h09^m40^s.950$	$-15°42'40''.673$
0642+449	J0646+4451	OH 471	Q	3.396	$06^h46^m32^s.026$	$+44°51'16''.590$
0648−165	J0650−1637	PKS 0648-16			$06^h50^m24^s.582$	$-16°37'39''.725$
0716+714	J0721+7120	S5 0716+71	B	0.31	$07^h21^m53^s.448$	$+71°20'36''.363$
0727−115	J0730−1141	PKS 0727-11	Q	1.591	$07^h30^m19^s.112$	$-11°41'12''.601$
0730+504	J0733+5022	TXS 0730+504	Q	0.72	$07^h33^m52^s.521$	$+50°22'09''.062$
0735+178	J0738+1742	OI 158	B		$07^h38^m07^s.394$	$+17°42'18''.998$
0736+017	J0739+0137	OI 061	Q	0.1894	$07^h39^m18^s.034$	$+01°37'04''.618$
0738+313	J0741+3112	OI 363	Q	0.631	$07^h41^m10^s.703$	$+31°12'00''.229$
0742+103	J0745+1011	PKS B0742+103	Q	2.624	$07^h45^m33^s.060$	$+10°11'12''.692$
0748+126	J0750+1231	OI 280	Q	0.889	$07^h50^m52^s.046$	$+12°31'04''.828$
0754+100	J0757+0956	PKS 0754+100	B	0.266	$07^h57^m06^s.643$	$+09°56'34''.852$
0804+499	J0808+4950		Q	1.436	$08^h08^m39^s.666$	$+49°50'36''.530$
0805−077	J0808−0751	PKS 0805-07	Q	1.837	$08^h08^m15^s.536$	$-07°51'09''.886$
0808+019	J0811+0146	OJ 014	B	1.148	$08^h11^m26^s.707$	$+01°46'52''.220$
0814+425	J0818+4222	OJ 425	B		$08^h18^m16^s.000$	$+42°22'45''.415$
0823+033	J0825+0309	PKS 0823+033	B	0.506	$08^h25^m50^s.338$	$+03°09'24''.520$
0827+243	J0830+2410	OJ 248	Q	0.942	$08^h30^m52^s.086$	$+24°10'59''.820$
0829+046	J0831+0429	OJ 049	B	0.174	$08^h31^m48^s.877$	$+04°29'39''.086$
0836+710	J0841+7053	4C +71.07	Q	2.218	$08^h41^m24^s.365$	$+70°53'42''.173$
0838+133	J0840+1312	3C 207	Q	0.681	$08^h40^m47^s.588$	$+13°12'23''.564$
0851+202	J0854+2006	OJ 287	B	0.306	$08^h54^m48^s.875$	$+20°06'30''.641$
0906+015	J0909+0121	4C +01.24	Q	1.0256	$09^h09^m10^s.092$	$+01°21'35''.618$

0917+624	J0921+6215	OK 630	Q	1.446	$09^h21^m36^s.231$	$+62°15'52''.180$
0923+392	J0927+3902	4C +39.25	Q	0.695	$09^h27^m03^s.014$	$+39°02'20''.852$
0945+408	J0948+4039	4C +40.24	Q	1.249	$09^h48^m55^s.338$	$+40°39'44''.587$
0955+476	J0958+4725	OK 492	Q	1.882	$09^h58^m19^s.672$	$+47°25'07''.842$
1036+054	J1038+0512	PKS 1036+054	Q	0.473	$10^h38^m46^s.780$	$+05°12'29''.087$
1038+064	J1041+0610	4C +06.41	Q	1.265	$10^h41^m17^s.163$	$+06°10'16''.924$
1045−188	J1048−1909		Q	0.595	$10^h48^m06^s.621$	$-19°09'35''.727$
1055+018	J1058+0133	4C +01.28	Q	0.888	$10^h58^m29^s.605$	$+01°33'58''.824$
1124−186	J1127−1857	PKS 1124-186	Q	1.048	$11^h27^m04^s.392$	$-18°57'17''.442$
1127−145	J1130−1449	PKS 1127-14	Q	1.184	$11^h30^m07^s.053$	$-14°49'27''.388$
1150+812	J1153+8058		Q	1.25	$11^h53^m12^s.499$	$+80°58'29''.155$
1156+295	J1159+2914	4C +29.45	Q	0.7246	$11^h59^m31^s.834$	$+29°14'43''.827$
1213−172	J1215−1731	PKS 1213-17			$12^h15^m46^s.752$	$-17°31'45''.403$
1219+044	J1222+0413	4C +04.42	Q	0.965	$12^h22^m22^s.550$	$+04°13'15''.776$
1222+216	J1224+2122	4C +21.35	Q	0.434	$12^h24^m54^s.458$	$+21°22'46''.389$
1226+023	J1229+0203	3C 273	Q	0.1583	$12^h29^m06^s.700$	$+02°03'08''.598$
1228+126	J1230+1223	M87	G	0.00436	$12^h30^m49^s.423$	$+12°23'28''.044$
1253−055	J1256−0547	3C 279	Q	0.536	$12^h56^m11^s.167$	$-05°47'21''.525$
1308+326	J1310+3220	OP 313	Q	0.9973	$13^h10^m28^s.664$	$+32°20'43''.783$
1324+224	J1327+2210	B2 1324+22	Q	1.4	$13^h27^m00^s.861$	$+22°10'50''.163$
1334−127	J1337−1257	PKS 1335-127	Q	0.539	$13^h37^m39^s.783$	$-12°57'24''.693$
1413+135	J1415+1320	PKS B1413+135	B	0.247	$14^h15^m58^s.818$	$+13°20'23''.713$
1417+385	J1419+3821	B3 1417+385	Q	1.831	$14^h19^m46^s.614$	$+38°21'48''.475$
1458+718	J1459+7140	3C 309.1	Q	0.904	$14^h59^m07^s.584$	$+71°40'19''.867$
1502+106	J1504+1029	OR 103	Q	1.8385	$15^h04^m24^s.980$	$+10°29'39''.199$
1504−166	J1507−1652		Q	0.876	$15^h07^m04^s.787$	$-16°52'30''.267$
1510−089	J1512−0905	PKS 1510-08	Q	0.36	$15^h12^m50^s.533$	$-09°05'59''.830$
1538+149	J1540+1447	4C +14.60	B	0.605	$15^h40^m49^s.492$	$+14°47'45''.885$
1546+027	J1549+0237	PKS 1546+027	Q	0.414	$15^h49^m29^s.437$	$+02°37'01''.163$
1548+056	J1550+0527	4C +05.64	Q	1.417	$15^h50^m35^s.269$	$+05°27'10''.448$
1606+106	J1608+1029	4C +10.45	Q	1.226	$16^h08^m46^s.203$	$+10°29'07''.776$
1611+343	J1613+3412	DA 406	Q	1.4	$16^h13^m41^s.064$	$+34°12'47''.909$
1633+382	J1635+3808	4C +38.41	Q	1.813	$16^h35^m15^s.493$	$+38°08'04''.501$
1637+574	J1638+5720	OS 562	Q	0.751	$16^h38^m13^s.456$	$+57°20'23''.979$
1638+398	J1640+3946	NRAO 512	Q	1.666	$16^h40^m29^s.633$	$+39°46'46''.028$
1641+399	J1642+3948	3C 345	Q	0.593	$16^h42^m58^s.810$	$+39°48'36''.994$
1655+077	J1658+0741	PKS 1655+077	Q	0.621	$16^h58^m09^s.011$	$+07°41'27''.540$
1726+455	J1727+4530	S4 1726+45	Q	0.717	$17^h27^m27^s.651$	$+45°30'39''.731$
1730−130	J1733−1304	NRAO 530	Q	0.902	$17^h33^m02^s.706$	$-13°04'49''.548$
1739+522	J1740+5211	4C +51.37	Q	1.379	$17^h40^m36^s.978$	$+52°11'43''.407$
1741−038	J1743−0350	PKS 1741-03	Q	1.054	$17^h43^m58^s.856$	$-03°50'04''.617$
1749+096	J1751+0939	4C +09.57	B	0.322	$17^h51^m32^s.819$	$+09°39'00''.728$
1751+288	J1753+2848	B2 1751+28	Q	1.118	$17^h53^m42^s.474$	$+28°48'04''.939$
1758+388	J1800+3848		Q	2.092	$18^h00^m24^s.765$	$+38°48'30''.698$
1800+440	J1801+4404	S4 1800+44	Q	0.663	$18^h01^m32^s.315$	$+44°04'21''.900$
1803+784	J1800+7828	S5 1803+784	B	0.6797	$18^h00^m45^s.684$	$+78°28'04''.018$
1807+698	J1806+6949	3C 371	B	0.051	$18^h06^m50^s.681$	$+69°49'28''.109$
1823+568	J1824+5651	4C +56.27	B	0.664	$18^h24^m07^s.068$	$+56°51'01''.491$
1828+487	J1829+4844	3C 380	Q	0.692	$18^h29^m31^s.781$	$+48°44'46''.161$
1849+670	J1849+6705	S4 1849+67	Q	0.657	$18^h49^m16^s.072$	$+67°05'41''.680$
1928+738	J1927+7358	4C +73.18	Q	0.302	$19^h27^m48^s.495$	$+73°58'01''.570$

1936−155	J1939−1525		Q	1.657	$19^{h}39^{m}26\overset{s}{.}658$	$-15°25'43\overset{''}{.}059$
1957+405	J1959+4044	Cygnus A	G	0.0561	$19^{h}59^{m}28\overset{s}{.}356$	$+40°44'02\overset{''}{.}099$
1958−179	J2000−1748	PKS 1958-179	Q	0.652	$20^{h}00^{m}57\overset{s}{.}090$	$-17°48'57\overset{''}{.}673$
2005+403	J2007+4029	TXS 2005+403	Q	1.736	$20^{h}07^{m}44\overset{s}{.}945$	$+40°29'48\overset{''}{.}604$
2008−159	J2011−1546	PKS 2008-159	Q	1.18	$20^{h}11^{m}15\overset{s}{.}711$	$-15°46'40\overset{''}{.}254$
2021+317	J2023+3153	4C +31.56			$20^{h}23^{m}19\overset{s}{.}017$	$+31°53'02\overset{''}{.}306$
2021+614	J2022+6136	OW 637	G	0.227	$20^{h}22^{m}06\overset{s}{.}682$	$+61°36'58\overset{''}{.}805$
2037+511	J2038+5119	3C 418	Q	1.686	$20^{h}38^{m}37\overset{s}{.}035$	$+51°19'12\overset{''}{.}663$
2121+053	J2123+0535	PKS 2121+053	Q	1.941	$21^{h}23^{m}44\overset{s}{.}517$	$+05°35'22\overset{''}{.}093$
2128−123	J2131−1207	PKS 2128-12	Q	0.501	$21^{h}31^{m}35\overset{s}{.}262$	$-12°07'04\overset{''}{.}796$
2131−021	J2134−0153	4C -02.81	B	1.284	$21^{h}34^{m}10\overset{s}{.}310$	$-01°53'17\overset{''}{.}239$
2134+004	J2136+0041	PKS 2134+004	Q	1.932	$21^{h}36^{m}38\overset{s}{.}586$	$+00°41'54\overset{''}{.}213$
2136+141	J2139+1423	OX 161	Q	2.427	$21^{h}39^{m}01\overset{s}{.}309$	$+14°23'35\overset{''}{.}992$
2145+067	J2148+0657	4C +06.69	Q	0.999	$21^{h}48^{m}05\overset{s}{.}459$	$+06°57'38\overset{''}{.}604$
2155−152	J2158−1501	PKS 2155-152	Q	0.672	$21^{h}58^{m}06\overset{s}{.}282$	$-15°01'09\overset{''}{.}328$
2200+420	J2202+4216	BL Lac	B	0.0686	$22^{h}02^{m}43\overset{s}{.}291$	$+42°16'39\overset{''}{.}980$
2201+171	J2203+1725	PKS 2201+171	Q	1.076	$22^{h}03^{m}26\overset{s}{.}894$	$+17°25'48\overset{''}{.}248$
2201+315	J2203+3145	4C +31.63	Q	0.2947	$22^{h}03^{m}14\overset{s}{.}976$	$+31°45'38\overset{''}{.}270$
2209+236	J2212+2355	PKS 2209+236	Q	1.125	$22^{h}12^{m}05\overset{s}{.}966$	$+23°55'40\overset{''}{.}544$
2216−038	J2218−0335	PKS 2216-03	Q	0.901	$22^{h}18^{m}52\overset{s}{.}038$	$-03°35'36\overset{''}{.}879$
2223−052	J2225−0457	3C 446	Q	1.404	$22^{h}25^{m}47\overset{s}{.}259$	$-04°57'01\overset{''}{.}391$
2227−088	J2229−0832	PHL 5225	Q	1.5595	$22^{h}29^{m}40\overset{s}{.}084$	$-08°32'54\overset{''}{.}435$
2230+114	J2232+1143	CTA 102	Q	1.037	$22^{h}32^{m}36\overset{s}{.}409$	$+11°43'50\overset{''}{.}904$
2243−123	J2246−1206	PKS 2243-123	Q	0.632	$22^{h}46^{m}18\overset{s}{.}232$	$-12°06'51\overset{''}{.}278$
2251+158	J2253+1608	3C 454.3	Q	0.859	$22^{h}53^{m}57\overset{s}{.}748$	$+16°08'53\overset{''}{.}561$
2331+073	J2334+0736	TXS 2331+073	Q	0.401	$23^{h}34^{m}12\overset{s}{.}828$	$+07°36'27\overset{''}{.}551$
2345−167	J2348−1631	PKS 2345-16	Q	0.576	$23^{h}48^{m}02\overset{s}{.}609$	$-16°31'12\overset{''}{.}022$
2351+456	J2354+4553	4C +45.51	Q	1.986	$23^{h}54^{m}21\overset{s}{.}680$	$+45°53'04\overset{''}{.}237$

References

Abdo A.A., Ackermann M., Ajello M., et al., 2010a, ApJS 188, 405
Abdo A.A., Ackermann M., Ajello M., et al., 2010b, ApJ 715, 429
Abdo A.A., Ackermann M., Ajello M., et al., 2010c, ApJ 708, 1310
Abdo A.A., Ackermann M., Ajello M., et al., 2009a, ApJS 183, 46
Abdo A.A., Ackermann M., Ajello M., et al., 2010d, Science 328, 725
Abdo A.A., Ackermann M., Ajello M., et al., 2010e, ApJ 719, 1433
Abdo A.A., Ackermann M., Ajello M., et al., 2009b, ApJ 700, 597
Abdo A.A., Ackermann M., Ajello M., et al., 2009c, Science 326, 1512
Abdo A.A., Ackermann M., Atwood W.B., et al., 2009d, ApJ 697, 934
Aharonian F., Akhperjanian A.G., Aye K.M., et al., 2005a, A&A 430, 865
Aharonian F., Akhperjanian A.G., Aye K.M., et al., 2005b, A&A 436, L17
Aharonian F., Akhperjanian A.G., Bazer-Bachi A.R., et al. 2007, ApJL 664, L71
Akritas M.G., Siebert J., 1996, MNRAS 278, 919
Alfvén H., 1942, Nat 150, 405
Alfvén H., Herlofson N., 1950, Physical Review 78, 616
Aller H.D., Aller M.F., Hughes P.A., 1996, In: Miller H.R., Webb J.R., Noble J.C. (eds.) Blazar Continuum Variability. ASP Conf. Series 110, p. 208
Angelakis E., Fuhrmann L., Nestoras I., et al., 2010, In: T. Savolainen, E. Ros, R. W. Porcas, and J. A. Zensus (ed.) Proceedings of the Workshop 'Fermi meets Jansky - AGN in Radio and Gamma-Rays., p. 81
Arnaud K., Dorman B., Gordon C., 2007, XSPEC Users Guide, HEASARC, NASA/GSFC
Arnett W.D., Bahcall J.N., Kirshner R.P., Woosley S.E., 1989, ARA&A 27, 629
Arnold J.R., Metzger A.E., Anderson E.C., van Dilla M.A., 1962, J. Geophys. Res. 67, 4878
Atoyan A., Dermer C.D., 2001, Physical Review Letters 87, 221102
Atwood W.B., Abdo A.A., Ackermann M., et al., 2009, ApJ 697, 1071
Atwood W.B., Bagagli R., Baldini L., et al., 2007, Astroparticle Physics 28, 422
Baade W., Minkowski R., 1954, ApJ 119, 206
Baixeras C., Bastieri D., Bigongiari C., et al., 2004, Nuclear Instruments and Methods in Physics Research A 518, 188
Ballantyne D.R., Fabian A.C., 2005, ApJ 622, L97
Barbieri C., Capaccioli M., Zambon M., 1975, MmSAI 46, 461
Bardeen J.M., Press W.H., Teukolsky S.A., 1972, ApJ 178, 347
Barthelmy S.D., Barbier L.M., Cummings J.R., et al., 2005, Space Sci. Rev. 120, 143
Basu D., 2006, AJ 131, 1231
Beasley A.J., Gordon D., Peck A.B., et al., 2002, ApJS 141, 13
Bechtold J., Dobrzycki A., Wilden B., et al., 2002, ApJS 140, 143
Begelman M.C., Blandford R.D., Rees M.J., 1984, Reviews of Modern Physics 56, 255
Belloni T.M., 2010, In: Belloni T. (ed.) Lecture Notes in Physics 794., Springer-Verlag, Berlin, p. 53
Bergeron J., Boissé P., Ménard B., 2011, A&A 525, A51

Beringer J., Arguin J.F., et al. (Particle Data Group) 2012, Phys. Rev. D 86, 010001
Bertsch D.L., Dingus B.L., Fichtel C.E., et al. 1993, ApJ 405, L21
Bignall H., Cimo G., Jauncey D., et al., 2008, In: From Planets to Dark Energy., PoS (MRU) 84
Bignall H.E., Jauncey D.L., Lovell J.E.J., et al., 2003, ApJ 585, 653
Bignall H.E., Macquart J.P., Jauncey D.L., et al., 2006, ApJ 652, 1050
Bignami G.F., Boella G., Burger J.J., et al., 1975, Space Science Instrumentation 1, 245
Birkinshaw M., Worrall D.M., Hardcastle M.J., 2002, MNRAS 335, 142
Blakeslee J.P., Lucey J.R., Barris B.J., et al., 2001, MNRAS 327, 1004
Blandford R.D., Königl A., 1979, ApJ 232, 34
Blandford R.D., McKee C.F., 1982, ApJ 255, 419
Blandford R.D., Payne D.G., 1982, MNRAS 199, 883
Blandford R.D., Rees M.J., 1978, Phys. Scr. 17, 265
Blandford R.D., Znajek R.L., 1977, MNRAS 179, 433
Bloemen H., Bennett K., Blom J.J., et al., 1995, A&A 293, L1
Blom J.J., Bennett K., Bloemen H., et al., 1995, A&A 298, L33
Böck M., Grinberg V., Pottschmidt K., et al., 2011, A&A 533, A8
Böck M., Kadler M., Müller C., et al., 2012, in prep.
Böck M., Kadler M., Ros E., et al., 2010a, In: 38th COSPAR Scientific Assembly, Vol. 38. COSPAR, Plenary Meeting, p. 3729
Böck M., Kadler M., Tosti G., et al., 2009, In: Conference proceedings "2009 Fermi Symposium". eConf Proceedings C091122
Böck M., Kadler M., Tosti G., et al., 2010b, In: T. Savolainen, E. Ros, R. W. Porcas, and J. A. Zensus (ed.) Proceedings of the Workshop "Fermi meets Jansky - AGN in Radio and Gamma-Rays"., p. 17
Böck, M. 2008, *Master's thesis*, Dr. Remeis Observatory Bamberg, Germany
Boella G., Butler R.C., Perola G.C., et al., 1997, A&AS 122, 299
Boisson C., Cayatte V., Sol H., 1989, A&A 211, 275
Bolton J.G., Gardner F.F., Mackey F.B., 1963, Nat 199, 682
Böttcher M., 2007, Ap&SS 309, 95
Böttcher M., Dermer C.D., 2010, ApJ 711, 445
Braatz J.A., Wilson A.S., Henkel C., et al., 2003, ApJS 146, 249
Brenneman L.W., Weaver K.A., Kadler M., et al., 2009, ApJ 698, 528
Brickhouse N.S., Desai P., Hoogerwerf R., et al., 2005, In: Smith R. (ed.) X-ray Diagnostics of Astrophysical Plasmas: Theory, Experiment, and Observation. AIP Conf. Series 774, p.405
Briggs M.S., Fishman G.J., Connaughton V., et al., 2010, Journal of Geophysical Research (Space Physics) 115, 7323
Brinkmann W., Maraschi L., Treves A., et al., 1994, A&A 288, 433
Brocksopp C., Puchnarewicz E.M., Mason K.O., et al., 2004, MNRAS 349, 687
Brown B.W., Hollander M., Korwar R.M., 1974, In: F. Proschan R.S. (ed.) Reliability and Biometry: Statistical Analysis of Lifelength, SIAM, Philadelphia., p.327
Bryant J.J., Hunstead R.W., 2002, MNRAS 337, 861
Burrows D.N., Hill J.E., Nousek J.A., et al., 2000, In: Flanagan K.A., Siegmund O.H. (eds.) Society of Photo-Optical Instrumentation Engineers (SPIE) Conf. Series, Vol. 4140., p.64
Camero-Arranz A., Finger M.H., Ikhsanov N.R., et al., 2010, ApJ 708, 1500
Cappi M., Matsuoka M., Comastri A., et al., 1997, ApJ 478, 492
Carroll B.W., Ostlie D.A., 2006, An introduction to modern astrophysics and cosmology, San Francisco: Pearson, Addison-Wesley
Carroll S.M., Press W.H., Turner E.L., 1992, ARA&A 30, 499
Case G.L., Cherry M.L., Wilson-Hodge C.A., et al. 2011, ApJ 729, 105
Cash W., 1979, ApJ 228, 939

Cassaro P., Stanghellini C., Bondi M., et al., 1999, A&AS 139, 601
Catanese M., Weekes T.C., 1999, PASP 111, 1193
Chandrasekhar S., 1931, ApJ 74, 81
Chang C.S., Ros E., Kadler M., et al., 2010a, In: T. Savolainen, E. Ros, R. W. Porcas, and J. A. Zensus (ed.) Proceedings of the Workshop 'Fermi meets Jansky - AGN in Radio and Gamma-Rays".
Chang C.S., Ros E., Kadler M., et al., 2010b, In: Proceedings of the 10th European VLBI Network Symposium and EVN Users Meeting: VLBI and the new generation of radio arrays., published online at http://pos.sissa.it/cgi-bin/reader/conf.cgi?confid=125, id.39
Chartas G., Worrall D.M., Birkinshaw M., et al., 2000, ApJ 542, 655
Cheung C.C., Urry C.M., Scarpa R., Giavalisco M., 2003, ApJ 599, 155
Chiang J., Fichtel C.E., von Montigny C., et al., 1995, ApJ 452, 156
Chiappetti L., Torroni V., 1997, IAU Circ. 6776, 2
Christiansen W.N., Frater R.H., Watkinson A., et al., 1977, MNRAS 181, 183
Cimo G., Ellingsen S., Carter S., et al., 2004, IAU Circ. 8403, 1
Circella M., ANTARES Collaboration 2009, Nuclear Instruments and Methods in Physics Research A 602, 1
Clarke D.A., Burns J.O., Norman M.L., 1992, ApJ 395, 444
Claussen M.J., Diamond P.J., Braatz J.A., et al., 1998, ApJ 500, L129
Cohen M.H., Cannon W., Purcell G.H., et al., 1971, ApJ 170, 207
Cohen M.H., Lister M.L., Homan D.C., et al., 2007, ApJ 658, 232
Compton A.H., 1923, Physical Review 21, 483
Cooke B.A., Lawrence A., Perola G.C., 1978, MNRAS 182, 661
Cooper B.F.C., Price R.M., Cole D.J., 1965, Australian Journal of Physics 18, 589
Courbin F., Hutsemekers D., Meylan G., et al., 1997, A&A 317, 656
Cowley A.P., Crampton D., Hutchings J.B., et al., 1983, ApJ 272, 118
Critchfield C.L., Ney E.P., Oleksa S., 1952, Physical Review 85, 461
Curtis H.D., 1918, Descriptions of 762 Nebulae and Clusters Photographed With the Crossley Reflector, Publications of the Lick Observatory, 31
Curtis H.D., 1921, The Scale of the Universe, Bull. Nat. Res. Coun. 2, 171
Danziger I.J., Fosbury R.A.E., Goss W.M., Ekers R.D., 1979, MNRAS 188, 415
Dauser T., Wilms J., et al. 2012, in prep. 409, X
Dauser T., Wilms J., Reynolds C.S., Brenneman L.W., 2010, MNRAS 409, 1534
Deller A.T., Tingay S.J., Bailes M., West C., 2007, PASP 119, 318
Denicoló G., Terlevich R., Terlevich E., et al., 2005, MNRAS 356, 1440
Dermer C.D., 1986, A&A 157, 223
Dermer C.D., Schlickeiser R., 1993, ApJ 416, 458
Diamond P.J., 1995, In: Zensus J.A., Diamond P.J., Napier P.J. (eds.) Very Long Baseline Interferometry and the VLBA. ASP Conf. Series 82, p. 227
Dodson R., Fomalont E.B., Wiik K., et al., 2008, ApJS 175, 314
Doeleman S., 2010, In: Proceedings of the 10th European VLBI Network Symposium and EVN Users Meeting: VLBI and the new generation of radio arrays., published online at http://pos.sissa.it/cgi-bin/reader/conf.cgi?confid=125, id.53
Dondi L., Ghisellini G., 1995, MNRAS 273, 583
Drinkwater M.J., Webster R.L., Francis P.J., et al., 1997, MNRAS 284, 85
Eckart A., Genzel R., Ott T., Schödel R., 2002, MNRAS 331, 917
Edwards P.G., Piner B.G., Tingay S.J., et al., 2006, PASJ 58, 233
Edwards P.G., Tingay S.J., 2004, A&A 424, 91
Einstein A., 1916, Annalen der Physik 354, 769
Elitzur M., Shlosman I., 2006, ApJ 648, L101

Elvis M., 2000, ApJ 545, 63
Elvis M., Fiore F., Siemiginowska A., et al., 2000, ApJ 543, 545
Fabian A.C., Iwasawa K., Reynolds C.S., Young A.J., 2000, PASP 112, 1145
Fabian A.C., Zoghbi A., Ross R.R., et al., 2009, Nat 459, 540
Falcke H., Körding E., Markoff S., 2004, A&A 414, 895
Falcke H.D., van Haarlem M.P., de Bruyn A.G., et al., 2007, Highlights of Astronomy 14, 386
Falomo R., Melnick J., Tanzi E.G., 1992, A&A 255, L17
Falomo R., Scarpa R., Bersanelli M., 1994, ApJS 93, 125
Fanaroff B.L., Riley J.M., 1974, MNRAS 167, 31P
Fang T., Marshall H.L., Bryan G.L., Canizares C.R., 2001, ApJ 555, 356
Fanti C., Pozzi F., Fanti R., et al., 2000, A&A 358, 499
Fath E.A., 1909, Ph.D. thesis, University of California, Berkeley
Fazio G.G., 1970, Nat 225, 905
Feenberg E., Primakoff H., 1948, Physical Review 73, 449
Fender R.P., Belloni T.M., Gallo E., 2004, MNRAS 355, 1105
Fender R.P., Gallo E., Russell D., 2010, MNRAS 406, 1425
Fender R.P., Stirling A.M., Spencer R.E., et al., 2006, MNRAS 369, 603
Ferrarese L., Merritt D., 2000, ApJ 539, L9
Ferreira J., Dougados C., Cabrit S., 2006, A&A 453, 785
Ferrero E., Brinkmann W., 2003, A&A 402, 465
Fey A.L., Clegg A.W., Fomalont E.B., 1996, ApJS 105, 299
Fichtel C.E., Hartman R.C., Kniffen D.A., et al., 1975, ApJ 198, 163
Fish V.L., Doeleman S.S., Beaudoin C., et al., 2011, ApJ 727, L36
Fomalont E., 1981, National Radio Astronomy Observatory Newsletter 3, 3
Fomalont E.B., 1999, In: Taylor G.B., Carilli C.L., Perley R.A. (eds.) Synthesis Imaging in Radio Astronomy II. ASP Conf. Series 180, p. 301
Fomalont E.B., Frey S., Paragi Z., et al., 2000, ApJS 131, 95
Fosbury R.A.E., di Serego Alighieri S., Courvoisier T.J.L., et al., 1990, In: Rolfe E. (ed.) ESA Special Publication, Vol. 310., p.513
Fosbury R.A.E., Mebold U., Goss W.M., Dopita M.A., 1978, MNRAS 183, 549
Fossati G., Maraschi L., Celotti A., et al., 1998, MNRAS 299, 433
Foster A.R., Ji L., Smith R.K., Brickhouse N.S., 2012, Submitted to ApJ, arXiv:1207.0576
Foukal P., Fröhlich C., Spruit H., Wigley T.M.L., 2006, Nat 443, 161
Fritsch U., 2013, Ph.D. thesis, Friedrich-Alexander-Universität Erlangen-Nürnberg, Germany (in prep.)
Fukugita M., Ichikawa T., Gunn J.E., et al., 1996, AJ 111, 1748
Fürst F., Wilms J., Rothschild R.E., et al., 2009, Earth and Planetary Science Letters 281, 125
Gabel J.R., Bruhweiler F.C., Crenshaw D.M., et al., 2000, ApJ 532, 883
Galloway D.K., Sokoloski J.L., 2004, ApJ 613, L61
García J., Kallman T.R., 2010, ApJ 718, 695
García J., Kallman T.R., Mushotzky R.F., 2011, ApJ 731, 131
Garmire G.P., Bautz M.W., Ford P.G., et al., 2003, In: Truemper J.E., Tananbaum H.D. (eds.) Society of Photo-Optical Instrumentation Engineers (SPIE) Conference Series 4851., p.28
Garrington S.T., Anderson B., Baines C., et al., 2004, In: Oschmann, Jr. J.M. (ed.) Society of Photo-Optical Instrumentation Engineers (SPIE) Conference Series 5489., p.332
Gehrels N., 1986, ApJ 303, 336
Gehrels N., Shrader C.R., 2001, In: S. Ritz, N. Gehrels, & C. R. Shrader (ed.) Gamma 2001: Gamma-Ray Astrophysics. AIP Conf. Series 587, p.3
Ghez A.M., Morris M., Becklin E.E., et al., 2000, Nat 407, 349
Ghez A.M., Salim S., Weinberg N., et al., 2008, In: A Giant Step: from Milli- to Micro-arcsecond

Astrometry, Proceedings of the International Astronomical Union. IAU Symposium 248, p.52
Ghisellini G., Maraschi L., Tavecchio F., 2009, MNRAS 396, L105
Ghisellini G., Tavecchio F., 2008, MNRAS 387, 1669
Giacconi R., Gursky H., Paolini F.R., Rossi B.B., 1962, Phys. Rev. Let. 9, 439
Giacconi R., Kellogg E., Gorenstein P., et al., 1971, ApJ 165, L27
Gies D.R., Bolton C.T., 1986, ApJ 304, 371
Gies D.R., Bolton C.T., Blake R.M., et al., 2008, ApJ 678, 1237
Gilmore G., 1980, MNRAS 190, 649
Ginzburg V.L., Syrovatskii S.I., 1964, The Origin of Cosmic Rays, New York, Macmillan
Golian S.E., Krause E.H., Perlow G.J., 1946, Phys. Rev. 70, 223
Goss W.M., Wellington K.J., Christiansen W.N., et al., 1977, MNRAS 178, 525
Govoni F., Falomo R., Fasano G., Scarpa R., 2000, A&AS 143, 369
Grandi P., Guainazzi M., Maraschi L., et al., 2003, ApJ 586, 123
Grandi S.A., 1983, MNRAS 204, 691
Greisen E.W., 1998, In: Albrecht R., Hook R.N., Bushouse H.A. (eds.) Astronomical Data Analysis Software and Systems VII. ASP Conference Series 145, p.204
Griffiths R.E., Briel U., Chaisson L., Tapia S., 1979, ApJ 234, 810
Guainazzi M., Oosterbroek T., Antonelli L.A., Matt G., 2000, A&A 364, L80
Gubbay J., Legg A.J., Robertson D.S., et al., 1969, Nat 224, 1094
Gulyaev S., Natusch T., Weston S., et al., 2011, ArXiv 1103.2830
Halpern J.P., Eracleous M., 1994, ApJ 433, L17
Halzen F., Hooper D., 2002, Reports on Progress in Physics 65, 1025
Hanke M., 2007, *Master's thesis*, Dr. Remeis Observatory Bamberg, Germany
Hanke M., 2011, Ph.D. thesis, Dr. Remeis Observatory Bamberg, Germany
Hardcastle M.J., Worrall D.M., Kraft R.P., et al., 2003, ApJ 593, 169
Harris G.L.H., Rejkuba M., Harris W.E., 2010, PASA 27, 457
Hartman R.C., Bertsch D.L., Bloom S.D., et al., 1999, ApJS 123, 79
Hartman R.C., Bertsch D.L., Fichtel C.E., et al. 1992, ApJ 385, L1
Hawley J.F., Krolik J.H., 2001, ApJ 548, 348
Hayakawa S., 1952, Progress of Theoretical Physics 8, 571
Healey S.E., Romani R.W., Cotter G., et al., 2008, ApJS 175, 97
Healey S.E., Romani R.W., Taylor G.B., et al., 2007, ApJS 171, 61
Helene O., 1983, NIMPR 212, 319
Hewitt A., Burbidge G., 1987, ApJS 63, 1
Hinton J.A., 2004, NewAR 48, 331
Ho L.C., Filippenko A.V., Sargent W.L.W., Peng C.Y., 1997, ApJS 112, 391
Högbom J.A., 1974, A&AS 15, 417
Holt J., Tadhunter C., Morganti R., et al., 2006, MNRAS 370, 1633
Horiuchi S., Fomalont E.B., Taylor W.K., et al., 2004, ApJ 616, 110
Houck J.C., 2002, In: Branduardi-Raymont G. (ed.) High Resolution X-ray Spectroscopy with XMM-Newton and Chandra. Mullard Space Science Laboratory
Houck J.C., Denicola L.A., 2000, In: Manset N., Veillet C., Crabtree D. (eds.) Astronomical Data Analysis Software and Systems IX. ASP Conf. Ser. 216, p. 591
Hovatta T., Valtaoja E., Tornikoski M., Lähteenmäki A., 2009, A&A 494, 527
Hubble E., 1927, Contributions from the Mount Wilson Observatory 3, 23
Hubble E., 1938, PASP 50, 97
Hudson M.J., Lucey J.R., Smith R.J., et al., 2001, MNRAS 327, 265
Hughes P.A., Aller H.D., Aller M.F., 1992, ApJ 396, 469
Hulsizer R.I., Rossi B., 1948, Physical Review 73, 1402
Hunstead R.W., Durdin J.M., Little A.G., et al., 1982, Proceedings of the Astronomical Society of

Australia 4, 447
Hunstead R.W., Murdoch H.S., 1980, MNRAS 192, 31P
Hunter S.D., Kanbach G., 1990, In: Fichtel C.E., Hunter S.D., Sreekumar P., Stecker F.W. (eds.) NASA Conference Publication, Vol. 3071., p.43
Hynes R.I., Steeghs D., Casares J., et al., 2003, In: Bulletin of the American Astronomical Society, Vol. 35., p. 615
Impey C.D., Tapia S., 1988, ApJ 333, 666
Impey C.D., Tapia S., 1990, ApJ 354, 124
Israel F.P., 1998, Astron. Astrophys. Rev. 8, 237
Israel W., 1987, Dark stars: the evolution of an idea., In: Hawking S.W., Israel W. (eds.) Three Hundred Years of Gravitation., Cambridge University Press, New York, p.199
Jackson C.A., Wall J.V., Shaver P.A., et al., 2002, A&A 386, 97
Jahoda K., Swank J.H., Giles A.B., et al., 1996, In: Siegmund O.H., Gummin M.A. (eds.) Proc. SPIE, Vol. 2808., p.59
Jansen F., Lumb D., Altieri B., et al., 2001, A&A 365, L1
Jansky K.G., 1933, PA 41, 548
Jensen J.B., Tonry J.L., Thompson R.I., et al., 2001, ApJ 550, 503
Jones D.L., Wrobel J.M., Shaffer D.B., 1984, ApJ 276, 480
Jones P.A., McAdam W.B., 1992, ApJS 80, 137
Kadler M., Kerp J., Ros E., et al., 2004a, A&A 420, 467
Kadler M., Ros E., Kerp J., et al., 2002, In: Ros E., Porcas R.W., Lobanov A.P., Zensus J.A. (eds.) Proceedings of the 6th EVN Symposium., p. 167
Kadler M., Ros E., Kerp J., et al., 2005, MemSAI 76, 126
Kadler M., Ros E., Lobanov A.P., et al., 2004b, A&A 426, 481
Kadler M., Ros E., Perucho M., et al., 2008, ApJ 680, 867
Kalberla P.M.W., Burton W.B., Hartmann D., et al., 2005, A&A 440, 775
Kalman D., 2008, The Journal of Online Mathematics and Its Applications 8, ID 1663
Kameno S., Inoue M., Wajima K., et al., 2003, PASA 20, 134
Kameno S., Sawada-Satoh S., Inoue M., et al., 2001, PASJ 53, 169
Kaspi S., Smith P.S., Netzer H., et al., 2000, ApJ 533, 631
Katz U.F., Km3NeT Consortium 2009, In: Giovannelli F., Mannocchi G. (eds.) Frontier Objects in Astrophysics and Particle Physics. Proc. Vulcano Workshop, p. 461
Kedziora-Chudczer L., 2006, MNRAS 369, 449
Kedziora-Chudczer L., Jauncey D., Wieringa M., et al., 1996, IAU Circ. 6418, 2
Kellermann K.I., 1966, Australian Journal of Physics 19, 195
Kellermann K.I., Lister M.L., Homan D.C., et al., 2004, ApJ 609, 539
Kellermann K.I., Pauliny-Toth I.I.K., 1969, ApJ 155, L71
Kellermann K.I., Sramek R., Schmidt M., et al., 1989, AJ 98, 1195
Kellermann K.I., Vermeulen R.C., Cohen M.H., Zensus J.A., 1999, In: Bulletin of the American Astronomical Society, Vol. 31., p. 856
Kellermann K.I., Vermeulen R.C., Zensus J.A., Cohen M.H., 1998, AJ 115, 1295
Kellogg E., Baldwin J.R., Koch D., 1975, ApJ 199, 299
Kerr R.P., 1963, Phys. Rev. Let. 11, 237
Komatsu E., Dunkley J., Nolta M.R., et al., 2009, ApJS 180, 330
Königl A., 1981, ApJ 243, 700
Körding E.G., Jester S., Fender R., 2006, MNRAS 372, 1366
Kormendy J., Richstone D., 1995, ARA&A 33, 581
Kovalev Y.Y., Kellermann K.I., Lister M.L., et al., 2005, AJ 130, 2473
Koyama K., Tsunemi H., Dotani T., et al., 2007, PASJ 59, 23
Kraft R.P., Vázquez S.E., Forman W.R., et al., 2003, ApJ 592, 129

Kraushaar W.L., Clark G.W., Garmire G.P., et al., 1972, ApJ 177, 341
Krishna G., Wiita P.J., 2000, A&A 363, 507
Krolik J.H., 1999, Active Galactic Nuclei : From the Central Black Hole to the Galactic Environment, Princeton University Press, Princeton, NJ, USA
Kuehr H., Witzel A., Pauliny-Toth I.I.K., Nauber U., 1981, A&AS 45, 367
Lasker B.M., 1994, In: Bulletin of the American Astronomical Society, Vol. 26., p. 914
Lauberts A., 1982, ESO/Uppsala survey of the ESO(B) atlas, Garching: European Southern Observatory (ESO), Germany
Laurent P., Rodriguez J., Wilms J., et al., 2011, Science 332, 438
Learned J.G., Mannheim K., 2000, Annual Review of Nuclear and Particle Science 50, 679
Lewis G.F., Williams L.L.R., 1997, MNRAS 287, 155
Lewis K.T., Eracleous M., Sambruna R.M., 2003, ApJ 593, 115
Lin Y.C., Bertsch D.L., Bloom S.D., et al., 1999, ApJ 525, 191
Lister M.L., Aller H.D., Aller M.F., et al., 2009a, AJ 137, 3718
Lister M.L., Homan D.C., 2005, AJ 130, 1389
Lister M.L., Homan D.C., Kadler M., et al., 2009b, ApJL 696, L22
Liu J., 2011, ApJS 192, 10
Lobanov A., 2007, ArXiv 0708.4280
Lobanov A.P., 1998, A&A 330, 79
Lovell J.E.J., Tingay S.J., Piner B.G., et al., 2000, In: H. Hirabayashi, P. G. Edwards, & D. W. Murphy (ed.) Astrophysical Phenomena Revealed by Space VLBI. Proceedings of the VSOP Symposium, p.215
Maiolino R., Risaliti G., Salvati M., et al., 2010, A&A 517, A47
Mannheim K., Biermann P.L., 1992, A&A 253, L21
Mannheim K., Stanev T., Biermann P.L., 1992, A&A 260, L1
Mao L.S., 2011, New Astronomy 16, 503
Markoff S., Nowak M.A., Maitra D., et al., 2011, In: Romero G.E., Sunyaev R.A., Belloni T. (eds.) Jets at all Scales, Proceedings of the International Astronomical Union. IAU Symposium 275, p.250
Markoff S., Nowak M.A., Wilms J., 2005, ApJ 635, 1203
Markowitz A., Uttley P., 2005, ApJ 625, L39
Marscher A.P., 2005, MemSAI 76, 13
Marscher A.P., Gear W.K., 1985, ApJ 298, 114
Marscher A.P., Jorstad S.G., Gómez J.L., et al., 2002, Nat 417, 625
Marshall H.L., Schwartz D.A., Lovell J.E.J., et al., 2005, ApJS 156, 13
Marzke R.O., Geller M.J., Huchra J.P., Corwin, Jr. H.G., 1994, AJ 108, 437
Mattox J.R., Bertsch D.L., Chiang J., et al., 1996, ApJ 461, 396
Mattox J.R., Hartman R.C., Reimer O., 2001, ApJS 135, 155
Mattox J.R., Schachter J., Molnar L., et al., 1997, ApJ 481, 95
Mayall N.U., 1939, Lick Observatory Bulletin 19, 33
McCulloch P.M., Ellingsen S.P., Jauncey D.L., et al., 2005, AJ 129, 2034
McHardy I.M., Koerding E., Knigge C., et al., 2006, Nat 444, 730
Meegan C., Bhat N., Connaughton V., et al., 2007, In: S. Ritz, P. Michelson, & C. A. Meegan (ed.) The First GLAST Symposium. AIP Conf. Series 921, p.13
Messier C., 1781, CdT for 1784, 227
Meyer E.T., Fossati G., Georganopoulos M., Lister M.L., 2011, ApJ 740, 98
Michelson P.F., Atwood W.B., Ritz S., 2010, Reports on Progress in Physics 73, 074901
Migliari S., Fender R.P., 2006, MNRAS 366, 79
Mitsuda K., Bautz M., Inoue H., et al., 2007, PASJ 59, 1
Miyoshi M., Moran J., Herrnstein J., et al., 1995, Nat 373, 127

Morganti R., Killeen N.E.B., Tadhunter C.N., 1993, MNRAS 263, 1023
Morganti R., Oosterloo T.A., Tadhunter C.N., et al., 2001, MNRAS 323, 331
Moskalenko I.V., Strong A.W., Reimer O., 2004, In: Cheng K.S., Romero G.E. (eds.) Cosmic Gamma-Ray Sources, Astrophysics and Space Science Library, Vol. 304., p. 279
Mrozinski R., Mendeck G., Cutri-Kohart R., 2002, In: 34th COSPAR Scientific Assembly, Vol. 34.
Müller C., Böck M., Wilms J., et al., 2012, In: Fermi & Jansky, Vol. eConf C1111101.
Müller C., Kadler M., Ojha R., et al., 2011, A&A 530, L11
Mushotzky R.F., Fabian A.C., Iwasawa K., et al., 1995, MNRAS 272, L9
Mushotzky R.F., Serlemitsos P.J., Boldt E.A., et al., 1978, ApJ 220, 790
Nandra K., O'Neill P.M., George I.M., Reeves J.N., 2007, MNRAS 382, 194
Neumayer N., 2010, PASA 27, 449
Newman E.T., Couch E., Chinnapared K., et al., 1965, J. Math. Phys. 6, 918
Nicastro F., Zezas A., Drake J., et al., 2002, ApJ 573, 157
Nicolson G.D., Glass I.S., Feast M.W., Andrews P.J., 1979, MNRAS 189, 29P
Nieppola E., Valtaoja E., Tornikoski M., et al., 2008, A&A 488, 867
Noble M.S., Houck J.C., Davis J.E., et al., 2006, In: Gabriel C., Arviset C., Ponz D., Enrique S. (eds.) Astronomical Data Analysis Software and Systems XV. ASP Conf. Series 351, p. 481
Noble M.S., Nowak M.A., 2008, PASP 120, 821
Nolan P.L., Abdo A.A., Ackermann M., et al., 2012, ApJS 199, 31
Nolan P.L., Bertsch D.L., Chiang J., et al., 1996, ApJ 459, 100
Oakes D., 1982, Biometrics 38, 451
O'Dea C.P., 1998, PASP 110, 493
Ojha R., Fey A.L., Charlot P., et al., 2005, AJ 130, 2529
Ojha R., Fey A.L., Johnston K.J., et al., 2004a, AJ 127, 3609
Ojha R., Fey A.L., Johnston K.J., et al., 2004b, AJ 127, 1977
Ojha R., Kadler M., Böck M., et al., 2010, A&A 519, A45
Öpik E., 1922, ApJ 55, 406
Oppenheimer J.R., Volkoff G.M., 1939, Physical Review 55, 374
Pariiski I.N., Bursov N.N., Lipovka N.M., et al., 1991, A&AS 87, 1
Peacock J.A., 1999, Cosmological Physics, Cambridge, UK: Cambridge University Press
Pellegrini S., Venturi T., Comastri A., et al., 2003, ApJ 585, 677
Penrose R., Floyd G.R., 1969, Riv Nuovo Cim 1, 252
Perley R.A., 1982, AJ 87, 859
Perlow G.J., Kissinger C.W., 1951, Physical Review 84, 572
Peterson B.A., Jauncey D.L., Condon J.J., Wright A.E., 1976, ApJL 207, L5
Peterson B.M., 1997, An Introduction to Active Galactic Nuclei, Cambridge, New York Cambridge University Press
Petrov L., Hirota T., Honma M., et al., 2007, AJ 133, 2487
Phinney E.S., 1989, In: Meyer F. (ed.) Theory of Accretion Disks, NATO ASI Proc., Vol. 290., p. 457
Piner B.G., Pant N., Edwards P.G., 2008, ApJ 678, 64
Piran T., 2004, Reviews of Modern Physics 76, 1143
Plutarch 2006, The Complete Works Volume 3: Essays and Miscellanies, Paperbackshop.Co.UK Ltd - Echo Library, Fairford, Gloucestershire, UK
Pogge R.W., Maoz D., Ho L.C., Eracleous M., 2000, ApJ 532, 323
Preston R.A., Jauncey D.L., Meier D.L., et al. 1989, AJ 98, 1
Preston R.A., Morabito D.D., Williams J.G., et al., 1985, AJ 90, 1599
Pringle J.E., 1981, ARA&A 19, 137
Pringle J.E., 1997, MNRAS 292, 136

Pringle J.E., Rees M.J., 1972, A&A 21, 1
Pucella G., Vittorini V., D'Ammando F., et al., 2008, A&A 491, L21
Quirrenbach A., Kraus A., Witzel A., et al., 2000, A&AS 141, 221
Readhead A.C.S., 1994, ApJ 426, 51
Resconi E., IceCube Collaboration 2009, Nuclear Instruments and Methods in Physics Research A 602, 7
Reynolds C.S., Miller M.C., 2009, ApJ 692, 869
Ricci R., Prandoni I., Gruppioni C., et al., 2004, A&A 415, 549
Risaliti G., Elvis M., Nicastro F., 2002, ApJ 571, 234
Risaliti G., Woltjer L., Salvati M., 2003, A&A 401, 895
Rodriguez J., Hannikainen D.C., Shaw S.E., et al., 2008, ApJ 675, 1436
Rohlfs K., Wilson T.L., 2004, Tools of radio astronomy, 4th rev. and enl. ed., Berlin: Springer
Romero G.E., Surpi G., Vucetich H., 1995, A&A 301, 641
Ros E., Kadler M., Kaufmann S., et al., 2007, In: Figueras F., Girart J.M., Hernanz M., Jordi C. (eds.) Highlights of Spanish Astrophysics IV., p. 165
Ros E., Marcaide J.M., Guirado J.C., et al., 1999, A&A 348, 381
Rossi B., 1949, Reviews of Modern Physics 21, 104
Rothschild R.E., Blanco P.R., Gruber D.E., et al., 1998, ApJ 496, 538
Rybicki G.B., Lightman A.P., 1979, Radiative processes in astrophysics, Wiley-Interscience, New York
Salpeter E.E., 1964, ApJ 140, 796
Sambruna R.M., Tavecchio F., Ghisellini G., et al. 2007, ApJ 669, 884
Sambruna R.M., Urry C.M., Ghisellini G., Maraschi L., 1995, ApJ 449, 567
Sargent W.L.W., Schechter P.L., Boksenberg A., Shortridge K., 1977, ApJ 212, 326
Scarpa R., Falomo R., Pian E., 1995, A&A 303, 730
Scarpa R., Urry C.M., Falomo R., Treves A., 1999, ApJ 526, 643
Schinzel F., 2011, Ph.D. thesis, Universität zu Köln, Germany
Schmidt M., 1963, Nat 197, 1040
Schödel R., Ott T., Genzel R., et al., 2002, Nat 419, 694
Schwartz D.A., Marshall H.L., Lovell J.E.J., et al., 2000, ApJL 540, L69
Schwarzschild K., 1916, Pr.Akad.Wiss. 1916, 189
Schwinger J., 1949, Phys. Rev. 75, 1912
Scott W.K., Fomalont E.B., Horiuchi S., et al., 2004, ApJS 155, 33
Seyfert C.K., 1943, ApJ 97, 28
Shakura N.I., Syunyaev R.A., 1973, A&A 24, 337
Shapiro, S. L. and Teukolsky, S. A. 1983, Black holes, white dwarfs, and neutron stars: The physics of compact objects, Wiley-Interscience, New York
Shapley H., 1921, The Scale of the Universe, Bull. Nat. Res. Coun. 2, 194
Shaposhnikov N., Titarchuk L., 2007, ApJ 663, 445
Shen Z.Q., Hong X.Y., Wan T.S., 1998a, Chinese Astronomy and Astrophysics 22, 133
Shen Z.Q., Wan T.S., Moran J.M., et al., 1997, AJ 114, 1999
Shen Z.Q., Wan T.S., Moran J.M., et al., 1998b, AJ 115, 1357
Shepherd M.C., 1997, In: Hunt G., Payne H. (eds.) Astronomical Data Analysis Software and Systems VI, ASP Conf. Series 125., p.77
Siebert J., Matsuoka M., Brinkmann W., et al., 1996, A&A 307, 8
Simpson C., Ward M., Clements D.L., Rawlings S., 1996, MNRAS 281, 509
Smith P.S., Hall P.B., Allen R.G., Sitko M.L., 1992, ApJ 400, 115
Smith R.K., Brickhouse N.S., Liedahl D.A., Raymond J.C., 2001, ApJ 556, L91
Sokolovsky K.V., Kovalev Y.Y., Pushkarev A.B., Lobanov A.P., 2011, A&A 532, A38
Sowards-Emmerd D., Romani R.W., Michelson P.F., Ulvestad J.S., 2004, ApJ 609, 564

Sparke L.S., Gallagher, III J.S., 2007, Galaxies in the Universe: An Introduction, Cambridge University Press, Cambridge, UK
Sreekumar P., Bertsch D.L., Dingus B.L., et al. 1998, ApJ 494, 523
Stickel M., Fried J.W., Kuehr H., 1988, A&A 206, L30
Stickel M., Meisenheimer K., Kuehr H., 1994, A&AS 105, 211
Sunyaev R.A., Titarchuk L.G., 1985, A&A 143, 374
Swanenburg B.N., Hermsen W., Bennett K., et al., 1978, Nat 275, 298
Tadhunter C., Dickson R., Morganti R., et al., 2002, MNRAS 330, 977
Tadhunter C., Wills K., Morganti R., et al., 2001, MNRAS 327, 227
Tadhunter C.N., Fosbury R.A.E., di Serego Alighieri S., et al., 1988, MNRAS 235, 403
Takahashi T., Abe K., Endo M., et al., 2007, PASJ 59, 35
Tanaka Y., Inoue H., Holt S.S., 1994, PASJ 46, L37
Tananbaum H., Avni Y., Branduardi G., et al., 1979, ApJ 234, L9
Tavani M., Barbiellini G., Argan A., et al., 2008, Nuclear Instruments and Methods in Physics Research A 588, 52
Tavecchio F., Maraschi L., Wolter A., et al., 2007, ApJ 662, 900
Tchekhovskoy A., McKinney J.C., 2012, MNRAS L445
Tchekhovskoy A., Narayan R., McKinney J.C., 2011, MNRAS 418, L79
Thomasson P., 1986, Q. J. R. Astron. Soc. 27, 413
Thompson A.R., Moran J.M., Swenson, Jr. G.W., 2001, Interferometry and Synthesis in Radio Astronomy, 2nd Edition, Wiley, New York
Thompson D.J., Bertsch D.L., Dingus B.L., et al., 1995, ApJS 101, 259
Thompson D.J., Bertsch D.L., Dingus B.L., et al., 1993a, ApJL 415, L13
Thompson D.J., Bertsch D.L., Fichtel C.E., et al. 1993b, ApJS 86, 629
Thorne K.S., 1974, ApJ 191, 507
Tingay S.J., Edwards P.G., Costa M.E., et al., 1996a, ApJ 464, 170
Tingay S.J., Jauncey D.L., King E.A., et al., 2003, PASJ 55, 351
Tingay S.J., Jauncey D.L., Reynolds J.E., et al., 1996b, AJ 111, 718
Tingay S.J., Jauncey D.L., Reynolds J.E., et al., 1997, AJ 113, 2025
Tingay S.J., Jauncey D.L., Reynolds J.E., et al., 2000, AJ 119, 1695
Tingay S.J., Murphy D.W., Lovell J.E.J., et al., 1998, ApJ 497, 594
Tingay S.J., Reynolds J.E., Tzioumis A.K., et al., 2002, ApJS 141, 311
Tolman R.C., 1939, Physical Review 55, 364
Tombesi F., Sambruna R.M., Marscher A.P., et al., 2012, MNRAS 424, 754
Tornikoski M., Jussila I., Johansson P., et al., 2001, AJ 121, 1306
Tornikoski M., Lähteenmäki A., Lainela M., Valtaoja E., 2002, ApJ 579, 136
Treves A., Morini M., Chiappetti L., et al., 1989, ApJ 341, 733
Trümper J., 1982, Advances in Space Research 2, 241
Tueller J., Baumgartner W.H., Markwardt C.B., et al., 2010, ApJS 186, 378
Tully R.B., 1988, Nearby galaxies catalog, Cambridge University Press, Cambridge and New York
Tzioumis A., King E., Morganti R., et al., 2002, A&A 392, 841
Tzioumis A., Morganti R., Tadhunter C., et al., 1996, In: Ekers R.D., Fanti C., Padrielli L. (eds.) Extragalactic Radio Sources, IAU Symposium 175., p.73
Tzioumis A.K., Jauncey D.L., Preston R.A., et al. 1989, AJ 98, 36
Tzioumis A.K., King E.A., Reynolds J.E., et al., 1998, In: Zensus J.A., Taylor G.B., Wrobel J.M. (eds.) IAU Colloq. 164: Radio Emission from Galactic and Extragalactic Compact Sources, ASP Conf. Series 144., p.179
Ubertini P., Lebrun F., Di Cocco G., et al., 2003, A&A 411, L131
Ulrich M.H., 1981, A&A 103, L1
Urry C.M., Padovani P., 1995, PASP 107, 803

Uttley P., Wilkinson T., Cassatella P., et al., 2011, MNRAS 414, L60
Vanden Berk D.E., Richards G.T., Bauer A., et al., 2001, AJ 122, 549
Vermeulen R.C., Ogle P.M., Tran H.D., et al., 1995, ApJL 452, L5
Vermeulen R.C., Ros E., Kellermann K.I., et al., 2003, A&A 401, 113
Verner D.A., Ferland G.J., Korista K.T., Yakovlev D.G., 1996, ApJ 465, 487
Véron-Cetty M.P., Véron P., 2006, A&A 455, 773
Vestrand W.T., Sreekumar P., 1999, Astroparticle Physics 11, 197
Vestrand W.T., Stacy J.G., Sreekumar P., 1995, ApJL 454, L93
Voges W., Aschenbach B., Boller T., et al., 1999, A&A 349, 389
Voges W., Aschenbach B., Boller T., et al., 2000, VizieR Online Data Catalog 9029, 0
von Kienlin A., Meegan C.A., Lichti G.G., et al., 2004, In: G. Hasinger & M. J. L. Turner (ed.) Society of Photo-Optical Instrumentation Engineers (SPIE) Conference Series, Vol. 5488., p.763
von Montigny C., Bertsch D.L., Chiang J., et al., 1995, ApJ 440, 525
Wall J.V., 1994, Australian Journal of Physics 47, 625
Wall J.V., Danziger I.J., Pettini M., et al., 1986, In: Swarup G., Kapahi V.K. (eds.) Quasars, IAU Symposium 119., p.59
Wandel A., Urry C.M., 1991, ApJ 367, 78
Wang J., Yaqoob T., Szokoly G., et al., 2003, ApJL 590, L87
Waxman E., 2007, Science 315, 63
Weaver K.A., Wilson A.S., Henkel C., Braatz J.A., 1999, ApJ 520, 130
Weekes T.C., Badran H., Biller S.D., et al., 2002, Astroparticle Physics 17, 221
Wegner G., Bernardi M., Willmer C.N.A., et al., 2003, AJ 126, 2268
Weidinger M., Spanier F., 2010, A&A 515, A18
White G.L., Jauncey D.L., Wright A.E., et al., 1988, ApJ 327, 561
Wielebinski R., Junkes N., Grahl B.H., 2011, Journal of Astronomical History and Heritage 14, 3
Wilkes B.J., 1986, MNRAS 218, 331
Wilkes B.J., Elvis M., Fiore F., et al., 1992, ApJL 393, L1
Wilks S.S., 1938, Ann. Math. Statist. 9, 60
Willick J.A., Courteau S., Faber S.M., et al., 1997, ApJS 109, 333
Wills B.J., Wills D., Breger M., et al., 1992, ApJ 398, 454
Wills K.A., Morganti R., Tadhunter C.N., et al., 2004, MNRAS 347, 771
Wilms J., Allen A., McCray R., 2000, ApJ 542, 914
Wilms J., Pottschmidt K., Pooley G.G., et al., 2007, ApJ 663, L97
Wilson A.S., Young A.J., Shopbell P.L., 2001, ApJ 547, 740
Winkler C., Courvoisier T.J.L., Di Cocco G., et al., 2003, A&A 411, L1
Winter L.M., Mushotzky R.F., Reynolds C.S., 2006, ApJ 649, 730
Wolter H., 1952, Annalen der Physik 445, 94
Wrobel J.M., 1984, ApJ 284, 531
Xie G.Z., Li K.H., Bai J.M., et al., 2001, ApJ 548, 200
Yaqoob T., George I.M., Nandra K., et al., 1999, ApJL 525, L9
Yaqoob T., George I.M., Turner T.J., et al., 1998, ApJL 505, L87
York D.G., Adelman J., Anderson, Jr. J.E., et al., 2000, AJ 120, 1579
Young A.J., Wilson A.S., Tingay S.J., Heinz S., 2005, ApJ 622, 830
Zensus J.A., Ros E., Kellermann K.I., et al., 2002, AJ 124, 662
Ziółkowski J., 2005, MNRAS 358, 851

Acknowledgements

First of all, I want to thank my supervisors Jörn Wilms and Matthias Kadler. I am grateful that they gave me the opportunity to work in the field of astronomy. Thanks to the help of my supervisors, I could attend several scientific conferences, present parts of my work, and establish contacts to international scientists. With their complementary expertise in different energy ranges, Jörn Wilms and Matthias Kadler were excellent supervisors of this multiwavelength work, and I profitted greatly from their knowledge and experience. Their friendly nature completed the pleasant working atmosphere.

My colleagues at the Dr. Karl Remeis-Observatory made me really enjoy my working time at this institute, for that I want to thank all of them. First and foremost, I thank my former office colleague Manfred Hanke. Especially in the early phase of my work, I benefited from his outstanding understanding of physics and computing. In particular, I am grateful for his help with *ISIS*, *S-Lang*, and *SLxfig*. Secondly, I thank Thomas Dauser for fruitful discussions, especially about fluorescence lines from accretion disks. Furthermore, I thank all my other colleagues, e.g., Felix Fürst for discussions about X-ray analyses, Christian Schmid for his explanations of X-ray instruments, Cornelia Müller for the good collaboration in the field of radio astronomy, Alex Markowitz for helpful advice about X-ray studies of AGN, Victoria Grinberg for the work on Cygnus X-1, Michael Wille for help with *Python* and *git*, Fritz Schwarm for suggestions about parallel computing, Christoph Grossberger for his work on jet kinematics, Matthias Kühnel for programming hints, and Andreas Irrgang for discussions about the analysis of optical spectra. The effort of the system administrators was highly appreciated. Many thanks to Ingo Kreykenbohm, Manfred Hanke, Thomas Dauser, and Fritz Schwarm for mainting of the computer system and the local cluster, which was intensively used for this work. Furthermore, I thank all members of the groups of Matthias Kadler and Karl Mannheim at the University of Würzburg, who always made me feel welcome.

I highly appreciate the effort of all those who read this work and contributed to improve it with numerous helpful comments and suggestions. For this help I thank Manfred Hanke, Jörn Wilms, Matthias Kadler, Irmela Bues, Cornelia Müller, and Thomas Dauser.

Financially, I acknowledge funding from the Bundesministerium für Wirtschaft und Technologie through the Deutsches Zentrum für Luft- und Raumfahrt (DLR) under contract 50OR0808. Additionally to the primary funding of my work by the DLR, I thank Matthias Kadler for managing subsequent funding for two months at the University of Würzburg. Furthermore, I thank the Max-Planck-Gesellschaft for a stipend at the Max-Planck-Institut für Radioastronomie in Bonn covering the final phase of this work.

I thank RadioNet and the organizors of YERAC 2009 for funding my stay at this conference in Porto 2009. USRA funded my stay in Washington and thus made the attendance at the *Fermi* Symposium 2009 possible. In addition, USRA funded the subsequent stay in Greenbelt. For the one-week visit of NASA Goddard Space Flight Center I thank Neil Gehrels and Matthias Kadler. Many thanks to Dave Thompson for the very interesting tour through NASA's satellite construction and testing laboratory. The Max-Planck-Institut für Radioastronomie partially funded my contribution to the 2010 Fermi-meets-Jansky conference in Bonn. I want to thank the COST

Action MP0905 – Black Holes in a Violent Universe, for a grant for my proposed Short Term Scientific Mission (STSM). This funding made a two-week exchange visit at the Universitat de València possible. During this stay I worked with Eduardo Ros, to whom I want to give many thanks for his excellent introduction into the usage of $\mathcal{AIPS}$. I strongly benefited from his experience in radio astronomy. I thank all members of the Osservatorio di Cagliari, as I always felt welcome there. In particular, I am grateful to Andrea Possenti, Federica Govoni, and Matteo Murgia for making my visits at this institute possible. Many thanks to Valentina Vacca for help with the usage of $\mathcal{AIPS}$ and suggestions concerning the CIAO X-ray Data Analysis Software. I thank the DAAD, who accepted and funded my proposed RISE project. I would like to thank Sherwood Andrew Richers, whom I could supervise for three months within the scope of this project, for his great work.

My work as a member of research teams and within collaborations was always a pleasure. I want to thank the complete TANAMI team for the excellent collaboration, especially Roopesh Ojha for the cooperative work, his enthusiam, the explanations of VLBI observations and their scheduling, and his hospitality during my stay in Washington. The work with the MOJAVE team was very fruitful for me. I could always count on helpful suggestions and good ideas. In this context, I thank especially Matt Lister and Tuomas Savolainen. The work within the *Fermi*/LAT collaboration was important for me, as well. I learned a lot from many collaboration members. In particular, I would like to thank Gino Tosti, who made a visit at the University of Perugia possible, where he explained to me the analysis methods of *Fermi*/LAT data in detail. I am very grateful for his help and the elaborate replies to my numerous questions during the subsequent months.

I would like to thank the Elite Network of Bavaria for the membership in the Elite Graduate Program "Physics with Integrated Doctorate Program", which led me to the University of Erlangen-Nürnberg, where I could work in the field of astronomy.

Finally, I acknowledge the many tools and services that have been used throughout this work. The SAO/NASA Astrophysics Data System[1] as well as the high-energy data browser[2] of NASA's High Energy Astrophysics Science Archive Research Center have been frequently used. This research has made use of data from the MOJAVE database that is maintained by the MOJAVE team (Lister et al., 2009a). The *Fermi*/LAT Collaboration acknowledges support from a number of agencies and institutes for both development and the operation of the LAT as well as scientific data analysis. These include NASA and DOE in the United States; CEA/Irfu and IN2P3/CNRS in France; ASI and INFN in Italy; MEXT, KEK, and JAXA in Japan; and the K. A. Wallenberg Foundation, the Swedish Research Council, and the National Space Board in Sweden. Additional support from INAF in Italy and CNES in France for science analysis during the operations phase is also gratefully acknowledged by the *Fermi*/LAT Collaboration. This research has made use of the NASA/IPAC Extragalactic Database (NED) which is operated by the Jet Propulsion Laboratory, California Institute of Technology, under contract with the National Aeronautics and Space Administration. This research has made use of data from the University of Michigan Radio Astronomy Observatory which has been supported by the University of Michigan and by a series of grants from the National Science Foundation, most recently AST-0607523.

[1] http://adsabs.harvard.edu/preprint_service.html
[2] http://heasarc.gsfc.nasa.gov/cgi-bin/W3Browse/w3browse.pl